

A STOCHASTIC FAILURE
INVESTIGATION OF COMPOSITES
UNDER COMBINED
COMPRESSION-SHEAR LOADS

Von der Fakultät für Bauingenieurwesen und
Geodäsie

der

Gottfried Wilhelm Leibniz Universität Hannover

zur Erlangung des akademischen Grades

DOKTOR-INGENIEUR
(DR.-ING.)

genehmigte Dissertation

von

NABEEL SAFDAR, M.SC.

2022

Referent: Prof. Dr.-Ing. habil. Raimund Rolfes
Institut für Statik und Dynamik
Gottfried Wilhelm Leibniz Universität Hannover

Korreferent: Prof. Michael Wisnom
Bristol Composites Institute (ACCIS)
University of Bristol

Tag der Promotion: 28.09.2022

Read! in the name of your Lord who created Man from a clinging
substance.

Read: Your Lord is most Generous,- He who taught by the pen-
Taught man that which he knew not.

Al-Quran 96:1-5

Knowledge is of no value unless you put it into practice.

Anton Chekhov

ABSTRACT

Because of their excellent specific strength and stiffness properties, fiber-reinforced polymers (FRPs) have become increasingly material of choice for advanced industries such as aerospace and wind turbines. One of the design limiting factors in FRPs is their lower compression strength in comparison to their tensile strength. Microbuckling (MB) is the dominant failure mode in unidirectional FRPs under predominant compression loads. The main factors dictating failure under compression dominated loads are the fiber misalignment and the nonlinear material behavior. Because of high sensitivity of MB failure to the fiber misalignment, the MB strength shows uncertainty. To enable reliable failure prediction, a quantification of the strength uncertainty is required.

The current investigation aims for a probabilistic prediction of MB failure under axial compression and combined compression-shear loads. Using a newly in-house developed combined loading fixture, a statistically significant number of specimens was tested under aforementioned load cases. Using the experimental strain measurements, a probabilistic failure envelope in strain space is presented. Results of the axial compression load case are interpreted in the context of the notion of the effective misalignment angle using an analytical model. A failure envelope in stress space is derived using an analytical solution for the combined compression-shear load cases and the effective global misalignment angle calculated from the measurements. Other experimental aspects of the problem are also investigated such as the material characterization and measurements of the fiber misalignment.

To represent the fiber misalignment in numerical models for the prediction of MB strength while preserving the spatial correlation information, the spectral representation method is employed in this investigation. A large number of realizations were developed based on spectral densities calculated from the measurements of the fiber misalignment. The numerically determined probabilistic failure envelopes in stress and strain spaces are presented with lower percentiles of distributions of failure. The failure envelopes are also compared against classical failure criteria from the literature to highlight the limitations of the classical criteria.

Since the sizes of the model and the experimental specimen were different, a comparison of numerically predicted strengths against experimentally obtained results under the axial compression loads was performed on the basis of a scaling law. A discussion on differences in the shape of the failure envelopes is provided. Conclusions are drawn at the end and an outlook for further research on the topic is given.

KEYWORDS: Fiber-reinforced polymers (FRPs); Microbuckling (MB); Compression and Shear; Probabilistic failure envelopes; Statistical properties/CT analysis

ZUSAMMENFASSUNG

Faserverstärkte Verbundwerkstoffe (CFK/GFK) sind aufgrund ihrer ausgezeichneten spezifischen Festigkeits- und Steifigkeitseigenschaften zunehmend zum bevorzugten Material für hochentwickelte Industrien wie die Luft- und Raumfahrt und Windkraftanlagen geworden. Einer der konstruktionsbegrenzenden Faktoren bei CFK/GFK ist ihre geringere Druckfestigkeit im Vergleich zu ihrer Zugfestigkeit. Microbuckling (MB) ist die vorherrschende Versagensart bei unidirektionalen CFK/GFK unter vorherrschenden Druckbelastungen. Die Hauptfaktoren, die das Versagen bei Druckbelastungen diktieren, sind die Faserimperfectionen und das nichtlineare Materialverhalten. Aufgrund der hohen Empfindlichkeit des MB-Versagens gegenüber der Faserimperfectionen ist die MB-Festigkeit mit Unsicherheit behaftet. Um eine zuverlässige Versagensvorhersage zu ermöglichen, ist eine Quantifizierung der Festigkeitsunsicherheit erforderlich.

Die aktuelle Studie zielt auf eine probabilistische Vorhersage des Versagens von MB unter axialer Druck- und kombinierter Druck-Schub-Belastung ab. Unter Verwendung einer neu entwickelten kombinierten Prüfvorrichtung wurde eine statistisch signifikante Anzahl von Proben unter den vorgenannten Lastfällen geprüft. Anhand der experimentellen Dehnungsmessungen wird eine probabilistische Versagenskurve im Dehnungsraum dargestellt. Die Ergebnisse des axialen Druckbelastungsfalls werden im Zusammenhang mit dem Begriff des effektiven Versatzwinkels anhand eines analytischen Modells interpretiert. Unter Verwendung einer analytischen Lösung für den kombinierten Druck-Schub-Lastfall und des aus den Messungen berechneten effektiven globalen Versatzwinkels wird eine Versagenshüllkurve im Spannungsraum abgeleitet. Andere experimentelle Aspekte des Problems werden ebenfalls untersucht, wie z. B. die Materialcharakterisierung und Messungen der Faserimperfectionen.

Um die Faserimperfectionen mit Berücksichtigung auf räumliche Korrelationsinformation in numerischen Modellen zur Vorhersage der MB-Festigkeit darzustellen, wird in dieser Untersuchung die Methode der spektralen Darstellung verwendet. Auf der Grundlage von Spektraldichten, die aus den Messungen der Faserverschiebung berechnet wurden, wurde eine große Anzahl von Realisierungen erstellt. Die numerisch ermittelten probabilistischen Versagenskurven in Spannungs- und Dehnungsräumen werden mit unteren Perzentilen der Versagensverteilungen dargestellt. Die probabilistische Versagenskurven werden auch mit klassischen Versagenskriterien aus der Literatur verglichen, um die Grenzen der klassischen Kriterien aufzuzeigen.

Da die Größen des Modells und der experimentellen Probe unterschiedlich waren, wurde ein Vergleich der numerisch vorhergesagten Festigkeiten mit den experimentell ermittelten Ergebnissen unter den axialen Druckbelastungen auf der Grundlage eines Skalierungsgesetzes durchgeführt. Es wird eine Diskussion über die Unterschiede in der Form der Versagenskurven geführt. Abschließend werden Schlussfolgerun-

gen gezogen und ein Ausblick auf weitere Forschungsaktivitäten zu diesem Thema gegeben.

SCHLAGWORTE: Faserverstärkte Verbundwerkstoffe; Microbuckling (MB); Druck und Schub; Probabilistische Versagenskriterien; Statistische Eigenschaften/CT-Analyse

ACKNOWLEDGEMENTS

First of all, I would like to thank Almighty Allah, the most beneficent and the most merciful, for providing me with strength and capability to complete the objectives put forth in this thesis.

A lot of people supported me through technical and personal advice, encouragement, and specially valuable critique during the course of my doctoral research. First and foremost, I would like to express my sincere and deepest gratitude to my doctoral supervisor Prof. Dr.-Ing. habil. Raimund Rolfes for never ending support and constant encouragement throughout. I am most grateful for his kind demeanor and for his contentment while seeing me grow in this phase of my career. I could not have imagined having a better adviser and mentor for my doctoral studies.

An important stage of my journey was a six month research stay at École normale supérieure Paris-Saclay (at the time in Cachan, France) under the supervision of Professeur de classe Exceptionnelle Olivier Allix. His priceless supervision through very interesting and frank discussions during my time in Cachan contributed immensely to my further development. The two very different styles of work and thought process which I accumulated in Germany and France are reflected in this work.

A special place in these acknowledgements should undoubtedly be held for Dipl.-Ing. Dr. Benedikt Daum for his scientific supervision and moral support especially at some very critical stages of my work. If it hadn't been for him, I would not have made it to the end. I also would like to thank Dr.ir. Eelco Jansen for his invaluable help during my first years at ISD. A special thanks goes to Dr.-Ing. Aamir Dean for help in the further development and calibration of the material model. Other colleagues who supported me through this journey such as Dr.-Ing. Sven Scheffler, Martin Brod, Christian Gerendt, and Jens Bryer along with the rest of ISD also deserve my acknowledgement.

Last but not least, I would like to give my special thanks to my family, especially to my mother and my late father, who always believed in me and supported me unconditionally in the most difficult of times. I would also like to thank my beloved wife and my siblings for constant encouragement and support.

This doctoral work was financially supported in the first three years by the German Research Foundation (DFG) in the course of the project International Research and Training Group (IRTG1627). Its support is gratefully acknowledged. The financial support during last two years of my work by ISD through state funding is also graciously acknowledged.

CONTENTS

Abstract	v
Zusammenfassung	vii
Acknowledgements	ix
List of figures	xiii
List of tables	xxii
Acronyms	xxiv
1 GENERAL INTRODUCTION	1
1.1 Motivation and Aim	1
1.2 Structure of the thesis	3
2 STATE OF THE ART	5
2.1 Phenomenology	5
2.2 Modeling of compression failure	8
2.2.1 Analytical models	8
2.2.2 Numerical models	10
2.3 Measurements of material imperfections	18
2.4 Experimental testing under axial compression	20
2.5 Failure under combined compression-shear loads	22
2.5.1 Experimental testing to failure under combined compression-shear	23
2.5.2 Analytical and numerical modeling of failure under combined	
compression-shear	25
2.6 Aims and objectives of the work	26
3 MATERIALS AND MEASUREMENTS	31
3.1 Mechanical properties characterization	31
3.2 Fiber misalignment measurements	35
4 QUANTIFICATION OF STATISTICAL PROPERTIES OF THE FIBER MISALIGNMENT	47
4.1 Spectral analysis of the measured fiber misalignment	49
4.1.1 Characterization of spectral densities in 3D frequency domain . .	49
4.1.2 Deficiency of characterizing spectral densities in 2D frequency	
domain	56
4.2 Generation of topology of the fiber misalignment	58
4.2.1 Generation of the volumetric misalignment topology	59
4.2.2 Generation of the planar misalignment topology	60
5 EXPERIMENTAL DETERMINATION OF FAILURE	65
5.1 Methodology	65
5.1.1 Specimen geometry	66
5.1.2 Fixture development	68

5.1.3	Testing procedure	71
5.2	Results and discussions	73
5.2.1	Design variables for testing to failure	74
5.2.2	Mode of failure in different load cases	76
5.2.3	Comparison of failure stresses for different load cases	78
5.2.4	Observing the formation of the kink band using DIC system	80
5.2.5	Failure envelope in the strain space	82
5.2.6	Interpretation of the axial compression load case results	84
5.2.7	An approximation of the failure envelope in the stress space	87
6	NUMERICAL MODELING OF PROBABILISTIC FAILURE ENVELOPES	91
6.1	Modeling methodology	91
6.1.1	Model geometry	92
6.1.2	Material model	94
6.2	Results and discussion	103
6.2.1	Effect of the misalignment dimensionality on prediction of the compression strength	103
6.2.2	Comparison of compression strength prediction of 3D numerical models	105
6.2.3	Stress-strain behavior of representative models under axial compression and combined compression shear	107
6.2.4	Probabilistic failure envelope in stress space using numerical modeling	108
6.2.5	Probabilistic failure envelope in strain space using numerical modeling	111
6.2.6	Assumption of functional forms for spectral densities	113
7	COMPARISON OF EXPERIMENTAL AND NUMERICAL APPROACHES	125
7.1	Comparison: numerical vs experimental using Weibull scaling	125
7.2	Comparison of failure envelopes	128
8	CONCLUSIONS AND OUTLOOK	133
8.1	Conclusions	133
8.2	Outlook	136
A	APPENDIX	139
A.1	Algorithm for generation of topologies	139
	BIBLIOGRAPHY	145
	Curriculum Vitae	159
	Publications	161
	Eidesstattlicheversicherung	163

LIST OF FIGURES

Figure 1.1	Usage of different materials in Boeing 787 Dreamliner. Dark colors represent components made of the corresponding material [20].	2
Figure 2.1	Fibre buckling modes according to Rosen [92]. In Fig. 2.1a the ‘extensional’ or ‘symmetrical’ mode is shown. It is only of theoretical interest for high volume fraction FRPs. In Fig. 2.1b the ‘shear’ mode is depicted. Shear mode is relevant MB failure mode in high volume fraction FRPs.	6
Figure 2.2	Representation of key stages in the microbuckling (MB) failure. Manufacturing induced initial misalignment θ_0 induces shear in the matrix leading to material hardening, see Fig. 2.2a. Fibers rotate at the location of initial misalignment under compression loads, leading to a localization into a shear band (also known as kink band) around peak load increasing the angle θ , see schematic in Fig. 2.2b and an optical microscopy image by Sun et. al. [105] near peak load in Fig. 2.2d. After or at peak load, debonding and/or fiber fracture occurs as sketched in Fig. 2.2c and shown by an optical microscopy image after peak load in Fig. 2.2e [105].	7
Figure 2.3	Splitting failure mode in the experiments of Oguni and coworkers [86]	8
Figure 2.4	Longitudinal stress against longitudinal strain under pure compression for different global misalignment values by Bishara et. al. [16]. Symbol λ represents amplitude of the modeled sine wave, and L represents model length. The figure shows typical snap-back response observed in modeling of the compression failure of FRPs and the dependency of the peak load on the modeled fiber misalignment.	12
Figure 2.5	A model by Allix et. al. [7] with random distribution of the fiber misalignment spread over the volume without consideration of correlation and corresponding response of the model under axial compression	18
Figure 2.6	Schematic of load transfer methods common in compression testing	23

Figure 2.7	Schematic of the test setup and the resulting failure envelope by Vogler et. al. [116, 118]. Experimental results are shown as markers in Fig. 2.7b whereas FE predictions using 2D and 3D modeling are shown through the lines. The horizontal axis represents applied shear stress and the vertical axis represents applied axial compression.	24
Figure 2.8	Schematic of the numerical modeling framework. The fiber misalignment characterized as spectral densities in frequency domain are used as an input to generate distributions of the misalignment in the spatial domain. The distributions are mapped onto a FE model, and the models are simulated under different load conditions to generate probabilistic failure envelopes in stress and strain spaces.	29
Figure 3.1	Stress-strain response	33
Figure 3.2	Results of the shear characterization tests	34
Figure 3.3	Schematic of the misalignment angles. Angles $\tilde{\theta}_{k,l,m}^i$ and $\tilde{\phi}_{k,l,m}^i$ are the misalignment in 1 – 2 and 1 – 3 planes, respectively. The angle $\tilde{\psi}_{k,l,m}^i$ shows the combined effect of $\tilde{\theta}_{k,l,m}^i$ and $\tilde{\phi}_{k,l,m}^i$	35
Figure 3.4	Schematic of the specimen for scanning, along with the dimensions of the scanned cylindrical volume	37
Figure 3.5	The 3D nature of the fiber misalignment is shown by Fig. 3.5a. The extracted cross sectional planes are marked on the scanned volume in Fig. 3.5a. Direction 1 indicates fiber direction, direction 2 represents the in-plane transversal direction and direction 3 points to the out-of-plane transversal direction. Stacking directions are marked in corresponding color of arrows of the coordinate system. (The original image of the scanned volume was provided by IfB, LUH). Fig. 3.5b shows schematic of the HRMA method for the measurements of the fiber misalignment on the images extracted from the scanned 3D volume.	38
Figure 3.6	3D contour plots of the in-plane misalignment $\theta_{k,l,m}$. Results shown here were measured over the cuboid-shaped domains extracted from the scanned cylindrical volumes. The dimensions of the cuboids are listed in Table 3.2. To view the interior of the topologies of the misalignment, $1/8^{th}$ of the domains are not shown. One can observe that the topologies of the misalignment angles show clear three dimensional behavior.	42

Figure 3.7	3D contour plots of the out-of-plane misalignment $\phi_{k,l,m}$. Misalignment angles were measured over the cuboid-shaped domains extracted from the scanned cylindrical volumes. The dimensions of the cuboids are provided in Table 3.2. To highlight the interior of the topologies of the misalignment, $1/8^{th}$ of the domains are cut out. It is clearly observable that topologies of the misalignment angles show clear three dimensional behavior.	43
Figure 3.8	Histograms of the in-plane misalignment $\theta_{k,l,m}$ and the out-of-plane misalignment $\phi_{k,l,m}$, along with the corresponding fits to the normal distributions. All data sets were transformed to zero mean, i.e. mean fiber direction. Note that the out-of-plane misalignment is more closely related to the normal distribution compared to the in-plane misalignment.	45
Figure 4.1	Examples of some standard functions and their autocorrelation $R(\tau)$. The τ axis in the bottom row plots represents number of total discrete points over which the function has been sampled and corresponds to the lag distances.	48
Figure 4.2	Sketch of a cuboid volume selected from a scanned cylindrical volume. The cylindrical scanned volume was obtained over a cuboid shape $[0]_4$ unidirectional FRP laminate by performing a CT scan.	52
Figure 4.3	Spectral density plots from the 3D spectral density data on planes $\omega_1=0$, $\omega_2=0$, and $\omega_3=0$. Spectral densities were calculated from the 3D fields of the in-plane misalignment angle $\theta_{k,l,m}$ and the out-of-plane misalignment angle $\phi_{k,l,m}$	54
Figure 4.4	Spectral density plots from the 3D spectral density data on axes ω_1 , ω_2 , and ω_3 . Spectral densities were calculated from the 3D fields of the in-plane misalignment angle $\theta_{k,l,m}$ and the out-of-plane misalignment angle $\phi_{k,l,m}$	55
Figure 4.5	2D spectral density plots. Spectral densities were calculated from the 2D fields of the in-plane misalignment angle $\theta_{k,l}^{2D}$ and the out-of-plane misalignment angle $\phi_{k,l}^{2D}$	58
Figure 4.6	Measured and virtually generated 3D contour plots of the in-plane misalignment angle $\theta_{k,l,m}$ and the out-of-plane misalignment angle $\phi_{k,l,m}$. Measurements were performed using CT scans and the angles were calculated using the HRMA method [127], also see Section 3.2. The spectral representation method was used for the generation of virtual topologies of the misalignment angles. It is evident that the misalignment fields depend on all three coordinate directions.	61

Figure 4.7	Measured and virtually generated 2D contour plots of the $\theta_{k,l}^{2D}$ and the $\phi_{k,l}^{2D}$. Measurements were performed using CT scans and the angles were calculated using the HRMA method [127] from the micrographs. The spectral representation method given by Liu et. al. [76] was used for the generation of virtual topologies of the 2D misalignment angles.	63
Figure 5.1	Schematic of the jig design for tabbing the testing to failure specimens. The jig proved helpful in achieving very high accuracy of the required gauge length. The location of a specimen to be cut is shown with dotted lines. A schematic of the specimen at the cross-section A-A is shown in Fig. 5.2.	67
Figure 5.2	Schematic of the testing to failure specimen with adhesive and tabbing. The cross section A-A of the Fig. 5.1 indicates the viewing direction. The outline of the jig is represented by the blue dashed lines.	67
Figure 5.3	Assembled view of the fixture design	68
Figure 5.4	Exploded view of the fixture along with different loading positions. Load was applied in global $1'$ direction. The local directions are defined on the specimen where 1 is in the nominal fiber direction, and 2 and 3 are the in-plane and the out-of-plane transverse directions, respectively. The rotations in case A and B are 30° and 45° , respectively.	70
Figure 5.5	The newly developed CLMAF for the axial compression and combined compression-shear load cases. In these images, a specimen is being tested under the combined compression-shear case B i.e. 45° load case.	71
Figure 5.6	Twice the out-of-plane displacements d_3 normalized by the average thickness t of a specimen during a test under the axial compression load at three points along the length of a specimen i.e. near the upper and lower clamps and at the middle of the specimen. The out-of-plane displacements were extracted using the DIC system on the surface of the specimen. The horizontal axis correspond to the image number captured during the DIC measurement.	72
Figure 5.7	Effect of tab taper angle on the strength under axial compression load	76

Figure 5.8	Gauge sections of the failed specimens showing microbuckling failure mode. (a), (b) and (c) show a specimen each from the axial compression series (0° load case), the combined compression-shear case A series (30° load case), and the combined compression-shear case B series (45° load case), respectively. The white spots are reminiscent from the paint used to create speckle pattern for the DIC system measurements.	77
Figure 5.9	Fracture surface of a specimen from the combined compression-shear case B series (45° load case). The laser scan was performed by the Institut für Werkstoffkunde, LUH.	78
Figure 5.10	Comparison of the applied far field stresses in the loading direction $\sigma_{1'1'}$. (a) represents empirical probability of survival of the applied stress $\sigma_{1'1'}$ for all three load cases. The values of $\sigma_{1'1'}$ were measured using the load cell of the machine. (b) shows the respective probability density functions fitted to each load case.	79
Figure 5.11	Images taken at different stages of a test under the combined compression-shear load case B (i.e. 45° load case), along with the shear strain field. The applied displacement was in $1'$ direction. (a) shows the frame just before the peak load. Localization of the in-plane shear in the form of a band is apparent from the contour plot. (b) shows the post peak failed specimen. The final failure location is in the same place as the localized shear band in (a).	82
Figure 5.12	Failure envelope in ε_{11} - ε_{12} plane based on the experimental results. Scatter points represent strains of corresponding specimens at failure for each load case. The solid lines are based on fitted equations at 25^{th} , 50^{th} (median), and 75^{th} percentiles of distributions of failure.	85
Figure 5.13	Analytical solutions of Eq. 5.3. (a) shows the histogram of the strength under the axial compression σ_{11}^c . (b) shows prediction of the compression strength against the misalignment angles implied by one of the two considered solution methods for Eq. 5.3. Projecting (a) on (b) yields (c). Image (c) shows the histograms of the inferred misalignment angles using Eq. 5.3 pertaining to the experimentally obtained strengths.	88
Figure 5.14	Derived failure envelope in σ_{11} - σ_{12} plane based on the experiments. Yellow scatter points represent median strengths for each load case. The solid (yellow) line is based on the fitted equation on median strengths, whereas dashed lines represent approximations for 25^{th} and 75^{th} percentiles of distribution of failure.	90

Figure 6.1	Schematic of the FE model geometry used for the development of probabilistic failure envelopes. (a) depicts a $[0]_4$ laminate with large in-plane dimensions compared to the thickness in 3-direction. The laminate consists of representative volumes which are periodic in directions $\mathbf{1}$ and $\mathbf{2}$. One such volume is marked in dark blue color. (b) illustrate the geometry of the representative volume used in numerical modeling. The contour of an in-plane distribution of the fiber misalignment angles is plotted on the back planes of the cuboid shaped volume. The direction $\mathbf{1}$ is the nominal fiber direction, and $\mathbf{2}$ and $\mathbf{3}$ are the in-plane and the out-of-plane transverse directions, respectively. The FE mesh is shown with the grid on the back planes of the cuboid with blue lines.	92
Figure 6.2	Schematic of a fiber (in black color) misaligned from the nominal fiber direction $\mathbf{1}$ to direction $\mathbf{1}'$	95
Figure 6.3	Generalized schematic of the deformed preferred direction in an element of a FE model. Dotted black line illustrates the preferred direction of the misaligned fiber \mathbf{a}' before the rigid body rotations and the shear rotations. The solid black line depicts the preferred direction of the misaligned fiber \mathbf{b}' after applying the combined effect of the in-plane $\Delta\theta^i$ and the out-of-plane $\Delta\phi^i$ rigid body rotations and the shear rotations ε_{12}^i and ε_{13}^i	101
Figure 6.4	Compression strength prediction of a single element model against the prediction using the analytical model. The results in (b) show that the prediction using the FE model with the aforementioned shear rotation correction of the material model shows a very good match with the prediction of the analytical model. This result verifies the accuracy of the FE model for prediction of compression strength, hence, it can be employed for later analyses incorporating complex topologies of the fiber misalignment.	102
Figure 6.5	Contour plots of 1D and 2D sine waves for 2D modeling, and 2D and 3D sine waves for 3D modeling of the in-plane misalignment angle θ . The maximum misalignment in each case is 2.5° and the minimum misalignment in each case is -2.5°	104
Figure 6.6	Comparison of results for compression strength σ_{11}^c from 2D and 3D models each containing a sinusoidal undulation with 1D, 2D and 3D characteristics	106
Figure 6.7	Empirical probability of survival $P(\sigma_{11}^c)$ over the compression strength σ_{11}^c along with the fitted 2-parameter Weibull distributions	107
Figure 6.8	Stress stain response of the model	108

Figure 6.9 Probabilistic failure envelope in stress space. Results of all realizations from each load case are plotted as black dots which fuse to form curve segments. The median of each load case is shown with hollow circles on the curve segments. The envelope was divided into two regions and functional forms of failure envelopes were defined for each region. A dashed line, which passes through median value of load case 45° , shows division between failure envelope regions MB1 and MB2. Using the functional forms of MB1 and MB2 given in Eq. 6.35a and Eq. 6.35b, a color code depicting the probability of failure $P(f_i)$ is plotted. 109

Figure 6.10 Probabilistic failure envelope in strain space. Failure strains of all realizations from each load case are plotted as black dots which fuse to form line segments. The median of each load case is shown with hollow circles. The failure envelope in strain space was divided into regions MB1 and MB2 by a white dashed line passing through the median value of load case 45° . The black dashed lines depict the loading direction of load cases $\arctan(u_2/u_1)=30^\circ, 75^\circ, \text{ and } 85^\circ$. A color code depicting the probability of failure $P(g_i)$ is plotted using the functional forms of MB1 and MB2 given in Eq. 6.36a and Eq. 6.36b. 112

Figure 6.11 Plots of assumed functional forms of spectral densities. The figures show spectral densities in plane $\omega_1 - \omega_2$ with anisotropic cutoff values of the frequencies i.e. ω_{c1} not equal to ω_{c2} . The cutoff frequencies as well as the initial value of spectral density are also marked in the figures. In these figures $\omega_3=0$, and is disregarded to allow 3D plots. 114

Figure 6.12 Virtually generated 3D contour plots of the in-plane misalignment angle $\theta_{k,l,m}$ using empirical forms of the spectral density as an input. The spectral representation method was used for the generation of virtual topologies of misalignment angles. For comparison with a virtually generated topology based on the experimentally characterized spectral densities, see Fig. 4.6b. . . 116

Figure 6.13 Virtually generated 3D contour plots of the in-plane misalignment angle $\phi_{k,l,m}$ using empirical forms of the spectral density as an input. The spectral representation method was used for the generation of virtual topologies of the misalignment angles. For comparison with a virtually generated topology based on the experimentally characterized spectral densities, see Fig. 4.6d. 118

Figure 6.14	Empirical probability of survival $P(\sigma_{11}^c)$ over the compression strength σ_{11}^c for models with cutoff frequencies and models without cutoff frequencies. The survival probability using the reference <i>avg</i> model is also plotted for comparison.	119
Figure 6.15	Empirical probability of survival $P(\sigma_{11}^c)$ over the compression strength σ_{11}^c for models with cutoff frequencies and different scaled values of the mean square spectral densities Ξ^θ and Ξ^ϕ	121
Figure 6.16	1^{st} , 50^{th} (median), and 99^{th} percentiles of the distribution of the compression strength σ_{11}^c as a function of Ξ based on results of models with cutoff frequencies and different scaled values of the mean square spectral densities Ξ^θ and Ξ^ϕ . The corresponding values from each cases are plotted as scatter points on each curve.	123
Figure 7.1	Comparison of σ_{11}^c from numerical models against experimental results using the Weibull scaling law. Parameter m is known as the Weibull modulus or the shape parameter. The Weibull scaling law is implied by, but not to be confused with, the Weibull strength distribution itself. The fitted Weibull strength distribution to the experimentally determined σ_{11}^c is presented in Fig. 5.10b and numerically calculated σ_{11}^c is plotted in Fig. 6.7.	127
Figure 7.2	Comparison of experimentally and numerically determined failure envelopes in ε_{11} - ε_{12} plane. The experimentally determined failure envelope was presented in Fig. 5.12 and the numerically obtained failure envelope was plotted in Fig. 6.10. The color code depicting the probability of failure $P(g_i)$ is based on numerical results and represents the numerical failure envelope. The solid lines represent experimental failure envelope at 25^{th} (in color magenta), 50^{th} (white), and 75^{th} (black) percentiles of distributions of failure.	129
Figure 7.3	Comparison of experimentally and numerically determined failure envelopes in σ_{11} - σ_{12} plane. The experimentally determined failure envelope was presented in Fig. 5.14 and the numerically obtained failure envelope was plotted in Fig. 6.9. The color code depicting the probability of failure $P(f_i)$ is based on numerical results and represents the numerical failure envelope. The solid lines represent an approximation of the experimental failure envelope at 25^{th} (in color magenta), 50^{th} (white), and 75^{th} (black) percentiles of distributions of failure.	130

Figure 8.1	Schematic of follow-up works. [Fig. (a) →(b)] Numerical determination of a statistical scaling law. [Fig. (a) and (b) →(d) →(e)] Development of a Stochastic First Ply Failure (FPF) criterion for homogeneously stressed laminate plates. [Fig. (a) →(b) →(c) →(f)] Numerical determination of a scaling law in the geometrical and the transition regimes. 137
------------	--

LIST OF TABLES

Table 2.1	Micromechanical models for prediction of the compression strength	14
Table 2.2	Homogenized models for prediction of the compression strength	16
Table 2.3	Different methods for measurements of material imperfections in FRPs	21
Table 3.1	Material properties from the characterization tests. The values E_{11} , E_{22} , R_{22} , G_{12} , and ν_{12} were obtained from the characterization tests. The equivalences $E_{22}=E_{33}$, $R_{22}=R_{33}$, and $G_{12}=G_{13}$ are based on the assumption of transversal isotropy.	34
Table 3.2	Dimensions of the scanned volume	38
Table 3.3	Statistics of the measurements of the fiber misalignment angles before shifting means of the misalignment to zero	40
Table 3.4	Statistics of the measurements of the fiber misalignment angles after shifting means of the misalignment to zero. It is to be noted that the standard deviation of the $\theta_{k,l,m}$ and $\phi_{k,l,m}$ for both specimens remain unchanged as shifting the mean of a distribution does not change it's spread i.e. standard deviation. Moreover, the average values of $\theta_{k,l,m}$ and $\phi_{k,l,m}$ have only meaning to them when the mean of the corresponding data sets has been transformed to zero.	44
Table 4.1	Calculation of different frequency values for the lengths of the measured volume and corresponding number of sampling points	53
Table 4.2	Statistics of the 3D fiber misalignment angles and the corresponding spectral parameters	57
Table 4.3	Statistics of the 2D fiber misalignment angles and the corresponding spectral parameters. The standard deviations of the in-plane and the out-of-plane misalignment are same as the complete data-sets given in Table 3.4 as the complete CT scan data was used in 2D calculations.	59
Table 5.1	Effect of bolt torque and testing speed on failure under the axial compression. The best choice values used in the rest of the testing to failure campaign are shown in the dark green color. .	75
Table 5.2	The table lists fit parameters of the three probability distributions on each load case, and the corresponding goodness of fit (gof) in percentage. The gof highlights the probability of a data set belonging to the respective probability distribution function.	81
Table 5.3	Fit parameters of Eq. 5.1 for median, 25 th , and 75 th percentile of distribution of failure envelopes in ε_{11} - ε_{12} plane	84

Table 6.1	Yielding parameters ζ_i at the onset of yielding for the carbon fiber UD300/M79 epoxy material	100
Table 6.2	Plastic potential parameters ς_i for the carbon fiber UD300/M79 epoxy material	100
Table 6.3	Statistics of the fiber misalignment angles and the corresponding spectral parameters. The mean value in all cases is 0° . Mean square spectral density Ξ^θ is a measure of fiber misalignment in frequency domain, and it is directly proportional to square of the standard deviation s^θ of the misalignment angle θ , cf. Eq. 4.12.104	
Table 6.4	Statistics of the axial compression strengths σ_{11}^c for different numerical models	107
Table 6.5	Fit parameters of 6.35 for 1^{st} , 50^{th} (median) and 99^{th} percentile of distribution of the failure envelope in the σ_{11} - σ_{12} plane	110
Table 6.6	Fit parameters of Eq. 6.36 for 1^{st} , 50^{th} (median) and 99^{th} percentile of distribution of the failure envelope in the ε_{11} - ε_{12} plane	113
Table 6.7	Mean and standard deviations of different models using functional forms of spectral densities with and without cutoff frequencies	119
Table 6.8	Mean and standard deviations of the compression strength σ_{11}^c for models based on functional forms of the spectral densities with cutoff frequencies. Mean squares of the spectral densities were scaled to observe effects of resulting mean and standard deviation of numerically predicted distributions of the compression strength.	121
Table 6.9	1^{st} , 50^{th} (median), and 99^{th} percentiles of the distribution of the compression strength σ_{11}^c for different models	123

ACRONYMS

BC	Boundary Condition
CFK	(German: Carbonfaserverstärkter Kunststoff)
CFRP	Carbon fiber-reinforced polymer/plastic
FE	Finite element
FEM	Finite element method
FRP	Fiber-reinforced polymer/plastic
GFK	(German: Glasfaserverstärkter Kunststoff)
GFRP	Glass fiber-reinforced polymer/plastic
ISD	Institute of Structural Analysis (German: Institut für Statik und Dynamik)
MB	Microbuckling
MD	Multidirectional
RP	Reference point
UD	Unidirectional
UMAT/VUMAT	User-defined material subroutine
USDFLD	User-defined field subroutine

GENERAL INTRODUCTION

1.1 MOTIVATION AND AIM

Advanced structural components are increasingly being made out of fiber reinforced polymers (FRPs) because of their exceptionally high strength and stiffness to weight ratios. The fields of applications of FRPs include highly loaded components in advanced engineering structures such as blades of wind turbines, structural components of modern rockets, and fins, rudders and fuselage panels of modern aircrafts, among others [20, 102]. Economic and environmental factors are the main driving factors behind this rapid shift in industry from metals and alloys towards composites. The advantages of using FRPs in advanced structures are typified by modern aircrafts such as Airbus A380 and Boeing 787 Dreamliner with more than half of their structures by weight comprising of FRPs, see Fig. 1.1.

The structures are generally made of multidirectional (MD) laminates undergoing complex stress states during service. Unidirectional (UD) layers are the building blocks of the MD laminates. The UD layers mainly support axial loads in the nominal fiber direction of the layer. However, the compression strength of UD layers can be as low as 60% of their tensile strength [24]. Because of this reason, strength under compression is a highly relevant mechanical property.

During the early days of commercial usage of FRPs, the strength under compression was predicted based on simple assumptions of fibers considered as straight beams supported by elastic matrix. Such predictions differed significantly from experimental observations of compression strength. These differences in combination with varying values of experimentally observed strengths lead to highly conservative design practices.

Fibers and matrix comprise different materials with differences in their thermal properties. Different manufacturing techniques, such as prepreg lamination or resin transfer moulding (RTM) or 3D printing, are employed for manufacturing components from FRPs. The matrix is cured in all the techniques by application of heat and pressure, either in autoclaves or through other means such as laser heating. Heating and cooling during these manufacturing processes expands and contracts fibers and matrix at different rates. This gives rise to misalignment of fibers which in turn is a decisive factor in lower value of strength under compression dominated loads along with material nonlinear shear behavior. With this knowledge at hand, the prediction models for compression behavior improved over time. With the rapid advances in computing and rise of numerical modeling, the effects of different parameters were explored further in detail. The effects of fiber misalignment on variation in strength

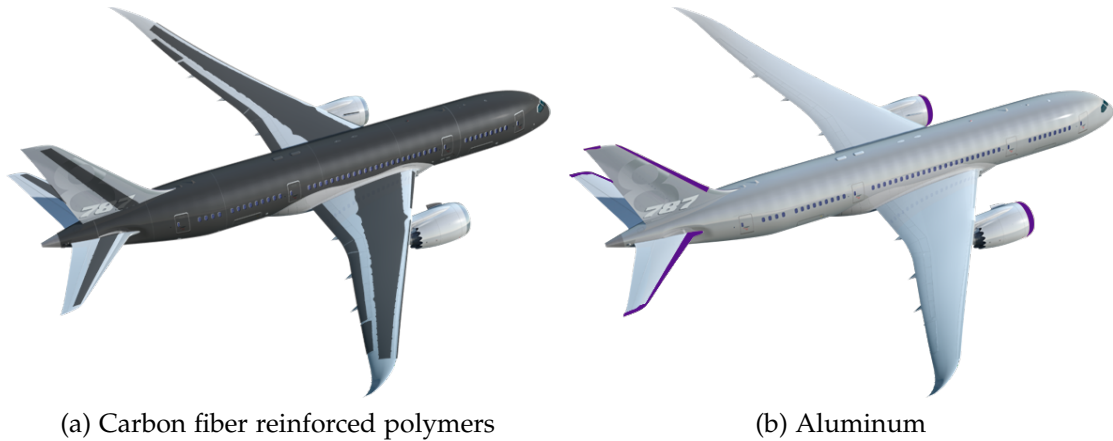


Figure 1.1: Usage of different materials in Boeing 787 Dreamliner. Dark colors represent components made of the corresponding material [20].

were also researched. However, mostly idealized or random representation of the fiber misalignment was modeled. For quantification of compression failure in an accurate manner, realistic representation of the fiber misalignment in the numerical models is needed .

In order to perform highly detailed analysis, the exact information about the extent of the fiber misalignment in the volume of a material is required. Modern scanning techniques such as confocal laser microscopy or computer tomographic scans allow for performing volumetric measurements over significant sizes for quantifying the fiber misalignment. Using a suitable scanning technique, the material imperfections in the form of the fiber misalignment can be characterized and used in prediction tools for failure under compression dominated loads.

Since failure under compression loads is a stochastic quantity, therefore, quantification of the variation in strengths under compression loads is of utmost importance. The variation of strengths is not only limited to axial compression loads, but also affects the failure under combined loads where compression is dominant. The non-linear shear behavior of FRPs, specifically the local yielding of the matrix material, is decisive in compression failure. Hence, failure under combined compression-shear application of loads becomes of high interest. Therefore, detailed failure analyses under these load cases need to be performed.

Experimental investigation generally serve as a reference. For this purpose, detailed experimental testing under combined compression-shear loads is needed to round off this work.

The main aim of this work, therefore, is the development of an experimental and a numerical methodology to determine the probabilistic failure envelopes under combined compression-shear loads for unidirectional fiber reinforced polymers. Using the peak load carrying capacity (i.e. strength) of the UD layers, the probabilistic failure envelopes are determined in the form of criterion. The strength of the material under

predominant compression loads is at the core of the current work. Other post peak related phenomenon of the MB failure, such as band orientation, band width, lock-up angle, band propagation stress, are out of scope of this work.

In this thesis, different aspects of the problem ranging from characterization of the fiber misalignment to realistic representation of said misalignment in numerical models are tackled. Detailed numerical analyses as well as experimental testing under combined loading were carried out to come up with the descriptions of probabilistic failure envelopes. The proposed methodologies are meant to expand the existing knowledge about failure under compression and combined compression-shear loads on one hand, and to quantify the uncertainties of the failure under aforementioned loads on the other, to finally exploit the true potential of FRP based structures to their full extent.

1.2 STRUCTURE OF THE THESIS

This thesis is divided into eight chapters.

After the brief introduction in chapter 1, chapter 2 presents a detailed overview of the current state of the art. First, the phenomenology of failure under compression loads is stated. Modeling of compression failure using different approaches is discussed next, followed by the measurements of material imperfection in the form of the fiber misalignment. The history of experimental testing of failure under pure axial compression is briefly discussed. The different approaches employed by researchers for investigating failure under combined compression-shear loads are presented. Finally, the open questions from the state of the art and the related objectives of the current work are listed.

Chapter 3 starts of with the choice of the material investigated and the specimen manufacturing technique. It is followed by the characterization of mechanical properties of the material, including the nonlinear shear behavior. Since the fiber misalignment along with nonlinear shear behavior of the material are the key factors affecting failure under compression dominated loads, three dimensional measurements of the fiber misalignment using computer tomography scans are presented.

In chapter 4, the statistical properties of the fiber misalignment are quantified in the form of spectral densities. Spectral densities have an additional advantage of preserving spatial correlation of a quantity over the commonly used representation of mean and standard deviations. Using the spectral representation method with the characterized spectral densities as an input, the topologies of the fiber misalignment are generated for 3D and 2D.

Chapter 5 and 6 can be considered as the core work of this thesis. In chapter 5, the experimental determination of failure is investigated. Building on the existing methods for testing of failure under compression, a novel testing concept for failure under combined compression-shear is presented. Besides pure axial compression, two distinct cases of combined compression-shear loads are considered. Experiments are

carried out in a probabilistic manner and results are shown in different forms, such as a comparison of the resulting failure stresses of different load cases, among others. Failure envelopes in stress and strain spaces based on experimental testing to failure are presented and the expression forms of failure envelopes are given.

Chapter 6 focuses on the numerical modeling aspects of the work. It starts off by presenting the representative finite element model and discussing the material model employed. A comparative investigation on using 2D and 3D modeling using homogenized modeling approach is presented. Comparison of 3D models based on different inputs of spectral densities of the measurements of the fiber misalignment is followed by a comparison of the stress-strain behavior of a representative 3D model under different load cases. Finally, failure envelopes in strain and stress spaces using numerical modeling are presented. Using the results of numerical modeling, functional forms of failure envelopes are defined. A color code to represent the probability of failure is also given in the figures representing numerical failure envelopes.

Chapter 7 provides a comparison of the results from the experimental and the numerical approaches. Since the sizes of specimens in experimental testing and numerical modeling are different, the comparison of failure under axial compression is carried out using a scale law. This is followed by a discussion of differences in the shapes of the resulting failure envelopes from both approaches. The effects of a shift in mean fiber misalignment on failure prediction using the numerical model are also presented.

Chapter 8 rounds off the work by drawing conclusions and summarizing major findings. At the end, open questions are shortly discussed, giving an outlook into further investigations for future works.

Fiber reinforced composite structures generally comprise multidirectional (MD) laminates loaded in complex stress states during their lifetime. The MD laminates consists of unidirectional (UD) layers. The UD layers support axial loads in the nominal fiber direction of the corresponding layers. Therefore, failure of UD layers is the of primary importance. Hence, a literature review on the failure analysis of unidirectional fiber reinforced polymers (FRPs) plies under predominant compression loads is given in this chapter. Different aspects related to the compression failure of unidirectional FRPs are reviewed, such as experimental characterization and testing, analytical and numerical modeling. Open questions and objectives are finally drawn based on the literature review. At first, the basic terminologies relevant to the compression failure are presented.

2.1 PHENOMENOLOGY

Before reviewing further details related to modeling, imperfection measurements, and testing to failure of FRPs, the phenomenology pertaining to the failure under compression loads is presented. Since FRPs display compression strengths significantly lower than the tensile strengths, compression failure becomes a critical design criterion. Typical FRPs comprise stiff fibers (carbon, glass, ceramic etc.) embedded in compliant matrix. Ideally, in unidirectional FRPs, the fibers should be completely aligned with the nominal fiber direction. However, the misalignment is introduced in the fibers during manufacturing. This misalignment, besides the material nonlinearities, is responsible for the lower compression strengths compared to their tensile strength.

The most common failure mode for FRPs under compression loads is known as microbuckling (MB). Rosen [92] stated that, in principle, MB can transpire along two competing modes as shown in Fig. 2.1. In the transverse extensional mode, the neighboring fibers deform in opposite directions resulting in a half wavelength phase shift in-between the fibers as sketched in Fig. 2.1a. In the shear mode of MB failure, all the fibers deform in the same direction and the resulting deformed fibers are without a phase shift as can be seen in Fig. 2.1b. In modern industrial grade FRPs with high fiber volume fractions, only shear mode of MB is relevant. A schematic representation of different stages of the shear mode MB failure is shown in Fig. 2.2. In an idealized form, the misalignment is represented as an initial angle θ_0 as shown in Fig. 2.2a. When compression load is applied, misaligned fibers rotate and induce shear stresses in the matrix. With increasing amount of compression loads, the material hardens and the shear stresses localize in the form of a shear band (also known in literature as kink

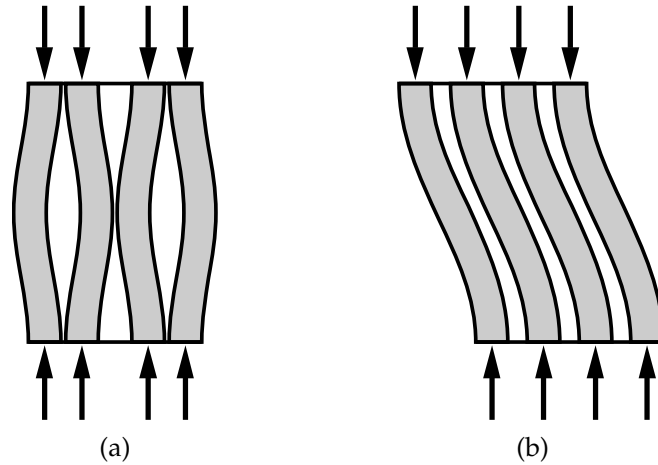


Figure 2.1: Fibre buckling modes according to Rosen [92]. In Fig. 2.1a the ‘extensional’ or ‘symmetrical’ mode is shown. It is only of theoretical interest for high volume fraction FRPs. In Fig. 2.1b the ‘shear’ mode is depicted. Shear mode is relevant MB failure mode in high volume fraction FRPs.

band), see schematic in Fig. 2.2b and an optical microscopy image by Sun et. al. [105] near peak load. When the geometrical softening in the misaligned region out paces the material hardening in the incipient shear band, failure occurs with a sudden drop in applied load [24, 36, 46]. The carried peak load at which failure occurs defines the compression strength of the material. The MB failure shows a sharp snap-back behavior in the stress-strain response [16]. The fibers break in bending at both ends of the shear band way past the peak load resulting in compression and tension surfaces of the failed fibers, see schematic in Fig. 2.2c and an optical microscopy image after peak load in Fig. 2.2e. The compression strength of the material is at the core of the current work. Other terminologies associated with the MB failure mode, such as band orientation, band width, lock-up angle, band propagation stress, are related to post peak analysis and are hence, out of scope of this work. Further discussions and elaborations on these terminologies can be found in the cited literature [33, 46].

Although shear mode MB is the most common failure mode for frequently used glass or carbon fiber FRPs, other failure modes can be observed for some loading conditions or typical composites. Such an example can be found in the works of Piggot [88], who observed failure in the form of fiber crushing for weak fibers embedded in strong matrices along with longitudinal debonding of fiber matrix interfaces. Oguni and coworkers [86] investigated 50% E-glass/Vinylester laminates and found failure mode transitioning from only splitting to MB upon change of load from uniaxial to multi-axial loading as seen in Fig. 2.3. Splitting was also shown to initiate MB failure as shown in Fig. 2.3b. Prabhakar and Waas [90] analyzed competing failure modes of MB and splitting through micromechanical models at different model sizes. Although there are no hard defined limits of existence of different failure modes in FRPs, fiber crushing and splitting tend to occur in FRPs comprising weak fibers in stronger matrix

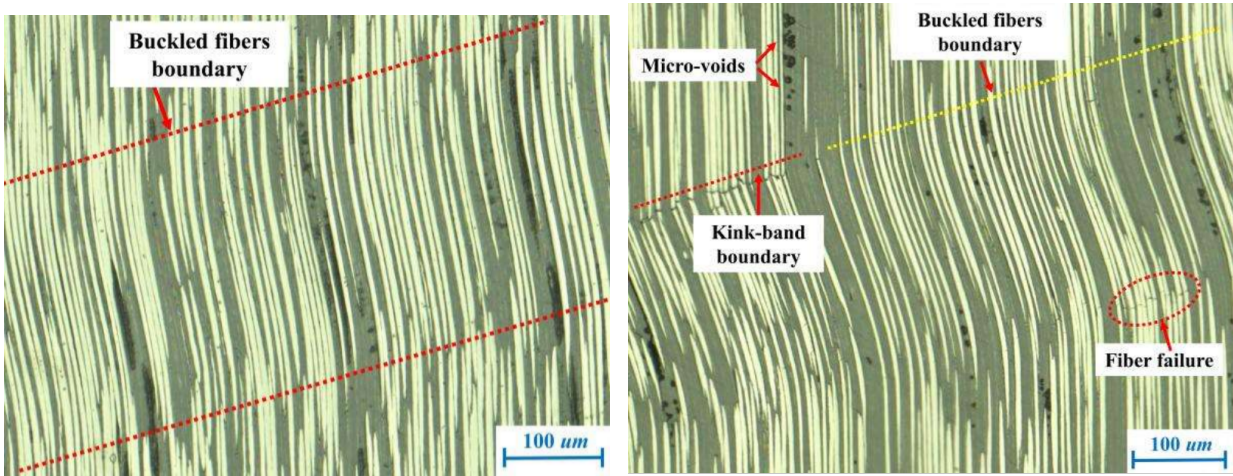
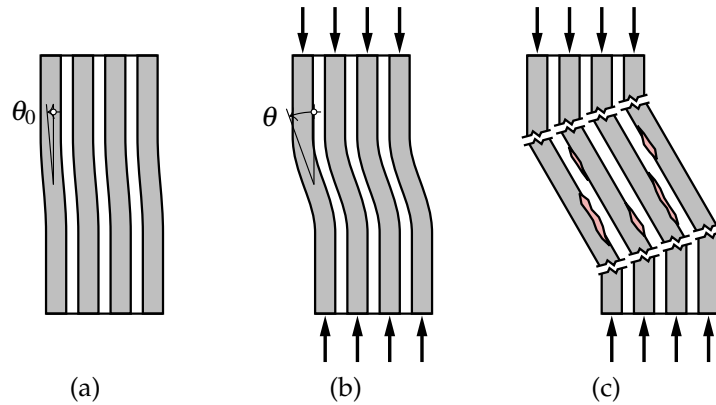
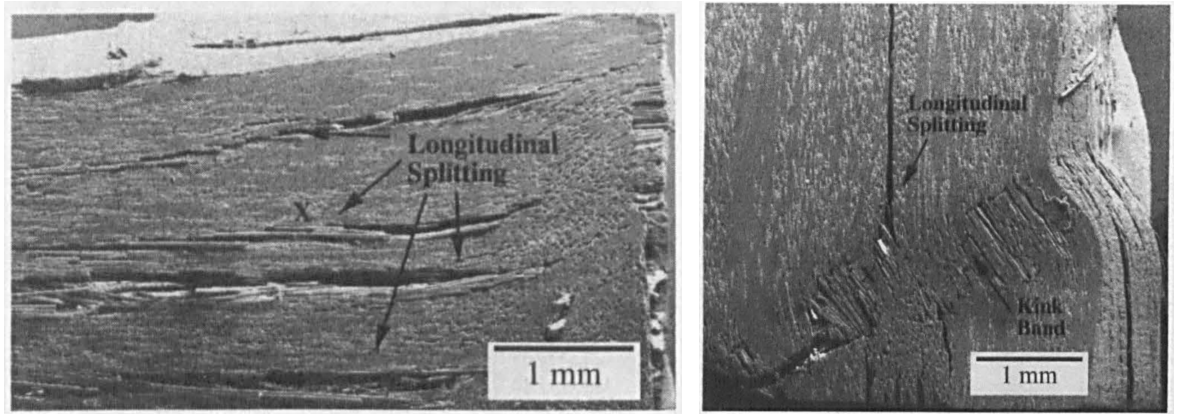


Figure 2.2: Representation of key stages in the microbuckling (MB) failure. Manufacturing induced initial misalignment θ_0 induces shear in the matrix leading to material hardening, see Fig. 2.2a. Fibers rotate at the location of initial misalignment under compression loads, leading to a localization into a shear band (also known as kink band) around peak load increasing the angle θ , see schematic in Fig. 2.2b and an optical microscopy image by Sun et. al. [105] near peak load in Fig. 2.2d. After or at peak load, debonding and/or fiber fracture occurs as sketched in Fig. 2.2c and shown by an optical microscopy image after peak load in Fig. 2.2e [105].



(a) Failed specimen with only longitudinal splitting (b) Longitudinal splitting induced kink band formation

Figure 2.3: Splitting failure mode in the experiments of Oguni and coworkers [86]

and for low to medium fiber volume fractions. Hence, fiber crushing and splitting as competing modes of failure need to be considered for such materials.

2.2 MODELING OF COMPRESSION FAILURE

The failure of industrial grade high volume fraction FRPs is a complex multi-staged phenomenon. The complexities and high relevance for industrial applications led to extensive research on the topic over the course of multiple decades. The modeling of compression failure has been done extensively using analytical and numerical techniques. A concise review of the literature with a focus on these modeling techniques for compression failure is carried out below.

2.2.1 Analytical models

The lower compression strength compared to tension strength was first observed by Dow and Gruntfest [83]. This observation rose interest in modeling the failure under compression for FRPs. The first modeling prediction using a closed form analytical solution is credited to Rosen [92]. Two modes of MB failure were defined by Rosen, namely the transverse extensional mode and the shear mode. The model is based on the assumption of perfectly aligned elastic fibers embedded inside an elastic matrix material. Failure is considered to be the elastic buckling of the fibers and a simple empirical solution for compression strength was suggested as:

$$\sigma_{11}^c = \frac{G_m}{1 - v_f} \quad (2.1)$$

where σ_{11}^c is the compression strength, G_m is the shear modulus of the matrix and v_f is the fiber volume fraction. This model overestimates strength by a factor of as much as

4 [21]. Moreover, the experimentally observed strength variations can not be explained through this model. Other similar models considering failure under compression to be an elastic MB phenomenon can also be found in literature [57, 58, 64, 96], however, these models add minor improvements on the pioneering analysis of Rosen [92].

Argon [8] realized the importance of initial misalignment of fibers θ_0 and the shear behavior of the matrix for prediction of strength under compression. Based on the argument of plastic microbuckling of initially misaligned elastic fibers embedded in a matrix with elastic-perfect plastic shear behavior having yield strength τ_y , the strength under compression was given by the Eq. 2.2a. Refining Argon's model further to include the effects of shear nonlinearity of matrix $\tau_{12}(\gamma)$ as a function of shear angle γ , Budiansky [21, 23] presented a generalized solution given in Eq. 2.2b. In this model, the total fiber rotation is given by the initial fiber misalignment θ_0 and the matrix shear deformation γ . The matrix nonlinearity is modeled generally by ideal plasticity or a nonlinear Ramberg-Osgood plasticity model. In case of nonlinear plasticity, the compression strength is given by solving the maximization problem over γ . In case of ideal plasticity, Budiansky's model of Eq. 2.2b regresses to Argon's model of Eq. 2.2a.

$$\sigma_{11}^c = \frac{\tau_y}{\theta_0} \quad (2.2a)$$

$$\sigma_{11}^c = \max_{\gamma} \left(\frac{\tau_{12}(\gamma)}{\theta_0 + \gamma} \right) \quad (2.2b)$$

The variation in experimental outcomes of testing for compression strength can be explained by dependence on initial misalignment θ_0 as suggested by Argon's and Budiansky's models.

Building on the previous works of Rosen and Budiansky, among others, Steif [103, 104] presented a theoretical model to investigate failure under compression. Using a single misaligned fiber as a representative, analysis was carried out in two parts. In the first part of the analysis [103], the strain at the failure was calculated and found to be similar to experimentally observed failure strains in FRPs. In the second part of the analysis [104], the focus was on the calculation of strains at final failure. It was argued by Steif that the fibers break in tension at the ends of the kink band, and the fiber breakage was recognized to be the limiting step in failure under compression. Experimental evidence [52] and numerical analysis [16] by later authors suggests that fibers break in bending with tension and compression surfaces.

Effect of fiber bending stiffness on the compression failure was studied analytically by Fleck et. al. [47]. Using a smeared representation of homogenized fiber-matrix material, the corresponding equation system was developed. Fiber diameters were introduced as an intrinsic length scale, giving rise to couple stresses. Considering or neglecting fiber bending stiffness gave rise to classification of the terms 'kinking theory' and 'bending theory', respectively. Detailed analysis using these models showed that for typical undulations of fibers found in common composites, fiber bending stiffness has negligible effect on prediction of compression strength and can be neglected.

Fiber bending stiffness is, however, important for prediction of other aspects of the compression failure, such as kink band width and kink band orientation. Further comprehensive reviews on analytical modeling can be found in the cited literature [24, 33, 46, 97].

2.2.2 Numerical models

With the availability of computational capabilities and use of numerical techniques such as finite element modeling, the numerical prediction of failure under compression loads became common since the 90s. Numerical modeling of compression failure can be broadly categorized into two types of approaches namely, micromechanical approaches and homogenized approaches.

2.2.2.1 *Micromechanical numerical models*

2D and 3D micromechanical models represent a section of a single UD-ply with layers of fiber and matrix sections. These models result from the intent of direct micromechanical representation of involved mechanisms at microscale. Such models allow for accurate representation of different failure mechanisms, such as MB, splitting, and fiber crushing. The key challenges with such approaches are associated with difficulty in characterizing the material properties of constituent fiber, matrix and their interfaces separately. A summary of micromechanical approaches is presented in Table 2.1.

Following their experimental outcomes on compression failure [70, 71], Kyriakides and coworkers modeled the FRPs as alternating periodic layers of imperfect fibers inside a matrix in 2D to predict the failure under compression loads [69, 71]. Different variations of the model with linear and nonlinear material properties for fiber and matrix were analyzed. The effect of fiber nonlinearity was found to be negligible, whereas the nonlinearity of the matrix material modeled as elastic-plastic isotropic solid (J_2 flow theory of plasticity) had significant effects on failure prediction. These predictions were in line with the earlier analytical predictions [21]. The effects of the fiber misalignment were studied by modeling the fibers as a uniform idealized sinusoidal (infinite band), and as a sinusoidal misalignment with decaying amplitudes in the transverse direction starting at different locations of the model. Strong dependence of compression failure on the fiber misalignment was found. The same group of Kyriakides et. al. continued the analysis further on failure under compression. The differences between the predictions of 2D and 3D models were analyzed by Hsu et. al. [59]. The effect of matrix compressibility was investigated by Vogler et. al. [117] through a 3D model by using a dilatant Drucker-Prager material model, and it was found to affect kink band properties. More importantly, it was found out that the nonlinear material properties of the pure matrix resin differ from those of the in-situ matrix. Transversal propagation of kink band originating from a local imperfection at an edge was also studied in this model. The phenomena in post peak response relat-

ing to plateau stress and band broadening were investigated by Hsu et. al. [60] using a 3D plane strain micromodel with periodic boundary conditions.

Micromechanical approaches generally assume a periodic arrangement of alternating fibers and matrix layers in the models. To verify the effects of this idealistic modeling assumption about fiber topology, Lee and Waas [72] modeled non-uniform fiber spacing and found it to have an insignificant effect on the prediction of the compression strength. Following this work, Yerramalli and Waas [136] compared modeling of 2D plane strain and 3D model of a cylindrical specimen. Fibers were modeled as orthotropic, whereas matrix was modeled with J_2 -plasticity. Matrix hardening curves were calibrated to the torsion response from an experimental specimen. It was concluded that the fiber bending stiffness and the complex 3D stress state in the matrix have significant effects on the peak load prediction. Since the model dimensions used were below half a millimeter, these results are in line with the bending theory of Fleck et. al. [47]. These results showing effects of the fiber bending stiffness have a theoretical importance, but the undulations found in common composites are on the order of a few millimeters at which scale the kinking theory of Fleck et. al. [47] becomes relevant and fiber bending stiffness can be neglected, see Section 2.2.1.

Feld et. al. [44] investigated the dependence of the peak load and dissipated energies on the initial fiber misalignment using a simplified 2D micromechanical model. The model considered the influence of a shear pre-stress in combination with an inelastic constitutive behavior of the matrix modeled using the damage theory. The dependence of the peak load on the fiber misalignment and the shear pre-stress was shown via statistical analysis. Wind et. al. [129] used a finite strain model, based on the work of Jensen and Christoffersen [63], in a plane strain micromechanical setting to investigate the relationship between fiber rotation and kink band angle. The band angle was found to be dependent on the width of the region of initial misalignment. It was also found that the condition of the volumetric incompressibility in the laminate holds approximately i.e. band angle was half of the observed fiber rotations.

Although most of the micromechanical models found in literature focus on modeling fibers and matrix with plasticity theory, some authors opted for interface debonding and matrix damage. Matrix damage and debonding between fibers and matrix can be considered as a diffuse phenomenon at a microscopic scale, either distributed over a region of the model or in a localized space. Prabhakar and Waas [90] modeled interaction between kinking and splitting failure through the use of a 2D stripes model with cohesive interfaces depicting mode I and mode II debonding. The matrix nonlinearity was accounted for using J_2 -plasticity. Parametric studies were performed by varying the interface strengths for mode I and mode II. The results showed that when lower values of interface strength of mode II were used, fiber matrix debonding competed with MB failure. It was concluded that in such cases, splitting failure mode in the form of fiber matrix debonding should also be accounted for in addition to kinking failure mode. Pimenta et. al. [89] also investigated the effects of debonding competing with MB failure in their 2D plane strain models. Bishara et. al. [16] per-

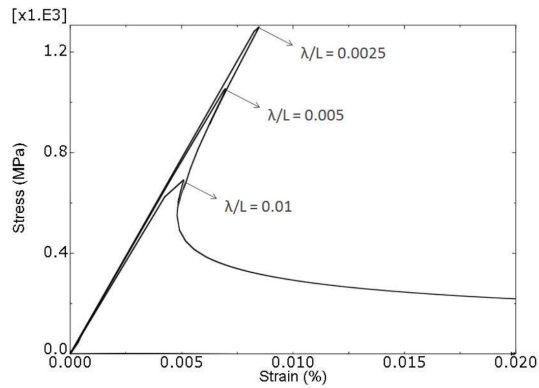


Figure 2.4: Longitudinal stress against longitudinal strain under pure compression for different global misalignment values by Bishara et. al. [16]. Symbol λ represents amplitude of the modeled sine wave, and L represents model length. The figure shows typical snap-back response observed in modeling of the compression failure of FRPs and the dependency of the peak load on the modeled fiber misalignment.

formed progressive failure analyses using 3D micromechanical models representing a slice of the material. It was revealed that fibers fail under bending at the edges of the kink band with resulting tension and compression surfaces on failed cross-section of the fibers. A strong correlation between fiber tensile strength and the band angle, anticipated analytically by Budiansky et. al. [22], was shown to exist in the numerical models. Parametric studies on local and global wavelengths and their effects on the resulting compression strength and kink band properties were investigated in detail, see Fig. 2.4 for a representative stress-strain response under longitudinal compression. In Ref. [17], the authors combined the micromechanical model of the 0° layer with the neighboring layers in a micro-meso hybrid approach. The off-axis plies were considered as a continuum represented by a transversely isotropic constitutive model. The interaction of different failure mechanism and the effects of matrix failure in the neighboring plies on the MB failure in 0° plies were explored. Sun et. al. [105, 106] modeled failure under compression on similar lines to Bishara et. al. [16]. In this model, voids were also considered, besides the fiber misalignment, as an additional initiation point for the kink band localization. Model predictions were compared against experimental results. Initial results of micromechanical models for loading under combined compression-shear were also presented. Another interesting micromechanical analysis incorporating the fiber misalignment and interface defects can be found in Ref. [108].

The micromechanical models presented heretofore represent the fiber misalignment either as an infinite band of misalignment transverse to the nominal fiber direction or an elliptical/circular patch of misalignment. These idealistic assumptions are not very well founded. The micrographs highlighted that the fibers have a rather correlated behavior with typical wavelengths [87]. On top of that, the values of misalignment angles or the amplitudes of misalignment are subject to significant variations within

UD plies [87, 137] and hence, it is unclear how single input values of the misalignment can be extracted from physical measurements. Occasionally, some authors assume an 'effective' misalignment angle and relate the experimental strengths with a certain percentile of the measured distribution of the fiber misalignment [127].

Recently, there has been growing interest in the scientific community to account for the aforementioned variations of the fiber misalignment in the micromechanical models. An interesting contribution to incorporate randomness of the fibre misalignment into the micromechanical model is from Bednarczyk et. al. [13, 91]. By using a High-Fidelity Generalized Method of Cells micromechanical model (HFGMC) and probability-weighted averaging of the stress concentration tensor of the subcell based on probability density function representation of the fibre misalignment, effective material moduli and damage initiation envelopes under varying input properties were predicted. Sebaey et. al. [98] presented an approach to transfer the misalignment measured experimentally into a micromechanical model. Varandes et. al. [114] presented a micromechanical approach, based on the algorithm by Sebaey et. al. [98] and Catalanotti and Sebaey [26], which can account for variations of the initial fiber misalignment via a combination of stochastic process and an optimization procedure. Linear elastic cylindrical fibers with varying fiber misalignment were modeled inside a damage degradable matrix to be a representative volume element (RVE). It was found that the variation of the fiber misalignment only affects failure under longitudinal compression, whereas longitudinal tension was indifferent to these uncertainties. Camarena et. al. [25] presented a deterministic FE micromechanical model which was found to be highly sensitive to the initial fiber misalignment. The physically measured fiber misalignment was then added to the micromechanical model and the model predictions were compared against experimental testing results. A comparison of square and hexagonal packing of fibers in micromechanical model and their comparison with the test data was also presented. Other approaches to account for the variations of the fiber misalignment, such as kriging and surrogate modeling, have also been recently presented [37].

2.2.2.2 Homogenized numerical models

Analytical and micromechanical approaches discussed so far led to the understanding of the mechanisms of failure under compression, the interaction between different failure modes, and the morphology of the resulting kink band. However, they are limited in representation of the realistic fiber misalignment observed in physical measurements and hence cannot capture the strength variations under compression for realistic materials. Although some micromechanical modeling approaches have recently accounted for the variations at the microscale [25, 26, 98, 114], prohibitively high computational costs, the possibility to model only limited sizes, and comparative difficulties involved in generating such micro models with inclusion of fiber misalignment variations makes them weaker contenders for detailed probabilistic analysis of FRPs.

Authors	Dimension	Key parameters	Outcomes
Kyriakides et. al. [70, 71]	2D	Linear and nonlinear material properties of fiber and matrix; Sinusoidal misalignment with infinite band and with transversely decaying band	Effect of fiber nonlinearity negligible; effect of matrix nonlinearity significant; Strong dependence on fiber misalignment
Hsu et. al. [59, 60]	2D & 3D	2D vs 3D modeling; Post peak response	Importance of 3D modeling; Predictions of plateau stress and band broadening
Vogler et. al. [117]	3D	Dilatant Drucker-Prager matrix model	Highlighted difference between nonlinear properties of pure resin and in-situ matrix
Lee and Waas [72]	3D	Non-uniform fiber matrix spacing	Insignificant effect of spacing
Yerramalli and Waas [136]	2D & 3D	Orthotropic fibers; I_2 -plasticity matrix	Importance of 3D stress states; Need of fiber bending stiffness at small sizes
Feld et. al. [44]	2D	Influence of shear pre-stress; Inelastic matrix model using damage theory	Effects of pre-stress and fiber misalignment through statistical analyses
Wind at. al. [129]	2D	Relation between fiber rotation and kink band angle	Band angle dependent on width of region of misalignment; Condition of volumetric incompressibility holds approximately
Prabhakar and Waas [90]	2D	I_2 -plasticity matrix; Cohesive zone interfaces for debonding	Need to model splitting along with MB if weak interface strength considered
Bishara et. al. [16, 17]	3D	Infinite band misalignment; Orthotropic fibers, isotropic matrix	Correlation between fiber tensile strength and band angle; Effect of wavelengths on strength; Matrix failure in non 0° plies
Sun et. al. [105, 106]	3D	Infinite band; Voids;	Voids can also initiate MB
Bednarczyk et. al. [13, 91]	3D	Accounted for misalignment distribution using HFGMC	Prediction of effective material moduli and damage initiation envelopes
Sebaey et. al. [26, 98]	3D	Variations of fiber misalignment via a combination of stochastic process and an optimization procedure	Misalignment variations affect compression failure; tensile failure is unaffected
Camarena et. al. [25]	2D	Use of measured misalignment in models; Square and hexagonal packing of fibers	High sensitivity of compression strength to fiber misalignment

Table 2.1: Micromechanical models for prediction of the compression strength

Driven on the basis of closed-form micromechanical methods of preserving simplified representation of the constituents, an alternate class of computational approaches can be found in the literature. Such approaches are modeled using homogenized or smeared material representation. A handful of these approaches consider an idealistic representation of the fiber misalignment and focus on the peak load prediction, the aspects related to the kink band morphology, and the plateau stress for energy dissipation because of failure under compression. A short summary of homogenized approaches found in literature is given in Table 2.2.

Investigations by Morais and coworkers [80, 82] used a unit cell comprising a single fiber and the surrounding matrix for prediction of the peak load. Roles of the material nonlinearity and the fiber misalignment were considered to be a fundamental aspect. Following FE modeling in 2D and 3D, a simplified closed form solution was also provided [81]. Davidson and Waas [36] used a 2D model similar to Morais and coworkers to show that sufficient shear hardening can offset geometrical softening because of fiber rotation, and that the MB failure doesn't happen at first yielding of the matrix. Extending the earlier works of Guimard et. al. [53], Feld et. al. [45] used a homogenization strategy based on energy consumption and defined energetic potential for a composite ply. The works of Wadee and coworkers [120, 121] and later Völlmecke et. al. [119, 138] used abstract representation of the composite through a set of rheological elements. These contributions focused on representation of perfectly aligned fibers in combination with modeling nonlinearities, either material nonlinearity using damage theory [45, 53] or geometric nonlinearity using rheological elements [119–121, 138], to predict the band properties and post peak response, hence, the peak load corresponded to Rosen's prediction.

To account for the statistics of misalignment in the numerical models based on homogenized or smeared approaches, a series of contributions were presented by Fleck's group [48, 76, 100]. Fleck and Shu [48] considered a 2D model with an ellipsoidal region of misaligned fibers using a smeared Cosserat continuum material model. The results of the models with the ellipsoidal misalignment were found to be stiffer than the models with the infinite band of misalignment. Using 1D bending theory, Slaughter and Fleck [100] presented a model accounting for the variations in the fiber misalignment. A stochastic distribution of the amplitudes of misalignment was modeled using spectral representation method with assumed forms of spectral densities. Spectral representation method uses a given spectral density of a distribution to generate multiple distributions, preserving statistical properties as well as the spatial correlation properties of the original distribution. Multiple correlated random realizations of the distributions of the fiber misalignment were modeled in a 1D couple stress problem to perform Monte Carlo analysis. The resulting peak load distribution was found to closely match a 2-parameter Weibull distribution. It was concluded that the model is controlled by its weakest link, i.e. the largest fiber misalignment. Liu et. al. [76] extended the earlier 1D model to 2D finite element model. Spectral representation method was used to model distributions of the fiber misalignment assuming different

Authors	Dimension	Key parameters	Outcomes
Morais et. al. [36, 80–82]	2D & 3D	Unit cell approach	Peak load dependence of fiber misalignment and material nonlinearity; Closed form solution
Feld et. al. [45, 53]	2D	Energy based mesomodel; Consideration of the fiber misalignment statistics	Prediction of energy absorption during MB failure under compression and under mixed loads
Wadee et. al. [119–121, 138]	2D	Aligned fibers; Energy based formulation	Band properties and post peak response
Fleck and Shu [48]	2D	Ellipsoidal region and infinite band misalignment; Smeared Cosserat continuum	Higher strength of ellipsoidal region model compared to infinite band model
Slaughter et. al. [100]; Liu et. al. [76]	1D & 2D	Cosserat continuum; Correlated topology of misalignment through spectral representation method	Peak load distribution closely matched a 2-parameter Weibull; Weakest link model
Lemanski and Sutcliffe [73, 109]	2D & 3D	Fibers as rebars/beams embedded inside matrix; Square and rectangular region of misalignment, later correlated topology by artificially smoothing random spread of misalignment	Dependence of compression strength on region of misalignment; Later, distribution of peak strength
Allix et. al. [7]	3D	Cells representing model geometry based on a priori known kink width and ply thickness; no consideration of correlation of misalignment	Compression strength prediction of homogeneously loaded laminate, open hole specimen, and notched specimen
Daum et. al. [34]	2D	Micropolar approach; Total-Lagrangian finite strain plasticity theory; Infinite band misalignment	Accurate prediction of post peak response and kink band characteristics

Table 2.2: Homogenized models for prediction of the compression strength

shapes of the power spectrum. The conclusions of the 2D analysis corroborated with the conclusions of the 1D model from before.

Lemanski and Sutcliffe [73] also used a homogenized representation of fiber and matrix, albeit devising a different technique to implement it in the FE models. Instead of using Cosserat continuum, fibers were represented as reinforcements via rebars and beams embedded inside a matrix material in the respective plane stress and shell models. Using this approach allowed for representation of nonlinear composite behavior solely through matrix properties. This investigation focused on placing the misalignment in different regions of the model. Fiber bending stiffness was not considered in this approach, as it was argued that it has no effect at larger wavelengths. The argument to neglect fiber bending stiffness was based on earlier analytical works of Fleck et. al. [47] and later numerical work of Liu et. al. [76], who had shown that fiber bending stiffness has an effect only for wavelengths below a millimeter. Since measurements showed that wavelengths are on the order of a few millimeters in FRPs [110], fiber bending stiffness was neglected by Lemanski and Sutcliffe [73] in their numerical models. A followup work by Sutcliffe [109] featuring distributions of the misalignment investigated edge effects. The misalignment was modeled by artificially smoothing a random spread of amplitudes of the misalignment to achieve the desired autocorrelation. The findings confirmed and extended the conclusions drawn in earlier works of Liu et. al. [76].

Extending the work of Feld et. al. [45], Allix et. al. [7] presented a homogenized model with a distribution of the fiber misalignment for the prediction of failure under compression load. The composite was represented via a diffuse continuum damage model. A cell approach was used to represent geometry of the model, where sizes of the cells were dictated by a priori known kink width and ply thickness. The fiber misalignment sampled from a distribution was randomly assigned as the material orientation of the cells without any consideration of correlation, see Fig. 2.5a. Fig. 2.5b shows the force displacement response of the model under different boundary conditions for a UD ply. The model was also capable of predicting failure for open hole specimen and notched specimen.

Recent work of Daum et. al. [34] used a 2D micropolar homogenized approach to model MB failure in FRPs. Micropolar solid theory is applied to regularize the microbuckling failure mode. The nonlinearity was modeled in a total-Lagrangian finite strain plasticity theory framework for the micropolar solid, whereas the infinite band assumption of the fiber misalignment was considered. Fiber bending stiffness only plays an important role in compression strength prediction for small wavelengths of the fiber misalignment. Even in the models where the compression strength is unaffected by the fiber bending stiffness, the post peak response cannot be accurately modeled without considering the fiber curvature and fiber bending stiffness. The main advantage of the micropolar approach is consideration of fiber curvature and fiber bending stiffness. Thus, not only compression strength but also the post peak response of the MB failure was modeled accurately.

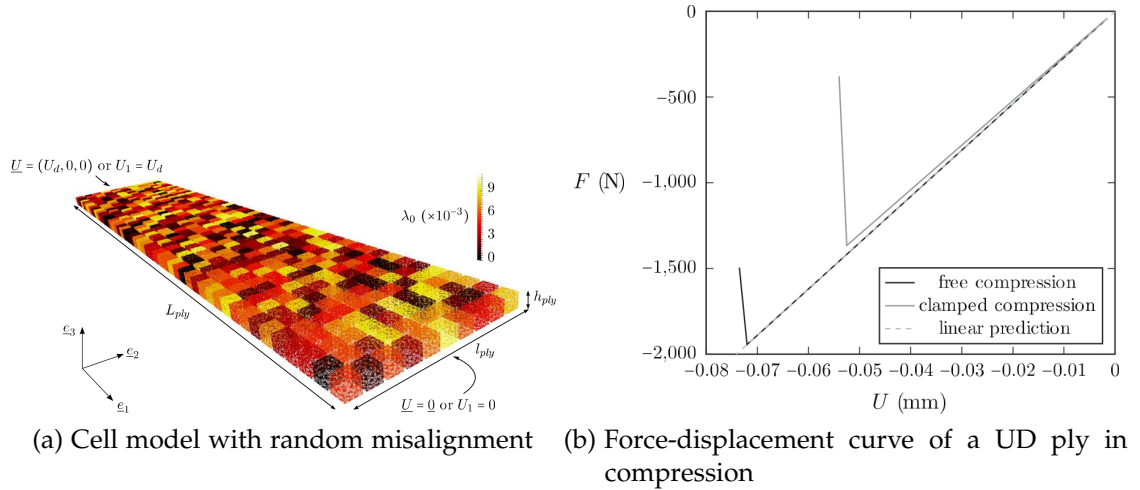


Figure 2.5: A model by Allix et. al. [7] with random distribution of the fiber misalignment spread over the volume without consideration of correlation and corresponding response of the model under axial compression

2.3 MEASUREMENTS OF MATERIAL IMPERFECTIONS

There is a consensus that the material imperfections reduce strength under compression loads [7, 8, 23, 46, 69]. The biggest contributor to the material imperfections is the unavoidable fiber misalignment. The fiber misalignment occurs during manufacturing. Whether the component is manufactured using Prepregs, RTM, or some other manufacturing technique, there are significant temperature gradients during heating and cooling processes involved in curing of the matrix. The thermal properties of fibers and matrix materials are significantly different. Heating and cooling steps involved in curing of the matrix during manufacturing give rise to different rates of expansion and contraction of fibers and matrix, resulting in wavy fibers in the laminate. Because of such fundamental importance of the fiber misalignment in prediction of failure under compression, it is of utmost importance to measure and characterize them. The problem of measuring the fiber misalignment is, however, cost intensive and difficult.

The methods for measurements of the fiber misalignment can be broadly divided into the following: (i) in a plane perpendicular to fiber direction or at a slight angle to this plane, (ii) in a plane parallel to fiber direction, and (iii) through structural tensor calculation from voxel data of CT-scans. The first group of methods can be found in literature in the earlier contributions. They are characterized by measurements over limited sizes and destructive testing such as contributions by Yurgartis [137] and Paluch [87], but are also performed through non-destructive testing such as works of Clarke et. al. [29]. The second and third group of methods are non-destructive and can cover larger sizes [31, 68, 85, 126]. A summary of different methods of the fiber misalignment measurements is provided in Table 2.3.

The first investigation of the fiber misalignment of FRPs commonly available in literature is the one by Yurgartis [137]. Yurgartis [137] assumed the fibers to have a perfectly cylindrical shape, i.e. fibers have a perfectly circular cross section. Whenever a circle is projected on another plane which is at an angle to the normal of the plane in which the circle exist, the projection appears as an ellipse. Given the radius of the original circle and the major axis value of it's ellipsoidal projection at an angled plane, the angle between the two planes can be calculated. This principle was exploited by Yurgartis [137] to measure the fiber misalignment by successively sectioning the material at angled planes. The micrographs of the material were obtained through the thickness in the nominal fiber and in the transverse direction by carefully grinding the material at fixed distances, giving a 3D description of the misalignment. The results showed Gaussian distributions of the fiber misalignment for the in-plane and the out-of-plane angles. It was also observed that the misalignment is axially symmetric in the plies, however, it changed when measured after lamination. Paluch [87] investigated regularly spaced cut-out section using a microscope to measure the fiber misalignment in a 3D manner. The fiber paths were reconstructed by stitching all the studied sections and following the centers of the fibers from each section. This method allowed to investigate non-circular fibers too, which was not possible in Yurgartis' method. 3D view reconstruction of misaligned fibers was also possible with this technique. The results were provided as distributions of misalignment angles. Additionally, the correlations between the in-plane and the out-of-plane misalignment were also calculated. It was concluded that the fibers interact only at very short distances, and idealistic representation of all fibers undulating in phase is unrealistic. Clarke and coworkers [29] presented a non-destructive technique of measuring the fiber misalignment in a volumetric sense using a confocal laser scanning microscope. The limitations of considering straight fibers over longer distances in Yurgartis' method [137] and the limitation of translational shifts between adjacent cut section in Paluch's method [87] were pointed out. The measurement of the fiber misalignment over the scanned volume was performed through an automated process. The determination of the fiber orientation followed the principle employed by Paluch i.e. following centers of fibers over successive images/micrographs. Results were provided in the forms of distributions of the misalignment for FRPs. It was shown that the technique is also applicable to short fiber reinforced polymers. Following measurements of the fiber misalignment, Clarke et. al. [28] characterized the misalignment as power spectral densities of amplitudes of the misalignment in a separate contribution. This was done following the work of Slaughter and coworkers [100] discussed earlier, which highlighted the importance of power spectral density as an input to predictive tools of compression strength.

Creighton et. al. [31] presented a simpler technique called Multiple Field Image Analysis (MFIA) for the measurement of distribution of the fiber misalignment and used the results in an FE analysis to explain strength reduction in different FRPs [30]. Micrographs taken parallel to fiber direction through optical microscope were divided into several domains, and the light intensity of the domains was compared to find av-

erage orientation within each domain. Measurement of higher misalignment angles, such as in porous materials, which could not be captured by previous methods, were possible. Results were provided as a distribution and a contour plot of misalignment angles. The method is extendable to 3D if the micrographs through the thickness are available. The application of the MFIA to 3D measurement was successfully shown by Sutcliffe et. al. [74, 110]. Kratmann and coworkers [68] presented an alternate way of measuring the misalignment from micrographs called Fourier Transform Misalignment Analysis (FTMA). Individual domains were Fourier transformed and a power spectrum of the light intensity was calculated. Through filtering the frequencies, images were cleared to track individual fibers. It was shown that the method is more robust and provides better results. The FTMA was used for the measurement of the misalignment in combination with experimental testing to investigate the compression prediction models [111]. Wilhelmsson and Asp [126] presented High Resolution Misalignment Analysis (HRMA) for tracing individual fibers in micrographs. Micrographs were divided into smaller units called cells, binarized to simplify the image, fibers were traced, and finally the misalignment was measured through regression. Although orientation of individual fibers can be measured, the number of fibers could be different in each cell. Hence, average orientation of each cell was given as a measure of misalignment. The results of the method were compared against those using MFIA and FTMA. When the cell sizes were reasonably small, the accuracy of the method was on par with earlier methods with higher computational efficiency. The HRMA method has an advantage in its ease of implementation compared to MFIA and FTMA.

Nguyen et. al. [85] presented an alternate methodology for measurement of the misalignment using structural tensors. The fiber orientations were measured by calculation of orientation vectors from the micro computer tomography data as an eigenvector of the three dimensional structural tensor. Using this technique, the misalignment of multiple plies in a laminate was measured.

2.4 EXPERIMENTAL TESTING UNDER AXIAL COMPRESSION

Unidirectional FRPs have exceptionally high mechanical properties, such as strength and modulus in fiber direction. On the other hand, the fibers do not offer support in transverse directions, resulting in a high degree of anisotropy. Such a mechanical behavior of unidirectional FRPs makes it quite challenging to perform experimental testing. The task becomes even more difficult when testing under axial compression because of the possibility of global buckling. The crux of the matter lies in on how to transfer applied loads into the gauge section of the specimen with minimal external effects. With all these factors to consider, different mechanism of transferring applied loads to the gauge section of the specimen have been devised over the course of time. Since flat specimens are the representative of the most common applications of the FRPs and the standard tests are performed on them, the focus of the discussion will

Authors	Method	Key features and results
Yurgartis [137]	in planes at an angle to fiber direction	Destructive method; Gaussian distributions of misalignment for in-plane and out-of-plane angles; Different misalignments measured before and after lamination process
Paluch [87]	in planes at an angle to fiber direction	Destructive measurement technique; Reconstructed fiber paths from micrographs; Measurement of non-circular fibers possible; Measured distributions of in-plane and out-of-plane angles
Clarke et. al. [28, 29]	in planes at an angle to fiber direction	Non-destructive technique; Automated process following principle of Paluch [87]; Characterization of misalignment as power spectral densities
Creighton et. al. [31]	in planes parallel to fiber direction	Multiple Field Image Analysis (MFIA); Division into domains, measure of light intensity in domain give misalignment; 2D measure of distributions of misalignment; Application to 3D by Sutcliffe et. al. [74, 110]
Kratmann et. al. [68]	in planes parallel to fiber direction	Fourier Transform Misalignment Analysis (FTMA); Individual domains Fourier transformed and power spectrum of the light intensity calculated; More robust than MFIA
Wilhelmsson and Asp [126]	in planes parallel to fiber direction	High Resolution Misalignment Analysis (HRMA); Micrographs' division into cells, binarization, and tracking of fibers; Ease of implementation; 2D distributions of misalignment; Application to 3D by Safdar et. al. [95]
Nguyen et. al. [85]	Measurement using structural tensors	Calculation of orientation vectors from the micrographs; Measurement of misalignment of multiple plies in a laminate

Table 2.3: Different methods for measurements of material imperfections in FRPs

be on them. Testing for failure under applied axial compression can be categorized into three groups based on the method of load introduction from a fixture into a test specimen. A schematic representing possible mechanisms of load transfer into flat specimens is shown in Fig. 2.6.

The load is transferred through the end surfaces of the flat specimens via contact forces normal to the surface in the *end loaded methods*, see schematic in Fig. 2.6a. Generally, the specimen is supported laterally through some form of anti-buckling mechanism to avoid global buckling. The contact of specimen with the buckling plate/device can introduce unwanted frictional forces in the specimen. These types of fixtures are also limited to testing of composites with low to medium modulus as invalid failure in form of end crushing can occur in high modulus composites. End loaded fixtures are easy to use with added benefit of alignment of the specimen in the fixture through end contact. Examples of this type of fixture include ASTM standard D-695 [4], Modified standard D-695 [18, 19], and NASA short block.

To avoid the possible failure at the location of load introduction in *end loaded methods*, load can be introduced through shear, as shown in Fig. 2.6b. In *shear loaded methods* ASTM standard D-3410 [2] and German DIN-65 380, load is introduced into the gauge section of the specimen through shearing of the sides of tabs/specimen held in the jaws of the fixture. The main issues with these fixtures can be in gripping surfaces and in the alignment of specimen. However, they allow testing of high modulus and strength composites. Examples of the fixtures falling under this category are IITRI compression test fixture, Celanese compression test fixture, German DIN 65 380 Celanese compression, and their different modifications.

Combining the advantages of the *end loading* and *shear loading* methods, a Combined Loading Compression (CLC) method was developed at the university of Wyoming [6, 122, 124]. In the *CLC method*, load is introduced into the specimen through a combination of aforementioned methods of load introduction, as shown in Fig. 2.6c. The main advantage is limiting stress concentrations in the specimen, along with the possibility of introducing higher loads than earlier methods. The corresponding standard is called ASTM D-6641 [3] and the fixture following the *CLC method* is labeled Wyoming Combined Loading Compression test fixture.

2.5 FAILURE UNDER COMBINED COMPRESSION-SHEAR LOADS

The focus of most of the investigations found in the literature is on the failure under pure axial compression. For practical engineering applications, however, it is important to have the characterization of failure under combined load cases. MB is the dominant failure mode under pure axial compression, as well as under combined compression-shear loads where compression part of the load is dominant. The investigations to characterize/predict failure under combined compression-shear are discussed below.

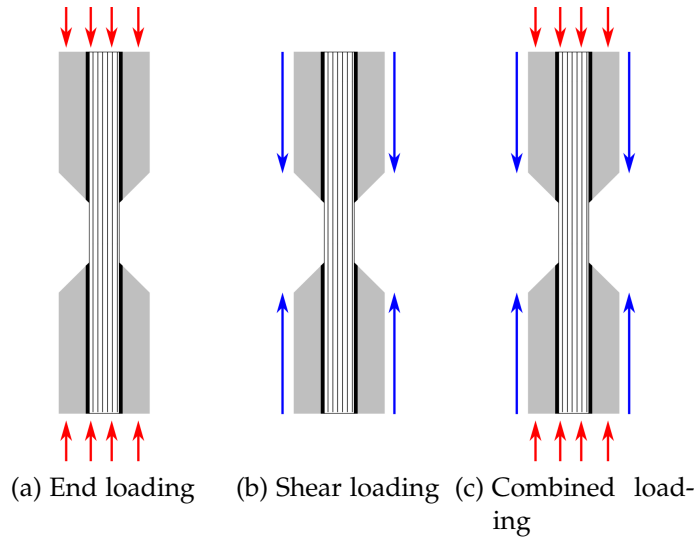


Figure 2.6: Schematic of load transfer methods common in compression testing

2.5.1 Experimental testing to failure under combined compression-shear

The literature on experimental testing of failure of FRPs under multi-axial loading is quite limited. Vogler et. al. [116, 118] devised a technique for combined compression-shear testing of flat specimens of unidirectional FRPs. Specimens were prepared in such a way that the edges of the specimen were parallel to the nominal fiber direction. The loading was done sequentially by using two separate load actuators, i.e. compression load followed by shear or vice versa. Load transfer to the gauge section appears to be through combined end and shear mechanisms, as in ASTM D-6641 standard. It was shown that MB is the dominant failure mode even at significantly high values of the applied shear in combination with moderate values of the applied compression load. The results proved useful for development of an experimental failure envelope under combined compression-shear loads. Although some scatter was observed in the experimental results, the failure envelope was provided in terms of a deterministic criterion. There was no consideration of variation in failure strengths because of the underlying fiber misalignment. A drawback of this technique seems to be the lack of simultaneous loading. A schematic representation of the test setup and the resulting failure envelope are shown in Fig. 2.7.

Bing and Sun [14, 15] devised an alternate technique to investigate failure under combined compression-shear load. Applied combined compression-shear loading was achieved by using off-axis specimens. In the off-axis specimens, the nominal fiber direction was oriented at an angle to the specimen edges. In this investigation, blocked shape specimens were used instead of the more commonly used flat coupon specimens. Block shape specimens have a small difference in dimensions in all three directions compared to large difference in dimensions of the more common flat specimens, e.g. Bing and Sun [14, 15] used specimens with dimensions of $10 \times 7 \times 6$. The load

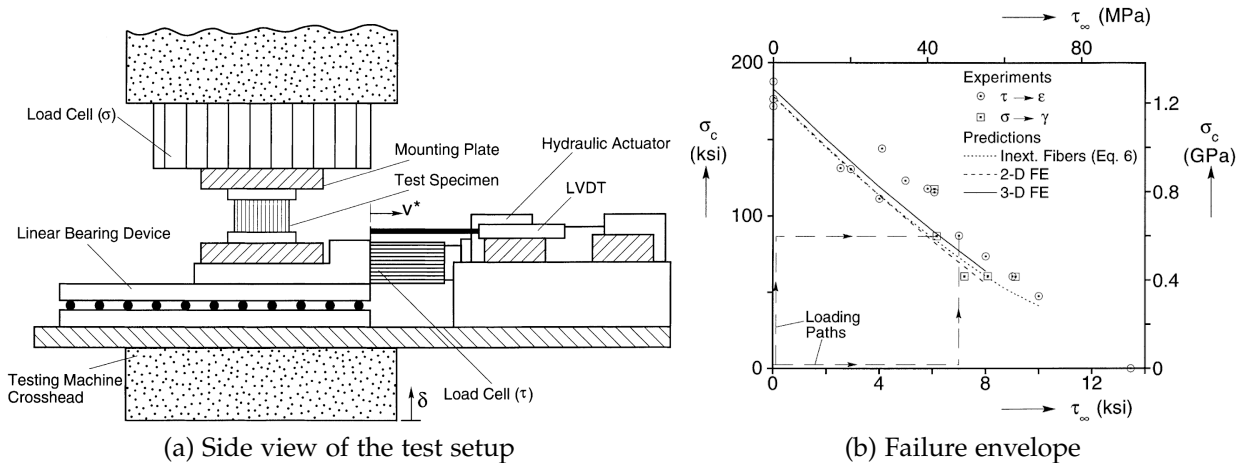


Figure 2.7: Schematic of the test setup and the resulting failure envelope by Vogler et. al. [116, 118]. Experimental results are shown as markers in Fig. 2.7b whereas FE predictions using 2D and 3D modeling are shown through the lines. The horizontal axis represents applied shear stress and the vertical axis represents applied axial compression.

transfer to the gauge section was through loading the ends of the specimens. Cutting the specimens at an angle to the nominal fiber direction allowed for introduction of multi-axial loading without need for additional actuators. However, a drawback of this technique appears to be the non-uniform length of fibers in the gauge section. It apparently promoted longitudinal splitting instead of MB failure in the off-axis specimens. It was concluded from this observation that splitting is the dominant failure mode at higher off-axis angles. Edgren et. al. [42] used a similar technique to Bing and Sun [15] to test non-crimp fabric (NCF) composites under combined compression-shear loading using flat specimens. The nominal fiber direction was oriented at an angle to the specimen edges, allowing for multi-axial load states using a single load actuator. Specimen preparation was made easy through the use of flat specimens. Results were provided as deterministic failure envelopes in the compression-shear plane, and a failure criterion was presented based on the experimental results.

Another alternative to obtain combined compression-shear loading using single actuators was through the use of tubular specimens. These investigations [78, 101, 135] were driven by the renowned World Wide Failure Exercise (WWFE) for FRPs. The load transfer from the fixture to the gauge section was through the ends of the specimens in these approaches. The tubular geometry of the specimen loaded in axial direction induced combined compression-shear loads in the laminates. Based on the resulting failure stresses, failure envelopes were presented by the authors. The degree of complexity involved in the preparation and the handling of the non-flat specimens in these approaches is quite challenging. Recently, Gan et. al. [50] devised an Arcan like fixture for testing multidirectional laminates under different combinations of combined loads. Since the fixture was seemingly designed for butterfly specimens, failure

was induced in the corresponding area. Thus, there seems to be a limited focus on quantifying the strength variations under multi-axial load states. The placement of guide pins near the specimen on the rotatable plates seemingly limits them to work only against in-plane bending. The load transfer appears to be through the shear mechanism.

2.5.2 Analytical and numerical modeling of failure under combined compression-shear

Deterministic forms of failure envelopes defined by analytically developed failure criteria are most common because of requirements of a limited number of experimental tests for calibration to a particular material. A simple stress based failure criterion developed analytically was presented by Edge [41]. The relationship between axial and shear stresses was considered to be linear. Starting from the analytical formula for compression failure under applied far-field compression and shear loads from Fleck's group [21, 99], Edgren and coworkers [42] derived a failure criterion for the NCF composites. Incidentally, this criterion is the same as the linear criterion of Edge [41]. Quadratic forms of failure criterion developed analytically are more common, e.g. Tsai-Wu criterion [77]. Such criteria also take into account the combined effect of different stresses on failure. An analytical approach on failure envelopes under multi axial loading was performed by Whiteside et. al. for stochastic ply failure of unidirectional composites through parallelized Monte Carlo Simulation of a physically based quadratic failure criteria [125]. The uncertainties because of the fiber misalignment were accounted for in their analysis, however, the spatial correlation of the distributions of the fiber misalignment was neglected.

Besides the experimental and the analytical investigations, failure analyses through numerical modeling under combined compression-shear loads can also be found in the literature. Following their experiments, Vogler et. al. [116, 117] used numerical modeling to predict failure under combined compression-shear loads. Using 2D and 3D finite element modeling, effects of the initial misalignment as well as material nonlinearities were investigated. Models were based on the idealistic form of misalignment. The resulting failure envelopes for different values of initial misalignment were compared to the analytical prediction using the formula by Budiansky and Fleck [21]. The misalignment was modeled to be 'cooperative' with the applied far-field shear stress. By having opposing misalignment and the applied shear, the models showed strengthening effects under combined loads. On similar lines to Vogler and coworkers [116], Basu et. al. [10] used a micromechanical model to present a deterministic failure envelope under combined compression-shear loads. Based on the direction of the applied shear compared to the direction of the initial misalignment, the concept of positive and negative shear was introduced. The result was a non-symmetrical failure envelope around the axial stress axis. Tsai and Sun [112, 113] performed an analysis to investigate strain rate dependency of failure in specimens loaded under combined

compression-shear. It was concluded that the compression strength is rate sensitive and the applied in-plane shear can significantly reduce compression strength. Following their analyses using micromechanical modeling on the mechanisms of MB failure [55, 56], Gutkin et. al. [54] presented a deterministic failure envelope under combined compression-shear loads. The failure envelope was defined by two regions, i.e. one where failure was controlled by the compression strength of the fibers and the remaining was defined by MB and splitting failure modes. The effects of different shear behaviors were analyzed, and it was concluded that the linear and nonlinear composite shear behavior result in corresponding linear and nonlinear shapes of the failure envelope. Using their micromechanical model [106], Sun and coworkers [107] presented numerically developed failure envelopes under combined compression-shear loads at different values of the initial fiber misalignment, along with failure envelopes for other combined load cases. The terms for the initial fiber misalignment and the fiber volume fraction were introduced as an update into the definition of the Tsai-Wu failure criterion.

2.6 AIMS AND OBJECTIVES OF THE WORK

The problem of failure under compression dominated load of unidirectional fibers reinforced polymers has been extensively investigated for more than half a century using different approaches ranging from analytical modeling to numerical modeling and experimental testing. Although the basic mechanisms of failure under compression dominated loads are well understood, there are still hosts of open questions about quantification of failure uncertainty. Based on the literature review carried out above, following open questions and corresponding objectives are outlined:

1. The importance of the fiber misalignment in failure under compression dominated loads for unidirectional FRPs is well established. Therefore, it is required for investigations of failure to measure the fiber misalignment in the material under consideration. For this purpose, non-destructive scanning over larger volumes using a CT scan machine is carried out. The HRMA method, which was originally developed for 2D micrographs, is applied to 3D in order to measure the in-plane and the out-of-plane fiber misalignment. It is followed by subsequent representation of the in-plane and the out-of-plane misalignment fields in three dimensional space. The results are also presented as distributions of the misalignment angles and their relevant statistical information.
2. Different researchers have shown, through analytical and numerical modeling, the importance of nonlinear material behavior on compression failure. Although basic material properties such as stiffness moduli and Poisson's ratio are provided by the material suppliers. Nonetheless it is advisable to carry out the required standard tests for mechanical properties characterization. Most importantly the complete characterization of the nonlinear shear stress strain curve for

MB failure analysis is required. Hence, the mechanical tests required for modeling of failure under compression dominated loads are carried out in the current investigation.

3. The literature review has shown that the statistical as well as spatial correlation properties of the fiber misalignment can be preserved when they are characterized as spectral densities. Therefore, the measured in-plane and the out-of-plane fiber misalignment is characterized in the form of spectral densities dependent on three spatial frequencies.
4. To represent the fiber misalignment realistically in numerical models, different approaches can be found in literature as discussed in the state of the art review. It was found that the spectral representation method offers an excellent solution for the generation of virtual distribution of the fiber misalignment which can in turn be used in numerical models. Using this method with an input of spectral density characterized in previous step, not only the usual statistical properties such as mean and standard deviation but also the spatial properties, such as the correlation of the distributions of the fiber misalignment, can be preserved in the virtual generated distributions. In literature, the examples of using spectral representation method for 1D and 2D problems are available. Herein, the method is extended to 3D for generation of the virtual distributions of the correlated random fiber misalignment, taking the characterized spectral densities as the input.
5. Most of the existing analytical, numerical as well as experimental approaches to failure under combined compression-shear loads are not associated with survival probabilities, i.e. probability distributions of the strengths under compression and combined compression-shear loads. For better design practices, the quantification of failure probabilities because of the underlying variations of the fiber misalignment needs to be done. Therefore, the focus of the current investigation is on development of novel probabilistic failure envelopes under compression and combined compression-shear load cases at different percentiles of failure. For this purpose, a novel testing concept combining the advantages of the Arcan type fixtures and the ASTM D-6641 standard CLC fixture is developed. The load transfer in the gauge section is through the ends and through shearing of sides of the specimens. The multi-axial load states are achieved by rotating the internal disc of the fixture at an angle to the loading axis of the machine. The testing concept allows the use of easy to manufacture flat specimens in which the nominal fiber direction is parallel to the edges of the specimen. Based on the results of the testing campaign, failure envelopes in strain and stress spaces are presented. Median and percentiles are relatively unbiased statistical measures compared to mean and standard deviation because of their lower susceptibility to outliers. Moreover, the percentile representation is more common in engineering design practices and is rather easy to understand. Hence, the failure

envelopes are also given in expression forms and the expression forms are fitted to median and certain percentiles of failure. The results of testing to failure are discussed in lieu of the well-known analytical formula of Budiansky.

6. From the literature of numerical modeling approaches, it is realized that the homogenized representation of fiber and matrix in numerical models allows for ease of modeling and computational efficiency over significantly larger model sizes. The homogenized (continuum) modeling approach has been applied in 2D or pseudo 3D manner in literature as the representation of the fiber misalignment was done only for the in-plane fiber misalignment dependent on two spatial directions. Herein, a fully 3D numerical modeling framework incorporating both the in-plane and the out-of-plane distributions of the fiber misalignment, each dependent on three spatial directions, is presented. The limitation in using anisotropic homogenized models because of inconsistent material axis rotation is alleviated by extending the material model by including the effect of shear on the rotation of the material axis. The verification of the numerical model against the analytical prediction of failure under axial compression is carried out. Using the 3D numerical model equipped with a complete and realistic representation of the fiber misalignment, failure envelopes in stress and strain space are developed. Numerical modeling offers a cheap solution for performing a large number of analyses. Taking full advantage of these capabilities of numerical modeling, much lower percentiles of failure than the experimental testing based failure envelope are presented. The expression forms of failure envelope are also presented based on results of numerical modeling, and the resulting envelopes are compared to the failure criteria commonly found in literature. Fig. 2.8 shows a schematic representation of the numerical modeling approach. Moreover, use of functional forms of spectral density for generating virtual distributions of the fiber misalignment is also investigated.
7. For validation purposes, the predictions of numerical modeling are compared against the results of the experimental testing. Since the sizes of the specimens tested in experiments and the sizes of the numerical models differed significantly, a scaling law is employed to compare the results of the two approaches. Although the complete failure envelopes from numerical and experimental approaches cannot be compared directly because of differences in specimen sizes, the reasons behind the differences in shapes of the resulting failure envelopes are explored.

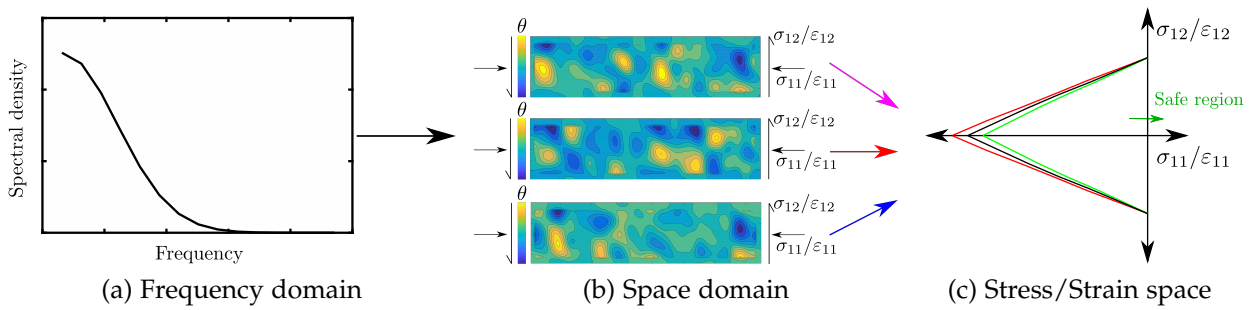


Figure 2.8: Schematic of the numerical modeling framework. The fiber misalignment characterized as spectral densities in frequency domain are used as an input to generate distributions of the misalignment in the spatial domain. The distributions are mapped onto a FE model, and the models are simulated under different load conditions to generate probabilistic failure envelopes in stress and strain spaces.

MATERIALS AND MEASUREMENTS

A suitable model for prediction of onset/initiation of MB in fiber reinforced composites (FRPs) can be constituted using the nonlinear shear response and the mechanical properties of the composite [76, 100, 109]. To quantify the uncertainty in the failure prediction under compression loads, measurements of the fiber misalignment are required. These characterizations and measurements are essential for numerical modeling of microbuckling (MB) failure presented in later parts of the work. In this chapter, characterization of mechanical properties and measurements of material imperfections are presented.

Most structural applications such as aircraft fuselages and rotor blades of wind turbines of the FRPs, whether unidirectional, multidirectional or NCF composites, involve prepreg lamination or resin transfer molding (RTM) as the manufacturing techniques. The fiber misalignment resulting from either of the manufacturing processes show quite similar behavior [110]. Because of simplicity and flexibility of prepreg lamination process, a unidirectional prepreg based material is an optimal choice for a representative investigation. Moreover, the prepreg unidirectional FRPs found in most of the advanced industrial applications have fiber volume fractions ranging from 50%-60%. Therefore, considering the aforementioned observation about commonly used unidirectional FRPs, prepreg UD300 high strength carbon fibers with M79 Hexply epoxy resin Hexcel¹ system was chosen as an optimum representative material for the current investigation. In this material, a resin content of 34% results in the fiber volume fraction v_f of 55% according to the supplier. The UD300 corresponds to 300 g/m² density of the fibers. The mean cured ply thickness of the material is 0.30 mm.

The material was delivered in the form of a roll with 1300 mm width. For manufacturing of the specimens, required sizes of the material were cut for lamination into plates. Each plate contained multiple specimens. The exact lamination sequence for each specimen's manufacturing will be given with the discussion of the corresponding test series. For specimen preparation for all the test series, the curing cycle in the autoclave suggested by the supplier was used.

3.1 MECHANICAL PROPERTIES CHARACTERIZATION

TEST STANDARDS: The mechanical material properties of the material under consideration i.e. carbon fiber UD300/M79 epoxy system were characterized using three standard tests. Material characterization in fiber direction was performed following the *DIN EN 2561* standard. The transverse tension characterization was done using

¹ supplied by *Lange+Ritter Faserverstärkte Kunststoffe GmbH, Germany*

the method outlined in *DIN EN 2597* standard. For material characterization in shear, the tests were performed following the *EN ISO 14129*, *ASTM D3518*, *DIN 65466* standard. This particular shear characterization test is performed as a tension test on a $[+45/-45]_{2s}$ specimen. It has the advantages of easy testing and cheaper manufacturing of specimens compared to the other shear characterization tests, such as *ASTM D5379* standard test, *ASTM D4255* standard test, or 10° tension test for shear characterization, while still giving accurate results.

SPECIMEN PREPARATION: The specimens for the material characterization tests were prepared in a single batch using the autoclave cure cycle suggested by the supplier. The lamination sequences of $[0_6]$ and $[90_6]$ were used for preparing the specimens for the axial tension and the transversal tension tests, resulting in an average specimen thickness of 1.81 mm. Similarly, for the shear characterization tests, a lamination sequence of $[+45/-45]_{2s}$ was used, which resulted in an average specimen thickness of 2.39 mm. Tabs made of $[+45/-45]_{2s}$ glass fiber reinforced polymer (GFRP) were applied on each cured plate using *3M's DP490* adhesive with a 90° tab taper angle. Plates were subsequently cut into the required specimen dimensions, as stated by the corresponding test standards. In order to enable measurements using a digital image correlation (DIC) system, a black speckle pattern on a white background was applied on the gauge section surfaces of the specimens with matt spray paints. The sizes of the speckles were kept proportional to the specimen dimensions for the speckle pattern to stay in the suitable range for measurements of DIC system.

TESTING PROCEDURE: The mechanical tests were performed on a 100 kN servo-hydraulic universal testing machine from Sincotec. The specimens were mounted in the flat grips of the machine and aligned with the machine axis. The specimens were tested using a displacement controlled load at the constant rate of 1 mm/min. The measurements for applied force were obtained through a 100 kN load cell attached to the upper crosshead of the testing machine. The *Aramis 12M Adjustable 3D²* system was employed for the measurement of the strain fields on the surface of the specimens. The region of interest in the post processing software *GOM Correlate* for measuring strain fields on the surface of the gauge section in the characterization tests was defined with facets sized 19 pixels placed 16 pixels apart from one another [49]. The virtual extensometer feature of *GOM Correlate* was used to measure average strains ε on the surfaces of the specimens. The virtual extensometer of the DIC system functions like a physical extensometer. Additionally, physical extensometers were employed on the specimens in the characterization tests for measurement of strains in the loading direction. The strains measured through both physical and virtual extensometers were compared to obtain confidence in the results. The strain measurements from both methods showed matching values with a maximum deviation of 1.5% near

² from GOM GmbH

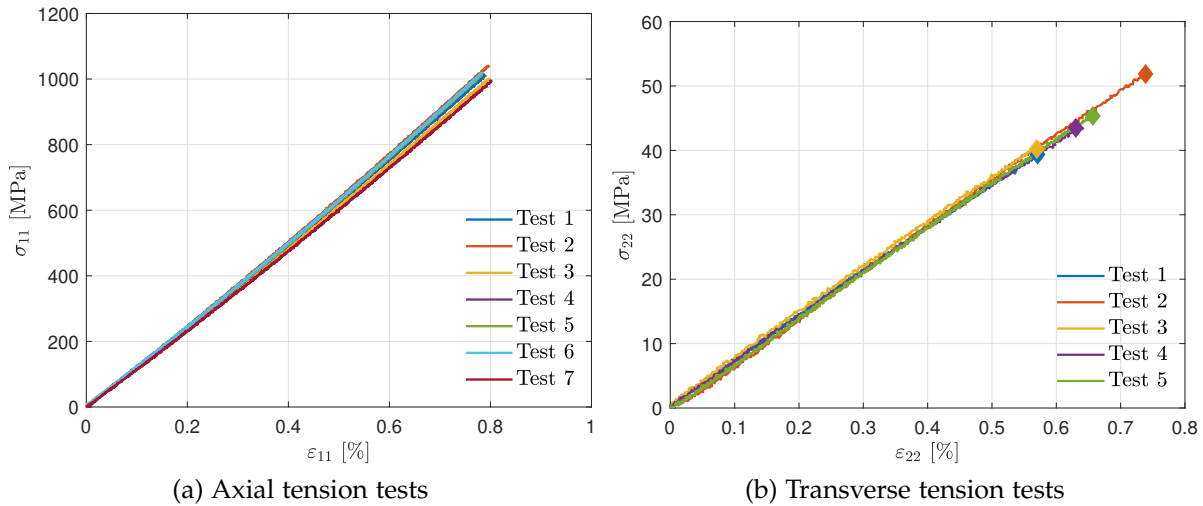


Figure 3.1: Stress-strain response

the end of the test. It is to be noted that the engineering definitions of strains and stresses are used throughout this work.

RESULTS: For the material characterization in the fiber direction, eight specimens were prepared and tested. Seven tests were successful in this series, whereas one specimen got damaged during test preparation. Since the failure strength under axial tension load is not of interest, the axial tension tests were performed up to 50 kN load only. The resulting stress-strain curves of the axial tension tests are plotted in Fig. 3.1a. The stiffness modulus in the fiber direction E_{11} is calculated by taking the initial slope of the stress-strain curves. Additionally, the Poisson's ratio is calculated from this series of tests. For this purpose, strains in the transverse direction ϵ_{22} and the strains in the fiber direction ϵ_{11} were obtained using the DIC system. Taking the ratio $\epsilon_{22}/\epsilon_{11}$ gives the Poisson's ratio ν_{12} . The resulting values of E_{11} and ν_{12} are listed in Table 3.1.

Eight specimens were prepared for transverse tension tests, of which three were destroyed unsuccessfully during test setup because of high brittleness of transverse test specimens while loading in the machine grips. For the five successfully carried out transverse tension tests, the resulting stress-strain curves are plotted in Fig. 3.1b. The stiffness moduli in the transverse direction E_{22} is calculated by taking the initial slope of the stress-strain curves. The material shows brittle behavior in the transverse direction. The resulting elastic stiffness modulus E_{22} as well transverse tension strength R_{22} obtained directly from the characterization tests are listed in Table 3.1. Generally in the literature, transversal isotropic material behavior is assumed for the unidirectional FRPs. Hence, the equivalences $E_{22}=E_{33}$ and $R_{22}=R_{33}$ of the material properties mentioned in the Table 3.1 are based on this assumption of transversal isotropy.

Eight specimens were prepared and successfully tested for the shear characterization tests using the $[+45/-45]_{2s}$ specimen loaded in tension. Fig. 3.2b shows the

E_{11} [GPa]	$E_{22}(=E_{33})$ [GPa]	$R_{22}(=R_{33})$ [MPa]	$G_{12}(=G_{13})$ [GPa]	ν_{12} [-]
118.43	7.03	44.19	3.88	0.299

Table 3.1: Material properties from the characterization tests. The values E_{11} , E_{22} , R_{22} , G_{12} , and ν_{12} were obtained from the characterization tests. The equivalences $E_{22}=E_{33}$, $R_{22}=R_{33}$, and $G_{12}=G_{13}$ are based on the assumption of transversal isotropy.

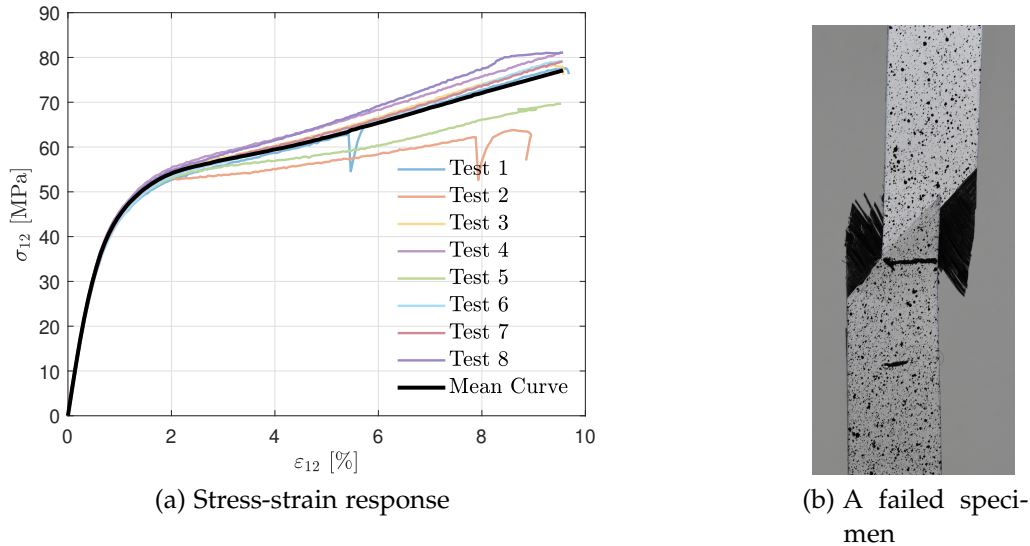


Figure 3.2: Results of the shear characterization tests

typical failure pattern of the shear characterization tests. The damage builds gradually in the specimen and it is distributed over the length of the gauge section. Final failure of the specimen occurs in the gauge section of the specimen around the mid-section of the specimen. It can be seen that the failure mode is clearly shearing of the material. In this particular shear test, the shear stress and the shear strain are calculated as follows:

$$\sigma_{12} = \frac{F}{2wt} \quad (3.1a)$$

$$\epsilon_{12} = \frac{\epsilon_{ax} - \epsilon_{tr}}{2} \quad (3.1b)$$

where F is the force measured by the machine load cell, w and t are the specimen width and thickness, and ϵ_{ax} and ϵ_{tr} are the strains in the axial and the transversal directions of the specimen. The strains ϵ_{ax} and ϵ_{tr} were measured using the DIC system on the surfaces of the specimens.

Fig. 3.2a shows the stress-strain response of the shear characterization tests, along with the mean curve. The elastic stiffness moduli G_{12} is calculated as the initial slope of the stress-strain curves and are given in Table 3.1. Based on the aforementioned

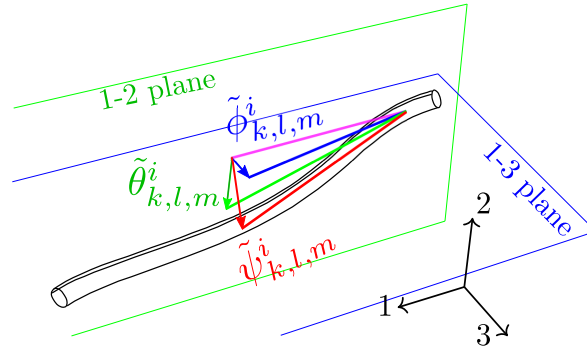


Figure 3.3: Schematic of the misalignment angles. Angles $\tilde{\theta}_{k,l,m}^i$ and $\tilde{\phi}_{k,l,m}^i$ are the misalignment in 1 – 2 and 1 – 3 planes, respectively. The angle $\tilde{\psi}_{k,l,m}^i$ shows the combined effect of $\tilde{\theta}_{k,l,m}^i$ and $\tilde{\phi}_{k,l,m}^i$.

transversal isotropy assumption, the equivalence $G_{12}=G_{13}$ is given in Table 3.1. The drops in the stress-strain curves present in two of the curves are because of the intermittent unloading, and hence, are not considered in the mean curve. It can be seen that the shear response is highly nonlinear, with final failure strains of approximately 9.57[%]. The variation in stress-strain curves at large strain levels is expected as the damage starts at multiple locations in the gauge section, only one of which matures to be the final failure location. For microbuckling prediction models, the initial shear response is of utmost importance. Large shear strains as those at the tail end of the characterization tests are not expected to play a major role in the prediction of failure under compression dominated loads. Hence, the variations in the shear stress-strain curves are not detrimental for prediction models of compression failure. Therefore, the mean curve can be used for such modeling purposes.

3.2 FIBER MISALIGNMENT MEASUREMENTS

The question arises, how many angles would be needed to represent a three dimensional misalignment of a fiber in space from its mean direction. If one follows the Euler angles representation and considers that the fiber rotation around its own axis does not affect MB failure, then it suffices to have two independent angles for representing the fiber misalignment in FRPs. These two angles correspond to the in-plane misalignment angle $\tilde{\theta}_{k,l,m}^i$ and the out-of-plane misalignment angle $\tilde{\phi}_{k,l,m}^i$ of a fiber. This assumption is consistent with the transverse isotropic behavior of the material. Hence, these two angles are sufficient for a complete volumetric representation of the total misalignment $\tilde{\psi}_{k,l,m}^i$ from the nominal fiber direction i.e. 1-direction, see Fig. 3.3.

SCANNED SAMPLE: To measure the fiber misalignment of the material, computed tomography (CT) scans were carried out. Three dimensional scans were performed in order to obtain volumetric measurements of the fiber misalignment. With the goal to obtain a statistically independent measure of the fiber misalignment, the scans

were performed on two specimens. The specimens with dimensions of $15 \times 15 \times 1.15$ mm were cut at two different locations from two separate plates. These plates were prepared for obtaining specimens for testing to failure series for strength characterization under compression and combined compression-shear. The testing to failure series will be discussed in Chapter 5. It is to be noted here that performing scans on a larger number of specimens would further improve the confidence in the measurements of the fiber misalignment. However, scanning of only two specimens was carried out in the current investigation because of the high costs associated with it for the required resolution. The size of the scanned volume is similar to the dimensions of the gauge section of the specimen for the testing to failure series. Moreover, the topologies of the in-plane misalignment and the topologies of the out-of-plane misalignment were measured independently. Therefore, these scans are deemed sufficient for the measurements of the fiber misalignment in the current investigation.

MISALIGNMENT ANGLE MEASUREMENTS: The volumetric scans were performed by the institutes for Building Materials (IfB) and Wind Energy Systems (IWES) of Leibniz University Hannover (LUH) using the X-ray microscope *Zeiss Xradia 410 Versa* with 80 kV voltage, 6 W power and a 10x magnification setting. This device can perform scans of a cylindrical volume in space with very fine resolutions. The diameter and the height of the resulting scanned cylindrical volume are dictated by the scan resolution and the scan time. To ensure that the algorithms for measurements of the fiber misalignment in the form of misalignment angles can differentiate between the matrix and the fiber materials, a fine enough resolution with voxel size smaller than the fiber diameter is required. The fiber diameter of the UD300 carbon is approximately 5.6-5.8 μm , therefore, a voxel resolution of 1.902 μm was selected. The selected resolution limited the diameter of the scanned cylinder to approximately 2 mm. The resulting scanned volume is approximately $2 \times 7 \times 1.15$ mm, cf. schematic in Fig. 3.4.

Briefly recalling Section 2.3 from the state of the art, there are three main methods for the measurements of misalignment angles of unidirectional FRPs: (i) following fiber cross sections in planes perpendicular to the mean fiber direction, as measured by Yurgartis [137], Paluch [87], and Clarke [29]; (ii) following measurements in planes parallel to the mean fiber direction, as investigated by Creighton [31], Kratmann [68], and Wilhelmsson [126]; (iii) through the calculation of a structural tensor from the measured voxel data of volumetric/surface CT-scans, such as the investigation by Nguyen et. al. [85]. The second group of methods gives accurate results with additional benefit of very high efficiency [127]. It also offers the possibility to measure the misalignment over longer distances because of the measurement scheme. Some fibers may be broken in the scanned volume or spread out of the ordinary across the layers. Such fibers can not be measured with this group of methods, as they do not allow following an individual fiber endlessly. However, such broken and randomly spread fibers are relatively rare. Therefore, they can be neglected for the purposes of predicting compressive strength [29]. Moreover, it is well accepted now that mea-

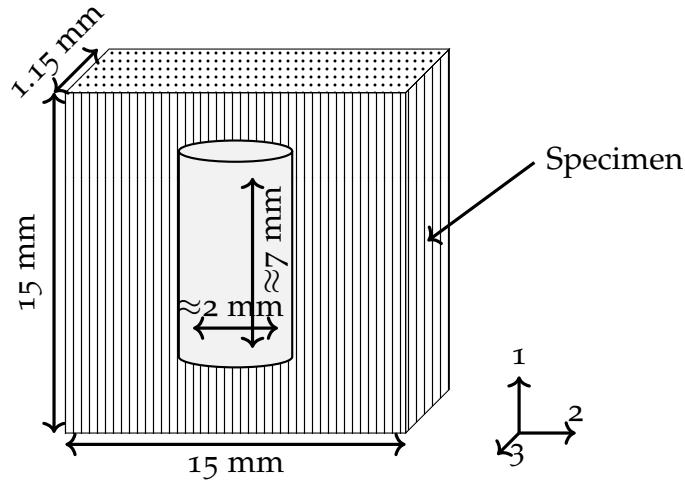


Figure 3.4: Schematic of the specimen for scanning, along with the dimensions of the scanned cylindrical volume

measurements of the fiber misalignment can be performed separately in the form of the in-plane and the out-of-plane misalignment, with either of the aforementioned methods of measurements. Therefore, it was decided to measure the fiber misalignment in the form of the in-plane misalignment and the out-of-plane misalignment using the second group of methods.

It was not possible to obtain cuboid volumes for measurements over the whole thickness of specimens because of the cylindrical shape of the scanned volumes as seen in Fig. 3.4. Hence, it was decided to extract micrograph images over cuboid shapes for the in-plane and the out-plane misalignment with dimensions given in Table 3.2 from the cylindrical CT-scans measurements of both specimens. An extracted cuboid volume of the CT measurement marked with planes of view is shown in Fig. 3.5a. The **1-2** planes in Fig. 3.5a marked in green color represent locations of micrograph images for the measurement of the in-plane misalignment on a cuboid volume, whereas the **1-3** planes marked in red color represent the locations of images for the measurement of the out-of-plane misalignment. As the samples were not perfectly aligned in the scanning machine, the resulting cylindrical measurements were also slightly tilted from the global coordinate system defined in the machine software. Therefore, the cuboid volumes obtained from these measurements in the machine coordinate for each plane of view, i.e. the in-plane (**1-2** plane) and the out-of-plane (**1-3** plane), had slight differences in the cuboid dimensions as seen in Fig. 3.4. The scanned volumetric data stored by *Xradia* in the format *.txm* was read into commercial software *Avizo* for the extraction of the required cross-sectional images. The images for each plane of view, i.e. the in-plane and the out-of-plane, were extracted in *.tif* format, cf. Fig. 3.5. The images were extracted in such a way that the image stacking direction corresponds to either direction **3** (for the in-plane misalignment) or direction **2** (for the out-of-plane misalignment), see Fig. 3.5a. The distance between the neighboring

	Number of images	Number of cells in an image	Volumetric dimensions 1-2-3 [mm]
In-plane measurement section 1-2	516	70×12	$6.657 \times 1.141 \times 0.979$
Out-of-plane measurement section 1-3	702	70×10	$6.657 \times 1.329 \times 0.951$

Table 3.2: Dimensions of the scanned volume

images in the stacking direction is equal to the length of a voxel edge, i.e. $1.902 \mu\text{m}$, see Fig. 3.5b. Dimensions of the resulting cuboids are presented in Table 3.2.

ALGORITHM FOR MEASUREMENT OF ANGLES: The High Resolution Misalignment Analysis (HRMA) method proposed by Wilhelmsson [126], which is the latest from the second group of methods for measurement of misalignment, was used for the calculation of misalignment angles from the extracted cross-sectional images. The HRMA method is faster because of a simpler algorithm in comparison to the similar methods such as the Multiple Field Image Analysis (MFIA) by Creighton [31] and the Fourier Transform Misalignment Analysis (FTMA) by Kratmann [68], and produces accurate results. The HRMA method is chosen here because of its direct approach, in which fiber paths are calculated by tracing them over the image.

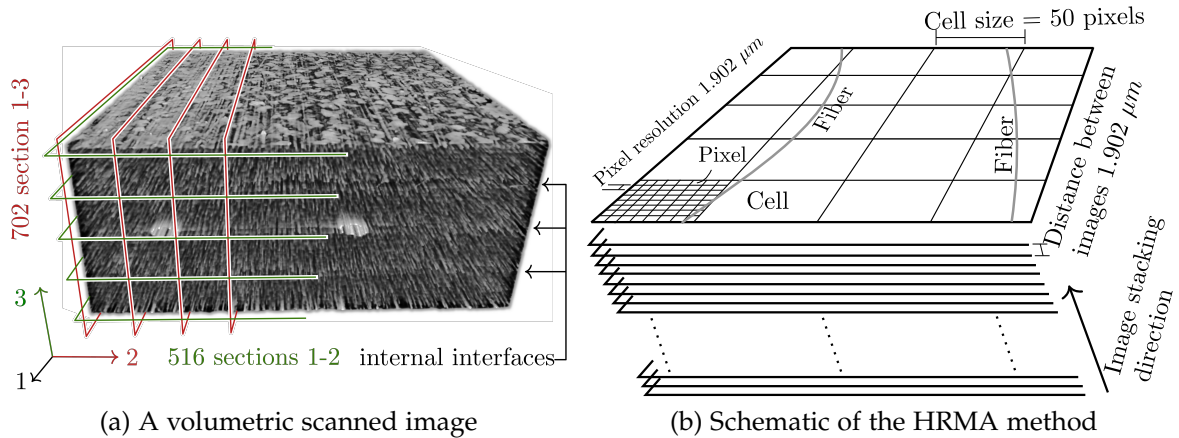


Figure 3.5: The 3D nature of the fiber misalignment is shown by Fig. 3.5a. The extracted cross sectional planes are marked on the scanned volume in Fig. 3.5a. Direction 1 indicates fiber direction, direction 2 represents the in-plane transversal direction and direction 3 points to the out-of-plane transversal direction. Stacking directions are marked in corresponding color of arrows of the coordinate system. (The original image of the scanned volume was provided by IfB, LUH). Fig. 3.5b shows schematic of the HRMA method for the measurements of the fiber misalignment on the images extracted from the scanned 3D volume.

As mentioned earlier, each specimen gave two sets of micrograph images, i.e. one in **1-2** plane for the in-plane misalignment and one in **1-3** plane for the out-of-plane misalignment. The algorithmic steps of the HRMA method were implemented in the commercial software Matlab for measurement of the misalignment on the four sets of extracted micrograph images. For the application of the HRMA method on each set of image data, each cross-sectional 2D image from each set was further divided into small subdivisions called cells, see Fig. 3.5b. Different authors had pointed the observation of the minimum wavelengths of the fiber misalignment in unidirectional FRPs to be >0.5 mm [29, 110]. Hence, square cells with edge lengths of 50 pixels (i.e. $95.1\mu\text{m}$) were chosen, which gives at least five measurement points for the shortest expected wavelength. Within the cells, fibers are assumed to be approximately straight. Each individual cell contains four to seven fibers with an average of five fibers.

A schematic of the in-plane misalignment $\tilde{\theta}_{k,l,m}^i$ and the out-of-plane misalignment $\tilde{\phi}_{k,l,m}^i$ measurements on a single fiber is shown in Fig. 3.3. Misalignment angles can be calculated using the start point coordinate of the fiber $x_{1/2/3}^{ai}$ and the end point coordinate of the fiber $x_{1/2/3}^{bi}$ via Eq. 3.2a for each tracked fiber with index i inside a cell with index k, l, m . The indices k, l , and m are the location indices of a cell in a micrograph image for direction **1**, **2**, and **3**, respectively. An equivalent angle $\tilde{\psi}_{k,l,m}^i$ representing a combined effect of the in-plane misalignment $\tilde{\theta}_{k,l,m}^i$ and the out-of-plane misalignment $\tilde{\phi}_{k,l,m}^i$ is also defined via Eq. 3.2a. Subsequently, the mean in-plane misalignment $\theta_{k,l,m}$ and the mean out-of-plane misalignment $\phi_{k,l,m}$ for each cell k, l, m were calculated via Eq. 3.2b. The mean angle within a cell was calculated by averaging misalignment of all fibers within that cell. The mean angles $\theta_{k,l,m}$ and $\phi_{k,l,m}$ of each cell were stored in respective matrices corresponding to their spatial positions. The resulting number of cells for images in each cross section, i.e. **1-2** cross section for the in-plane misalignment and **1-3** plane for the out-of-plane misalignment, are given in Table 3.2. After running the HRMA method on all sets of images and assembling the average misalignment of fiber within each cell in the corresponding spatial positions of each cell for each specimen and plane of view, two matrices of the in-plane misalignment with $70 \times 12 \times 516$ data points and two matrices of the out-of-plane measurements with $70 \times 702 \times 10$ data points were obtained. The 3D matrices exhibit complete 3D representation of the in-plane and the out-of-plane misalignment angles.

$$\tilde{\theta}_{k,l,m}^i = \tan^{-1} \left(\frac{x_2^{bi} - x_2^{ai}}{x_1^{bi} - x_1^{ai}} \right)_{k,l,m}, \quad \tilde{\phi}_{k,l,m}^i = \tan^{-1} \left(\frac{x_3^{bi} - x_3^{ai}}{x_1^{bi} - x_1^{ai}} \right)_{k,l,m} \quad (3.2a)$$

$$\text{and } \tilde{\psi}_{k,l,m}^i := \sqrt{\left(\tilde{\theta}_{k,l,m}^i\right)^2 + \left(\tilde{\phi}_{k,l,m}^i\right)^2}$$

$$\theta_{k,l,m} = \frac{1}{n} \sum_{i=1}^n \tilde{\theta}_{k,l,m}^i \quad \text{and} \quad \phi_{k,l,m} = \frac{1}{m} \sum_{i=1}^m \tilde{\phi}_{k,l,m}^i \quad (3.2b)$$

	In-plane $\theta_{k,l,m}$		Out-of-plane $\phi_{k,l,m}$	
	Specimen 1	Specimen 2	Specimen 1	Specimen 2
s [°]	0.6458	0.6995	0.5652	0.4147
P_1 [°]	-1.375	-2.050	-1.116	-0.812
P_{99} [°]	2.558	1.432	1.654	1.291

Table 3.3: Statistics of the measurements of the fiber misalignment angles before shifting means of the misalignment to zero

RESULTS: If a specimen made of unidirectional plies of a FRP material is perfectly cut in the mean fiber direction and it is also perfectly aligned with the coordinate frame of the CT-device during the measurements, the resulting mean of the measured misalignment angles would be 0° . However, the mean values of the measured in-plane misalignment $\theta_{k,l,m}$ and the out-of-plane misalignment $\phi_{k,l,m}$ are 1.3426° and 0.2512° for specimen 1 and -0.2230° and 0.2405° for specimen 2, respectively. It is to be noted that the non zero mean values of misalignment are not indicative of the manufacturing induced fiber misalignment. They are rather the global alignment errors of the specimen that may have occurred during sawing of the specimens or positioning of the specimens in the CT-device. The focus of the campaign is on measuring the fiber misalignment from the nominal fiber direction intrinsic to the material which causes MB failure under compression loads, and avoiding any additional inputs to the misalignment measurements from the global alignment errors of the specimen. Therefore, the misalignment data of each specimen for each measurement plane of view was shifted to obtain zero mean misalignment in order to eliminate the global alignment errors. This was done by subtracting/adding the measured mean values from each corresponding data set, since subtraction/addition of a constant value does not change the spread of a distribution. The statistics of the misalignment angles before shifting means of the distributions of the misalignment to zero are provided in Table 3.3. The standard deviations of the in-plane misalignment angles are higher than those of the out-of-plane misalignment angles.

The resulting data sets of the measurements of the fiber misalignment $\theta_{k,l,m}$ and $\phi_{k,l,m}$ after shifting the mean of each data set to zero are plotted in the form of 3D contour plots in Fig. 3.6 and Fig. 3.7 using the commercial software Mathematica [134] with the plotting functionality *ListSliceContourPlot3D*, respectively. The distance of $1.902 \mu\text{m}$ between neighboring images is too small for any noticeable changes in the contours of the fiber misalignment. In order to reduce noise in the contour lines of the Fig. 3.6 and Fig. 3.7 and to get a clearer picture of the topologies of the misalignment angles, the measurement data of every 50^{th} image is used in the 3D contour plots. Comparing Fig. 3.6a and Fig. 3.6b with Fig. 3.7a and Fig. 3.7b, it is recognizable that the misalignment topologies of the in-plane misalignment $\theta_{k,l,m}$ and the out-of-plane misalignment $\phi_{k,l,m}$ are completely independent to each other. This

is because the underlying waviness behavior which gave rise to the misalignment of fiber has independent behavior in 1-2 and 1-3 planes, i.e. the in-plane misalignment and the out-of-plane misalignment. A similar observation on the independence of the in-plane and the out-of-plane misalignment was made by Yurgartis [137]. It can also be seen that the topologies of the in-plane misalignment have a bias towards longer wavelengths in the 1-direction which is visible in the form of longer contours of misaligned regions in Fig. 3.6. Additionally, rather large misaligned regions at the layer interfaces can be observed in the topologies of the in-plane misalignment, cf. Fig. 3.6b. Matrix material is an excess at the interface regions and fibers are not tightly packed as inside the plies, It allows the fibers at the interface regions to expand rather freely, giving rise to larger regions of misalignments seen in Fig. 3.6. On the other hand, wavelengths of the topologies of the out-of-plane misalignment are quite evenly spread in all three spatial directions as can be seen in Fig. 3.7. The reasons behind such a biased behavior of the in-plane misalignment compared to the uniform behavior of the out-of-plane misalignment can be found in the lamination and the subsequent curing processes. Pressure in the autoclave acts normal to the lamination plane during the curing process. The pressure during curing gives fibers a higher possibility to spread out in this plane. On the contrary, compaction limits the misalignment out-of-plane. Hence, the observation of the relatively even spread of the misaligned regions in the out-of-plane topologies is the natural outcome. Since the prepreg layers are laid out over one another in-plane during the lamination process, it becomes an additional driving factor in the development of the observed long regions of imperfections.

The misalignment angles are also plotted in the more commonly found form of histograms in Fig. 3.8. Histograms show that the spread of the misalignment angles is approximately mirrored around the mean values for all the data sets of the measurements. Consequently, each measurement data set is fitted with a normal distribution based on the observation of the spread of data around corresponding mean values, which are in turn plotted along with the histograms in Fig. 3.8. The larger spread of the in-plane distributions, which arises because of the reasons explained earlier, is also reflected in the larger width of the fitted normal distributions. It is to be noted that normal distribution implies possibility of an existence of infinitely large values of misalignment angles. In reality, the maximum/minimum values of the misalignment angles are only up to a few degrees. A fit to a normal distribution is shown here only to highlight the nature of the distribution of misalignment angles. The probability of extreme values predicted by the normal distributions in this case is quite low. Moreover, only standard deviations and the selected percentiles of the misalignment angles are required for models of MB failure prediction, hence, a fit to a normal distribution for the misalignment angles can be accepted here as an approximation.

Some statistical properties of the misalignment angles $\theta_{k,l,m}$ and $\phi_{k,l,m}$ after transforming the mean of each data set to zero are given in Table 3.4 for further reference. There, the symbol s denotes the standard deviation and the symbols P_1 and P_{99} denote 1st and 99th percentiles of the real numbered measurements of the fiber misalignment,

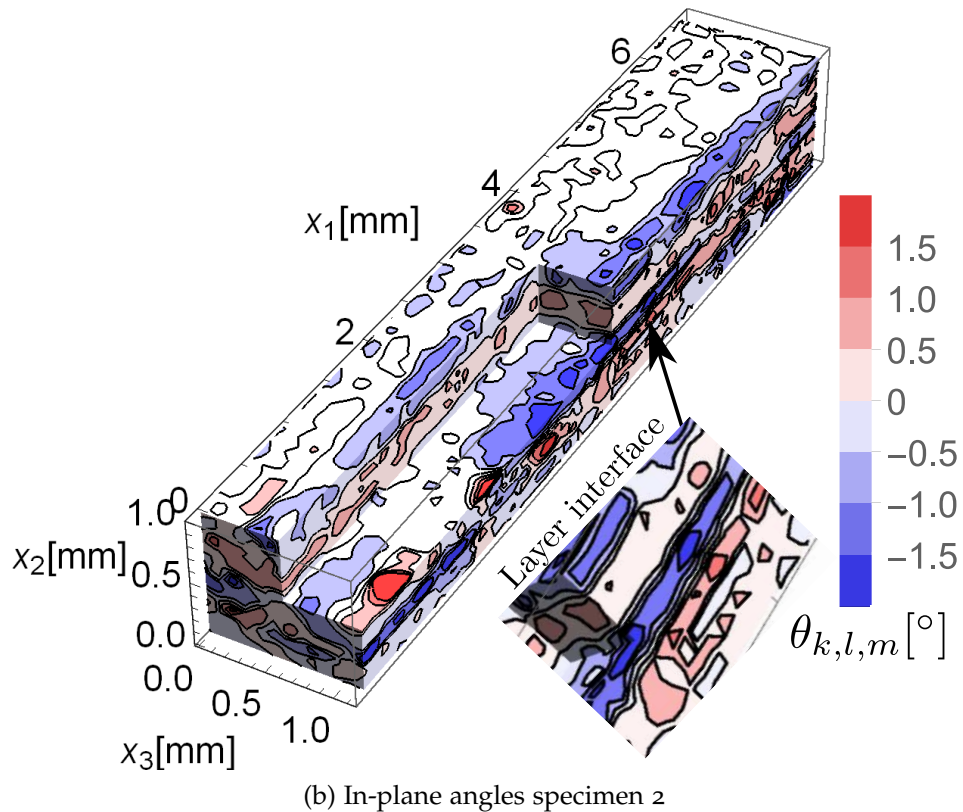
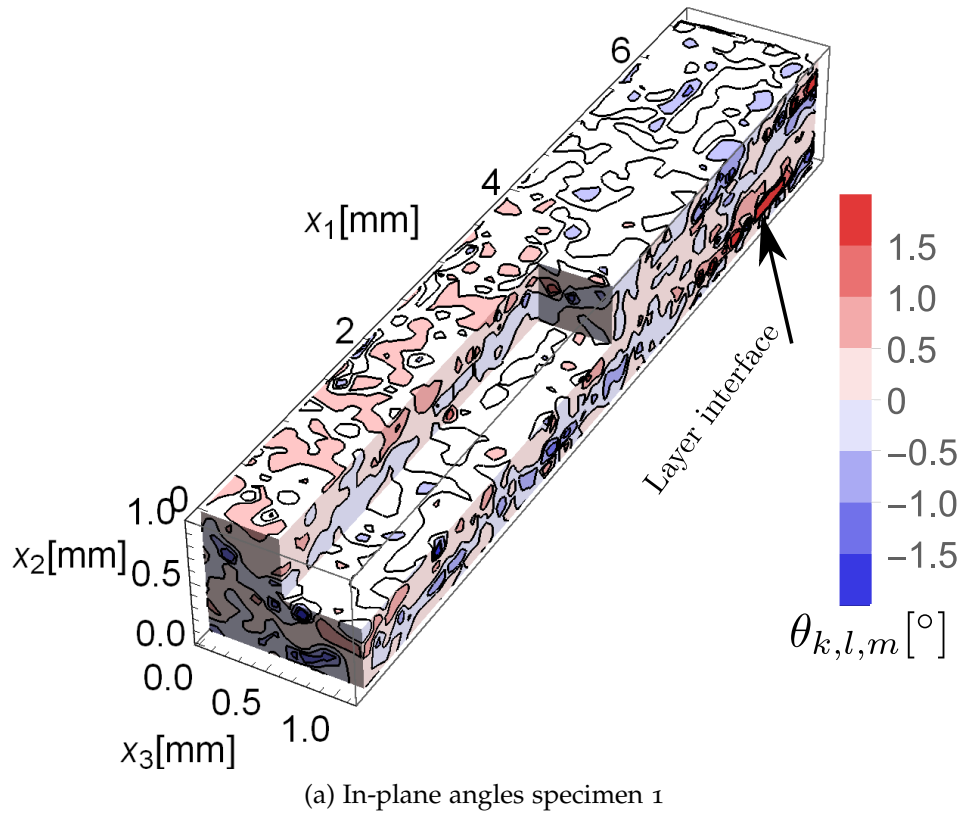


Figure 3.6: 3D contour plots of the in-plane misalignment $\theta_{k,l,m}$. Results shown here were measured over the cuboid-shaped domains extracted from the scanned cylindrical volumes. The dimensions of the cuboids are listed in Table 3.2. To view the interior of the topologies of the misalignment, $1/8^{th}$ of the domains are not shown. One can observe that the topologies of the misalignment angles show clear three dimensional behavior.

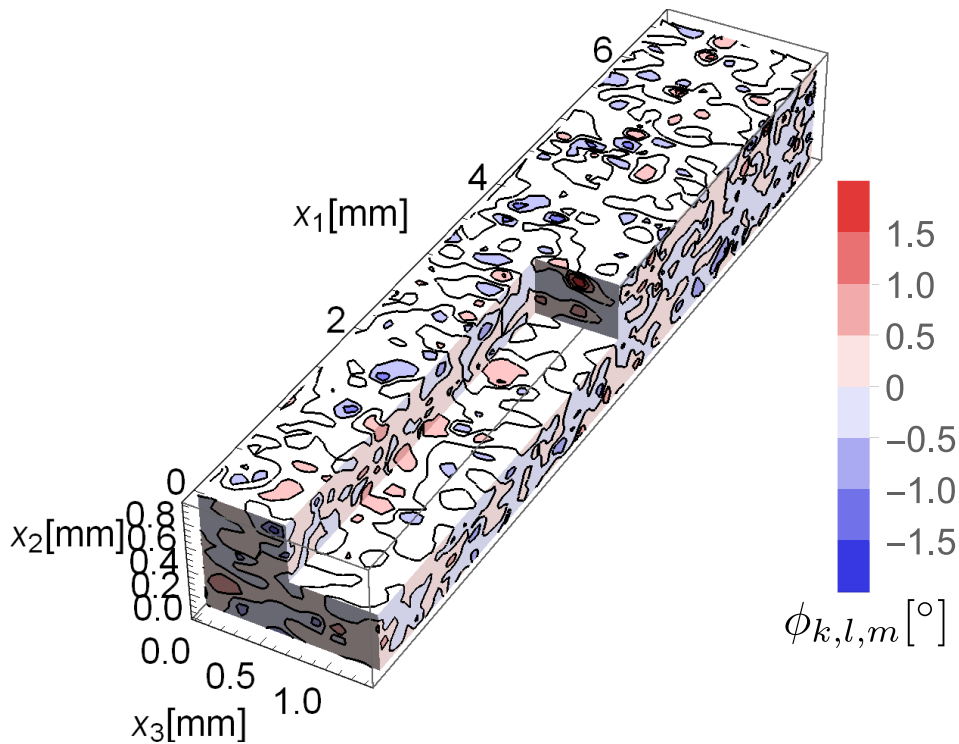
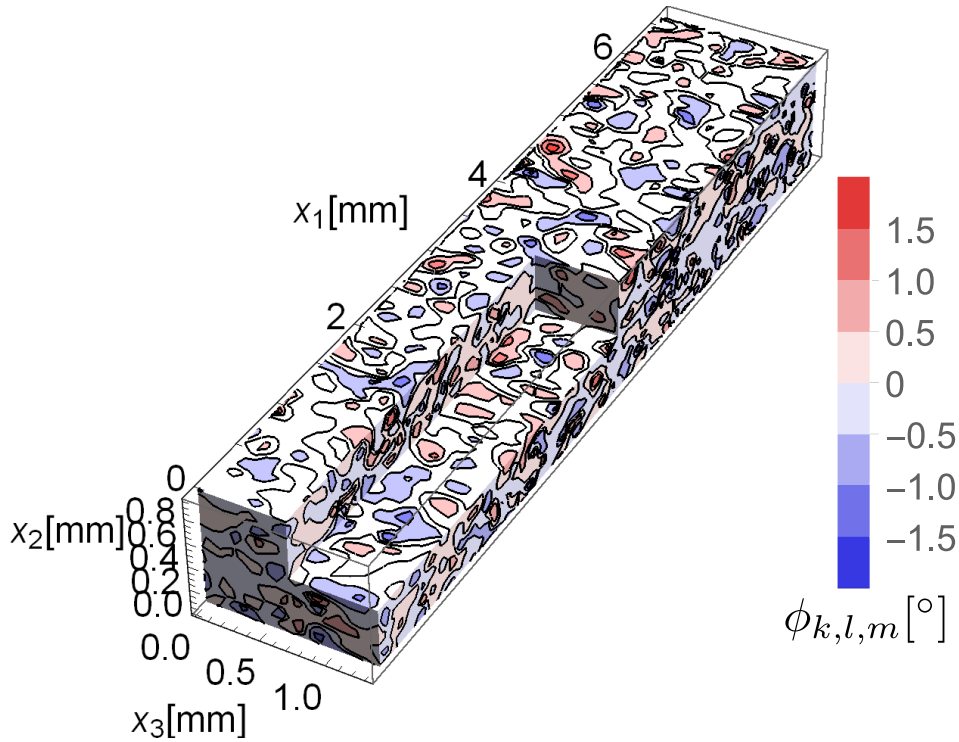


Figure 3.7: 3D contour plots of the out-of-plane misalignment $\phi_{k,l,m}$. Misalignment angles were measured over the cuboid-shaped domains extracted from the scanned cylindrical volumes. The dimensions of the cuboids are provided in Table 3.2. To highlight the interior of the topologies of the misalignment, $1/8^{th}$ of the domains are cut out. It is clearly observable that topologies of the misalignment angles show clear three dimensional behavior.

	In-plane $\theta_{k,l,m}$			Out-of-plane $\phi_{k,l,m}$		
	Specimen 1	Specimen 2	Average	Specimen 1	Specimen 2	Average
s [°]	0.6458	0.6995	0.6726	0.5652	0.4147	0.4899
P_1 [°]	-2.178	-1.827	-2.002	-1.367	-1.052	-1.209
P_{99} [°]	1.215	1.655	1.435	1.403	1.050	1.226
$P_{99}(\theta_{k,l,m})$ $P_{99}(\phi_{k,l,m})$ [°]	2.445	2.230	2.337	1.572	1.227	1.399

Table 3.4: Statistics of the measurements of the fiber misalignment angles after shifting means of the misalignment to zero. It is to be noted that the standard deviation of the $\theta_{k,l,m}$ and $\phi_{k,l,m}$ for both specimens remain unchanged as shifting the mean of a distribution does not change its spread i.e. standard deviation. Moreover, the average values of $\theta_{k,l,m}$ and $\phi_{k,l,m}$ have only meaning to them when the mean of the corresponding data sets has been transformed to zero.

respectively. Since some analytical solutions for prediction of failure under compression loads use a single representative effective angle considering absolute values of angles $|\theta_{k,l,m}|$ and $|\phi_{k,l,m}|$ such as the investigation by Wilhelmsson [127], the respective 99th percentiles $P_{99}(|\theta_{k,l,m}|)$ and $P_{99}(|\phi_{k,l,m}|)$ are also tabulated for all measurement data sets. The average $s=0.6726^\circ$ for the in-plane misalignment $\theta_{k,l,m}$ is significantly higher than that of the out-of-plane misalignment $\phi_{k,l,m}$ having a value of $s=0.4899^\circ$. A similar trend can be seen in the percentile statistics. There are some extreme values, as high as 8° , at the tail end of the measured distribution of the in-plane misalignment. This observation further solidifies the argument presented earlier to explain the differences in the spread of the in-plane and the out-of-plane misalignment that the fibers are more prone to imperfections in the in-plane directions because of the lamination and the curing process in a prepreg based material. It is interesting to observe from statistics given in Table 3.4 that the standard deviation of the in-plane misalignment angle $\theta_{k,l,m}$ of specimen 1 is lower compared to that of specimen 2. On the other hand, the standard deviations of the out-of-plane misalignment angle $\phi_{k,l,m}$ of specimen 1 is higher compared to that of specimen 2. It again provides further support for the Yurgartis's observation about the independence of the in-plane and the out-of-plane misalignment distributions from one another.

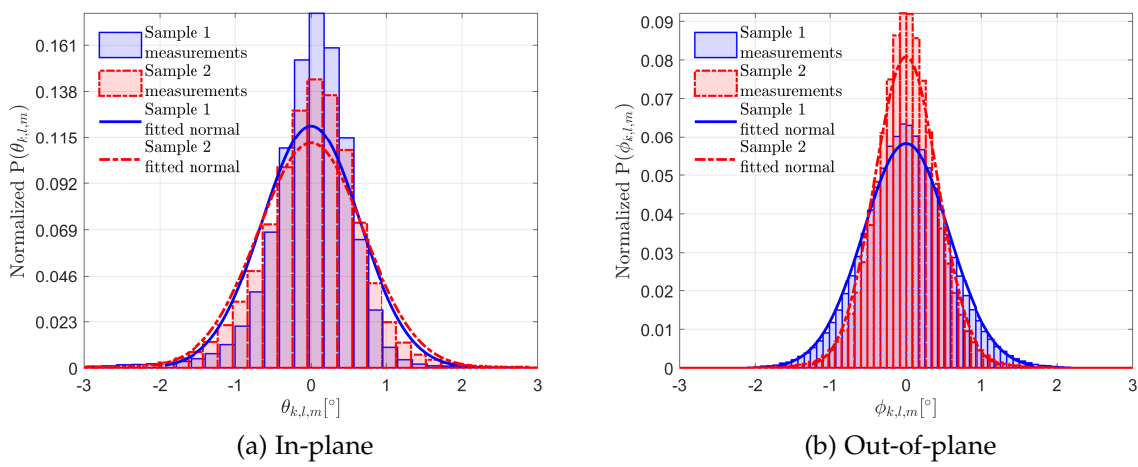


Figure 3.8: Histograms of the in-plane misalignment $\theta_{k,l,m}$ and the out-of-plane misalignment $\phi_{k,l,m}$, along with the corresponding fits to the normal distributions. All data sets were transformed to zero mean, i.e. mean fiber direction. Note that the out-of-plane misalignment is more closely related to the normal distribution compared to the in-plane misalignment.

QUANTIFICATION OF STATISTICAL PROPERTIES OF THE FIBER MISALIGNMENT

THEORETICAL BASICS Of the different approaches available in the literature for generating topologies of the misalignment, the spectral representation method is the most promising one [76, 100]. The representation of the fiber misalignment through the spectral representation method provides a procedure to define both the statistical distribution as well as the correlation properties observed experimentally in unidirectional FRPs. The spectral representation method applies to stationary random fields. The term stationary implies that the spectral characteristics of the field are independent of spatial interval in which they are measured/sampled/modeled, and hence can be accounted as a material characteristics. Assuming that a misalignment angle $f(x)$ (with x being a spatial dimension) is a stationary random field, the spectral density $S(\omega)$ of the fiber misalignment angle $f(x)$ can be used to represent the random correlated field through the spectral representation method [76, 100]. Similar approaches have also been successfully employed in other engineering problems such as surface generation for contact mechanics [27, 61], and sea surface generation for visual imagery or optical analysis [43, 67], among others.

The spectral representation method is based on Fourier analysis. Fourier analysis yields a representation of a function in terms of an infinite series of superposed harmonic functions of different wavelengths and amplitudes. Fourier transform of a topology of the fiber misalignment angles $f(x)$ is given by:

$$F(\omega) = \frac{1}{2\pi} \int_{-\infty}^{\infty} f(x) dx \quad (4.1)$$

and the inverse Fourier transform is given by:

$$f(x) = \int_{-\infty}^{\infty} F(\omega) d\omega \quad (4.2)$$

For a fiber having an infinite length, the autocorrelation function for the fiber misalignment in the nominal fiber direction is defined as:

$$R(\tau) = \int_{-\infty}^{\infty} f(\tau) \cdot f(x + \tau) dx \quad (4.3)$$

The autocorrelation function $R(\tau)$ defines by how much the values of a function are correlated with itself over a lag distance τ . Examples of the autocorrelation functions for some standard functions are given in Fig. 4.1 for a better understanding. In Fig. 4.1a, Fig. 4.1b, and Fig. 4.1c three basic functions are shown i.e. a sine wave, a

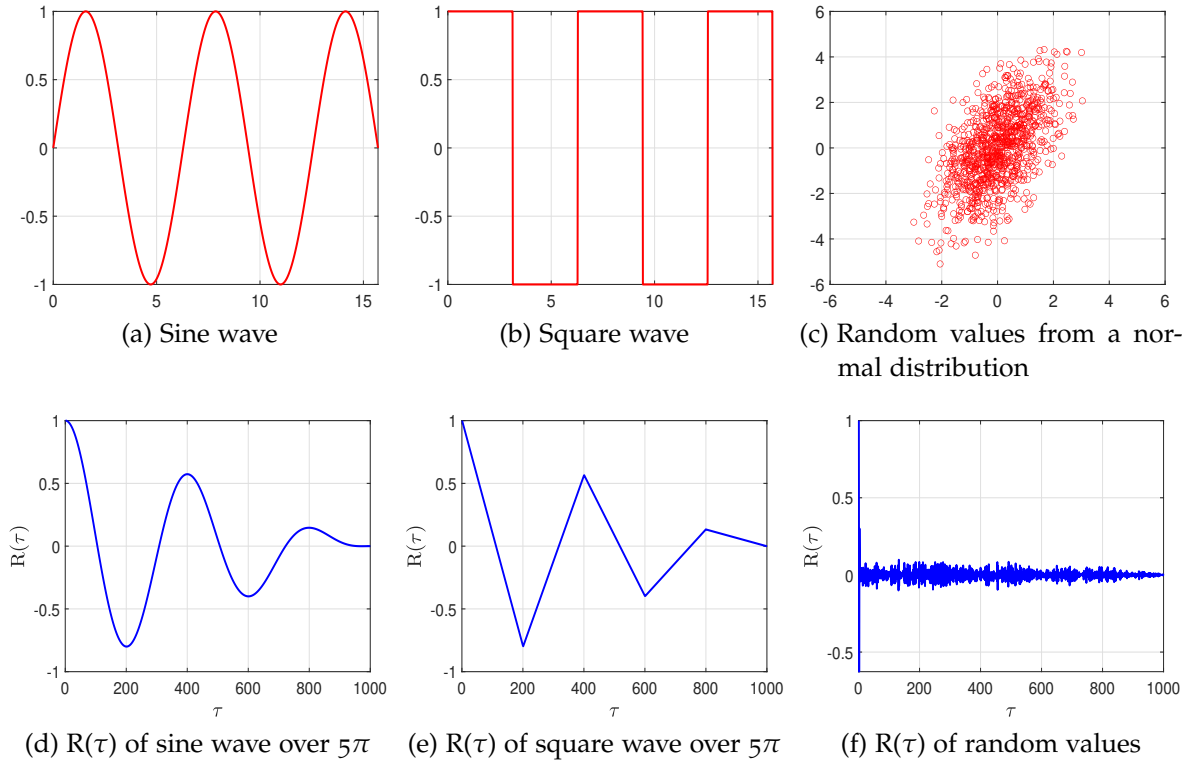


Figure 4.1: Examples of some standard functions and their autocorrelation $R(\tau)$. The τ axis in the bottom row plots represents number of total discrete points over which the function has been sampled and corresponds to the lag distances.

square wave, and random values sampled from a standard normal distribution, respectively. In Fig. 4.1d, Fig. 4.1e, and Fig. 4.1f, the autocorrelation functions $R(\tau)$ of the plots in Fig. 4.1a, Fig. 4.1b, and Fig. 4.1c are shown. The autocorrelation functions of an infinite sine and an infinite square wave are an infinite cosine and an infinite triangular wave with constant amplitude, respectively. However, when the autocorrelation is calculated over a finite distance following Eq. 4.3, the autocorrelation function slowly decays to zero. The plotted functions in Fig. 4.1 are over a finite range (i.e. 5π in these examples), therefore, the decay of the autocorrelation function $R(\tau)$ can be seen in the plots in Fig. 4.1d and Fig. 4.1e. For the random functions, it can be seen easily that after a spike at zero lag (i.e. $\tau=0$) the correlation becomes approximately 0 over a very short lag distance. This implies that the points are independent of each other, which is true for random sampling. Additionally, it can be noted that the autocorrelation takes positive and negative values. Looking at the example of the sine wave, it is clear that any given point is perfectly correlated with itself. The correlation decreases with increasing lag distance τ , and when the original function changes sign the correlation becomes negative.

Spectral density $S(\omega)$ is defined as the Fourier transform of the autocorrelation $R(\tau)$ of a function. Mathematically, it can be written as:

$$S(\omega) = \frac{1}{2\pi} \int_{-\infty}^{\infty} R(\tau) \cdot e^{-i\omega\tau} d\tau \quad (4.4)$$

Spectral density provides information about the amplitudes of the harmonic functions associated with different frequencies ω (or wavelengths λ) in that function. One can find different definitions of frequencies in terms of either the angular frequency ω or in terms of the ordinary frequency $f=\omega/2\pi$ in the literature. In the current implementation, the angular frequencies $\omega=2\pi/\lambda$ are considered. Angular frequency ω is the number of waves contained in 2π units of dimensions.

Spectral density can also be related to the Fourier transform of the original function $F(\omega)$ and the conjugate of the Fourier transform $F(\omega)^*$ by Eq. 4.5, [84].

$$S(\omega) = \frac{1}{2\pi} F(\omega)^* F(\omega) \quad (4.5)$$

This relationship is useful in discrete calculations as will be explained in next subsection. The total area under the spectral density curve Ξ equals the mean square of the function (see Eq. 4.6). The mean square value Ξ is a material characteristic quantity in the current representation [28, 76, 100].

$$\Xi = \int_{-\infty}^{\infty} S(\omega) d\omega \quad (4.6)$$

4.1 SPECTRAL ANALYSIS OF THE MEASURED FIBER MISALIGNMENT

In this section, the discrete spectral analysis on the measured topologies of the fiber misalignment is presented. Since the misalignment was measured over a volume in space, the corresponding volumetric representation of the spectral densities is given. Moreover, the deficiencies of characterizing the spectral density in 2D frequency domain of the measured 3D misalignment are discussed.

4.1.1 Characterization of spectral densities in 3D frequency domain

The misalignment is measured over finite distances L_1 , L_2 , and L_3 in a discrete manner in the experimental investigations. Hence, for the characterization of the fiber misalignment in the form of spectral densities, the discrete definitions of the Fourier analysis are followed. In the experimental investigations, the misalignment is measured Δ_1 , Δ_2 , and Δ_3 distances apart from each other for N_1 , N_2 , and N_3 times. The intervals between the measurement points are defined as $\Delta_1=L_1/N_1$, $\Delta_2=L_2/N_2$, and

$\Delta_3=L_3/N_3$. The topologies of the in-plane misalignment angle θ and the out-of-plane misalignment angle ϕ can be represented as follows:

$$\theta_{k,l,m} = \theta({}^1x_k, {}^2x_l, {}^3x_m) = f_{k,l,m}^\theta \quad (4.7a)$$

$$\phi_{k,l,m} = \phi({}^1x_k, {}^2x_l, {}^3x_m) = f_{k,l,m}^\phi \quad (4.7b)$$

where ${}^1x_k=k\Delta_1$, ${}^2x_l=l\Delta_2$, and ${}^3x_m=m\Delta_3$ (for $k=\{0, 1, \dots, N_1 - 1\}$, $l=\{0, 1, \dots, N_2 - 1\}$, and $m=\{0, 1, \dots, N_3 - 1\}$). The rest of the equations will be shown only for $\theta_{k,l,m}$ and they hold analogously for $\phi_{k,l,m}$. The discrete Fourier transform of $f_{k,l,m}^\theta$ is given by:

$$F_{k,l,m}^\theta = \frac{1}{N_1 N_2 N_3} \sum_{r=0}^{N_1-1} \sum_{s=0}^{N_2-1} \sum_{t=0}^{N_3-1} f_{r,s,t}^\theta \exp \left(-2\pi i \left(\frac{kr}{N_1} + \frac{ls}{N_2} + \frac{mt}{N_3} \right) \right) \quad (4.8)$$

It is necessary to take the number of sampling points $N_1 > \omega_{c_1} L_1 / \pi$, $N_2 > \omega_{c_2} L_2 / \pi$, and $N_3 > \omega_{c_3} L_3 / \pi$ to avoid aliasing which is an accuracy eroding artifact in Fourier analysis [84]. The symbols ω_{c_1} , ω_{c_2} , and ω_{c_3} correspond to the maximum components of frequencies (proportional to minimum wavelengths λ_{min_1} , λ_{min_2} , and λ_{min_3}) present in the fiber misalignment field $f_{k,l,m}^\theta$. It is to be noted that the minimum wavelengths that can be measured on a specimen are twice the distance between measurement points in the respective direction i.e. $\lambda_{min_1}=2\Delta_1$, $\lambda_{min_2}=2\Delta_2$, and $\lambda_{min_3}=2\Delta_3$. Spectral densities can then be calculated in discrete form by Eq. 4.9, see also Ref. [84].

$$S_{k,l,m}^\theta = S^\theta(\omega_k, \omega_l, \omega_m) = \frac{L_1 L_2 L_3}{(2\pi)^3} F_{k,l,m}^{\theta*} F_{k,l,m}^\theta = \frac{L_1 L_2 L_3}{(2\pi)^3} |F_{k,l,m}^\theta|^2 \quad (4.9)$$

where $F_{k,l,m}^{\theta*}$ is the complex conjugate to $F_{k,l,m}^\theta$. For $f_{k,l,m}^\theta=\theta_{k,l,m}$ and $f_{k,l,m}^\phi=\phi_{k,l,m}$, the sum of the respective spectral densities $S_{k,l,m}^\theta$ and $S_{k,l,m}^\phi$ will be subsequently related to the standard deviations of $f_{k,l,m}^\theta$ and $f_{k,l,m}^\phi$. For this purpose, the mean square spectral density Ξ^θ (analogously Ξ^ϕ) is introduced in Eq. 4.10.

$$\Xi^\theta = \sum_{k=1}^{N_1-1} \sum_{l=1}^{N_2-1} \sum_{m=1}^{N_3-1} S^\theta(\omega_k, \omega_l, \omega_m) \quad (4.10)$$

Parseval's identity given in Eq. 4.11 provides the relation between the fiber misalignment and its Fourier transform components.

$$\frac{1}{N_1 N_2 N_3} \sum_{k=0}^{N_1-1} \sum_{l=0}^{N_2-1} \sum_{m=0}^{N_3-1} |f_{k,l,m}^\theta|^2 = \sum_{r=0}^{N_1-1} \sum_{s=0}^{N_2-1} \sum_{t=0}^{N_3-1} |F_{r,s,t}^\theta|^2 \quad (4.11)$$

The quantity on the left in Eq. 4.11 equals the variance (square of standard deviation s^θ) of a distribution with zero mean. This is the case here, since the nominal fiber direction i.e. 1-direction is identified with the mean of the random fiber misalignment.

Hence, the relation between the mean square spectral density Ξ^θ and the standard deviation s^θ of a distribution of misalignment angles comes out to be:

$$\Xi^\theta = \frac{L_1 L_2 L_3}{(2\pi)^3} (s^\theta)^2 \quad (4.12)$$

Ideally, an ensemble averaged value of the spectral density has to be calculated by measuring the misalignment experimentally in a statistical manner for the spectral density of the fiber misalignment to be a material characteristic. However, only two specimens were scanned for the characterization of spectral densities in the experimental campaign because of the steep costs per CT-scan. The resulting voxel data was used to determine both the topologies of the in-plane misalignment angle $\theta_{k,l,m}$ and the topologies of the out-of-plane misalignment angle $\phi_{k,l,m}$ via the image processing technique High Resolution Misalignment Analysis (HRMA) proposed by Wilhelmsson and Asp [126], see Section 3.2 for a more detailed description of this process and the corresponding results. Image processing using the HRMA method rendered $70 \times 12 \times 516$ matrices for the misalignment angle $\theta_{k,l,m}$ over measurement volumes of $6.657 \times 1.1412 \times 0.979$ mm and $70 \times 702 \times 10$ matrices for the misalignment angle $\phi_{k,l,m}$ over measurement volumes of $6.657 \times 1.329 \times 0.951$ mm.

The cuboids for the in-plane and the out-of-plane measurements in Section 3.2 have slight differences in the dimensions due to the cylindrical nature of the scans and the corresponding image extraction from the CT-scan data. For the numerical analysis, same volumes with same number of sampling points are required for both $\theta_{k,l,m}$ and $\phi_{k,l,m}$ misalignment angles. Moreover, the distance of $1.902 \mu\text{m}$ between neighboring images is too small for any noticeable changes in the the fiber misalignments $\theta_{k,l,m}$ and $\phi_{k,l,m}$, hence, every 50th image's data is used in the 3D calculation of the spectral densities. This resulted in distances between measurement points Δ_1 , Δ_2 , and Δ_3 of $95.1 \mu\text{m}$ (i.e. 50 pixels) for both topologies $\theta_{k,l,m}$ and $\phi_{k,l,m}$. Therefore, the volume of $6.657 \times 1.1412 \times 0.951$ mm with $70 \times 12 \times 10$ sample points was chosen for all measurement data sets. A schematic of a cuboid volume selected from a cylindrical scanned volume is shown in Fig. 4.2. The viewing planes in **1-2** and **1-3** planes, i.e. the in-plane and the out-of-plane, are marked in green and red colors, respectively. A real extracted cuboid CT scan volume is shown in Fig. 3.5a with location of planes for the in-plane and the out-of-plane images marked in green and red colors, respectively. Subsequent discrete Fourier transformation on the misalignment data sets rendered $70 \times 12 \times 10$ matrices for the corresponding spectral densities $S^\theta(\omega_k, \omega_l, \omega_m)$ and $S^\phi(\omega_k, \omega_l, \omega_m)$.

Since the calculated spectral densities are dependent on three spatial/frequency variables, it is not straightforward to plot them meaningfully. When analyzing the matrices of spectral densities $S^\theta(\omega_k, \omega_l, \omega_m)$ and $S^\phi(\omega_k, \omega_l, \omega_m)$, it was observed that the spectral densities have highest values at the lowest frequencies, i.e. larger wavelengths. The values of the spectral densities reduced sharply moving away from the origin, eventually approaching zero towards higher frequencies. Hence, the most representative plots are on planes $\omega_1=0$, $\omega_2=0$, and $\omega_3=0$. Therefore, the results are plotted for the spectral densities $S^\theta(\omega_k, \omega_l, \omega_m)$ and $S^\phi(\omega_k, \omega_l, \omega_m)$ of the in-plane and

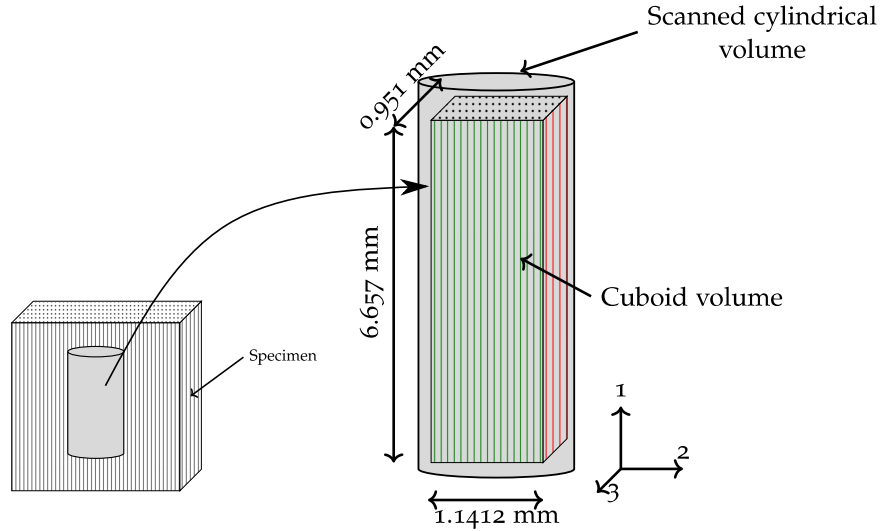


Figure 4.2: Sketch of a cuboid volume selected from a scanned cylindrical volume. The cylindrical scanned volume was obtained over a cuboid shape $[0]_4$ unidirectional FRP laminate by performing a CT scan.

the out-of-plane measurements, and the corresponding averages over specimen 1 and 2 on planes $\omega_1=0$, $\omega_2=0$, and $\omega_3=0$ in Fig. 4.3. Since the nominal fiber direction was along the 1-axis, the misalignment angle for the infinite wavelength λ_∞ (which corresponds to zero frequency) is equal to zero i.e. $S^\theta(0,0,0)=0$ and $S^\phi(0,0,0)=0$. The range of the non-zero frequencies ω_{R_1} , ω_{R_2} , and ω_{R_3} spans from the fundamental frequencies ω_{f_1} , ω_{f_2} , and ω_{f_3} to the Nyquist frequencies ω_{N_1} , ω_{N_2} , and ω_{N_3} for each case, cf. [94]. Subsequent frequencies are mirrored aliases, hence, the spectra are plotted till ω_N in Fig. 4.3. Analyzing the spectral density $S^\theta(\omega_k, \omega_l, \omega_m)$ depicted in Fig. 4.3a, Fig. 4.3b, and Fig. 4.3c closely, it can be seen that highest values of $S^\theta(\omega_k, \omega_l, \omega_m)$ are close to origin and show an anisotropic behavior. This is a characterization of the measured misalignment angles of Section 3.2 in spectral domain, where the contour plots of the in-plane misalignment angles showed an anisotropic behavior. On the other hand, the spectral density $S^\phi(\omega_k, \omega_l, \omega_m)$ plotted in Fig. 4.3d, Fig. 4.3e, and Fig. 4.3f show a rather uniform spread in the spectral domain. This is because the corresponding measured out-of-plane angles seen in Fig. 3.7 showed a uniform spread in physical space. Additionally, the figures of $S^\theta(\omega_k, \omega_l, \omega_m)$ and $S^\phi(\omega_k, \omega_l, \omega_m)$ show that the spectral values at higher frequencies (i.e. small wavelengths) are either zero or close to zero. Based on this observation of near zero values of $S^\theta(\omega_k, \omega_l, \omega_m)$ and $S^\phi(\omega_k, \omega_l, \omega_m)$ at higher frequencies (i.e. small wavelengths), it can be concluded that the smaller wavelengths have negligible contribution to the the fiber misalignment in physical space.

One might notice that plots of $S_{k,l,m}^\theta$ and $S_{k,l,m}^\phi$ for each specimen in Fig. 4.3 show rather spiky data whereas the average plots of $S_{k,l,m}^\theta$ and $S_{k,l,m}^\phi$ are comparatively smooth. Similar spiky data was observed in spectral characterization of a 2D misalign-

Direction	1	2	3
Length L [mm]	6.657	1.1412	0.951
Sampling points N [-]	70	12	10
Fundamental frequency $\omega_f=2\pi/L$ [mm ⁻¹]	0.943846373	5.505770511	6.606924613
Nyquist frequency $\omega_N=\frac{N\pi}{L}=\frac{N\omega_f}{2}$ [mm ⁻¹]	33.03462307	33.03462307	33.03462307
Frequency interval $\Delta\omega=\omega_f=\frac{\omega_N-\omega_f}{N/2-1}$ [mm ⁻¹]	0.943846373	5.505770511	6.606924613
Frequency range $\omega_R=\omega_N - \omega_f$ [mm ⁻¹]	32.09077669	27.52885256	26.42769845
Minimum wavelength $\lambda_{min}=\frac{2\pi}{\omega_N}$ [mm]	0.1902	0.1902	0.1902

Table 4.1: Calculation of different frequency values for the lengths of the measured volume and corresponding number of sampling points

ment data in Fig. 3 of Ref. [35]. The relatively smooth average plots of $S_{k,l,m}^\theta$ and $S_{k,l,m}^\phi$ in Fig. 4.3 indicate that further CT scans would yield reasonably smoother spectra of the spectral densities. It is to be noted that the spiky data of the spectral densities does not affect the accuracy of the evaluation. This argument is supported by the use of these characterized spectral densities in generation of the virtual topologies of the fiber misalignment which resulted in smooth contours of the fiber misalignment angles seen in Fig. 4.6b and Fig. 4.6d.

The values of different frequencies in each direction of the measured volume in the current investigation are given in Table 4.1. The minimum measurable wavelengths in the current investigation are considerably lower than the minimum wavelengths observed in unidirectional FRP materials [28, 127], therefore, the measurements can be considered representative of the misalignment in FRPs.

Although 1D plots of the spectral densities are not useful for modeling purposes because of a lack of complete volumetric characterization of the 3D misalignment, they can still give insights into the wave behavior in each direction. Therefore, in addition to the 3D plots of spectral densities in Fig. 4.3, the more commonly found in literature [28, 127] form of 1D spectral illustration of the fiber misalignment is shown in Fig. 4.4. Since the calculation of the spectral density was performed in a discrete manner, the plots in Fig. 4.4 are made in the form of staircases. The 1D plot depicts the spectral density $S^{\theta/\phi}(\omega_{1/2/3})$ in each direction in ranges $\omega_{f_{1/2/3}}$ to $\omega_{N_{1/2/3}}$ for both measurements of the misalignment angles $\theta_{k,l,m}$ and $\phi_{k,l,m}$ over specimens 1 and 2, and averages thereof. These plot are drawn on the axes ω_1 , ω_2 , and ω_3 . The axes corresponds to waviness behavior λ_1 , λ_2 , and λ_3 in directions 1, 2, and 3, respectively.

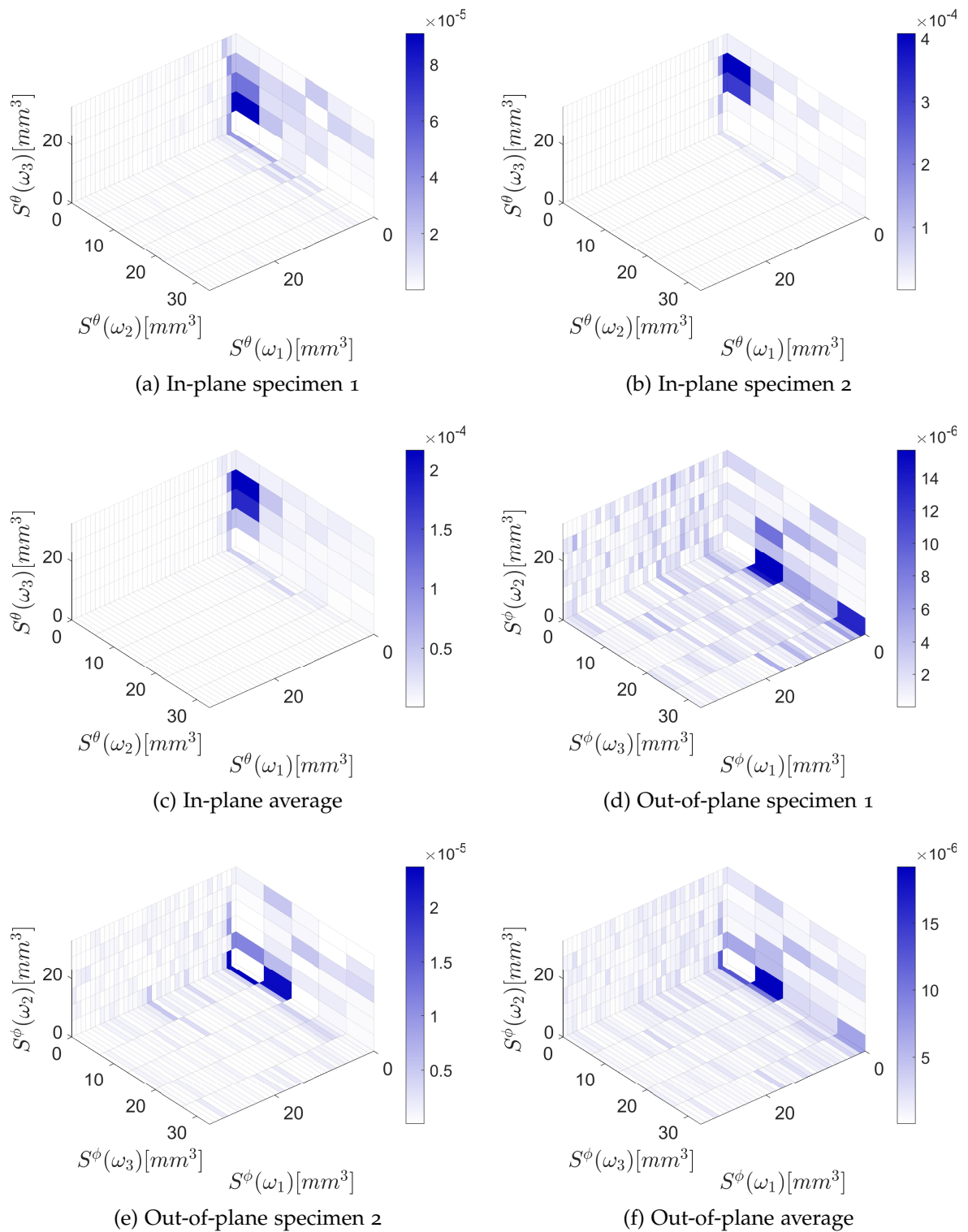


Figure 4.3: Spectral density plots from the 3D spectral density data on planes $\omega_1=0$, $\omega_2=0$, and $\omega_3=0$. Spectral densities were calculated from the 3D fields of the in-plane misalignment angle $\theta_{k,l,m}$ and the out-of-plane misalignment angle $\phi_{k,l,m}$.

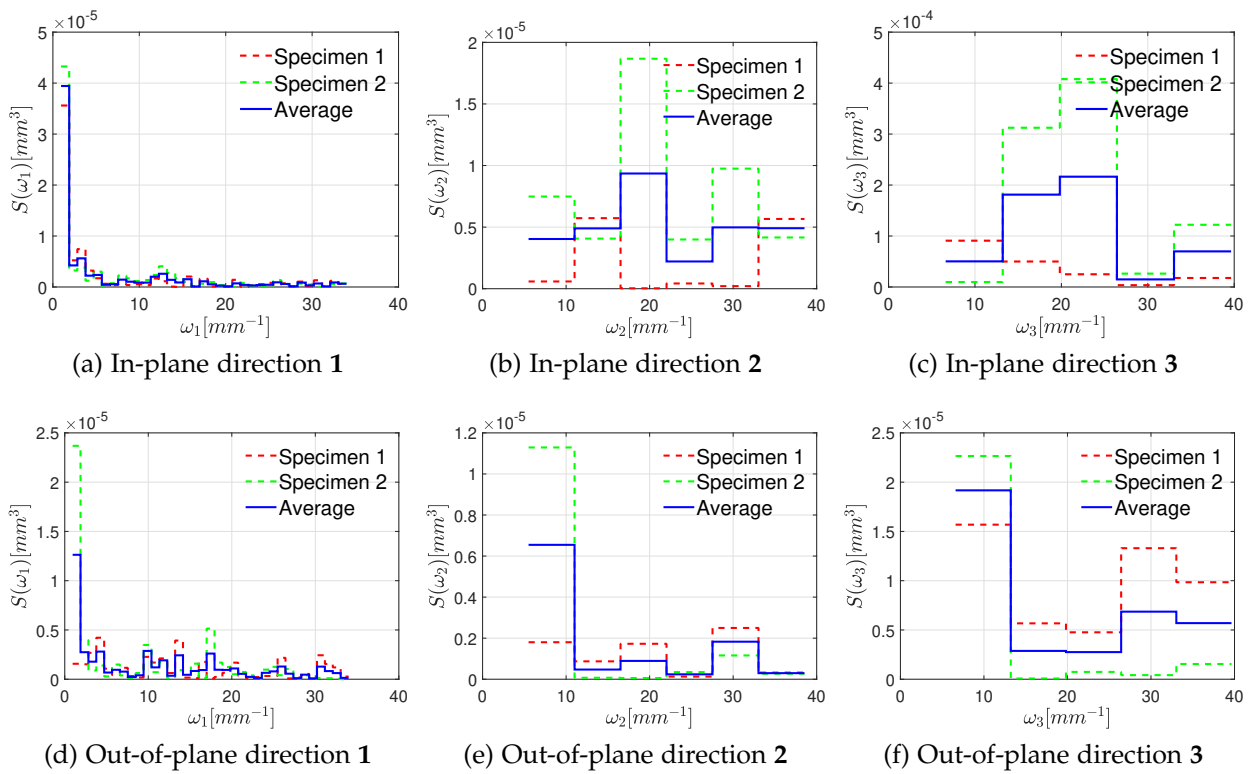


Figure 4.4: Spectral density plots from the 3D spectral density data on axes ω_1 , ω_2 , and ω_3 . Spectral densities were calculated from the 3D fields of the in-plane misalignment angle $\theta_{k,l,m}$ and the out-of-plane misalignment angle $\phi_{k,l,m}$.

The spectral densities of the out-of-plane misalignment have a consistent trend in all three directions, see Fig. 4.4d, Fig. 4.4e, and Fig. 4.4f. They show higher values of spectral densities at smaller frequencies (i.e. larger wavelengths) which reduce consistently towards larger frequencies (i.e. smaller wavelengths). This uniform behavior of spectral densities in all three directions in the spectral domain is illustrative of the uniform spread of the out-of-plane misalignment angles $\phi_{k,l,m}$ in the physical domain, see Fig. 3.7. Similarly, the spectral density of the in-plane misalignment in direction **1** also shows a peak at smaller frequencies (i.e. larger wavelengths), although with a faster decline of the spectral density value towards zero in comparison. The spectral density of the in-plane misalignment in directions **2** and **3** shown in Fig. 4.4b and 4.4c, however, depict different behavior. They show a peak in the middle frequencies. The spectral density of the in-plane misalignment angle in direction **1** has highest values at lower frequencies (i.e. larger wavelengths) and almost negligible values at higher frequencies (i.e. smaller wavelengths). The values of spectral densities of the in-plane misalignment angle in directions **2** and **3** are more uniform. The anisotropy in the spectral behavior of the in-plane misalignment angle is indicative of the anisotropic nature of the measured in-plane misalignment angles, see contour plots of the in-plane misalignment angles in Fig. 3.6.

It is, however, to be stated that there are only a small number of sampling points for the plots in directions **2** and **3** for both the in-plane and the out-of-plane misalignment angles. Further scans over larger volumes could still improve the characterization.

The mean square values Ξ^θ and Ξ^ϕ of the spectral densities of the in-plane $\theta_{k,l,m}$ and the out-of-plane $\phi_{k,l,m}$ three dimensional measurements for both specimens and the corresponding averages over the specimens are given in Table 4.2. The standard deviations s^θ and s^ϕ of the misalignment angles measured over the volume of $6.657 \times 1.1412 \times 0.951$ mm with $70 \times 12 \times 10$ sample points, which are linked to Ξ^θ and Ξ^ϕ via Eq. 4.11, are also provided. The mean misalignment of each distribution is 0. Since there is a direct relation between the mean square of spectral densities Ξ^θ and Ξ^ϕ and the standard deviation of the misalignment angles s^θ and s^ϕ as given in Eq. 4.12, a larger spread of the in-plane misalignment angles compared to the out-of-plane misalignment angles indicated by large values of s^θ result in large values of Ξ^θ . Alternatively said, large values of the mean square of spectral densities means that the misalignment angles in physical space have a large spread.

4.1.2 Deficiency of characterizing spectral densities in 2D frequency domain

From the measurements of the fiber misalignment presented in Section 3.2 and the corresponding spectral analysis presented in Section 4.1.1, it is evident that the misalignment is a truly three dimensional phenomenon. However, different misalignment measurements and spectral analysis of FRPs found in literature tend to represent them in a two-dimensional space [28, 29, 127]. Herein, the deficiencies of characterizing spectral densities in 2D frequency domain will be highlighted. It is stated for

	In-plane $\theta_{k,l,m}$			Out-of-plane $\phi_{k,l,m}$		
	Specimen 1	Specimen 2	Average	Specimen 1	Specimen 2	Average
Ξ^θ [$^\circ^3$] and Ξ^ϕ [$^\circ^3$]	0.0112	0.0166	0.0139	0.0094	0.0047	0.0071
s^θ [$^\circ$] and s^ϕ [$^\circ$]	0.6214	0.7560	0.6920	0.5667	0.4038	0.4920

Table 4.2: Statistics of the 3D fiber misalignment angles and the corresponding spectral parameters

clarity that the 2D calculation is only a detour for comparative purposes and it can not capture the complete picture of a real three-dimensional misalignment field.

The misalignment in 2D form can be measured using the extracted micrograph images from the volumetric scan using the HRMA method [126]. This can be done independently for the in-plane and the out-of-plane misalignment fields. For this purpose, the HRMA algorithm was used to measure the in-plane misalignment on 516 images in **1-2** plane from each specimen where each image was divided into 70×12 cells. The location of images in **1-2** plane are sketched in green color on a volumetric scanned image shown in Fig. 3.5a. For the measurement of the 2D out-of-plane misalignment on 702 images in **1-3** plane from each specimen using the HRMA method, each image was divided into 70×10 cells. The location of images in **1-3** plane are sketched in red color on a volumetric scanned image shown in Fig. 3.5a.

After removing the global misalignment of each specimen from the measured 2D in-plane and the 2D out-of-plane misalignment, spectral densities were calculated for each image separately. The resulting discrete matrices of spectral densities from the in were averaged over each specimen i.e. 702 matrices of $\theta_{k,l}^{2D}$ and 516 matrices of $\phi_{k,l}^{2D}$ from each specimen were averaged to find the corresponding 2D spectral density matrix of each specimen. The 2D spectral densities of $\theta_{k,l}^{2D}$ and $\phi_{k,l}^{2D}$ from each specimen were also used to find the average of the in-plane and out-of-plane spectral densities over both the specimens. The resulting data sets are used to depict 2D spectral densities as surface plots in Fig. 4.5. The spectral densities are plotted till Nyquist frequencies. Similar to the 3D depiction, the 2D diagrams show maximum values of spectral densities at lowest frequencies which gradually decrease away from the origin. It again highlights that the largest frequencies (i.e. smallest wavelengths) have minimum to negligible contribution to the overall misalignment. It can be observed that with large data-sets for each plane-of-view, the resulting spectral density calculations give smooth plots. This is indicative that a larger number of volumetric CT-scans would also result in smooth characteristic spectral density plots in 3D space.

When comparing the 2D spectral plots in-lieu of the earlier presented 3D spectral plots, it is obvious that the 2D representation doesn't give a complete characterization of the underlying 3D misalignment fields. Moreover, the anisotropy observed in

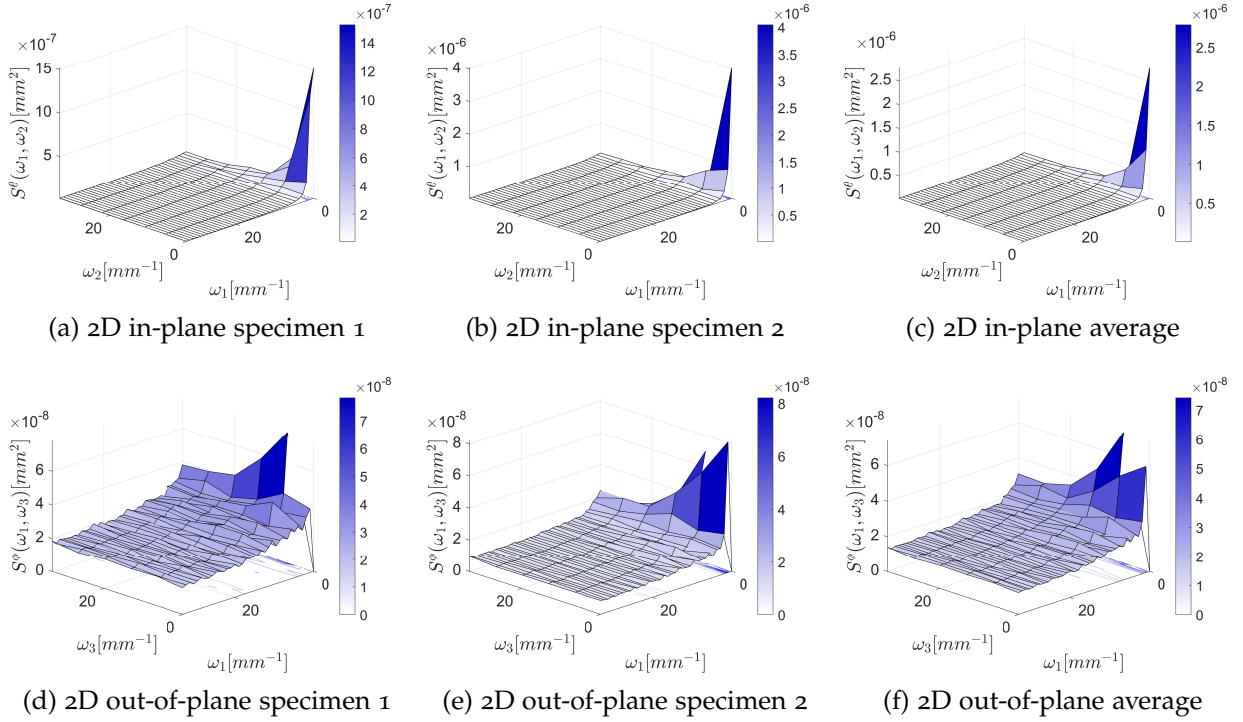


Figure 4.5: 2D spectral density plots. Spectral densities were calculated from the 2D fields of the in-plane misalignment angle $\theta_{k,l}^{2D}$ and the out-of-plane misalignment angle $\phi_{k,l}^{2D}$.

the 3D measurements of the i-plane misalignment, which were easily observable in the 3D spectral representation in Fig. 4.3a, Fig. 4.3b, and Fig. 4.3c, does not appear in the 2D spectral density characterization. For sake of completeness, the standard deviations $s^{\theta^{2D}}$, $s^{\phi^{2D}}$ and the mean square spectral densities $\Xi^{\theta^{2D}}$, $\Xi^{\phi^{2D}}$ are also given in Table 4.3. Higher values of $\Xi^{\theta^{2D}}$ compared to those of $\Xi^{\phi^{2D}}$ indicate a larger spread of the in-plane misalignment compared to the out-of-plane misalignment. It is to be noted that the values of $s^{\theta^{2D}}$, $s^{\phi^{2D}}$ are same as those of the complete 3D data-sets given in Table 3.4, since the complete CT scan data was subdivided into separate images for the 2D calculations of the spectral densities. However, the relation given in Eq. 4.12 between the mean square spectral density and the standard deviation of the underlying distribution does not hold for the 2D calculation. This is because of the reduction of 3D misalignment fields into separate 2D fields. All these limitations highlight the importance of the complete 3D characterization of spectral densities.

4.2 GENERATION OF TOPOLOGY OF THE FIBER MISALIGNMENT USING SPECTRAL REPRESENTATION METHOD

In this section, the virtual generation of the topologies of the fiber misalignment is presented. Since the misalignment was measured over a volume in space and subsequently characterized in three dimensional frequency domain, the corresponding

	$\Xi^{\theta^{2D}} [^{\circ^2}]$	$s^{\theta^{2D}} [^{\circ}]$	$\Xi^{\phi^{2D}} [^{\circ^2}]$	$s^{\phi^{2D}} [^{\circ}]$
Specimen 1	1.2706e-04	0.6458	9.7026e-05	0.5652
Specimen 2	1.4906e-04	0.6995	5.1986e-05	0.4147
Average	1.3806e-04	0.6726	7.4506e-05	0.4899

Table 4.3: Statistics of the 2D fiber misalignment angles and the corresponding spectral parameters. The standard deviations of the in-plane and the out-of-plane misalignment are same as the complete data-sets given in Table 3.4 as the complete CT scan data was used in 2D calculations.

generation of topologies of the misalignment is performed for a volume in space. Additionally, the 2D generated topologies of the misalignment using an algorithm from the literature are also presented along with examples of corresponding 2D measurements.

4.2.1 Generation of the volumetric misalignment topology

The algorithms for generating topologies of the misalignment for FRPs from a given spectral density function are available in the literature for 1D [100] and 2D [76], which are based on the algorithm developed by Newland [84]. Herein, a modified version of the algorithm for a 3D representation is presented [93].

In the 3D extension, the spectral density and the generated topologies of the misalignment are dependent on three frequency and three spatial variables, respectively. The algorithm for generating a 3D topology of the fiber misalignment, along with all the steps for implementation, is given in the Appendix A. The algorithm takes discrete matrices of spectral densities $S_{k,l,m}^{\theta}$ and $S_{k,l,m}^{\phi}$ of either the in-plane or the out-of-plane misalignment as input. The spectral density matrices can either be sampled from a functional form of the spectral density or they can be calculated directly from the measurements of the misalignment, as was done in Section Section 4.1.1. To generate different virtual topologies having preserved statistical as well as spectral quantities, a random angle $\beta_{k,l,m}$ is used. The random angle $\beta_{k,l,m}$ introduces phase shifts in contributing frequencies. $\beta_{k,l,m}$ is sampled with certain conditions mentioned in Appendix A from a uniform distribution $[0, 2\pi]$. Discrete Fourier transforms $F_{k,l,m}^{\ominus}$ and $F_{k,l,m}^{\Phi}$ of the resulting topologies can then be calculated using the method explained in the Appendix A. Taking inverse Fourier transforms of $F_{k,l,m}^{\ominus}$ and $F_{k,l,m}^{\Phi}$ gives spatial topologies of the misalignment angles $\theta_{k,l,m}$ and $\phi_{k,l,m}$. As measurements were done in a discrete manner, it is to be noted that the spectral representation method has certain limitations, such as limits on minimum wavelengths (corresponding to Nyquist frequencies) and maximum modeled wavelengths (corresponding to fundamental frequencies). These wavelengths are based on the sampling density and model lengths, respectively, cf. Table 4.1.

Using the calculated 3D spectral densities $S_{k,l,m}^\theta$ and $S_{k,l,m}^\phi$ from Section 4.1.1 as input, topologies for the in-plane misalignment and the out-of-plane misalignment were generated through the algorithm given in Appendix A. Since there are three sets of spectral densities each for the in-plane and the out-of-plane measurements, one from each specimen and one average thereof, three series of topologies each were generated for the in-plane and the out-of-plane misalignment. The aim was to compare the axial compression strengths from each series and select the appropriate series for further investigations in Chapter 6.

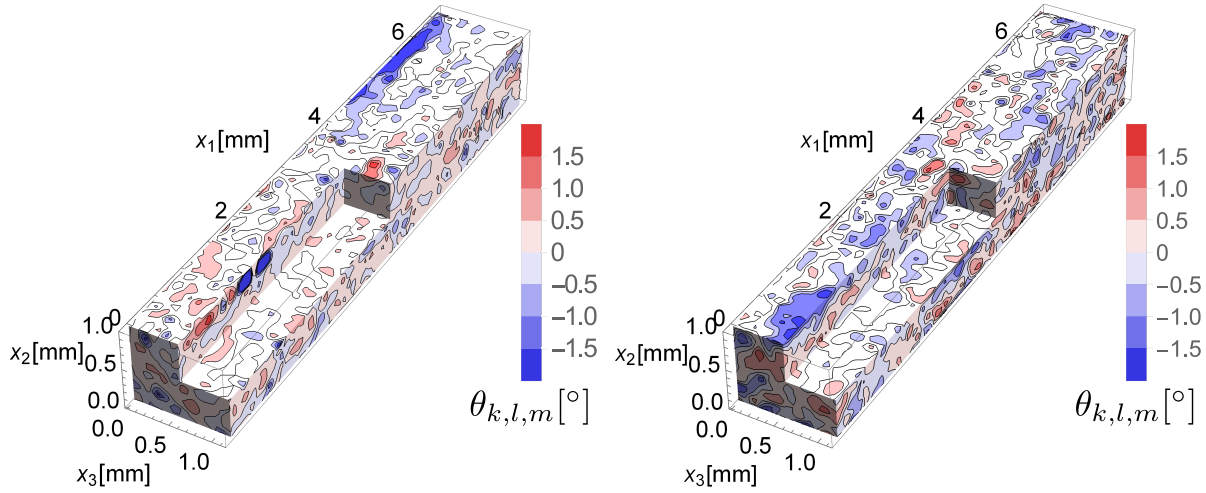
Fig. 4.6 shows selected realizations of measured versus generated topologies for the in-plane misalignment angles and the out-of-plane misalignment angles as 3D contour plots. The in-plane as well as the out-of-plane misalignment are spread out over the volume in a correlated random manner. The in-plane misalignment from the measurements of a specimen plotted in Fig. 4.6a shows an anisotropic behavior. The regions of in-plane misalignment are elongated in the 1-axis direction. A virtually generated topology of the in-plane misalignment using the spectral representation method is shown in Fig. 4.6b. The virtually generated topology of the in-plane misalignment replicates the anisotropy observed in the measurements. On the other hand, the measured out-of-plane misalignment shown in Fig. 4.6c shows a uniform spread of the regions of misalignment. The virtually generated topology of the out-of-plane misalignment using the spectral representation method is shown in Fig. 4.6d. Again, the uniform spread of the misaligned regions in the measured topology of the out-of-plane misalignment is replicated in the virtually generated topology. It should be noted that if one uses only probability distribution functions of the misalignment angles as a basis for the model generation procedure without any consideration of the correlation, the aforementioned differences in the spatial distribution of misalignment topologies can not be modeled.

4.2.2 Generation of the planar misalignment topology

For sake of completeness, topology of the misalignment in 2D planes is also presented. The algorithm for generation of a misalignment topology dependent on two spatial direction is available in literature [76]. Using this algorithm from literature, misalignment topologies for the planar in-plane misalignment $\theta_{k,l}^{2D}$ and the planar out-of-plane misalignment $\phi_{k,l}^{2D}$ were generated.

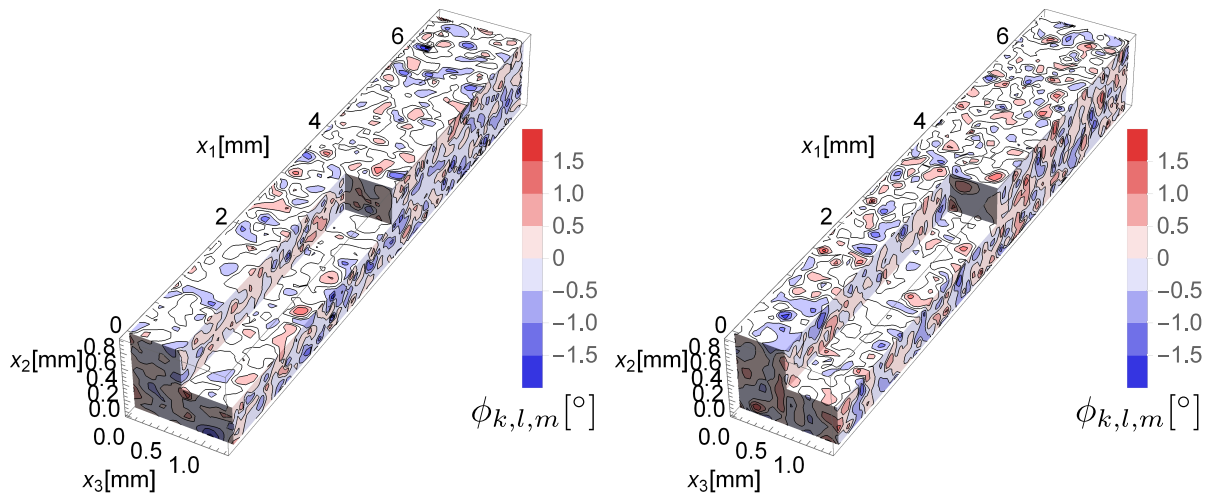
Fig. 4.7 shows selected realizations of the $\theta_{k,l}^{2D}$ and the $\phi_{k,l}^{2D}$ topologies, along with exemplary 2D measurements on extracted micrographs from the original volumetric scan data. It is obvious that 2D topologies of either the $\theta_{k,l}^{2D}$ or the $\phi_{k,l}^{2D}$ can only represent waviness within that plane. They are also unable to represent effects of the 3rd dimension on the waviness behavior of the $\theta_{k,l}^{2D}$ and the $\phi_{k,l}^{2D}$ topologies.

Analyzing the 2D contour plots given in Fig. 4.7, a similar behavior to 3D contour plots of Fig. 4.6 can be observed. The in-plane misalignment regions in 2D also show anisotropic behavior, cf. Fig. 4.7a and Fig. 4.7b. The contours of in-plane misalignment



(a) Measured contours of the in-plane misalignment angle from a specimen

(b) Contours of a virtually generated realization of the in-plane misalignment angle



(c) Measured contours of the out-of-plane misalignment angle from a specimen

(d) Contours of a virtually generated realization of the out-of-plane misalignment angle

Figure 4.6: Measured and virtually generated 3D contour plots of the in-plane misalignment angle $\theta_{k,l,m}$ and the out-of-plane misalignment angle $\phi_{k,l,m}$. Measurements were performed using CT scans and the angles were calculated using the HRMA method [127], also see Section 3.2. The spectral representation method was used for the generation of virtual topologies of the misalignment angles. It is evident that the misalignment fields depend on all three coordinate directions.

are elongated in $\mathbf{1}$ -direction. On the other hand, the 2D out-of-plane misalignment topologies depicted in Fig. 4.7c and Fig. 4.7d show uniform spread of regions of misalignment. The reasons behind the differences in the $\theta_{k,l}^{2D}$ and the $\phi_{k,l}^{2D}$ topologies stem from the lamination and subsequent compaction during curing process as explained in Section 3.2.

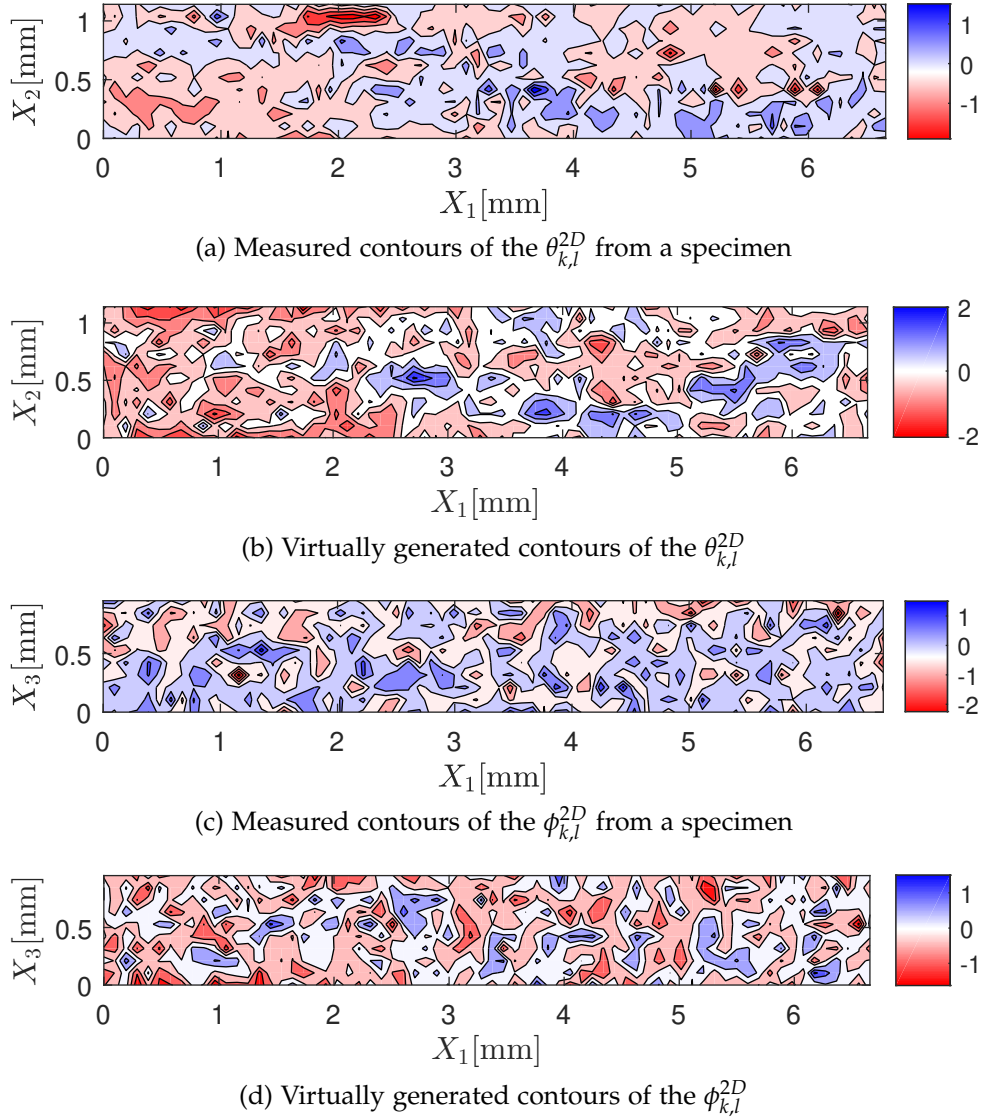


Figure 4.7: Measured and virtually generated 2D contour plots of the $\theta_{k,l}^{2D}$ and the $\phi_{k,l}^{2D}$. Measurements were performed using CT scans and the angles were calculated using the HRMA method [127] from the micrographs. The spectral representation method given by Liu et. al. [76] was used for the generation of virtual topologies of the 2D misalignment angles.

EXPERIMENTAL DETERMINATION OF FAILURE UNDER COMBINED COMPRESSION-SHEAR LOADS

Failure of composites under compression dominated loads is a complex phenomenon as has been shown in different investigations over past half a century. The experimental determination of failure serves as an independent approach in itself for characterizing failure under certain conditions. It also provides information for validation of numerical analysis. Over the decades, there has been pronounced interest in testing to failure under multi-axial loads for unidirectional fiber reinforced composites [50, 116, 118]. The term load case refers to a certain loading direction where a multi-axial load state can be achieved, either through loading at an angle to the specimen nominal direction or by specific geometry of the specimen. In addition to testing to failure of simple axial compression, experimental investigations of complex load cases can also prove helpful for design engineers giving more confidence in exploiting the FRPs to their maximum potential. Moreover, quantification of the uncertainties expected in failure under compression dominated loads is also of great interest. In this regard, a new approach for failure under combined compression-shear load is developed. In this new testing to failure approach, combined compression-shear loads can be transferred to the specimen gauge section simultaneously through a combination of shear and end load transfer mechanisms similar to the currently accepted compression testing standard. The new testing to failure approach accommodates easy to manufacture flat specimens, where mean fiber direction is same as the nominal specimen direction. Tests to failure were performed over statistically significant number of samples to characterize the failure uncertainty. This chapter presents the methodology of testing to failure in details followed by the discussions on the outcomes of the investigation.

5.1 METHODOLOGY

As motivated in Section 2.6 after a comprehensive review of the state of the art, the focus of this contribution lies in the development of failure envelopes under axial compression and combined compression-shear loads using a simple testing concept. Therefore, developing further on previous investigations available in the literature, a new testing approach using flat specimens is introduced in this study. The details of the new approach to testing to failure are discussed in this section.

5.1.1 Specimen geometry

Microbuckling strength of fiber reinforced composites shows uncertainty with changes in component size. This phenomenon is called size effect and is a major topic of interest in research [109, 130, 132]. In defining the specimen geometry for the current investigation, the size effect phenomenon was also taken into account. Motivated by the intention to increase sizes of the specimens for the follow-up size effect investigations, the dimensions of the gauge section for the current investigation were kept smaller compared to the ranges suggested in different compression testing standards. The nominal value of the compression strength given by the supplier was 1165 MPa. The load range required for the gauge section under the axial compression in the current investigation was estimated to be 6 kN, $\pm 2-3$ kN to account for expected variation in strength because of the underlying manufacturing induced fiber misalignment. Based on the load range, the dimensions of the gauge section required for the current investigation were calculated to be 5×5 mm with a thickness of 1.15 mm. The total length of specimen was designed to be 105 mm for a resolute placement in the fixture during testing. These gauge section dimensions were chosen to consider subsequent volumetric increase in sizes to $15 \times 15 \times 2.30$ mm and $30 \times 30 \times 3.45$ mm. These larger sizes would require loads of approximately 35-45 kN and approximately 105-115 kN, respectively.

Moreover, the typical wavelengths of the fiber misalignment measured by different authors in literature [29, 110] are of the order of a few millimeter. Similar range of wavelengths was observed in the measurements of the misalignment performed in the current work in Section 3.2 and the corresponding spectral analysis in Section 4.1. The major contribution to the misalignment is from wavelengths of the order of a few millimeters. The resulting regions of the misalignment are of the order of 1 mm in size as depicted by the sizes of the contours in the 3D plots in Fig. 3.6 and Fig. 3.7. Hence, the in-plane dimensions of 5×5 mm cover the range of typically observed wavelengths of the fiber misalignment.

The calculation of minimum specimen thickness required to avoid global Euler buckling under boundary conditions of a pin-ended column for a gauge length of 5 mm using the formula given in ASTM D6641 standard resulted in a value of 0.68 mm. This is well below the thickness of the specimens, thus the designed specimen with an average thickness of 1.15 mm is not susceptible to the global Euler buckling.

The prepreg was laminated in four layers $[0]_4$ giving an average thickness of 1.15 mm. Since FRPs have very low transverse strength (see Table 3.1), a single large sized cured plate with only four layers for manufacturing all the specimens in a single attempt would be prone to transverse breaking during handling. Therefore, four plates of $150 \times 300 \times 1.15$ mm area were manufactured for preparation of specimens of testing to failure series. For ease of applying tabs, the manufactured plates were subdivided into smaller ones of approximately $150 \times 80 \times 1.15$ mm area. Although 90° tab taper angle is relatively common due to ease of specimen preparation for compression testing,

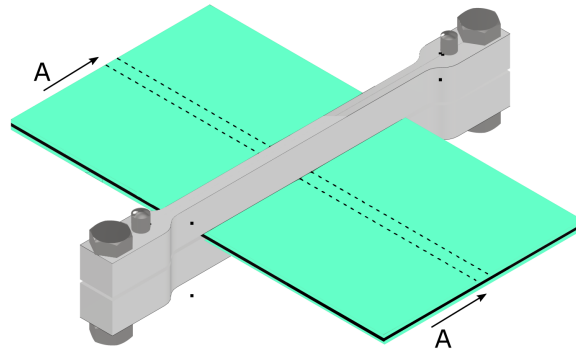


Figure 5.1: Schematic of the jig design for tabbing the testing to failure specimens. The jig proved helpful in achieving very high accuracy of the required gauge length. The location of a specimen to be cut is shown with dotted lines. A schematic of the specimen at the cross-section A-A is shown in Fig. 5.2.

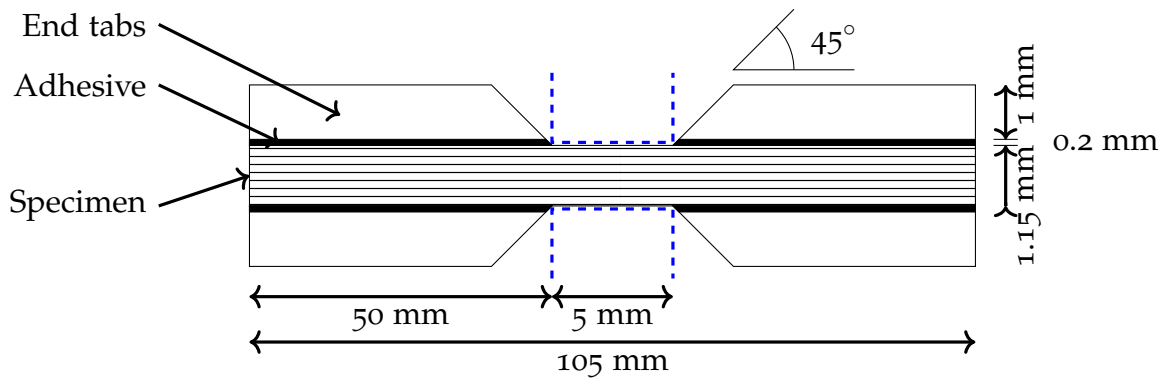


Figure 5.2: Schematic of the testing to failure specimen with adhesive and tabbing. The cross section A-A of the Fig. 5.1 indicates the viewing direction. The outline of the jig is represented by the blue dashed lines.

45° tab taper angle is an optimum choice to reduce invalid failure modes driven by stress concentrations at the tab ends. An investigation to affirm the use of 45° tab taper angle (see Fig. 5.2) over the other available choices of 60° and 90° tab taper angle was carried out before final testing to failure series. The results of the study on tab taper angle along with other design parameters will be discussed later in Section 5.2.1.

For the specimens of testing to failure series, $[+45/-45]_{2s}$ GFRP tabs with 45° tab taper angle were applied with 3M's DP490 adhesive on each plate subdivision of $150 \times 80 \times 1.15$ mm dimension. A small jig shown in Fig. 5.1 was designed for the tabbing process. The jig helped in achieving very high accuracy of the required gauge length which is not possible when tabbing is done without any jig. Such mechanical jigs have proven to be useful in accurate specimen manufacturing [40, 79]. A total of 99 specimens with the schematic shown in Fig. 5.2 for testing to failure series were then cut into required dimensions with a rotary cutter. The cutter has a diamond tip and can cut with a precision of 0.01 mm.

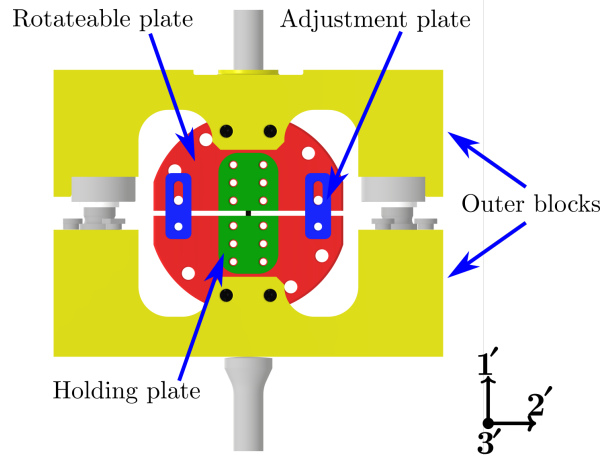


Figure 5.3: Assembled view of the fixture design

5.1.2 Fixture development

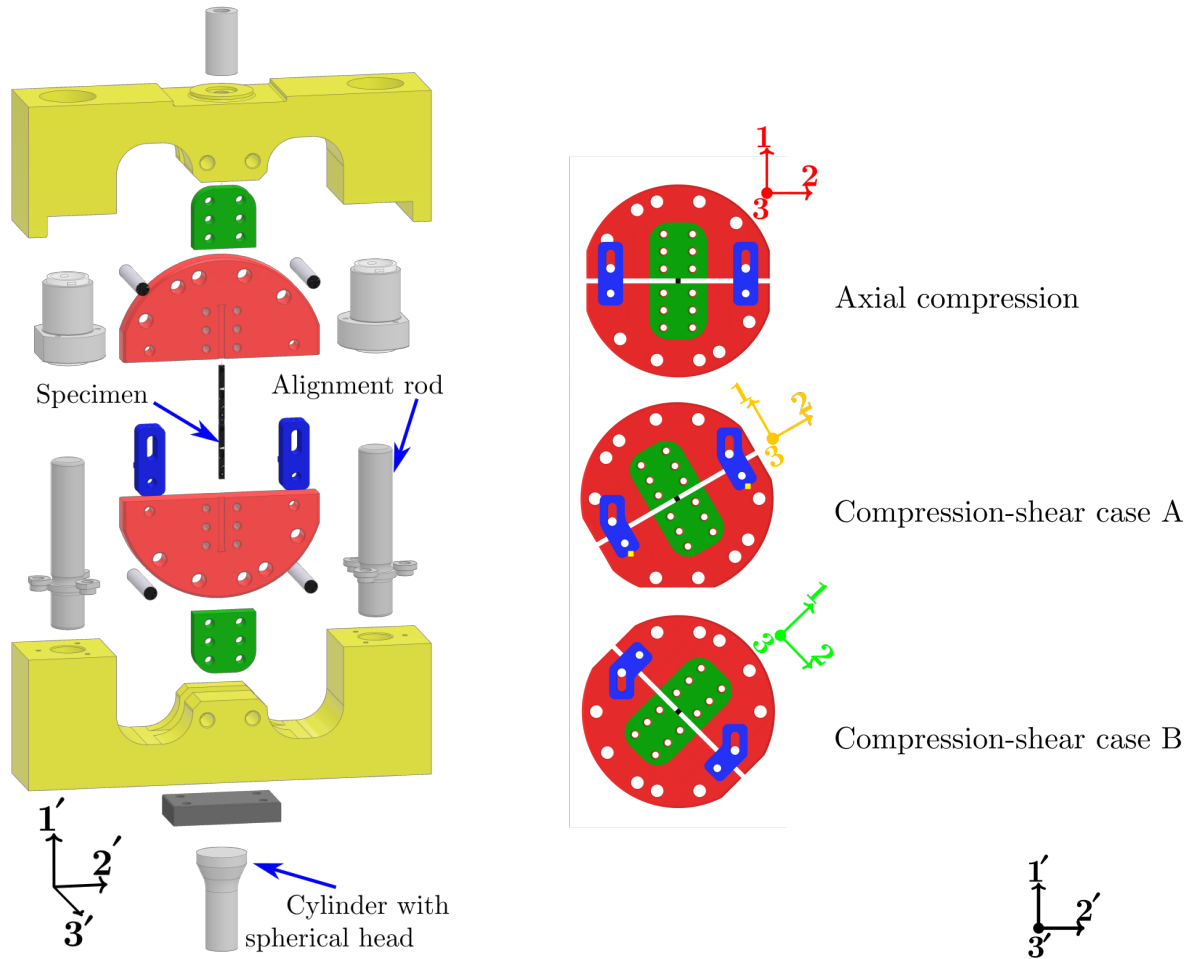
The newly developed Combined Loading Modified Arcan Fixture (CLMAF) for testing under axial compression and combined compression-shear loads is shown in Fig. 5.3. The fixture is based on the principles used in the standard Arcan fixture and the Combined Loading Compression (CLC ASTM D6641) fixture. The standard Arcan fixture allows for adjustable load angles by rotating the internal part of the fixture. This advantage can be exploited for applying multi-axial loads in a specimen as was done by Gan et. al. in their modified Arcan fixture [50]. The current compression testing standard CLC ASTM D6641 fixture has an advantage of transferring loads into the gauge section of a specimen through combined end and shear load transfer mechanisms. This allows for testing of high strength FRPs using easy to manufacture rectangular specimens. By combining these two advantages of the standard Arcan fixture and the compression testing standard CLC ASTM D6641 fixture, a new fixture is developed for testing high strength FRPs under axial compression and combined compression-shear loads.

The fixture consists of a pair of central rotateable plates (red shaded parts in Fig. 5.3 and Fig. 5.4a). The rotateable plates can be positioned at specified angular positions to obtain required load cases, see Fig. 5.4a and 5.4b. The test specimen is placed in precisely milled grooves in the rotateable plates in such a way that it has end, and front and back contact. The specimen is subsequently fixed in place with the help of a pair of smaller holding plates (green). Such a placement of the specimen allows for a combined end and shear load transfer mechanism defined in the ASTM D6641 standard, see schematic in Fig. 2.6. The holding plates have grit surfaces. Grit surfaces of the holding plates enhance frictional contact and consequently transfer shear loads into the specimen. The holding plates are secured in place with the help of six screws each. A small study was carried out for finding the optimum bolt torque value to tighten the screws of holding plates, the details of which will be discussed in Section 5.2.1.

The optimum value of the bolt torque value for the testing to failure series turned out to be 2.5 Nm. This value is also suggested by the ASTM D6641 standard which gives the required 1:2 ratio of end to shear loading. The pair of rotateable plates is fixed in the outer blocks (yellow) with the help of pairs of pins for each plate having tight tolerance at the desired loading angle.

The upper block of the fixture is fixed and aligned to the upper crosshead of the machine with the help of a cylindrical part (silver) and a screw. The upper and the lower blocks of the fixture are aligned with one another with the help of 30 mm diameter alignment rods, see Fig. 5.4a. The alignment rods are fixed in the lower block of the assembly, and are free to move in the bushings. The alignment rods can move only in the global loading direction inside low friction bushings, thus preventing global buckling or the out-of-plane movement of the assembly. The external assembly of alignment rods, outer blocks, and the cylinder with spherical head is also to counter any misalignments in the machine movements, thus avoiding any unwanted loads in the specimen. Both the outer blocks are kept perfectly aligned because of the alignment rods. If the bottom cross-head of the machine does not move exactly in the global $\mathbf{1}'$ direction, the cylinder with spherical head (which is fixed with bottom cross-head of the machine) adjusts the contact with lower part of the outer block. This way, the load applied from the machine on the outer blocks of the fixture, and consequently in the gauge section of the specimen, is always in the global $\mathbf{1}'$ direction. As the lower block is only upheld over a cylindrical part (silver) having a spherical head and the upper block is fixed in the machine crosshead, two adjustment plates (blue) with L-shaped holes are employed holding upper and lower blocks together to avoid the fixture falling apart under gravity in-between the tests, see Fig. 5.3. The adjustment plates containing L-shaped holes are specific for each load case. The L-shaped holes are 1 mm larger than the screws used there to avoid any contact while loaded, and allow for up to 15 mm axial movement of the assembly. As the displacement to failure in the current specimen sizes is much less than 1 mm, this range of movement is more than sufficient, and allows for ease of specimen replacements for testing of multiple specimens.

A cylindrical part (silver) having a spherical head is clamped in the lower part of the machine, and transfers load into the lower block of the fixture by coming in contact with a hardened plate (dark gray). The spherical head is made in this part in order to mitigate any angular misalignment in load introduction from the testing machine. Both, the upper cylindrical part fixed with a screw and the lower cylindrical part having a spherical head fixed in the machine jaws, are employed for the universal testing machine in the current testing campaign. It is worth noting that the fixture can also be employed without these cylindrical parts, just as in the case of the standard ASTM D6641 fixture. It is to be noted that the fixture is not limited to the pure axial compression and combined compression-shear load cases, but can also be used for the pure axial tension and combined tension-shear load cases. A cylindrical part, similar to the one on the upper part, can be screwed to the bottom head of the fixture for



(a) Exploded view of the fixture design

(b) Different loading positions

Figure 5.4: Exploded view of the fixture along with different loading positions. Load was applied in global $1'$ direction. The local directions are defined on the specimen where 1 is in the nominal fiber direction, and 2 and 3 are the in-plane and the out-of-plane transverse directions, respectively. The rotations in case A and B are 30° and 45° , respectively.

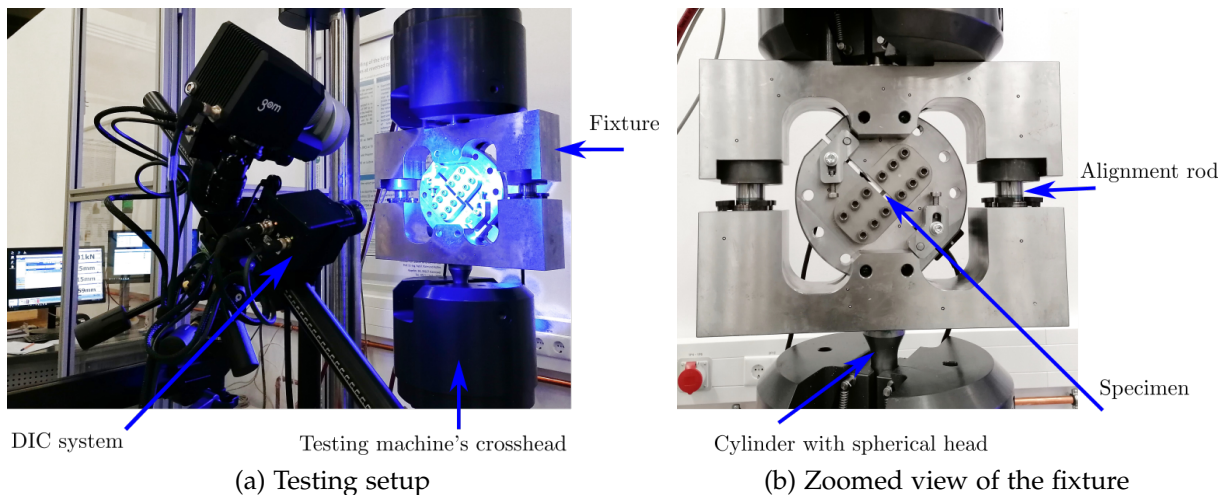


Figure 5.5: The newly developed CLMAF for the axial compression and combined compression-shear load cases. In these images, a specimen is being tested under the combined compression-shear case B i.e. 45° load case.

applying tension loads for such applications. However, the interest of the current investigation lies in testing to failure under compression and combined compression-shear load cases only.

5.1.3 Testing procedure

The tests to failure were carried out using the CLMAF with the following procedure. The fixture was mounted into the machine with the central rotateable plates set in the required loading positions, as shown in the setup Fig. 5.5. The specimen was then placed in the grooves, brought in contact with the upper end, and the upper holding plate was loosely screwed on top. After that, the lower end of the fixture was moved upwards slowly until contact was established, which was verified by a change of approximately 30-40 N in the force signal. Then the lower holding plate was screwed on top of the specimen, and all twelve screws of the holding plates were tightened in a zigzag manner with a torque of 2.5 Nm.

The calibrated cameras of the DIC system were then brought into place, and the test was carried out at a rate of 1.3 mm/min until failure was achieved. A preliminary study on the testing speeds in range of 0.25-1.5 mm/min and the torque in range of 2.5-5.0 Nm required for tightening the holding plates of the fixture was carried out, since the specimen dimensions were non-standard. The resulting optimum speed and torque values of 1.3 mm/min and 2.5 Nm coincide with the parameters suggested by the ASTM D6641 standard.

Since the fixture is a new design, it was deemed necessary to confirm the sufficient rigidity of the fixture. Any unwanted out-of-plane displacement of the fixture in global z' -direction might lead to undesirable bending of the specimen. The rigidity

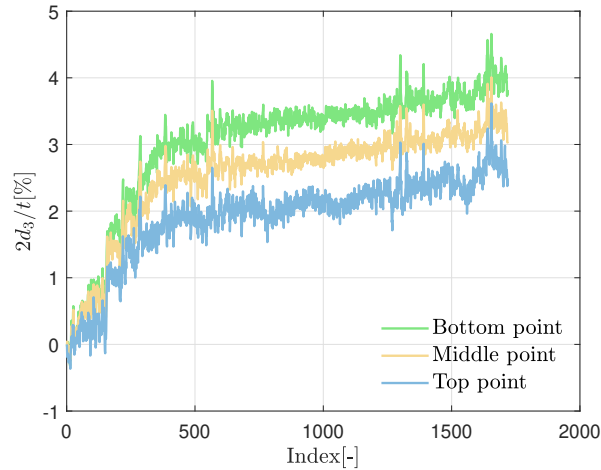


Figure 5.6: Twice the out-of-plane displacements d_3 normalized by the average thickness t of a specimen during a test under the axial compression load at three points along the length of a specimen i.e. near the upper and lower clamps and at the middle of the specimen. The out-of-plane displacements were extracted using the DIC system on the surface of the specimen. The horizontal axis correspond to the image number captured during the DIC measurement.

of the fixture was confirmed by tracking the movement of the fixture using the DIC system. The movement of the fixture was tracked for three initial tests under axial compression load showing approximately 3-4% displacements in the transverse out-of-plane direction compared to the displacements in the nominal fiber direction. This verification was repeated on multiple samples in the testing to failure series, this time tracking the motion of specimens.

The specimen gauge sections were too small to employ back to back strain gauges as recommended by the standard. Hence, the in-plane strains were measured using the DIC system directly at the specimen front surface, as elaborated in the next paragraph. Moreover, the DIC system can also track out-of-plane movements and hence, it was used to measure the out-of-plane displacements. Fig. 5.6 shows the out-of-plane displacements d_3 multiplied by 2 and normalized by the average thickness t of a specimen loaded under axial compression measured on the surface at three different points i.e. near the top clamp, near the bottom clamp, and at the middle of the specimen. Since the d_3 measurements were performed on only the front surface of specimens, hence, the normalization of evolution of d_3 in Fig. 5.6 was done by half of thickness t . It resulted in Y-axis term of Fig. 5.6 to be $2d_3/t$. It can be seen in Fig. 5.6 that the normalized out-of-plane displacements along the length of the specimen in the testing to failure were fairly close to each other and were approximately 3-4% at final failure, hence ruling out undue bending during the tests. Since the bottom cross-head of the machine moves applying load from the bottom of the specimen, the bottom point in Fig. 5.6 shows highest values of $2d_3/t$ during the test followed by middle and top points.

The region of interest of approximately 2.5×2.5 mm for the testing to failure series for measuring strain fields in the DIC system was defined at the center of the gauge sections of the specimens. The region of interest was defined in the *GOM Correlate* software by facets sized 14 pixels placed 2 pixels apart from one another on the images captured during the DIC system measurements. Since the aim of the current investigation is development of failure envelopes for far field strains and stresses in the specimen coordinate frame, the values of strains and stresses used throughout the work represent the averaged far field quantities, unless stated specifically otherwise. The tensorial symbols ε_{11} and ε_{12} are used to represent the far field axial and the far field shear strains, respectively. In order to obtain far field strains in the specimen coordinate frame, the coordinate system of the DIC measurement system was aligned with the testing to failure specimens in such a way that the 1-axis was in the nominal fiber direction and the 2-axis was in the in-plane transverse direction. The far field axial strains ε_{11} and the far field shear strain ε_{12} in the specimen coordinate frame were extracted using two methods of measurements (a) arithmetic mean of the local strains in the defined region of interest, and (b) using the virtual extensometers. Virtual extensometers are defined in the *GOM Correlate* software of the DIC system on the captured images of the DIC measurement. The virtual extensometer works like a physical extensometer and provides the averaged measure of the strains over the length of the extensometer. All strain values extracted through either method of measurement refer to the engineering/technical definition of strains. The far field shear strains ε_{12} and the far field shear angles γ_{12} are related in the usual way, i.e. $\gamma_{12} = 2\varepsilon_{12}$. The shear strains ε_{12} from the virtual extensometers were calculated using the half rosette bridge concept. Two equal length virtual extensometers at $+45$ and -45 angle from the 2-axis were used for this purpose. This resulted in a configuration of the virtual extensometers 90° apart from each other with 2-axis being their bisector. The shear strains using the half rosette bridge concept are then calculated using the relation $\varepsilon_{12} = (\varepsilon_{-45} - \varepsilon_{+45})/2$. The reason behind using two methods of strain measurements was to avoid measurement errors, and verify them against one another giving higher confidence in the results.

5.2 RESULTS AND DISCUSSIONS

In the following section, the results of the testing to failure campaign under compression and combined compression-shear will be discussed. It starts with presentation of the results of design variables of the new approach to testing to failure. A closer look at the failure mode is followed by a comparison of failure strengths under different loading directions. The localization in the form of a shear band leading to microbuckling failure and kink band formation is shown with the help of the DIC system. Using failure strains measured on surfaces of the specimens, a failure envelope in strain space is presented. The results of the axial compression case are interpreted using

the analytical solution of Budiansky [21, 23]. A derived approximation of the failure envelope in the stress space is presented at the end of the chapter.

5.2.1 Design variables for testing to failure

Since non standard dimensions of the gauge section were designed in the current investigation, it was deemed necessary to investigate the effects of design variable such as tab taper angle, testing speed, and value of bolt torque on the strength under the axial compression load. The results of these investigation are discussed briefly below.

BOLT TORQUE AND TESTING SPEED: To verify the applicability of by standard ASTM D-6641 suggested values of the testing speed and the bolt torque required for tightening the screws of the holding plate for the current investigation, a small study was carried out. These tests were carried out with specimens having a 45° tab taper angle. The summary of these tests is given in Table 5.1. There, torque and speed parameters of each test are listed along with the resulting failure mode. The validity of the tests is also marked and the resulting values of the observed peak loads are listed for comparison. The test validity is defined based on the valid/invalid failure of compression testing given in ASTM D-6641 standard. In the current investigation, all the valid tests showed microbuckling failure mode inside the gauge section. Other valid failure modes defined in ASTM D-6641, such as brooming of fibers inside the gauge section or the longitudinal splitting inside the gauge section, were not observed in the current investigation.

Two values of torque on the screws of the holding plate of the fixture were used for all six testing speeds considered. Torque value of 5 Nm on the screws of the holding plate of the fixture resulted in lower strengths due to stress concentrations near the tab ends of the gauge section compared to torque value of 2.5 Nm for all testing speeds. Six testing speeds, i.e. 0.25, 0.50, 0.75, 1.00, 1.25, and 1.30 mm/min speed of the machine cross-head, were considered for choosing an optimum value for the newly developed fixture. Lower values of testing speeds tended to incur failure in the tabbed region leading to an invalid failure mode. Lower speeds of testing apparently did not transfer loads completely into the gauge section, which resulted in stress concentration inside the tabbed region near ends of specimen. The description of failure modes and location for each test is given in Table 5.1. Delamination and/or kink band formation inside tabbed region was deemed invalid based on failure definitions given in ASTM D-6641 standard. It was concluded that the torque value of 2.5 Nm and the testing speed of 1.3 mm/min suggested by the standard ASTM D-6641 are also the best choice for the current investigation. These value are used in all the tests to follow.

Torque [Nm]	Speed [mm/min]	Failure mode	Validity	Peak load [MPa]
2.5	0.25	Delamination of tabs	X	1086.67
5.0	0.25	MB inside tabbed region	X	554.91
2.5	0.50	MB inside tabbed region	X	1007.56
5.0	0.50	MB in gauge section near tab	✓	940.53
2.5	0.75	MB in gauge section near tab	✓	938.56
5.0	0.75	MB in gauge section near tab	✓	704.54
2.5	1.00	MB inside tabbed region	X	809.07
5.0	1.00	MB in gauge section near tab	✓	701.36
2.5	1.25	MB in gauge section near tab	✓	1037.96
5.0	1.25	MB in gauge section near tab	✓	893.47
2.5	1.30	MB in gauge section	✓	1184.59
5.0	1.30	MB in gauge section near tab	✓	1055.71

Table 5.1: Effect of bolt torque and testing speed on failure under the axial compression. The best choice values used in the rest of the testing to failure campaign are shown in the dark green color.

TAB TAPER ANGLE: It has been shown in the literature that specimens with tapered tab, although have a longer unsupported length, generally result in higher strengths under the axial compression because of a reduction in stress concentrations at the tab end [5, 40]. The current standard testing method for compression ASTM D-6641, however, suggests the use of untapered tabs as the increase in strength is considered negligible in-lieu of the increased complexity for preparation of the tapered tabs. The current investigation considers a smaller gauge length i.e. 5mm compared to the standard range of compression testing specimens i.e. 10-13 mm. The smaller gauge section with untapered tab could lead to a number of invalid tests with failure propagating inside the tabbed region due to stress concentrations.

To investigate the effect of the tab taper angle on the compression strengths, an investigation with three different tab taper angles i.e. 90° , 60° , and 45° was carried out. Eight specimens each were prepared with a tab taper angle of 90° and 60° , and an initial eight specimens with a tab taper angle of 45° . According to the ASTM D-6641 compression testing standard, a test is valid if the failure occur inside the gauge section. In the current investigation, the only microbuckling failure mode was observed inside the gauge section. Other valid failure modes, such as brooming inside the gauge section or longitudinal splitting inside the gauge section, were not observed in any test. Six, four, and five tests from specimens with 90° , 60° , and 45° tab taper angle, respectively, resulted in a valid MB failure inside gauge sections of specimens. The compression strength of all valid tests from this study are plotted in Fig. 5.7

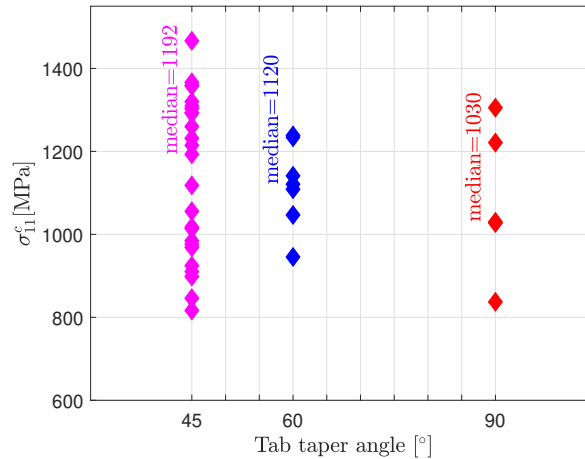


Figure 5.7: Effect of tab taper angle on the strength under axial compression load

against tab taper angle. Failure in specimens with 90° tab taper angle tended to occur near the tab ends with a lower rate of successful tests, and a lower median strength. In specimens with 45° tab taper angle, the failure was more central which is indicative of failure due to the misalignment. The results of the specimens with 60° tab taper angle were somewhat in-between. It is concluded that the median strength increases with a decrease in tab taper angle as seen in Fig. 5.7. Although effects of stress concentration due to tabbing can not be completely eliminated, higher compression strength values of specimens with 45° tab taper angle indicate a minimum effect of stress concentration. Based on these outcomes, a tab taper angle of 45° was chosen for further tests. Further tests were carried out under axial compression and combined compression-shear loads to obtain 25 valid tests for each load case. The results of those tests are used for the development of failure envelopes, see Section 5.2.3, Section 5.2.5, and Section 5.2.7.

5.2.2 Mode of failure in different load cases

In order to develop experimental failure envelopes, failure tests were performed under three distinct load cases as defined earlier i.e. axial compression, combined compression-shear load case A (30° load case), and combined compression-shear load case B (45° load case). Tests were performed on a large number of specimens in order to obtain a statistically significant sample sizes of valid test results for each load case. Only the tests which showed valid microbuckling failure according to the failure modes defined in the standard ASTM D6641 were considered. In total, 99 specimens were tested out of which 44 (25 valid) were under the axial compression, 30 (23 valid) were under the combined load case A, and 25 (25 valid) were under the combined load case B. All the tests where failure occurred inside the tabbed region were considered invalid. The lower success rate in the axial compression case was expected

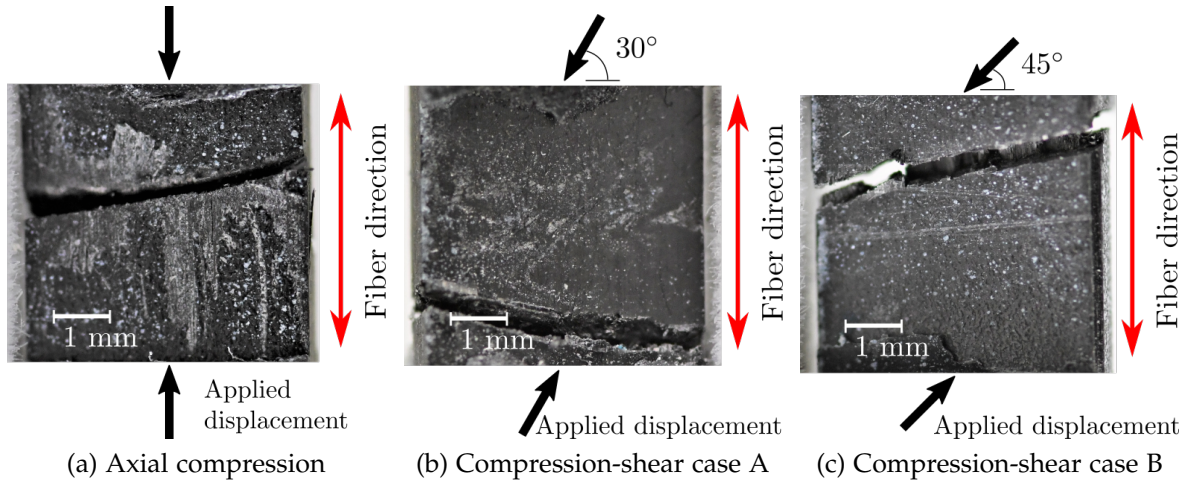


Figure 5.8: Gauge sections of the failed specimens showing microbuckling failure mode. (a), (b) and (c) show a specimen each from the axial compression series (0° load case), the combined compression-shear case A series (30° load case), and the combined compression-shear case B series (45° load case), respectively. The white spots are reminiscent from the paint used to create speckle pattern for the DIC system measurements.

as stress concentrations near the tab ends and the small gauge section tend to incur failure propagation inside the tabs, making a portion of the tests invalid.

Representative gauge sections of a failed specimen each from the axial compression, the combined compression-shear case A, and the combined compression-shear case B series are shown in Fig. 5.8. The direction of the applied displacement load and the mean fiber direction of each representative gauge section is also marked with arrows in Fig. 5.8. When the failure pattern of each representative gauge section is compared to the guide given in the ASTM D-6641 standard for compression testing, it is evident that the failure mode is microbuckling.

To give further evidence about microbuckling being the mode of failure under the combined compression-shear load cases, the surface of a specimen from the combined compression-shear case B series was scanned using a Keyence laser microscope at the Institut für Werkstoffkunde, LUH. The fractographic features, visible on the surfaces of the broken fibers shown in Fig. 5.9(a), depict the morphology particular to microbuckling failure [52]. Across each fiber's face is a chop-mark like line, which represents a neutral axis of the fibers as they undergo bending. Bundles of fibers collapse in the same direction at the ends of the localized kink band resulting in the alignment of the neutral axis as seen in Fig. 5.9(a). This alignment of the neutral axes is a demonstration of the so-called 'domino' fracture which occurs during the microbuckling failure. Microbuckling may occur on several planes resulting in a series of steps on the fracture surface [52]. A closer look at the failed fiber surfaces shows that the fibers break at the ends of the kink band in bending, resulting in a tension surface and a compression surface on either side of the neutral axis, cf. Fig. 5.9(b). Further

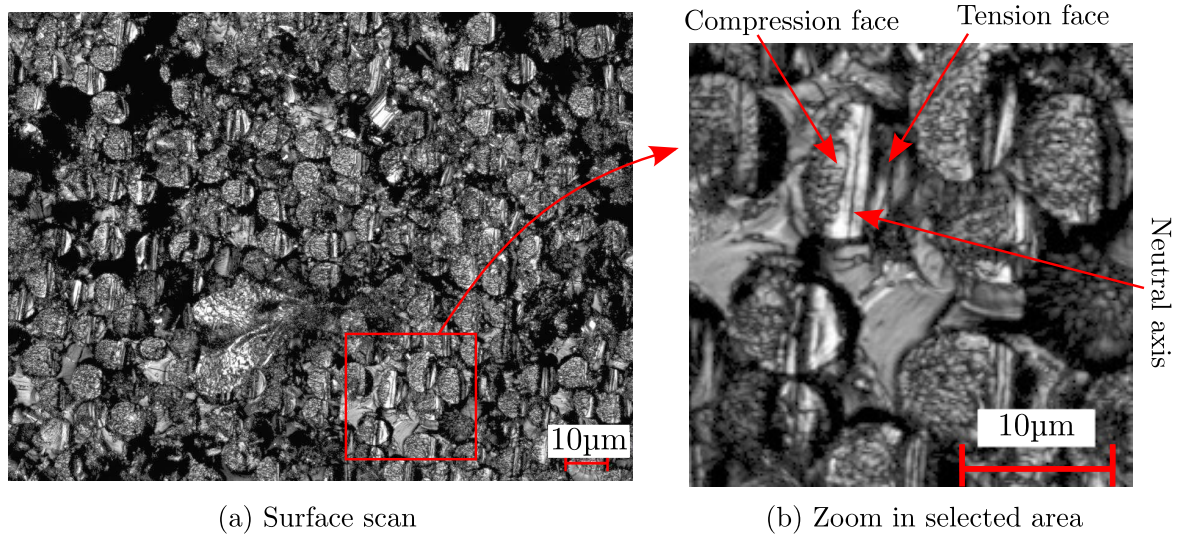


Figure 5.9: Fracture surface of a specimen from the combined compression-shear case B series (45° load case). The laser scan was performed by the Institut für Werkstoffkunde, LUH.

discussion and interpretation of results of testing to failure under compression and combined compression-shear are presented in subsections to follow.

5.2.3 Comparison of failure stresses for different load cases

It is suggested in literature that the load applied in the global $1'$ -direction as can be seen in Fig. 5.4, which is measured using one load cell only, can be divided into its components for the combined load cases using simple trigonometric relations [50]. This seems appropriate only, when the material behavior has a linear relation between the load components. However, the material behavior of the unidirectional FRPs under the axial compression is approximately linear up to failure whereas highly nonlinear in shear as shown in Fig. 3.2a, also see Figs. 5a and 5b in [116]. Hence, it is proposed that such a division of applied loads without consideration of the material behavior can not be carried out. The reason for that is the lack of a one to one relation up to failure between compression and shear response of the material.

Moreover, the testing was displacement controlled in the current investigation. Therefore, the stresses in the machine coordinate frame $\sigma_{1'1'}$, $\sigma_{2'2'}$, and $\sigma_{1'2'}$ as well as the stresses in the specimen coordinate frame σ_{11} , σ_{22} , and σ_{12} have non zero values in the combined compression-shear load cases. One would assume that using the usual transformation matrices, stress components maybe transformed from the machine coordinate frame to the specimen coordinate frame in the combined compression-shear load cases. The load was only measured with one load cell in the global machine loading direction $1'$ giving only $\sigma_{1'1'}$ stress component. The stress components $\sigma_{2'2'}$ and $\sigma_{1'2'}$ are unknown in the machine coordinate frame, therefore, transformation

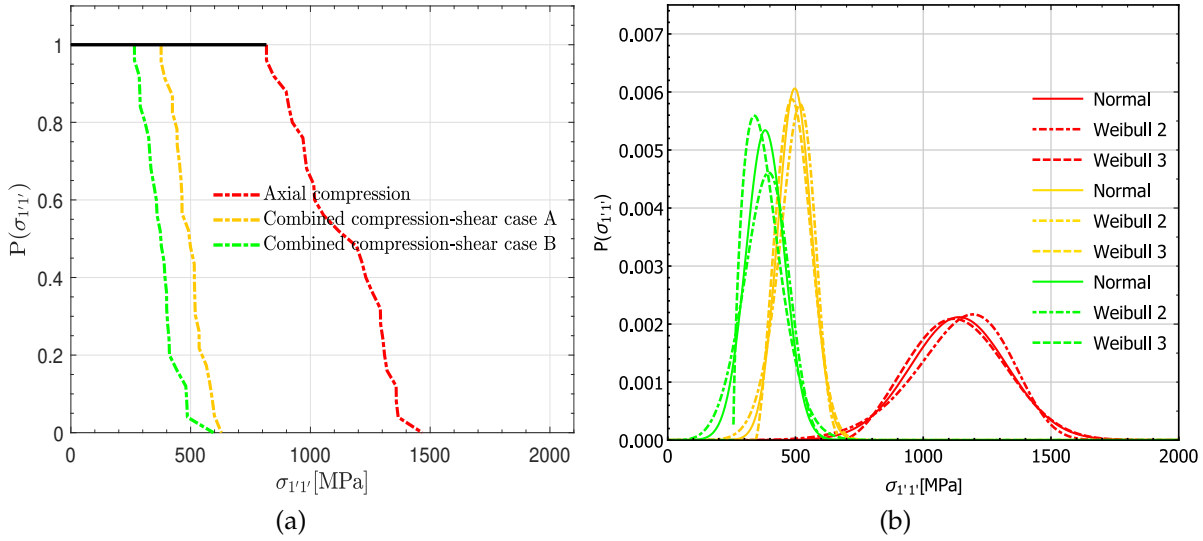


Figure 5.10: Comparison of the applied far field stresses in the loading direction $\sigma_{1'1'}$. (a) represents empirical probability of survival of the applied stress $\sigma_{1'1'}$ for all three load cases. The values of $\sigma_{1'1'}$ were measured using the load cell of the machine. (b) shows the respective probability density functions fitted to each load case.

of stresses using the usual stress transformation matrices from the machine coordinate frame to the specimen coordinate frame in the combined compression-shear load cases cannot be done.

However, failure loads of different cases can be compared in the form of applied stresses $\sigma_{1'1'}$ in the global loading direction $\mathbf{1}'$ i.e. applied force/initial area perpendicular to the fiber direction, see Fig. 5.4b. The initial area was calculated by a product of the average thickness and the average width for each specimen, where thickness and width were measured at two locations, each, in the gauge section of each specimen. As the loading was in the mean fiber direction of the specimens, the relation $\sigma_{1'1'} = \sigma_{11}$ holds for the axial compression load case.

Fig. 5.10a shows the empirical probability of survival of the applied stress $\sigma_{1'1'}$ measured in all three load cases. As expected, introduction of the shear load along with the compression load in the specimen coordinate frame reduces $\sigma_{1'1'}$ of the machine coordinate frame significantly for the combined compression-shear load cases compared to the pure axial compression load case. A quick glance at the plots in Fig. 5.10 shows that the spread of the strengths $\sigma_{1'1'}$ around corresponding mean values is significantly higher for the axial compression case. The reason behind a larger variation in the applied stresses in the axial compression case is the dependence on the underlying fiber misalignment. When the compression stress σ_{11} proportion of the total applied stress $\sigma_{1'1'}$ is reduced, the effect of the fiber misalignment is also reduced. The consequential result is the lower variation of the applied stresses $\sigma_{1'1'}$ in the combined load cases.

The $\sigma_{11'}$ values for all three cases are fitted with a normal distribution and 2/3-parameter Weibull distributions using the maximum likelihood method. The plots are shown in corresponding colors in Fig. 5.10b. The parameters for fits of different distributions are reported in Table 5.2 for each load case. The parameters referring to the 2-parameter Weibull fit are represented with an over-script tilde symbol. For all fitted distributions, the goodness of fit (gof) was determined via Pearson's χ^2 -test. The normal distribution shows a high value of the gof for all load cases. If one was to consider a normal distribution of the $\sigma_{11'}$ values, a prediction of zero strength and infinitely large strength also has a probability to occur. The strength of a material cannot be zero or infinitely large, hence, the normal distribution can be rejected based on this fact that it gives probability to infinitely extreme values which is physically impossible. Experimental investigation [62] and numerical analysis [76, 100] in the literature propose that the axial compression strength closely fits to the 3-parameter Weibull distribution. In the current investigation, the gof value of 34% suggest a loose fit of the axial compression load case for the 2-parameter Weibull whereas a slightly better fit with a gof value of 46% for the 3-parameter Weibull. The spread of the axial compression strengths in the current investigation resembles the results of Jelf and Fleck [62], where the authors proposed a 3-parameter Weibull fit. $\sigma_{11'}$ for the load case A shows a high gof for the 2-parameter Weibull and a moderate gof value for the 3-parameter Weibull distribution. In load case B, the trend is similar to the axial compression where the 3-parameter Weibull shows a better fit. Although the values of gof for the 2-parameter and 3-parameter Weibull distributions for all load cases are moderate, these distributions do not predict infinitely extreme values unlike normal distribution. Therefore, from the physical interpretation of the problem, Weibull distribution is a better choice. Based on these observations, it is concluded that the 3-parameter Weibull model is better suited to all load cases among the three distributions discussed here, as expected.

5.2.4 Observing the formation of the kink band using DIC system

It is clear from post mortem inspection that the failure under the compression dominated loads is caused by microbuckling, which is a shear localization phenomenon. It is generally quite difficult to observe the dynamic progression of this phenomenon [16, 17]. In the current investigation, the maximum temporal resolution possible on the current specimen size for the DIC system is approximately 90 Hz. This was not enough for observing the shear localization in the axial compression case, as the speed to failure under the axial compression was quite fast. However, the speed to failure in the combined load cases is slower. This allowed an insight into the shear localization phenomenon.

An example of observing the formation of the kink band using the DIC system is shown in Fig. 5.11 for the load case B. The figure shows snapshots just before the peak load and after the failure has occurred. Green arrows of the coordinate frame in

		Load case		
		Axial compression	Comb. comp.-shear case A	Comb. comp.-shear case B
Normal distribution fit	mean [MPa]	1139.89	497.22	381.44
	s [MPa]	188.28	65.83	74.70
	gof [%]	69	72	84
2-parameter Weibull fit	shape \tilde{m} [1]	7.11	8.22	5.06
	scale \tilde{R}_0 [MPa]	1219.76	526.40	412.72
	gof [%]	34	80	34
3-parameter Weibull fit	shape m [1]	2.74	2.53	1.69
	scale R_0 [MPa]	521.31	173.76	139.48
	thresh. R_t [MPa]	677.58	343.11	256.65
	gof [%]	46	55	61

Table 5.2: The table lists fit parameters of the three probability distributions on each load case, and the corresponding goodness of fit (gof) in percentage. The gof highlights the probability of a data set belonging to the respective probability distribution function.

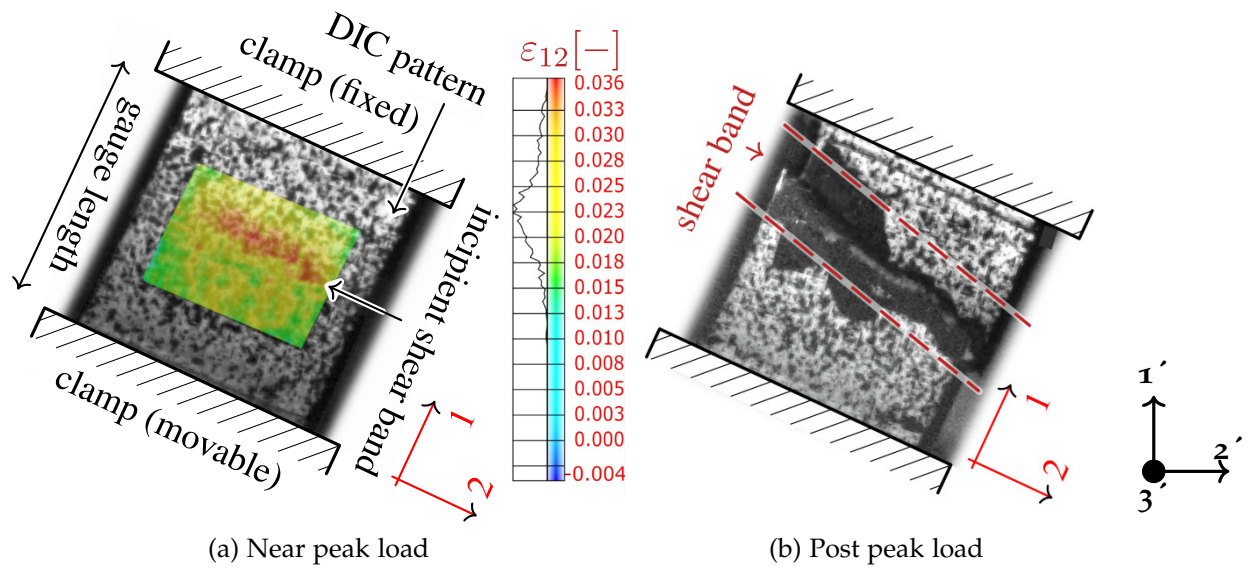


Figure 5.11: Images taken at different stages of a test under the combined compression-shear load case B (i.e. 45° load case), along with the shear strain field. The applied displacement was in $1'$ direction. (a) shows the frame just before the peak load. Localization of the in-plane shear in the form of a band is apparent from the contour plot. (b) shows the post peak failed specimen. The final failure location is in the same place as the localized shear band in (a).

the sub-figures point in the fiber direction whereas red arrows point in the in-plane transverse direction in the specimen coordinate frame. Applied loading was in the global $1'$ direction in the machine coordinate frame. Just approaching the peak load, shear has begun to localize in the form of a band at certain angle to the axial direction of the specimen. After failure, the fracture shown in Fig. 5.11b can be seen at the exact same location as the incipient shear band apparent in Fig. 5.11a. Since the defined region of interest in the DIC system vanished because of the damage to the black and white speckle pattern caused by a sudden release of energy in microbuckling failure, the strain field can not be tracked anymore in Fig. 5.11b after failure has occurred.

5.2.5 Failure envelope in the strain space

Typically, failure envelopes are defined in the stress space. For this purpose, the applied forces must be measured for each loading direction under consideration. As argued in Section 5.2.3, the applied force in the $1'$ -direction can not be subdivided into its components in the specimen coordinate frame without consideration of the nonlinear material behavior. In contrast to the stress components, strain components can be measured directly at the specimen level for each direction using the DIC system. Hence, the primary failure envelope representation from the experimental results is done in the strain space.

Only the intersection of the failure envelope with the ε_{11} - ε_{12} plane is considered here. For this purpose, axial and shear strains were extracted from the DIC measurement system from all the specimens of the testing to failure series. The details of strain extraction method are detailed in Section 5.1.3. It is observed from the results that the strain ratios at failure in combined compression-shear case A and case B are not as intended. One of the possible reasons for it could be that the holding plates of the fixture were not rigid, as they were held only by screws. Since screws only have a line contact along screw threads compared to surface contact of other parts of the fixture, such as guide pans and holding blocks, they are prone to slight slippage. As a consequence, the strain ratios deviated from the intended compression to shear ratios of $\sqrt{3} : 1$ and $1 : 1$ for case A and case B, respectively. However, the failure modes were valid according to the ASTM D6641 standard albeit at a mix of strain ratios at failure in the combined load cases. Additionally, the strains at failure were measured directly on the specimens using the DIC system, hence, these values are admissible for the development of a failure envelope. The shear strains of case B are negative in the current coordinate convention. However, the shear behavior is symmetric around the axial direction, henceforth, absolute values of shear strain are taken.

The resulting 75 data points are plotted as a scatter in Fig. 5.12. For the failure strain under the pure in-plane shear, the mean value from the shear characterization tests mentioned in Section 3.1 is employed. This mean value of the in-plane shear failure strain is 9.57[%] which is taken as deterministic, as the spread thereof is negligible as can be seen in the experimental results depicted in Fig. 3.2a. The axial compression case shows the highest spread having mean and standard deviation values of -1.11[%] and 0.24[%] of the axial strain. The spread reduces with increasing value of the applied shear load and becomes deterministic quantity under the pure in-plane shear load as can be seen in Fig. 5.12. The shear behavior in FRPs is independent of the fiber misalignment and only the axial compression is dependent on the fiber misalignment. In case of combined compression-shear cases, an increase in the shear load and a simultaneous decrease in the compression load compared to the axial compression case reduces overall spread of the failure strains. Therefore, with reduced ratio of applied compression loads, the spread of failure strains reduces compared to the pure axial compression case.

The envelopes were defined in terms of the median and percentiles since they provide a relatively unbiased statistical measure compared to the mean and the standard deviation. Moreover, the percentile representation is easier to understand and implement in an engineering design. Eq. 5.1 represents failure envelopes f_i associated with certain percentiles of distribution of failure. This particular form of the equation for failure envelopes is chosen as it provides the best fit for each percentile with least amount of complexity. Other common functions for fitting failure strain data, such as Fourier series, exponential function, power law, and sum of sines, were also tried but they either did not provide a good fit or resulted in increased complexity. The functional form of the failure envelope in Eq. 5.1 was fitted to the respective percentiles

i	p_i	q	r_i
25 th percentile	-1.5244	0.1042	0.9681
Median	-0.8598		0.9088
75 th percentile	-0.6583		0.6847

Table 5.3: Fit parameters of Eq. 5.1 for median, 25th, and 75th percentile of distribution of failure envelopes in ε_{11} - ε_{12} plane

of distributions of the failure strains of each load case to identify constants p_i and r_i for each envelope f_i , delimiting the $i = 25^{\text{th}}, 50^{\text{th}}, 75^{\text{th}}$ percentile of distribution of failure. The functions f_i were fitted with a gof of 99.9% for each percentile. The parameters of Eq. 5.1 are enumerated in Table 5.3, and the equations are plotted on top of scatter points in Fig. 5.12. The i^{th} percentile of distribution of failure is reached when corresponding function $f_i(\varepsilon_{11}, \varepsilon_{12})$ becomes equal to zero. The green 25th percentile line indicates 25% chance of failure or alternatively 75% chance of survival at these load levels. Similarly, blue and red lines represent 50% (median) and 75% chances of failure respectively.

$$f_i(\varepsilon_{11}, \varepsilon_{12}) = p_i \varepsilon_{11} \varepsilon_{12} + q \varepsilon_{12} - r_i \varepsilon_{11} - 1 \quad (5.1)$$

Generally, failure envelopes or yield surfaces are convex. These surfaces/envelopes generally define either the start of yielding or activation of a failure mode. However, the strain based failure envelope here is not convex, and represents the ultimate failure of specimens. The reason behind the concave shape can be understood in differences of failure behaviors of the axial compression and the pure shear cases. Under the axial compression, failure is brittle and the activation of failure coincides with the ultimate load carrying capacity. On the contrary, the shear failure is progressive and the final failure occurs after considerable yielding of the matrix, cf. 3.2a. Such ductile behavior under shear stretches failure under the combined loads outwards, giving the failure envelope a concave shape. If one was to gather data for the activation of failure, e.g. through intermittent loading/unloading, the failure envelope based on the activation might still be convex.

5.2.6 Interpretation of the axial compression load case results in-lieu of an analytical formula

Results for the axial compression load case are further interpreted by referring to analytical estimates of the peak load. There are different models available in the literature for predicting the axial strength of FRPs under compression [8, 21, 23, 75], but only the classical model proposed by Budiansky et. al. shall be considered further. The expressions for the compressive strength predicted by this model are stated as Eq. 5.2, see also Eq. 62 in [21]. The model in Eq. 5.2b provides a relation among the applied

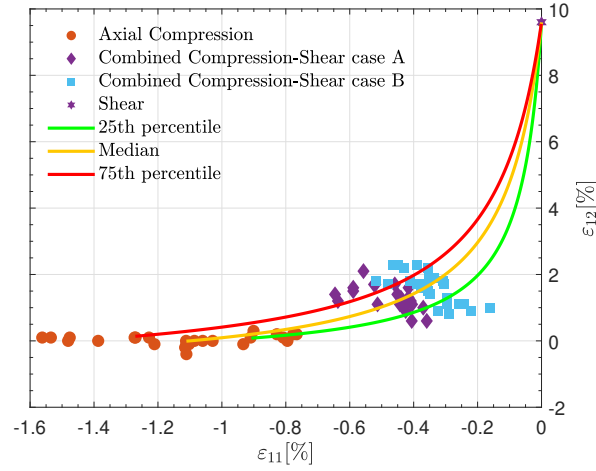


Figure 5.12: Failure envelope in ε_{11} - ε_{12} plane based on the experimental results. Scatter points represent strains of corresponding specimens at failure for each load case. The solid lines are based on fitted equations at 25th, 50th(median), and 75th percentiles of distributions of failure.

far field compressive stress σ_{11}^{∞} , the magnitude of the in-plane misalignment $\psi=|\theta|$, the applied far field shear stress σ_{12}^{∞} and/or the applied far field shear strain γ_{12}^{∞} , considering the nonlinear in-plane shear response of the material. The function $\tau(\gamma_{12})$ represents the nonlinear shear response under the uniaxial shear, i.e. $\tau(\gamma_{12})=\sigma_{12}(\gamma_{12})$ as shown in Fig. 3.2a. Symbol γ_{12} denotes the in-plane shear angle where $\gamma_{12}=2\varepsilon_{12}$ in the usual sense. In this model, the misalignment angle ψ is representative of a single positive valued misalignment without consideration of any spatial variability. Solving for the maximization problem, as stated in Eq. 5.2c, provides the prediction of the compressive strength σ_{11}^c . Eq. 5.2 assumes plane strain with respect to **1** – **2** plane and does not consider any out-of-plane deformations, hence, the magnitude of misalignment ψ is defined in terms of the in-plane misalignment θ only, see Eq. 5.2a.

$$\psi = |\theta| \quad (5.2a)$$

$$\sigma_{11}^{\infty} = \frac{\tau(\gamma_{12}) - \sigma_{12}^{\infty}}{\psi + \gamma_{12} - \gamma_{12}^{\infty}} \quad (5.2b)$$

$$\sigma_{11}^c = \max_{\gamma_{12}} (\sigma_{11}^{\infty}) = \max_{\gamma_{12}} \left(\frac{\tau(\gamma_{12}) - \sigma_{12}^{\infty}}{\psi + \gamma_{12} - \gamma_{12}^{\infty}} \right) \quad (5.2c)$$

In this section only pure compression case will be considered, although, mixed compression/shear load cases A and B will be considered further down in Section 5.2.7. There is no applied far field shear load for the special case of the pure axial compression, hence, $\sigma_{12}^{\infty}=0$ and $\gamma_{12}^{\infty}=0$. In this case, a straightforward extension of Budiansky's plane strain model to account for the effect of the out-of-plane misalignment ϕ is obtained by redefining ψ as given by Eq. 3.2. In Eq. 5.3, angles ψ and γ refer to the

misalignment and the shear, respectively, in a common plane in between the 1 – 2 plane and the 1 – 3 plane.

$$\sigma_{11}^c = \max_{\gamma} (\sigma_{11}^{\infty}) = \max_{\gamma} \left(\frac{\tau(\gamma)}{\psi + \gamma} \right) \quad (5.3)$$

The modified Budiansky model given in Eq. 5.3 links the compressive strength σ_{11}^c to a single misalignment angle ψ i.e. given the compressive strength and material properties, the angle ψ can be calculated by performing an inverse analysis using Eq. 5.3 as explained below. A similar analysis using Argon's analytical formula [8] to obtain inferred values of ψ corresponding to the experimental strengths was performed by Jelf and Fleck, see Figs. 9(a) and 9(b) in [62]. Taking advantage of Budiansky's analytical solution given in Eq. 5.3, an analysis is performed to find the misalignment angles ψ associated with the experimentally obtained strength values. Results of this analysis are shown in Fig. 5.13. Red line in Fig. 5.13b represents the generalized analytical solution of Eq. 5.3 for a range of ψ using nonlinear shear relation shown in Fig. 3.2a. Each experimentally observed strength result is projected from the vertical axis onto the red curve of Fig. 5.13b, and subsequently onto the horizontal axis. This procedure renders a histogram (in red color in Fig. 5.13c) of an inferred misalignment angle ψ from the histogram of the experimentally observed strength values plotted as histogram in Fig. 5.13a. The resulting data set of ψ , plotted as a histogram in Fig. 5.13c (red line), has a median value of $Q_{50}(\psi)=1.13^{\circ}$ with maximum and minimum values of 2.09° and 0.77° , respectively.

The misalignment angles ψ implied by Eq. 5.3 in conjunction with peak loads observed experimentally can be compared to the measurement data of distributions of misalignment angles presented earlier in Section 3.2. Results of the measurements of the fiber misalignments presented in Section 3.2 clearly indicate that a single representative angle is an overly simplistic approximation, nonetheless, one may consider an angle to be derived in some manner from the actual distributions of the misalignment angles for comparison with ψ . In this sense, an equivalent to ψ may be considered as the effective misalignment for the purpose of applying Eq. 5.3.

In this spirit, an effective misalignment angle $\eta_{k,l,m} := \sqrt{\theta_{k,l,m}^2 + \phi_{k,l,m}^2}$ is defined in terms of the measured in-plane $\theta_{k,l,m}$ and the out-of-plane $\phi_{k,l,m}$ misalignments. In a Monte Carlo approach, values for $\theta_{k,l,m}$ and $\phi_{k,l,m}$ were randomly sampled from the normal distributions reported in Table 3.4 for $j=1 \cdots 10^7$ to obtain the distribution of $\eta_{k,l,m}$.

Generally, the analytical solution considers the maximum magnitude of the fiber misalignment angle. Since there are extreme outliers in the measurements of the fiber misalignment due to some rare broken fibers or spurious angles associated with the method of measurement, as presented in Section 3.2, identifying ψ with maximum of distribution of $\eta_{k,l,m}$ would result in unrealistically high values. Therefore, identifying ψ with a certain percentile of distribution of the effective misalignment angle $\eta_{k,l,m}$ appears as a reasonable assumption. A similar procedure was carried out by

Wilhelmsson et. al. [127] for non crimp fabric (NCF) composites. In that investigation, ψ was identified with the 99th percentile of the absolute values of the measured distribution of the in-plane fiber misalignment angle. In the current investigation, the 99th percentile $P_{99}(\eta_{k,l,m})=2.45^\circ$ turns out to be quite far off from the median misalignment angle of $Q_{50}(\psi)=1.13^\circ$. Hence, the 99th percentile $P_{99}(\eta_{k,l,m})$ gives a very conservative prediction of the median value of the compressive strength. The 90th percentile $P_{90}(\eta_{k,l,m})=1.17^\circ$ is however, in good agreement with the median value of $Q_{50}(\psi)=1.13^\circ$.

Thus, the percentile level used to define the effective angle from the measurements of the fiber misalignments for the prediction of median value of the compressive strength appears as an undetermined tuning parameter. Its dependencies are unclear and readjustments may be required for different materials. It should be noted that the prediction of the median strength was the goal. Hence, the magnitude of the misalignment angle ψ related to the median strength i.e. $Q_{50}(\psi)$ was compared with the identified percentile $P_{90}(\eta_{k,l,m})$ of the measured effective misalignment angle $\eta_{k,l,m}$.

Some authors employed the assumption of elastic-perfect plastic material behavior in shear for using analytical solution of Eq. 5.3 [109, 127]. Considering Fig. 3.2a, it is not clear what could be an equivalent representative value of the shear yield stress σ_{12}^y in an idealization of perfect plasticity yield behavior. In lieu of a well defined yield stress σ_{12}^y , the shear modulus changes significantly at the value of 55 MPa. Additionally, $\sigma_{12}^y=35$ MPa is also considered. In Fig. 5.13b, the prediction by Eq. 5.3 for the axial compression strength against ψ for aforementioned values of yield stress under assumptions of elastic-perfect plastic behavior is also plotted. Again projecting the experimentally observed peak stresses from Fig. 5.13a on the elastic-perfect plastic behavior based solutions, the corresponding values of ψ are inferred. Histograms of inferred misalignment angles ψ at $\sigma_{12}^y=35$ MPa and $\sigma_{12}^y=55$ MPa are plotted in Fig. 5.13c in colors green and blue, respectively. It can be seen that the perfect plasticity solution at $\sigma_{12}^y=35$ MPa is closest to the generalized nonlinear solution, which is neither at the start of matrix nonlinearity value of 21 MPa nor at the value of 55 MPa where it seems logical from the shear stress-strain curve. This finding highlights that for materials with nonlinear shear behavior, the assumption of perfect plasticity is overly simplistic and can not predict compression strength accurately.

5.2.7 An approximation of the failure envelope in the stress space

As argued earlier in Section 5.2.5, a direct determination of the failure envelope in the stress space from the current series of experiments is not possible. However, an approximate representation through an indirect calculation can be carried out. The strength values under the pure axial compression and under the pure in-plane shear are directly available, see Sections Section 5.2.3 and Section 3.1. To also obtain data points for mixed load cases A and B, a simple estimate via an equation system involving a further modification of the classical Budiansky model is considered in the fol-

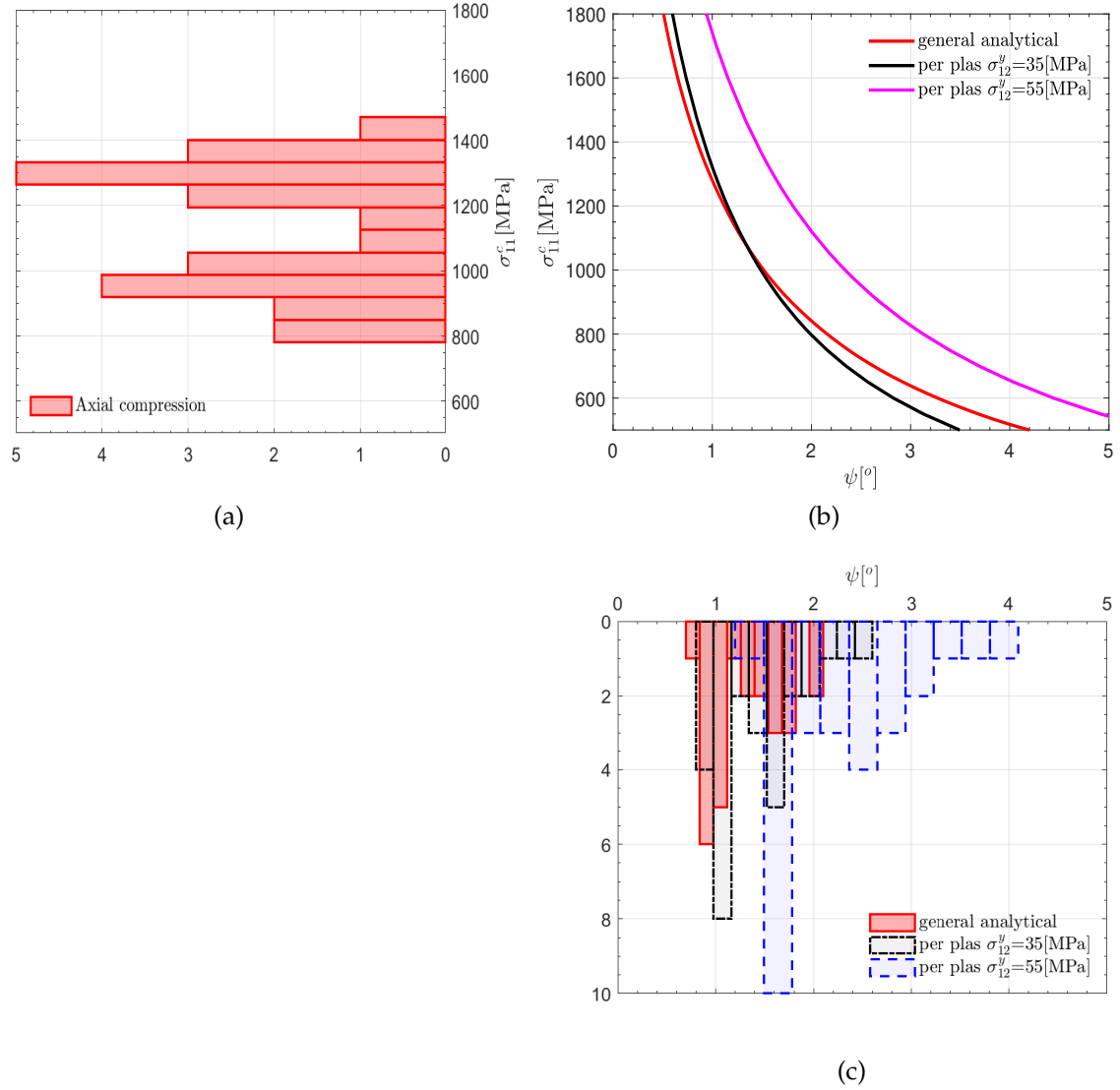


Figure 5.13: Analytical solutions of Eq. 5.3. (a) shows the histogram of the strength under the axial compression σ_{11}^c . (b) shows prediction of the compression strength against the misalignment angles implied by one of the two considered solution methods for Eq. 5.3. Projecting (a) on (b) yields (c). Image (c) shows the histograms of the inferred misalignment angles using Eq. 5.3 pertaining to the experimentally obtained strengths.

lowing. For this purpose, the far field applied in-plane shear strains ε_{11}^c and $\gamma_{12}^\infty=2\varepsilon_{12}^\infty$ are directly available from measurements. The first Eq. 5.4a is provided by the linear relation between σ_{11}^c and ε_{11}^c . It can be used here as the behavior under the pure axial compression load case is approximately linear up to failure. The second equation is provided via Eq. 5.4b. The original form in Eq. 5.2c neither accounts for the out-of-plane misalignment ϕ nor for any out-of-plane shear γ_{13} . Here, this is accepted as a simplification and it is assumed that contributions of the out-of-plane quantities are negligible in the mixed load cases A and B. This simplification appears justified, since the expression is dominated by the far field applied in-plane shear strain γ_{12}^∞ . The misalignment angle ψ with the simplified assumption of the in-plane behavior is identified as the 90th percentile P_{90} of absolute values of measured distribution of the in-plane angles $|\Theta_{k,l,m}|$.

$$\sigma_{11}^c = E_{11}\varepsilon_{11}^c \quad (5.4a)$$

$$\sigma_{11}^c = \max_{\gamma_{12}} \left(\frac{\tau(\gamma_{12}) - \sigma_{12}^\infty}{\psi + \gamma_{12} - \gamma_{12}^\infty} \right) \quad (5.4b)$$

$$\gamma \approx \gamma_{12} \quad \gamma_{13} \approx 0 \quad (5.4c)$$

$$\psi = P_{90}(|\Theta_j|) = 1.11^\circ \quad (5.4d)$$

Solving equation system given in Eq. 5.4 numerically for σ_{12}^∞ in terms of given values for ε_{11}^c and γ_{12}^∞ renders respective data points for mixed load cases A and B in stress space. The median values of numerically calculated σ_{11}^c and σ_{12}^∞ for cases A and B, along with experimentally obtained median value of the pure axial compression σ_{11}^c and the value for the pure in-plane shear are plotted as blue dots in Fig. 5.14. These four points fall approximately on a straight line. Therefore, they are fitted with a linear function g_i , see Eq. 5.5. There, R_{12} is the strength under the pure in-plane shear. The symbol R_{11}^i represents 25th, 50th (median) and 75th percentiles of strengths under the pure axial compression with $R_{11}^{25th}=974$ MPa, $R_{11}^{50th/median}=1192$ MPa, and $R_{11}^{75th}=1304$ MPa. There, symbol $R_{12}=77$ MPa represents the in-plane shear strength. The failure envelope based on Eq. 5.5 for the median strengths is plotted by a solid yellow line in Fig. 5.14. In the current investigation, the failure envelope in stress space shows a linear trend, which is in line with the experimentally obtained failure envelopes reported in the literature [10, 116]. The linear relation between σ_{11}^c and σ_{12}^∞ as found out in the current investigation is also proposed by the analytical solution of Eq. 5.2 under combined compression-shear loads [21]. Similar to the median strengths, a linear relation can be assumed for other percentiles of strengths for failure envelopes in stress space. In such a scenario, only the percentiles of the axial compression strength are needed to construct the failure envelopes for a given percentile of failure, as the shear strength is deterministic. Under this assumption, the 25th and 75th percentiles of the distribution of failure envelope in stress space are also plotted in Fig. 5.14 with dotted green and red lines, respectively.

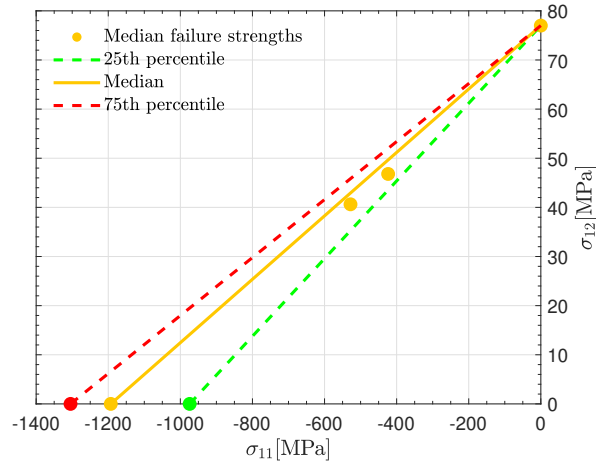


Figure 5.14: Derived failure envelope in σ_{11} - σ_{12} plane based on the experiments. Yellow scatter points represent median strengths for each load case. The solid (yellow) line is based on the fitted equation on median strengths, whereas dashed lines represent approximations for 25th and 75th percentiles of distribution of failure.

$$g_i(\sigma_{11}, \sigma_{12}) = \frac{\sigma_{11}}{R_{11}^i} + \frac{\sigma_{12}}{R_{12}} - 1 \quad (5.5)$$

NUMERICAL MODELING OF PROBABILISTIC FAILURE ENVELOPES

As highlighted in the previous chapter through the results of the experimental campaign in Section 5.2.2, the leading failure mode in unidirectional FRPs under compression dominated loads is microbuckling (MB). MB is highly sensitive to material imperfections and nonlinear material behavior. Material imperfections are spread in the form of the fiber misalignment in the volume of the material as shown by measurements of the fiber misalignment in Section 3.2. The spectral representation method is employed in this work to represent the misalignment in numerical models for the prediction of MB strength while preserving the spatial correlation information, see Section 4.1 and Section 4.2. The MB strength shows uncertainty because of a high sensitivity to the fiber misalignment. Quantification of uncertainty in MB failure is essential for reliable design practices. Therefore, the aim of the current chapter is the probabilistic prediction of MB failure under axial compression and combined compression-shear loads using numerical modeling. Different series of 3D models, each containing a large number of realizations, were developed based on spectral densities calculated from the measurements of the fiber misalignment from different specimens, cf. Section 4.1.1. The resulting distributions of strengths under the axial compression load case from these model series are compared and a suitable model series was chosen for further analysis. The stress-strain response under different combinations of combined compression-shear loads is discussed. Finally, the numerically determined probabilistic failure envelopes in stress and strain spaces are presented with lower percentiles of distributions of failure compared to the experimentally determined failure envelopes. The failure envelopes are also compared against classical failure criteria from the literature to highlight the limitations of the classical criteria.

6.1 MODELING METHODOLOGY

The review of the state of the art given in Section 2.6 shows that the homogenized representation of fiber and matrix materials in numerical models allows for ease of modeling and computational efficiency over large model sizes, which are necessary characteristics to perform statistically significant number of numerical simulations for quantifying the uncertainties of MB strength. Therefore, the extension of the available 2D homogenized modeling approaches to 3D as well as the details of the material model used herein are presented in this section in a concise manner.

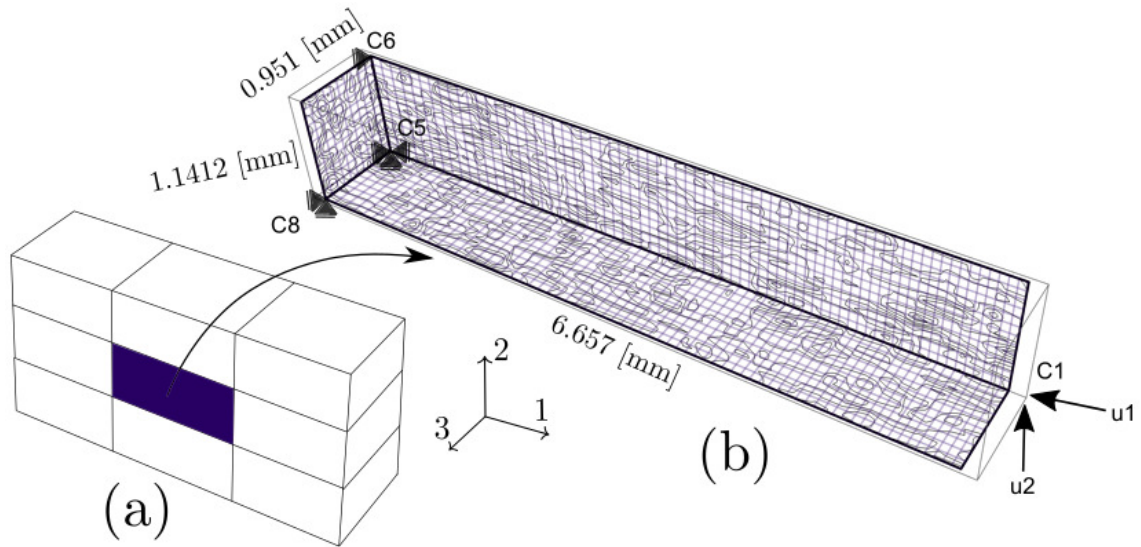


Figure 6.1: Schematic of the FE model geometry used for the development of probabilistic failure envelopes. (a) depicts a $[0]_4$ laminate with large in-plane dimensions compared to the thickness in 3-direction. The laminate consists of representative volumes which are periodic in directions 1 and 2. One such volume is marked in dark blue color. (b) illustrate the geometry of the representative volume used in numerical modeling. The contour of an in-plane distribution of the fiber misalignment angles is plotted on the back planes of the cuboid shaped volume. The direction 1 is the nominal fiber direction, and 2 and 3 are the in-plane and the out-of-plane transverse directions, respectively. The FE mesh is shown with the grid on the back planes of the cuboid with blue lines.

6.1.1 Model geometry

For the development of failure envelopes using numerical modeling, 3D models were constructed in the form of cuboids representing a region of a unidirectional FRP laminate. Fig. 6.1 illustrates the schematic of the FE model geometry used in the current work. Nominal fiber direction is parallel to the 1-axis, whereas 2 and 3 are the in-plane and the out-of-plane transverse directions, respectively. The nominal dimensions of the FE models for the development of the probabilistic failure envelopes under combined compression-shear were $6.657 \times 1.1412 \times 0.951$ mm in 1-2-3 directions, respectively. The FE model dimensions and the discretization were kept same as the volumetric dimensions and the discretization of the virtually generated topologies of the in-plane and the out-of-plane misalignment through the spectral representation method presented in Section 4.2.1. The dimensions and the discretization of the virtually generated topologies were based on the volumetric dimensions and the discretization of the experimentally measured topologies of the in-plane and the out-of-plane misalignment. The CT measurements of the in-plane and the out-of-plane

misalignment were performed on two specimens. CT scan of each specimen provided a measure of the in-plane misalignment as well as of the out-of-plane misalignment.

3D models were meshed using cubic three dimensional fully integrated 20 node C3D20 elements in the commercial software Abaqus. The resulting mesh comprised $70 \times 12 \times 10$ cubic elements with 0.0951 mm edge length, each. The 3D topologies of the fiber misalignment generated using the method presented in Section 4.2.1 were mapped onto the integration points of each element of the corresponding mesh as the material orientations.

Since the FE models were considered as a representative cutout region from a unidirectional FRP laminate based structure with same thickness but larger in-plane dimensions, periodic boundary conditions were used in directions 1 and 2 only. Both the surfaces perpendicular to direction 3 had traction free boundary conditions. To suppress rigid body motions, corner node C5 was constrained in all directions and corner node C8 and C6 were fixed in both transverse directions and in-plane transverse direction, respectively. The axial compression and the combined axial-compression-in-plane-shear loads were applied in the form of displacements $u1$ and $u2$ at the corner node C1. Node C1 was coupled to the whole of the right surface, therefore, the load applied on node C1 got transferred to whole of the right surface. The simulated displacement ratios were $\arctan(u2/u1) = 0^\circ, 30^\circ, 45^\circ, 75^\circ, 85^\circ$, and will from here onward labeled as 0° load case, 30° load case etc. Additionally, node C1 was constrained in direction 3 for the compression-shear load cases and directions 2 and 3 for the axial compression load case as the failure envelope in strain space $\varepsilon_{11}-\varepsilon_{12}$ was the primary focus.

It is well established in the literature, that the failure under compression loads for unidirectional FRPs is MB caused by geometrical and material non-linearities. The response of FRPs until the peak load in MB failure is approximately linear. MB failure in FRPs is unstable with a snap-back response. Thus, the peak load was defined as the failure point of the model. Hence, the peak load was considered as the primary result for the development of the probabilistic failure envelopes in stress and strain spaces. Therefore, the analyses were terminated when reaction force RF_1 in the direction 1 at the control node C1 dropped by 5% from the peak load with the help of URDFIL user subroutine of Abaqus. The solution was performed in two load steps for higher efficiency. The 1st step up to approximately 40% of the expected mean failure strain was solved with larger sub-steps as the response was linear in this range. Both the implicit dynamic and the arc-length based Riks' solver gave the same prediction. The major advantage of the arc-length method is the prediction of the snap-back response, which is out of scope of the current work. The arc-length method suffers from convergence problems whereas the implicit dynamic solver is more reliable and shows convergence past the peak load. With the implicit dynamic method, there was the added advantage of easier post processing because the reaction forces RF_1 , RF_2 and displacements $u1$, $u2$ from multiple steps could be extracted simultaneously. This was not possible in the Riks' arc-length method in Abaqus. Therefore, the implicit

dynamic solver was deemed better suited for probabilistic simulations. Hence, the geometrically non-linear dynamic implicit solver with quasi static load application was employed [1].

Engineering definitions of stresses σ and strains ε are used in this work. Since displacement loads u_1 and u_2 were applied at the reference node C_1 , resulting applied stresses were defined by the reaction forces RF_1 and RF_2 at the node C_1 divided by the initial cross sectional area perpendicular to the nominal fiber direction A_1 i.e. $\sigma_{11}=RF_1/A_1$ and $\sigma_{12}=RF_2/A_1$ where $A_1=1.1412 \times 0.951 \text{ mm}^2$ for the models employed for development of the probabilistic failure envelopes. Similarly, strains were defined as the displacement of control node C_1 divided by the initial length in the nominal fiber direction L_1 i.e. $\varepsilon_{11}=u_1/L_1$ and $\varepsilon_{12}=u_2/L_1$ where $L_1=6.657 \text{ mm}$ for the model series used in the development of probabilistic failure envelopes. To calculate percentage strains, they were multiplied by the factor 100. For the sake of brevity, the peak load for the axial compression load case was given a special symbol i.e. $\sigma_{11}^c := \min(\sigma_{11})$.

6.1.2 Material model

As discussed in the state of the art in Section 2.6, homogenized approaches offer ease of modeling over larger sizes with lower computational effort when choosing from a variety of approaches available to model FRPs numerically for failure prediction under compression. The fiber orientation in homogenized approaches is usually represented via the vector of the preferred material axis at the integration point of a finite element. In the current work, the homogenized material was modeled using a transversely isotropic material model in which geometrical nonlinearities were accounted for using a co-rotational formulation [39]. The model is an extension of the small strain transversely isotropic material model for unidirectional FRPs [115] and provides a modified yield and plastic potential function definitions. Along with accounting for the geometrical nonlinearities, the modified model allows for an easier calibration of the yield surface and plastic potential function with the experimental data. The material model provides an explicit expression for the algorithmic consistent tangent moduli and has been implemented in the commercial software Abaqus. The details about mathematical formulation and numerical implementation of the material model can be found in the Ref. [39], also see [115]. For the sake of completeness, the constitutive formulation of the model is summarized below.

6.1.2.1 Constitutive formulation

The constitutive formulation of the anisotropic invariant-based model for FRPs is presented in this section. The constitutive model proposed here is a modification of the small strain model presented by Vogler et. al. [115]. The modifications include new forms of the yield and the plastic potential functions along with the inclusion of the geometrical nonlinearities in the model. It should be noted that the constitutive equations of the material model are formulated with respect to the co-rotational frame.

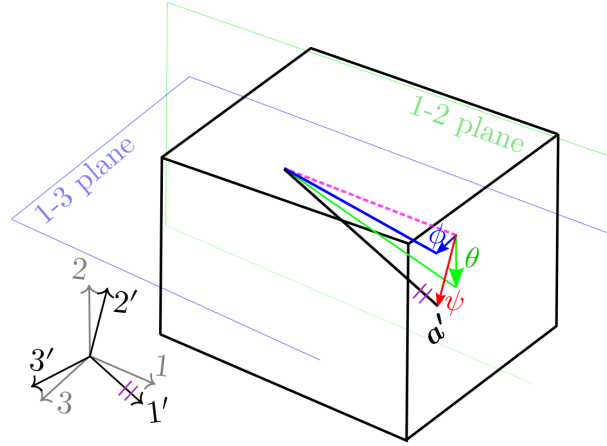


Figure 6.2: Schematic of a fiber (in black color) misaligned from the nominal fiber direction $\mathbf{1}$ to direction $\mathbf{1}'$

TRANSVERSELY ISOTROPIC FREE-ENERGY Transversely isotropic materials are characterized by a preferred direction vector \mathbf{a}' , which in case of FRPs is the fiber direction. This implies that the material response is invariant with respect to arbitrary rotations around the preferred direction \mathbf{a}' , to reflections at fiber parallel planes, and with respect to the reflection at the plane whose normal is \mathbf{a}' .

Fig. 6.2 shows a schematic of the preferred direction vector \mathbf{a}' in black with the initial in-plane misalignment θ and the initial out-of-plane misalignment ϕ contributing to the total initial misalignment ψ . Here the nominal, i.e. perfectly aligned fiber direction, corresponds to the $\mathbf{1}$ -direction.

From the modeling standpoint, the anisotropic mechanical response admits a tensor-based representation in the free energy definition through a second order structural tensor \mathbf{A}' in the rotated frame. The structural tensor represents the anisotropic material inherent structure and is defined as:

$$\mathbf{A}' := \mathbf{a}' \otimes \mathbf{a}' \quad (6.1)$$

where preferred direction vector \mathbf{a}' is in the rotated frame.

The total strain tensor $\boldsymbol{\varepsilon}$ is additively decomposed into elastic $\boldsymbol{\varepsilon}^e$ and plastic $\boldsymbol{\varepsilon}^p$ parts based on the hypothesis of the flow theory of plasticity as follows:

$$\boldsymbol{\varepsilon} = \boldsymbol{\varepsilon}^e + \boldsymbol{\varepsilon}^p \quad (6.2)$$

The existence of a Helmholtz free-energy function, $\Pi(\boldsymbol{\varepsilon}^e, \mathbf{A}', \boldsymbol{\omega})$, is assumed for the constitutive formulation. This free-energy is a function of the structural tensor \mathbf{A}' , the elastic strain $\boldsymbol{\varepsilon}^e$, and the internal variable set $\boldsymbol{\omega}$ that accounts for the inelastic material response along the deformation process:

$$\Pi(\boldsymbol{\varepsilon}^e, \mathbf{A}', \boldsymbol{\omega}) = \frac{1}{2} \boldsymbol{\varepsilon}^e : \mathbf{C}^e : \boldsymbol{\varepsilon}^e + \Pi^{\text{hard}}(\mathbf{A}', \boldsymbol{\omega}) \quad (6.3)$$

where \mathbf{C}^e is the constitutive elastic tensor and $\Pi^{\text{hard}}(\mathbf{A}', \boldsymbol{\omega})$ is the hardening part of the free-energy function due to plastic effects.

With the free energy function definition being available, the constitutive stress tensor $\boldsymbol{\sigma}$ is obtained as the first derivative of the free energy function with respect to the elastic strain tensor, while the elastic constitutive operator \mathbf{C}^e is defined as the second derivative of the free energy with respect to elastic strain tensor:

$$\boldsymbol{\sigma} := \frac{\partial \Pi}{\partial \boldsymbol{\varepsilon}^e} = \mathbf{C}^e : \boldsymbol{\varepsilon}^e \quad (6.4)$$

For transversely isotropic materials, the constitutive transversely isotropic elasticity tensor is represented as follows:

$$\mathbf{C}^e := \frac{\partial^2 \Pi}{\partial \boldsymbol{\varepsilon}^e \partial \boldsymbol{\varepsilon}^e} = \lambda \mathbf{1} \otimes \mathbf{1} + 2\mu_T \mathbb{I} + \alpha(\mathbf{1} \otimes \mathbf{A}' + \mathbf{A}' \otimes \mathbf{1}) + 2(\mu_L - \mu_T) \mathbb{I}_{A'} + \beta \mathbf{A}' \otimes \mathbf{A}' \quad (6.5)$$

where \mathbb{I} refers to the fourth-order identity tensor, whereas $\mathbb{I}_{A'} = A'_{im} \mathbb{I}_{jmkl} + A'_{jm} \mathbb{I}_{mikl}$, and λ , α , β , μ_T and μ_L are the elastic constants. Their definition and relationship to the engineering constants are given in Ref. [38].

THERMODYNAMICS CONSIDERATIONS The second-law of thermodynamics restricts the constitutive equations in the form of the Clausius–Duhem inequality. Under the assumption of isothermal deformations, this inequality reads the following for internal energy dissipation \mathcal{D}_{int} :

$$\mathcal{D}_{\text{int}} = \boldsymbol{\sigma} : \dot{\boldsymbol{\varepsilon}} - \dot{\Pi} \geq 0 \quad (6.6)$$

Recalling the previous definitions, the restriction over the internal dissipation implies:

$$\mathcal{D}_{\text{int}} = \boldsymbol{\sigma} : \dot{\boldsymbol{\varepsilon}}^p + \boldsymbol{\Gamma} * \dot{\boldsymbol{\omega}} \geq 0 \quad (6.7)$$

where $\boldsymbol{\Gamma}$ denotes the so-called hardening force and $*$ stands for any arbitrary product.

YIELD FUNCTION The elastic domain \mathbb{E} , assuming the maximum dissipation principle, is defined as:

$$\mathbb{E} = \{(\boldsymbol{\omega}, \bar{\boldsymbol{\varepsilon}}^p) \mid \mathcal{F}(\boldsymbol{\sigma}, \mathbf{A}', \bar{\boldsymbol{\varepsilon}}^p) \leq 0\} \quad (6.8)$$

where $\bar{\boldsymbol{\varepsilon}}^p$ identifies the equivalent plastic strain. The definition of the equivalent plastic strain in the present formulation is given by:

$$\bar{\boldsymbol{\varepsilon}}^p := \sqrt{\frac{1}{2}} \|\boldsymbol{\varepsilon}^p\| \quad (6.9)$$

The construction of a transversely isotropic yield surface $\mathcal{F}(\boldsymbol{\sigma}, \mathbf{A}', \bar{\boldsymbol{\varepsilon}}^p)$, which accounts for the pressure-dependency and plastic-inextensibility in FRPs along the fibre direction, yields:

$$\mathcal{F}(\boldsymbol{\sigma}, \mathbf{A}', \bar{\boldsymbol{\varepsilon}}^p) = \zeta_1 I_1 + \zeta_2 I_2 + \zeta_3 I_3 + \zeta_4 I_3^2 - 1 \leq 0 \quad (6.10)$$

I_i ($i = 1, 3$) are the stress invariants which symbolize the integrity basis of an isotropic tensor function representing a transversely isotropic response:

$$I_1 = \frac{1}{2}(\text{tr}[\boldsymbol{\sigma}^{\text{pind}}])^2 - \text{tr}[\mathbf{A}'(\boldsymbol{\sigma}^{\text{pind}})^2]; \quad I_2 = \text{tr}[\mathbf{A}'(\boldsymbol{\sigma}^{\text{pind}})^2]; \quad I_3 = \text{tr}[\boldsymbol{\sigma}] - \text{tr}[\mathbf{A}'(\boldsymbol{\sigma})] \quad (6.11)$$

where $\boldsymbol{\sigma}^{\text{pind}}$ is the plasticity-inducing stress:

$$\boldsymbol{\sigma}^{\text{pind}} := \boldsymbol{\sigma} - \frac{1}{2}(\text{tr}[\boldsymbol{\sigma}] - \mathbf{a}'\boldsymbol{\sigma}\mathbf{a}')\mathbf{1} + \frac{1}{2}(\text{tr}[\boldsymbol{\sigma}] - 3\mathbf{a}'\boldsymbol{\sigma}\mathbf{a}')\mathbf{A}' \quad (6.12)$$

Here, $\zeta_i(\bar{\boldsymbol{\varepsilon}}^p)$ ($i = 1, 4$) refers to four yield parameters which together with their corresponding invariants represent different loading states. A compact representation of the yield function takes the form:

$$\mathcal{F}(\boldsymbol{\sigma}, \mathbf{A}', \bar{\boldsymbol{\varepsilon}}^p) = \frac{1}{2}\boldsymbol{\sigma} : \mathbb{K} : \boldsymbol{\sigma} + \mathbf{L} : \boldsymbol{\sigma} - 1 \leq 0 \quad (6.13)$$

where

$$\mathbb{K} := \zeta_1 \mathbb{P}^{\text{pind}} + (\zeta_2 - \zeta_1) \mathbb{P}_{\mathbf{A}'}^{\text{pind}} + 2\zeta_4(\mathbf{1} - \mathbf{A}') \otimes (\mathbf{1} - \mathbf{A}'); \quad \mathbf{L} := \zeta_3(\mathbf{1} - \mathbf{A}') \quad (6.14)$$

where the operators \mathbb{P}^{pind} and $\mathbb{P}_{\mathbf{A}'}^{\text{pind}}$ are defined as:

$$\begin{aligned} \mathbb{P}^{\text{pind}} &= \mathbb{I} - \frac{1}{2}(\mathbf{1} \otimes \mathbf{1}) + \frac{1}{2}(\mathbf{A}' \otimes \mathbf{1} + \mathbf{1} \otimes \mathbf{A}') - \frac{3}{2}(\mathbf{A}' \otimes \mathbf{A}') \\ \mathbb{P}_{\mathbf{A}'}^{\text{pind}} &:= \mathbb{P}_{\mathbf{A}'ijkl}^{\text{pind}} = \mathbf{A}'_{im} \mathbb{P}_{mjkl}^{\text{pind}} + \mathbf{A}'_{mj} \mathbb{P}_{imkl}^{\text{pind}} \end{aligned} \quad (6.15)$$

In comparison to the six-parameter yield surface definition used in the earlier iteration of the model given in Ref. [115], this model considers a four-parameter yield surface. This allows for an easier calibration of the yield surface and reduces the experimental effort. Nevertheless, the six-parameter yield function definition regards a better description of biaxial stress states which is crucial for accurate modeling of FRPs undergoing high hydrostatic pressures. This was achieved in Ref. [115] via the case differentiation concerning the invariant I_3 based on its sign.

PLASTIC POTENTIAL FUNCTION To predict realistic plastic deformations, a non-associative flow rule is assumed. The construction of a non-associative transversely isotropic plastic potential function $\mathcal{G}(\boldsymbol{\sigma}, \mathbf{A}')$ yields:

$$\mathcal{G}(\boldsymbol{\sigma}, \mathbf{A}') = \zeta_1 I_1 + \zeta_2 I_2 + \zeta_3 I_3^2 - 1 \quad (6.16)$$

where ζ_i ($i = 1, 3$) denotes the plastic potential parameters. A condensed expression of the plastic flow potential is given by:

$$\mathcal{G}(\boldsymbol{\sigma}, \mathbf{A}') = \frac{1}{2} \boldsymbol{\sigma} : \mathbb{M} : \boldsymbol{\sigma} - 1 \leq 0 \quad (6.17)$$

where the fourth-order tensor \mathbb{M} is expressed as:

$$\mathbb{M} := \zeta_1 \mathbb{P}^{\text{pind}} + (\zeta_2 - \zeta_1) \mathbb{P}_{\mathbf{A}'}^{\text{pind}} + 2\zeta_3 (\mathbf{1} - \mathbf{A}') \otimes (\mathbf{1} - \mathbf{A}') \quad (6.18)$$

EVOLUTION EQUATIONS The evolution equations of the internal variables ($\boldsymbol{\varepsilon}^p$ and $\boldsymbol{\omega}$) are expressed as follows:

$$\dot{\boldsymbol{\varepsilon}}^p = \dot{\gamma} \frac{\partial \mathcal{G}(\boldsymbol{\sigma}, \mathbf{A}', \bar{\boldsymbol{\varepsilon}}^p)}{\partial \boldsymbol{\sigma}} = \dot{\gamma} \mathbf{n}_G = \dot{\gamma} \mathbb{M} : \boldsymbol{\sigma} \quad \text{with } \mathbf{n}_G = \mathbb{M} : \boldsymbol{\sigma} \quad (6.19)$$

$$\dot{\boldsymbol{\omega}} = \dot{\gamma} \frac{\partial \mathcal{G}(\boldsymbol{\sigma}, \mathbf{A}', \bar{\boldsymbol{\varepsilon}}^p)}{\partial \boldsymbol{\Gamma}} \quad (6.20)$$

where γ represents the so-called plastic multiplier. As customary, the Kuhn–Tucker loading/unloading conditions are defined by:

$$\dot{\gamma} \geq 0; \quad \mathcal{F}(\boldsymbol{\sigma}, \mathbf{A}', \bar{\boldsymbol{\varepsilon}}^p) \leq 0; \quad \dot{\gamma} \mathcal{F}(\boldsymbol{\sigma}, \mathbf{A}', \bar{\boldsymbol{\varepsilon}}^p) = 0 \quad (6.21)$$

and the consistency condition as:

$$\dot{\gamma} \dot{\mathcal{F}}(\boldsymbol{\sigma}, \mathbf{A}', \bar{\boldsymbol{\varepsilon}}^p) = 0 \quad (6.22)$$

PARAMETER IDENTIFICATION AND CALIBRATION In addition to the elastic material constants, the yield function parameters ζ_i ($i = 1, 4$) and the plastic potential parameters ζ_i ($i = 1, 3$) are to be determined. The parameters ζ_i ($i = 1, 4$) control the size and shape of the elastic domain \mathbb{E} as a function of the equivalent plastic strain variable $\bar{\boldsymbol{\varepsilon}}^p$. For each parameter, the relation $\zeta_i(\bar{\boldsymbol{\varepsilon}}^p)$ is determined from an independent experiment, thus a total of four different experiments is required for calibration. For instance, the following four experiments can be used for calibration: (i) in-plane shear test, (ii) transverse shear test, (iii) uniaxial transverse tension test, and (iv) uniaxial transverse compression test. The corresponding yield stress states are denoted as $\sigma_{is}^y, \sigma_{ts}^y, \sigma_{tt}^y$, and σ_{tc}^y , respectively. Similar to the procedure in [115], the four parameters $\zeta_i(\sigma_{is}^y, \sigma_{ts}^y, \sigma_{tt}^y, \sigma_{tc}^y)$ ($i = 1, 4$) can then be obtained by entering the stress states from each experiments above in Eq. 6.10 and setting the yield function state to yielding i.e., $\mathcal{F} = 0$. Accordingly, the coefficients ζ_i ($i = 1, 4$) are explicitly given in the following.

From the transverse shear test the first coefficient ζ_1 is expressed as:

$$\zeta_1 = \frac{1}{\sigma_{ts}^y 2} \quad (6.23)$$

and from the in-plane shear test the second coefficient ζ_2 is given by:

$$\zeta_2 = \frac{1}{\sigma_{ts}^y} \quad (6.24)$$

The third coefficient ζ_3 controls the tension-compression yield asymmetry and therefore is expressed in terms of the uniaxial transverse tension and uniaxial transverse compression tests as:

$$\zeta_3 = -\frac{1}{\sigma_{tc}^y} + \frac{1}{\sigma_{tt}^y} \quad (6.25)$$

Lastly, the coefficient ζ_4 is associated with transverse loading, hence is expressed as:

$$\zeta_4 = -\frac{1}{4\sigma_{ts}^y} + \frac{1}{\sigma_{tc}^y \sigma_{tt}^y} \quad (6.26)$$

To comply with the maximum dissipation principle, the convexity of the yield surface must be insured. This imposes the following restrictions to the relations $\zeta_i(\bar{\varepsilon}^p)$ ($i = 1, 4$) which must hold for any $\bar{\varepsilon}^p$:

$$\sigma_{tt}^y \leq \frac{4\sigma_{ts}^y}{\sigma_{tc}^y}. \quad (6.27)$$

Similarly, the parameters ζ_i ($i = 1, 3$) control the size and shape of the plastic potential surface. However, one of these parameters is a scaling parameter and can be set to any value since the size of the plastic potential has no inherent physical meaning. Accordingly, there are only two remaining parameters to be determined and to associate with experimental data. In the present case, ζ_1 is arbitrarily set to unity.

As mentioned above, the motive behind employing a non-associative plasticity scheme is to model realistic plastic deformation behavior as compared to associative plasticity, especially with regard to contractility/dilatancy effects resulting in different behavior under compression and tension as it is observed in fiber reinforced composites the identification of the so-called plastic Poisson coefficients. Hence, the evolution of the plastic strains is not governed by the gradient of the yield surface. Accordingly, the parameters ζ_i ($i = 2, 3$) are used to enforce certain plastic Poisson's ratios $\nu_{23}^p = \varepsilon_{22}^p / \varepsilon_{33}^p$ and plastic distortion behavior through the relation $\mu_{12}^p = \varepsilon_{12}^p / \varepsilon_{23}^p$:

$$\zeta_1 = 1 \quad (6.28)$$

$$\zeta_2 = \mu_{12}^p \quad (6.29)$$

$$\zeta_3 = \frac{-1 + \nu_{23}^p}{4(1 + \nu_{23}^p)} \quad (6.30)$$

ζ_1	ζ_2	ζ_3	ζ_4
0.00612503	0.00552784	0.00615730	0.00304666

Table 6.1: Yielding parameters ζ_i at the onset of yielding for the carbon fiber UD300/M79 epoxy material

ζ_1	ζ_2	ζ_3
1.0	1.0	-0.083333

Table 6.2: Plastic potential parameters ζ_i for the carbon fiber UD300/M79 epoxy material

Similarly, for the plastic potential function \mathcal{G} , the following must hold:

$$\mu_{12}^p \geq 0 \wedge -\frac{-1 + v_{23}^p}{4(1 + v_{23}^p)} \geq 0 \quad (6.31)$$

In contrast to the time-consuming iterative procedure presented in [115] for the determination of the plastic potential parameters, the aforementioned explicit expressions for the parameters are used. Using these expressions, the material model was calibrated for the material under consideration i.e. carbon fiber UD300/M79 epoxy. The elastic material properties are reported in Table 3.1. The yield function parameters ζ_i ($i = 1, 4$), that characterize the onset of yielding, were obtained by utilizing Equations (6.23)–(6.26) and are listed in Table 6.1. Furthermore, the plastic potential function parameters ζ_i ($i = 1, 3$) are provided in Table 6.2. These values were determined based on the plastic Poisson's ratio $v_{23}^p = 0.4$ and plastic distortion ratio $\mu_{12}^p = 1.0$. Due to the lack of experimental data concerning the transverse shear and the uniaxial transverse compression for the material under consideration, reasonable assumptions were made for the corresponding parameters based on the experimental data of similar class of materials available in the literature [66].

6.1.2.2 Abaqus limitation

Since the numerical modeling was performed in the commercial software Abaqus, it was important to ensure that the model is able to represent the large rotations observed in unidirectional FRPs when loaded under compression. Wisnom [133] highlighted a limitation of using a homogenized material representation for FRPs in the commercial software Abaqus. By default, Abaqus ignores the effect of shear strains on the material axes rotation. It considers the material axes rotation to be identical with the in-plane $\Delta\theta^i$ and the out-of-plane $\Delta\phi^i$ rigid body rotations. Since the effect of shear strains on the material axes rotation during loading is crucial in case of compression, the default implementation in Abaqus gives inaccurate results. To overcome this problem, the material model from Ref. [39] presented above was modified to account for the rotation of the material axes due to shear strains. The shear strains $\varepsilon_{12}^i = \gamma_{12}^i/2$

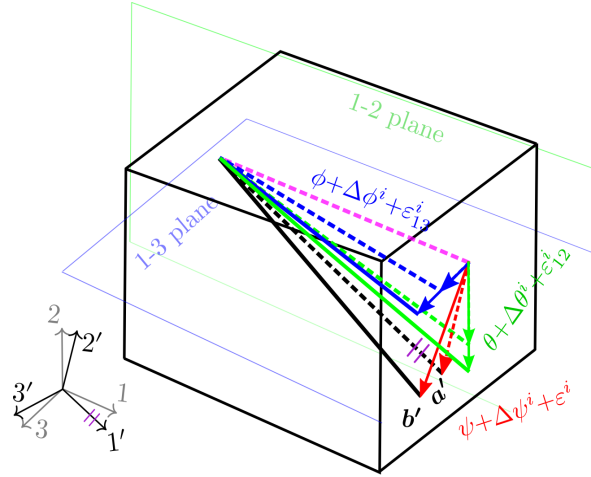


Figure 6.3: Generalized schematic of the deformed preferred direction in an element of a FE model. Dotted black line illustrates the preferred direction of the misaligned fiber \mathbf{a}' before the rigid body rotations and the shear rotations. The solid black line depicts the preferred direction of the misaligned fiber \mathbf{b}' after applying the combined effect of the in-plane $\Delta\theta^i$ and the out-of-plane $\Delta\phi^i$ rigid body rotations and the shear rotations ε_{12}^i and ε_{13}^i .

and $\varepsilon_{13}^i = \gamma_{13}^i / 2$ from the previous load step i were considered as Euler angle rotations. The preferred direction \mathbf{a}' of the fibers in the misaligned frame $\mathbf{1}' - \mathbf{2}' - \mathbf{3}'$ is given by Eq. 6.32a. The preferred direction \mathbf{a}' was rotated further by the shear strains to \mathbf{b}' via Eq. 6.32b. Fig. 6.3 depicts the misaligned fiber before shear rotations as \mathbf{a}' and after applying shear rotations as \mathbf{b}' .

$$\mathbf{a}' = [1 \quad 0 \quad 0] \quad (6.32a)$$

$$\mathbf{b}' = [\cos(\varepsilon_{12}^i) \cdot \cos(-\varepsilon_{13}^i) \quad \cos(-\varepsilon_{13}^i) \cdot \sin(\varepsilon_{12}^i) \quad -\sin(-\varepsilon_{13}^i)] \quad (6.32b)$$

6.1.2.3 Model verification

A verification investigation of the material model using a FE model loaded under axial compression load (0° load case) against the prediction using the Budiansky's analytical model [21] was carried out. For ease of understanding, Budiansky's analytical model is presented again below in Eq. 6.33. The analytical model predicts compression strength σ_{11}^c given the initial in-plane misalignment ψ and the nonlinear shear behavior of the material $\sigma_{12}(\gamma_{12})$.

$$\sigma_{11}^c = \max_{\gamma_{12}} \left(\frac{\sigma_{12}(\gamma_{12})}{\psi + \gamma_{12}} \right) \quad (6.33)$$

The FE model representing a homogenized fiber matrix composite consisted of a single C3D20 element in commercial software Abaqus, cf. Fig. 6.4a. The initial misalignment was given as the material axis orientation. To suppress rigid body motions

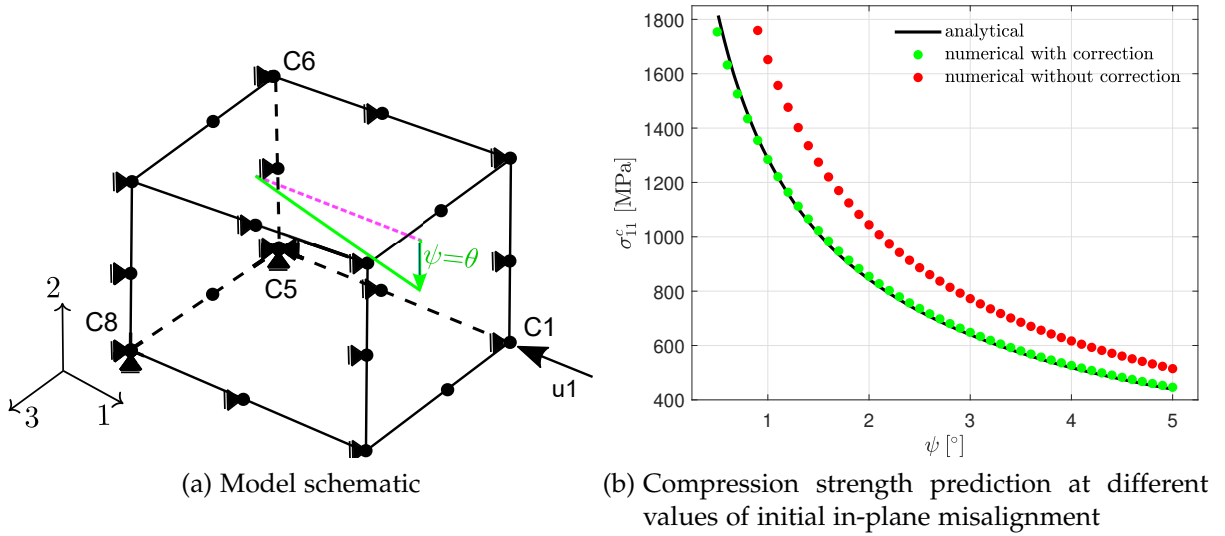


Figure 6.4: Compression strength prediction of a single element model against the prediction using the analytical model. The results in (b) show that the prediction using the FE model with the aforementioned shear rotation correction of the material model shows a very good match with the prediction of the analytical model. This result verifies the accuracy of the FE model for prediction of compression strength, hence, it can be employed for later analyses incorporating complex topologies of the fiber misalignment.

in the FE model, corner node C5 was constrained in all directions and corner node C8 and C6 were fixed in both transverse directions and in-plane transverse direction only, respectively. The axial compression load was applied in the form of displacement $u1$ at the corner node C1. Node C1 was coupled to the whole of the right surface, therefore, the load applied on node C1 got transferred to whole of the right surface. Periodic boundary conditions were applied in the 1 and the 2 directions. Displacements were not allowed in the 3 direction to replicate the in-plane conditions of the Budiansky's analytical model. Since Budiansky's model only accounts for the in-plane misalignment, the verification investigation was carried out for a range of the initial in-plane misalignment i.e. $\psi = \theta$, $\phi = 0$. Fig. 6.4b shows the predictions of Budiansky's analytical solution given in Eq. 2.2b along with the numerical predictions from the single element model. It can be seen that the numerical model over-predicted strength by a significant amount without the aforementioned correction of the material axis rotation, whereas the shear rotation corrected model shows very good prediction in comparison to the analytical model. This results verifies the applicability of the FE model incorporating the shear rotation corrected material model for the prediction of compression strength. Hence, this modeling scheme can be used for numerical analyses to develop failure envelopes in which the realistic topologies of the fiber misalignment are used.

6.2 RESULTS AND DISCUSSION

Results of numerical modeling under axial compression and combined compression-shear will be discussed in this section. Firstly, simple homogenized models containing single sine waves as the misalignment in 2D and 3D will be discussed to highlight the importance of 3D modeling. This is followed by a comparison of different model series containing the realistic modeling of the misalignment using the spectral representation method under the axial compression load. Once a model series has been selected to be representative, a comparison of different load cases on a selected realization is presented. Afterwards, numerically developed failure envelopes in stress and strain space are presented. The chapter is rounded off with a discussion on the use of an empirical function form of the spectral density for model generation.

6.2.1 Effect of the misalignment dimensionality on prediction of the compression strength

The deficiencies of characterizing the real 3D fiber misalignment into 2D were discussed in Section 4.1.2. It was shown that the generated 2D fields cannot capture the complete information of the fiber misalignment of the real structures and materials, cf. Section 4.2.2. In order to show the effect of the fiber misalignment dimensionality on the strength prediction, a comparative analysis using simple 2D and 3D models containing simple sinusoidal undulation only are considered here.

Four models, two in 2D with 4×2 mm dimensions and two in 3D with $4 \times 2 \times 2$ mm dimensions, were generated for the purpose of comparing the effect of underlying undulation dimensionality on prediction of the compression strength. The first 2D model contains a single sine wave undulation, in which the undulation is dependent on 1-direction only. This was achieved by only sampling a single harmonic in the input spectral density at the fundamental frequency, i.e. the wavelength is equal to the model length in that particular direction. The resulting contour plot of the undulation is shown in Fig. 6.5a. The second 2D model contains an undulation with two sine waves, each with the fundamental frequency in that particular direction, and the resulting contour plot of the undulation is shown in Fig. 6.5b. Both 2D models contained periodic boundary conditions in directions 1 and 2. A compression load in the form of displacement was applied in 1-direction.

The first 3D model also contains a 2D undulation i.e. it contains fundamental frequency sine waves in direction 1 and 2, see Fig. 6.5c. The second 3D model contains a fully three dimensional undulation with a fundamental frequency sine wave in each direction. The resulting contour plot of the undulation is shown in Fig. 6.5d. The undulation of both 3D models are given as the in-plane misalignment in the FE models for a direct comparison with the 2D models. The 3D models contained periodic boundary conditions in directions 1 and 2 and compression load in the form of displacement was applied, whereas no displacements were allowed in 3 to obtain the in-plane con-

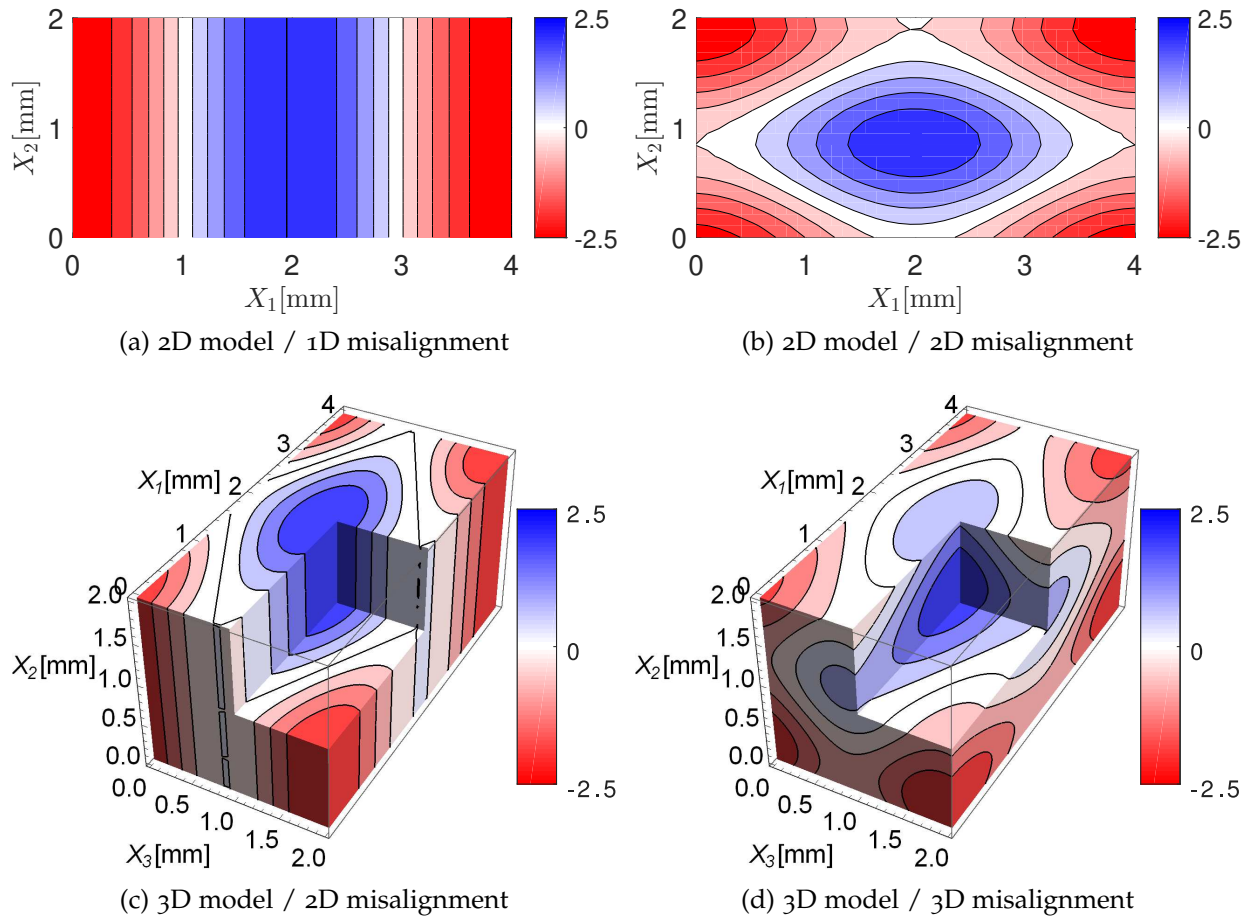


Figure 6.5: Contour plots of 1D and 2D sine waves for 2D modeling, and 2D and 3D sine waves for 3D modeling of the in-plane misalignment angle θ . The maximum misalignment in each case is 2.5° and the minimum misalignment in each case is -2.5° .

Model	Ξ^θ [$^\circ^2$] or [$^\circ^3$]	s^θ [$^\circ$]	$\max \theta $ [$^\circ$]
2D model with 1D sine wave	0.6355	1.7720	2.5
2D model with 2D sine wave	0.3178	1.2532	2.5
3D model with 2D sine wave	0.1012	1.2532	2.5
3D model with 3D sine wave	0.0674	1.0221	2.5

Table 6.3: Statistics of the fiber misalignment angles and the corresponding spectral parameters. The mean value in all cases is 0° . Mean square spectral density Ξ^θ is a measure of fiber misalignment in frequency domain, and it is directly proportional to square of the standard deviation s^θ of the misalignment angle θ , cf. Eq. 4.12.

ditions in the FE models for a direct comparison with the aforementioned 2D models. The maximum and minimum value of the angle in the undulation in all the models are 2.5° and -2.5° , respectively. The mean value in all the models is 0° . The corresponding statistics of the fiber misalignment angles and the spectral densities of each of the four models are given in Table 6.3.

The resulting stress-strain behavior of all four models are plotted in Fig. 6.6. Strength prediction using the Budiansky's analytical model given in Eq. 2.2b with an initial misalignment angle of 2.5° is also plotted as a dotted line in Fig. 6.6. The analytical model considers a single angle with a unidirectional undulation commonly known in literature as the infinite band assumption. Solving the maximization problem of the analytical model with the given initial misalignment angle and the experimentally characterized shear behavior of the material, the strength prediction turns out to be 721 MPa. The result of the 2D model with a 1D sine wave coincides with the prediction of the analytical model, as it resembles the misalignment assumptions of the analytical model. Counter-intuitively, the 2D model with same maximum and minimum values of the misalignment angle, i.e. the 2D model with a 2D undulation shows an increase in strength with a value of 1051 MPa. Similarly, 3D model with an in-plane 2D undulation and in-plane boundary conditions shows an equivalent prediction with a value of 1063 MPa to the 2D model with a 2D undulation. The 3D model with an in-plane 3D undulation and in-plane boundary conditions shows the stiffest response among four models with a strength value of 1326 MPa. The higher strengths of the models with a higher dimensional misalignment albeit with the same absolute value of the maximum angle can be understood from the statistics of the misalignment. The standard deviations s^θ of the misalignment angle from the models containing higher dimensional wave are smaller whereas mean value of misalignment angle in all the models is zero. This is due to the fact that a misaligned region with different waves contributing to it results in a smaller region in space as seen in Fig. 6.5d. In spatial sense, it means that only a few fibers are misaligned with a bigger portion of straight fibers providing support around the misaligned region. This shows that the use of absolute maximum value of angle alone for the prediction has significant drawbacks. Other factors such as the standard deviation s^θ of the misalignment angle θ and the mean square of the spectral density Ξ^θ also needs to be taken into account. Moreover, these results again highlight the limitations of modeling the misalignment in FRPs in 2D, and point towards the need for realistic modeling where the misalignment topologies contain 3D characteristics.

6.2.2 Comparison of compression strength prediction of 3D numerical models

In order to find the characteristic model series for further investigations of the probabilistic failure envelopes, three model series were first investigated. Each model series contained 250 realizations. Each model series was derived from a different measurement of the fiber misalignment. The first series contained misalignment topologies

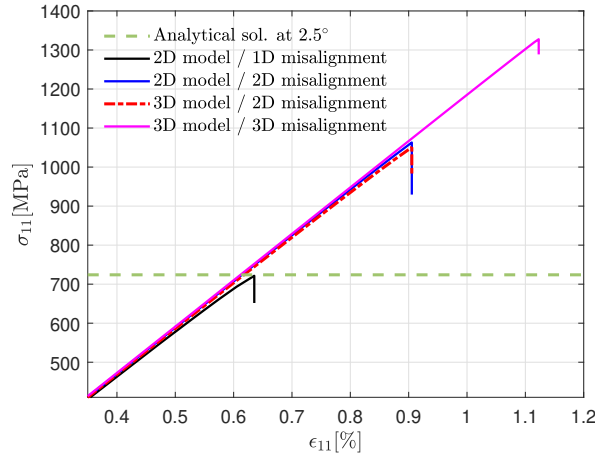


Figure 6.6: Comparison of results for compression strength σ_{11}^c from 2D and 3D models each containing a sinusoidal undulation with 1D, 2D and 3D characteristics

generated from the calculated in-plane and the calculated out-of-plane spectral densities of the specimen 1. Similarly, the second series was based on the spectral densities of the specimen 2. The averaged spectral densities shown in Fig. 4.3c and Fig. 4.3f were used to create the third series of models. Monte Carlo analysis was performed on each series for the failure prediction under the axial compression load.

The peak loads under axial compression σ_{11}^c for each series are plotted in the form of empirical probability of survival $P(\sigma_{11}^c)$ in Fig. 6.7. These empirical distributions were fitted with the 2-parameter Weibull distribution given in Eq. 6.34 using the maximum-likelihood method and are also plotted in Fig. 6.7. The shape parameter m and the scale parameter R_o of the Weibull distribution obtained from the fittings are reported in Table 6.4. As the names suggest, the scale parameter R_o defines the width of a Weibull distribution and the shape parameter m (also known as Weibull slope) defines the shape of a Weibull distribution. A positive value of m indicates an increasing failure rate with an increase of the applied load σ_{11} . Models derived from the measurements of specimen 1 ($s1$) and specimen 2 ($s2$) show significant difference in the mean probability of survival, although the spread of the failure distributions seems quite similar. Statistics of corresponding means and standard deviations s are also given in Table 6.4. The difference in the mean values of the compression strengths σ_{11}^c is approximately 180 MPa whereas the standard deviation values of both model series differ only by 6 MPa. The mean values of the fiber misalignment angles $\theta_{k,l,m}$ and $\phi_{k,l,m}$ for all model series are 0° . Although standard deviation of the in-plane misalignment $\theta_{k,l,m}$ of specimen 2 given in Table 4.2 is larger than that of specimen 1, the stronger response of FE model from specimen 2 can be attributed to the lower standard deviation of the out-of-plane misalignment $\phi_{k,l,m}$ compared to that of specimen 1. Since the FE models were not constrained in direction 3, the out-of-plane misalignment has a stronger influence on the strength prediction. The strength prediction of FE models derived from the average (*avg*) spectral densities of the fiber misalignment

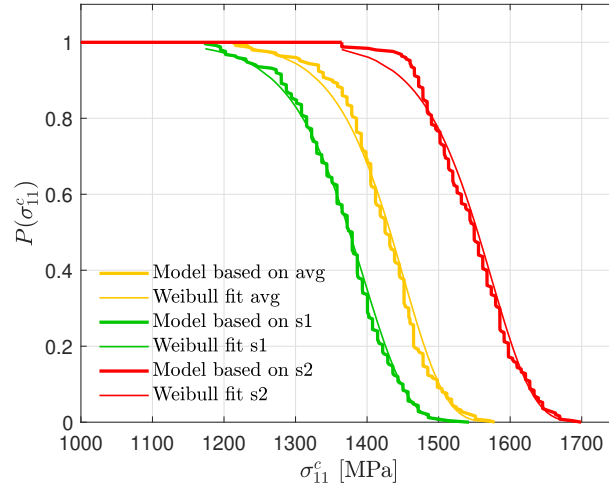


Figure 6.7: Empirical probability of survival $P(\sigma_{11}^c)$ over the compression strength σ_{11}^c along with the fitted 2-parameter Weibull distributions

	Mean [MPa]	s [MPa]	scale R_o [MPa]	shape m [-]
Model based on <i>avg</i>	1424.54	61.96	1452.96	25.77
Model based on <i>s1</i>	1366.64	66.52	1397.12	23.38
Model based on <i>s2</i>	1546.66	60.55	1575.50	27.52

Table 6.4: Statistics of the axial compression strengths σ_{11}^c for different numerical models

lie in-between the results of the other two models, as expected. With availability of further scans and corresponding spectral data, the results of the (*avg*) model could be further refined to be a better average response of the material. For further discussions, only the *avg* model will be considered.

$$P(\sigma_{11}^c) = \exp \left[- \left(\frac{\sigma^c}{R_o} \right)^m \right] \quad (6.34)$$

6.2.3 Stress-strain behavior of representative models under axial compression and combined compression shear

As mentioned in Section 6.1.1, failure was defined as the peak load carrying capacity and the solution process was terminated just past the peak load. It is of interest to see the stress-strain response up to the peak load under different combined load cases. Fig. 6.8 shows model responses for a realization from each load case. Since the model showed a distinct peak and a sudden drop afterwards in all load cases, failure in all load cases is categorized as the MB failure. Although the ratios of the applied displacements u_2/u_1 are constant, the resulting reaction forces (stresses) have

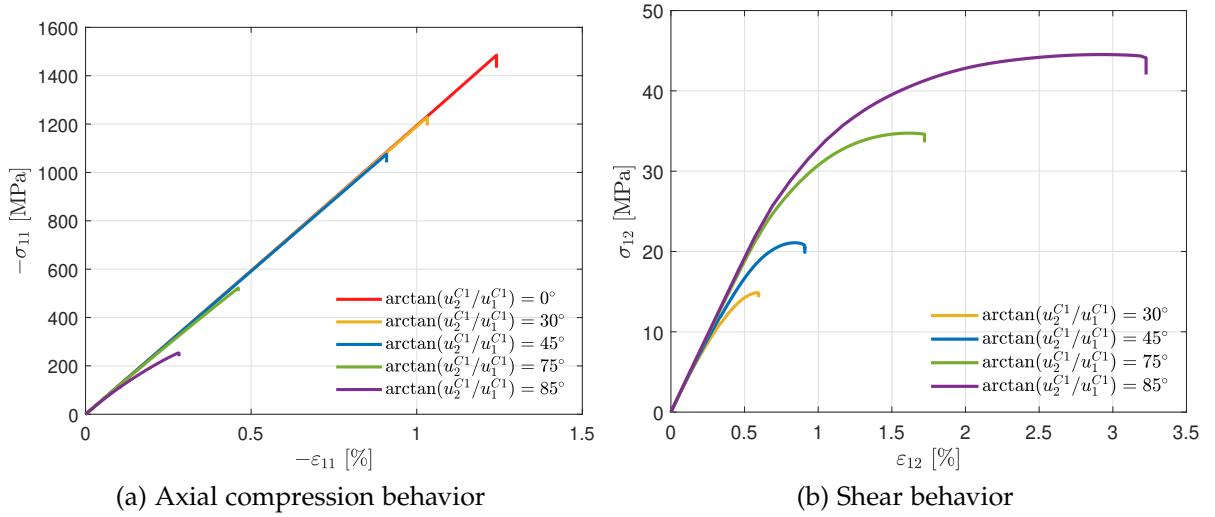


Figure 6.8: Stress strain response of the model

a nonlinear relationship because of the underlying differences in the material and the geometrical response of the laminate. The response in the global axial direction σ_{11} - ε_{11} was essentially linear up to peak load except in load case 85° , in which case the applied axial displacement (strain) was negligible compared to the shear counterpart. The shear response σ_{12} - ε_{12} was initially linear, but eventually became nonlinear in all load cases. There was no applied shear in the 0° load case, hence no resulting shear curve. The amount of shear nonlinearity in the shear response depends on the ratio of the applied shear displacements to the applied axial displacements i.e. the higher the amount of the applied shear, the higher the shear nonlinearity before the ultimate failure. This result shows that the shear response of the material is nonlinear not only at the local level i.e. material points, but also at the global level.

Just like the responses in the global axial direction σ_{11} - ε_{11} , the global shear responses σ_{12} - ε_{12} also show a sudden drop after the peak load, see Fig. 6.8b. In all the cases, the maximum value of shear stresses is well below the ultimate shear strength value of 77.11 MPa, hence, matrix fracture can be ruled out as the cause of the drop in stress. Matrix fracture might happen post peak, however, post peak response was not modeled in this investigation. Similarly, splitting failure is also not modeled as it is not expected to occur in high fiber volume fraction FRPs loaded homogeneously under compression dominated loads.

6.2.4 Probabilistic failure envelope in stress space using numerical modeling

The model series based on the *avg* spectral density was used to develop numerical failure envelopes in the σ_{11} - σ_{12} plane. Similar to the axial compression load case, 250 realizations each were carried out for all load cases in order to sample the σ_{11} - σ_{12} space. The resulting failure stresses of all realization are plotted in Fig. 6.9 as black

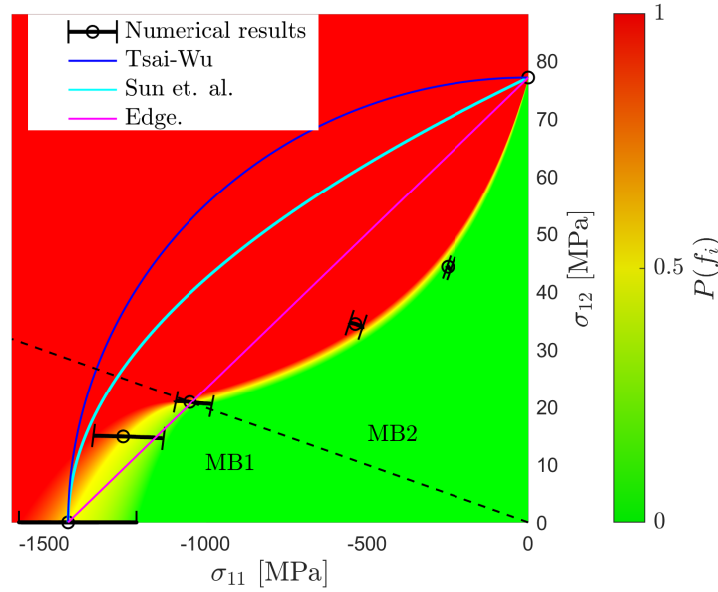


Figure 6.9: Probabilistic failure envelope in stress space. Results of all realizations from each load case are plotted as black dots which fuse to form curve segments. The median of each load case is shown with hollow circles on the curve segments. The envelope was divided into two regions and functional forms of failure envelopes were defined for each region. A dashed line, which passes through median value of load case 45° , shows division between failure envelope regions MB1 and MB2. Using the functional forms of MB1 and MB2 given in Eq. 6.35a and Eq. 6.35b, a color code depicting the probability of failure $P(f_i)$ is plotted.

dots denoting the respective far field stress coordinate at the instant of failure. In this instant, both the compression and the shear stresses attain their peak values and collapse is initiated, cf. Fig. 6.8. Because of the large number of realizations, the dots fuse to form a curve segment. Perpendicular bars at the ends of the curve segments denote the span between the lowest and the highest strength of the corresponding load cases. The median values of each load case are highlighted by hollow circles. The highest spread was shown by the axial compression case with a median value $\sigma_{11}^c = 1424.54$ MPa and a standard deviation value $s = 61.96$ MPa. Overall, the spread of failure stresses reduced with increasing values of applied shear and finally became deterministic when reaching the shear axis. This behavior is expected in unidirectional FRPs, since only compression behavior is dependent on misalignment. The value of the ultimate shear strength is 77.11 MPa, which was taken from the mean curve of the shear characterization tests given in Fig. 3.2a.

It is apparent from the failure strengths in the σ_{11} - σ_{12} plane that the envelope denoting MB failure can be divided into two regions. Hence, a division was made at load case $\arctan(u_2/u_1) = 45^\circ$ as shown by the dotted line in Fig. 6.9. MB1 is the compression dominated failure region and spans from pure axial compression until $\arctan(u_2/u_1) = 45^\circ$. On the other hand, MB2 is the shear dominated region and

	a_i	b_i	c_i
1 st percentile	-1.0525e-06	-0.00210	-0.01303
Median	-1.0712e-06	-0.00222	-0.01291
99 th percentile	-1.0748e-06	-0.00233	-0.01296

Table 6.5: Fit parameters of 6.35 for 1st, 50th (median) and 99th percentile of distribution of the failure envelope in the σ_{11} - σ_{12} plane

spans from $\arctan(u_2/u_1) = 45^\circ$ until the pure shear failure. The change in the behavior of the failure envelope can be attributed to the ductile behavior under far field applied shear stress compared to the brittle behavior under the far field applied pure axial compression stress. Functional forms of the failure envelope, which were defined by the authors for both regions MB1 and MB2 of the numerical results, are given in Eq. 6.35. Parameters for both regions of the failure envelope for 1st, 50th (median), and 99th percentiles are provided in Table 6.5.

$$f_i^{MB1}(\sigma_{11}, \sigma_{12}) = \sigma_{12} - a_i \sigma_{11}^2 - b_i \sigma_{11} + 1 \quad (6.35a)$$

$$f_i^{MB2}(\sigma_{11}, \sigma_{12}) = \sigma_{11} \sigma_{12} + c_i \sigma_{12} + 1 \quad (6.35b)$$

The i^{th} percentile of the distribution of failure is reached when the function $f_i^{MB1/MB2}(\sigma_{11}, \sigma_{12})$ becomes zero. To aid the understanding, a color code illustrating the probability of failure $P(f_i)$ is plotted in Fig. 6.9. Well below 1st percentile of distribution of failure, the material is considered safe and hence, the color code is green. The color changes gradually from green to yellow until the 50th percentile of the distribution of failure. The yellow color code depicts median strength, i.e. $P(f_i) = 0.5$. The color changes again gradually from yellow to red from the 50th percentile of the distribution of failure onward. The red color above $P(f_i) = 0.99$ denotes a stress state that is considered highly likely to result in failure. It is to be noted that the uncertainty of failure in the region MB1 is of the foremost interest here. In region MB2 failure is almost deterministic, since the transition from $P(f_i) \approx 0$ to $P(f_i) \approx 1$ is very rapid. The functional form (Eq. 6.35b) of the failure envelope in region MB2 is motivated by mathematical simplicity and the data points for load cases $\arctan(u_2/u_1) = 75^\circ$ and $\arctan(u_2/u_1) = 85^\circ$ are intercepted only approximately.

For comparison purposes, classical deterministic failure envelopes by Edge [41], Tsai-Wu [77], and Sun [107] are also plotted. These classical failure envelopes consider microbuckling failure under pure axial compression and shear driven matrix cracking failure under pure shear. The region of combined compression-shear load is generally mathematically interpolated between the compression strength and the shear strength in these classical failure envelopes. For illustrating the deterministic failure envelopes in Fig. 6.9, these envelopes were calibrated using the median value

of the axial compression strength from the *avg* numerical model and the ultimate shear strength. The quadratic failure envelopes by Tsai-Wu [77] and Sun [107] are non-conservative which is more prominent near the ultimate shear strength. The linear interaction proposed by Edge [41] is closer to the numerical prediction, however, it can not predict the changes in the shape of the envelope. Generally, failure envelopes or yielding envelopes are meant to be convex to satisfy Drucker's postulate [51] such as the classic failure envelopes shown from literature in Fig. 6.9. These definitions are based on either the activation of a failure mode or the start of yielding. Here, however, the numerically defined envelope denotes ultimate failure and exhibit non-convex shape. For pure compression load case, the initiation of nonlinearity and the ultimate failure are quite close, see Fig. 6.8a. Conversely, there is a large difference between the initiation of nonlinearity and the ultimate failure for the shear dominated loading, see Fig. 6.8b. Moreover, some examples of materials exhibiting non-convex failure or yield envelopes can be found in the literature [128].

It is to be stated that the numerically developed failure envelope is valid for the model size $V_{model}=6.657 \times 1.1412 \times 0.951$ mm which was determined by the scanned volumes of the specimens on which both the in-plane misalignment and the out-of-plane misalignment were measured. The shear strength is deterministic and does not change with size as is not affected by the fiber misalignment. Compression strength on the other hand, is uncertain and scales based on size as will be explained in the next chapter. Assuming the shape of the failure envelope is the same over different sizes and only compression axis scales with the Weibull scaling, one can generate failure envelopes for other model sizes by simply scaling the strength under the pure axial compression load. To verify whether the shape of the failure envelope stays the same for scaled sizes, the simulations would need to be repeated given that the misalignment data for larger volumes is available.

6.2.5 Probabilistic failure envelope in strain space using numerical modeling

Similar to failure envelope in the σ_{11} - σ_{12} plane, a probabilistic failure envelope in the ε_{11} - ε_{12} plane is presented. Failure strains of all realizations of the *avg* model from all load cases are plotted as black dots in Fig. 6.10. Because of the large number of realizations, the dots merge to form lines. These lines are straight, unlike the slightly curved segments in stress space, because of the constant ratio of applied strains for each load case. Perpendicular lines to the results' lines are drawn to highlight the maximum and minimum failure strains of each load case. The median values for each load case are highlighted by hollow circles. Again, the spread was highest for the axial compression load case and gradually diminished with the increasing amount of the applied shear. The ultimate failure strain for pure shear with a value of 9.57[%] was taken from the results of the shear characterization tests given in Fig. 3.2a. Similar to the σ_{11} - σ_{12} failure envelope, a division of the ε_{11} - ε_{12} envelope into two region was

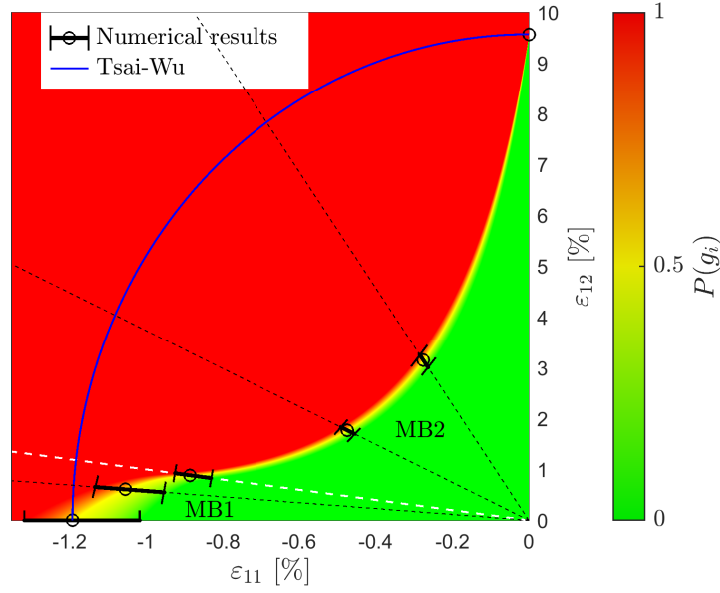


Figure 6.10: Probabilistic failure envelope in strain space. Failure strains of all realizations from each load case are plotted as black dots which fuse to form line segments. The median of each load case is shown with hollow circles. The failure envelope in strain space was divided into regions MB1 and MB2 by a white dashed line passing through the median value of load case 45° . The black dashed lines depict the loading direction of load cases $\arctan(u_2/u_1)=30^\circ, 75^\circ$, and 85° . A color code depicting the probability of failure $P(g_i)$ is plotted using the functional forms of MB1 and MB2 given in Eq. 6.36a and Eq. 6.36b.

made. Functional forms of the ε_{11} - ε_{12} failure envelope, which were defined for both regions MB1 and MB2 of the numerical results, are given in Eq. 6.36.

$$g_i^{MB1}(\varepsilon_{11}, \varepsilon_{12}) = \varepsilon_{12} - p_i \varepsilon_{11}^2 - q_i \varepsilon_{11} + 1 \quad (6.36a)$$

$$g_i^{MB2}(\varepsilon_{11}, \varepsilon_{12}) = \varepsilon_{11} \varepsilon_{12} + r \varepsilon_{12} - s_i \varepsilon_{11}^2 - t_i \varepsilon_{11} + 1 \quad (6.36b)$$

Parameters, for fitting the numerical results to Eq. 6.36 defining both regions of the envelope for 1^{st} , 50^{th} (median), and 99^{th} percentiles, are provided in Table 6.6. The i^{th} percentile of distribution of failure is reached when the function $g_i^{MB1/MB2}(\varepsilon_{11}, \varepsilon_{12})$ becomes equal to zero. Using these percentiles of the distribution of failure, a color code for the probability of failure $P(g_i)$ is given with a gradual change of color from green to yellow and yellow to red.

The shape of the ε_{11} - ε_{12} envelope is similar to the σ_{11} - σ_{12} failure envelope, however, the MB2 portion of strain based envelope is more elongated. It can be traced back to the strongly nonlinear behavior of the laminate under pure shear, see Fig. 3.2a. The difference of the strains from start of yielding till failure in pure shear is higher

	p_i	q_i	r	s_i	t_i
1 st percentile	-1.5522	-2.5619	-0.1045	-0.7215	-1.2785
Median	-1.4859	-2.6102		-0.8222	-1.3991
99 th percentile	-1.5234	-2.7658		-0.8135	-1.4080

Table 6.6: Fit parameters of Eq. 6.36 for 1st, 50th (median) and 99th percentile of distribution of the failure envelope in the ε_{11} - ε_{12} plane

than the difference of the corresponding stresses. These differences are apparently transferred to the failure envelopes under combined compression-shear loads. For comparison with classical failure criteria, the strain based variant of the classical Tsai-Wu failure criterion is also plotted in Fig. 6.10. The Tsai-Wu failure criterion considers microbuckling failure under axial compression, shear driven matrix cracking failure under pure shear, and a mathematical interpolation between these compression and shear strengths. The overestimation of the Tsai-Wu analytical failure criterion is even more so in the ε_{11} - ε_{12} plane as seen in Fig. 6.10. This is because of the consideration of only the ultimate failure stress/strain values in analytical formulations, and lack of consideration of the effects of fiber misalignment on failure under combined load cases. These limits were not reached in the numerical analysis of combined load cases, and MB failure occurred before any of the ultimate limits was reached.

6.2.6 Assumption of functional forms for spectral densities

Previous authors considered the idea of a functional form of spectral density for generating virtual distributions of the fiber misalignment. Herein, the previous assumptions in 1D by Slaughter et. al. [100] and 2D by Liu et. al. [76] are extended to 3D. Moreover, some further aspects of such an assumption for the spectral density are explored.

SPECTRAL DENSITY FUNCTIONS: Two forms of spectral density were considered namely, the square function S_{square} given in Eq. 6.37 and the exponential function S_{exp} given in Eq. 6.38.

$$S_{square} = S(\omega_1, \omega_2, \omega_3) = \begin{cases} S_o & \text{if } |\omega_1| \leq \omega_{c1} \text{ and } |\omega_2| \leq \omega_{c2} \text{ and } |\omega_3| \leq \omega_{c3} \\ 0 & \text{if } |\omega_1| > \omega_{c1} \text{ or } |\omega_2| > \omega_{c2} \text{ or } |\omega_3| > \omega_{c3} \end{cases} \quad (6.37)$$

$$S_{exp} = S(\omega_1, \omega_2, \omega_3) = \exp - \left(\left(\frac{\omega_1}{\omega_{c1}} \right)^2 + \left(\frac{\omega_2}{\omega_{c2}} \right)^2 + \left(\frac{\omega_3}{\omega_{c3}} \right)^2 \right) \quad (6.38)$$

where ω_{c1} , ω_{c2} , and ω_{c3} are the cutoff frequencies in direction **1**, **2**, and **3**, respectively. The spectral density functions were scaled by the parameter S_o , called the ini-

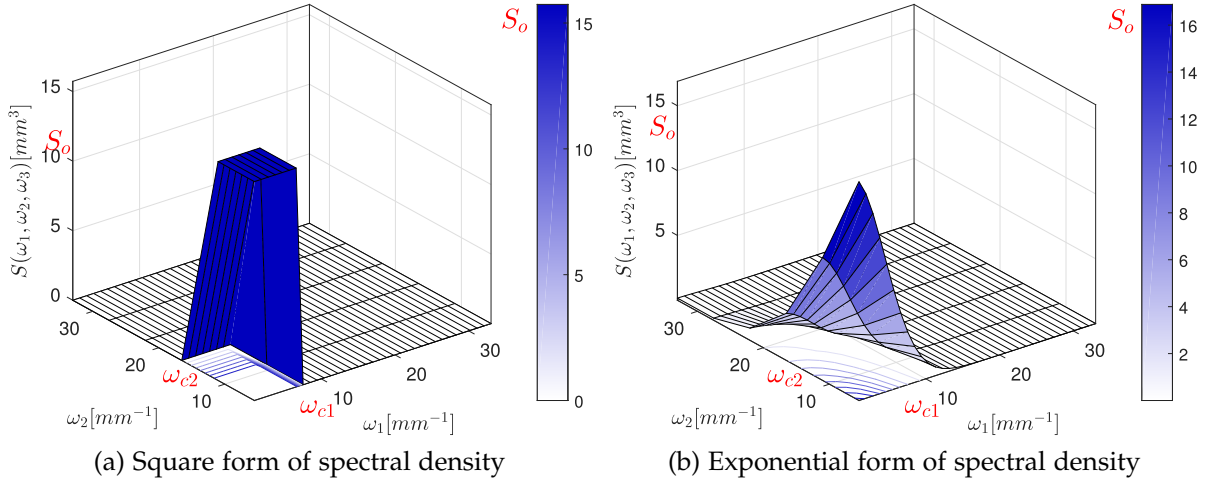


Figure 6.11: Plots of assumed functional forms of spectral densities. The figures show spectral densities in plane $\omega_1 - \omega_2$ with anisotropic cutoff values of the frequencies i.e. ω_{c1} not equal to ω_{c2} . The cutoff frequencies as well as the initial value of spectral density are also marked in the figures. In these figures $\omega_3=0$, and is disregarded to allow 3D plots.

tial spectral density. The mean square of the spectral density was used for comparing S_{square} and S_{exp} based models with each other, and the subsequent comparison with the *avg* spectral density based model driven from the CT measurements of the fiber misalignment. A section of the spectral density functions in plane $\omega_1 - \omega_2$ with anisotropic cutoff values of the frequencies, i.e. where ω_{c1} was not equal to ω_{c2} , are illustrated in Fig. 6.11. The fundamental difference between the square and the exponential forms of the spectral density can be observed in Fig. 6.11a and Fig. 6.11b. The square form gave an equal weightage to all the underlying frequencies (wavelengths) in the virtually generated topologies of the fiber misalignment. On the other hand, the exponential form of spectral density gave a higher weightage to smaller frequencies (larger wavelengths) in virtually generated topologies of the misalignment, which appears closer to the experimentally characterized spectral density given in Section 4.1.1.

MODELS BASED ON FUNCTIONAL FORMS OF SPECTRAL DENSITIES: In order to understand the effects of the parameters as well as the shape of the functional forms of the spectral densities on the prediction of the compression strength, different virtual topologies of the in-plane misalignment $\theta_{k,l,m}$ and the out-of-plane misalignment $\phi_{k,l,m}$ were generated. The dimensions of the models were kept same as the *avg* model which was employed for the development of the failure envelopes numerically i.e. $6.657 \times 1.1412 \times 0.951$ mm with equal discretization of 0.0951 mm in each direction. The models had same boundary conditions as the *avg* model, and axial compression load was applied in the form of displacements.

The virtual topologies of the misalignment for $\theta_{k,l,m}$ and $\phi_{k,l,m}$ were generated in such a way that the mean square spectral densities Ξ^θ and Ξ^ϕ for each misalignment correspond to the experimentally measured value given in Table 4.2. The first model series considered no cutoff frequency which implies that the model contained all possible frequencies from fundamental frequency (largest wavelength) to the Nyquist frequency (smallest wavelength) in each direction. Fig. 6.12a and Fig. 6.12c show 3D contour plots of $\theta_{k,l,m}$ for a realization each using square and exponential forms of the spectral density without a cutoff frequency, respectively. Similarly, contour plots of $\phi_{k,l,m}$ for a realization each are shown in Fig. 6.13a and Fig. 6.13c using square and exponential forms of spectral density, respectively. It can be seen that without using a reasonable cutoff in the discrete sampling of the spectral densities, the resulting virtual topologies of the misalignment show a noise in the pattern which is unlike the experimentally measured topologies shown in Section 3.2 and virtually generated topologies based on experimentally characterized spectral densities presented in Section 4.2.1. The noise in the pattern results in much smaller regions of misalignment compared to the experimentally measured and subsequent virtually generated topologies in Section 3.2 and Section 4.2.1. This is due to the effect of very small wavelengths contributing to the pattern of the virtually generated topologies where no cutoff is considered in functional forms of spectral densities. Moreover, the anisotropic behavior observed in the measurements of the topologies of $\theta_{k,l,m}$ can not be modeled in cases without a cutoff as the Nyquist frequency controlled by the discretization length of 0.0951 mm is equal in all directions.

To improve on the topologies generated using empirical functional forms of spectral density without a cutoff, a second model series with certain cutoffs was considered. For this purpose, cutoff frequencies of $\omega_{c1}=6.28$ (corresponding to $\lambda_{1min}=1$ mm) and $\omega_{c2}=\omega_{c3}=12.56$ (corresponding to $\lambda_{2min}=\lambda_{3min}=0.5$ mm) were used for the in-plane misalignment $\theta_{k,l,m}$. For the out-of-plane misalignment $\phi_{k,l,m}$, cutoff frequencies of $\omega_{c1}=\omega_{c2}=\omega_{c3}=12.56$ (corresponding to $\lambda_{2min}=\lambda_{3min}=0.5$ mm) were used. These values of the cutoff frequencies are approximately equal to the values observed in the experimentally measured topologies of the fiber misalignment and their virtual generated counterparts in Fig. 4.6. One can see in the contour plots of the misalignment angles in Fig. 4.6 that the regions of misalignment are approximately 1 mm long in 1-direction and 0.5 mm long in 2, 3-directions for the in-plane misalignment $\theta_{k,l,m}$ whereas the regions of misalignment are approximately 0.5 mm in size in all directions for the out-of-plane misalignment $\phi_{k,l,m}$. A realization each from the resulting virtually generated topologies of $\theta_{k,l,m}$ using square and exponential functional forms of spectral densities are plotted in Fig. 6.12b and Fig. 6.12d, respectively. Similarly, Fig. 6.13b and Fig. 6.13d show a realization each of $\phi_{k,l,m}$ using square and exponential spectral densities, respectively. It can be observed through comparing the sizes of the regions of the misalignment that by using appropriate cutoff frequencies when discretizing the spectral density functions, the generated topologies resembles quite closely the experimentally measured topologies and their virtually generated counterparts of Fig. 4.6.

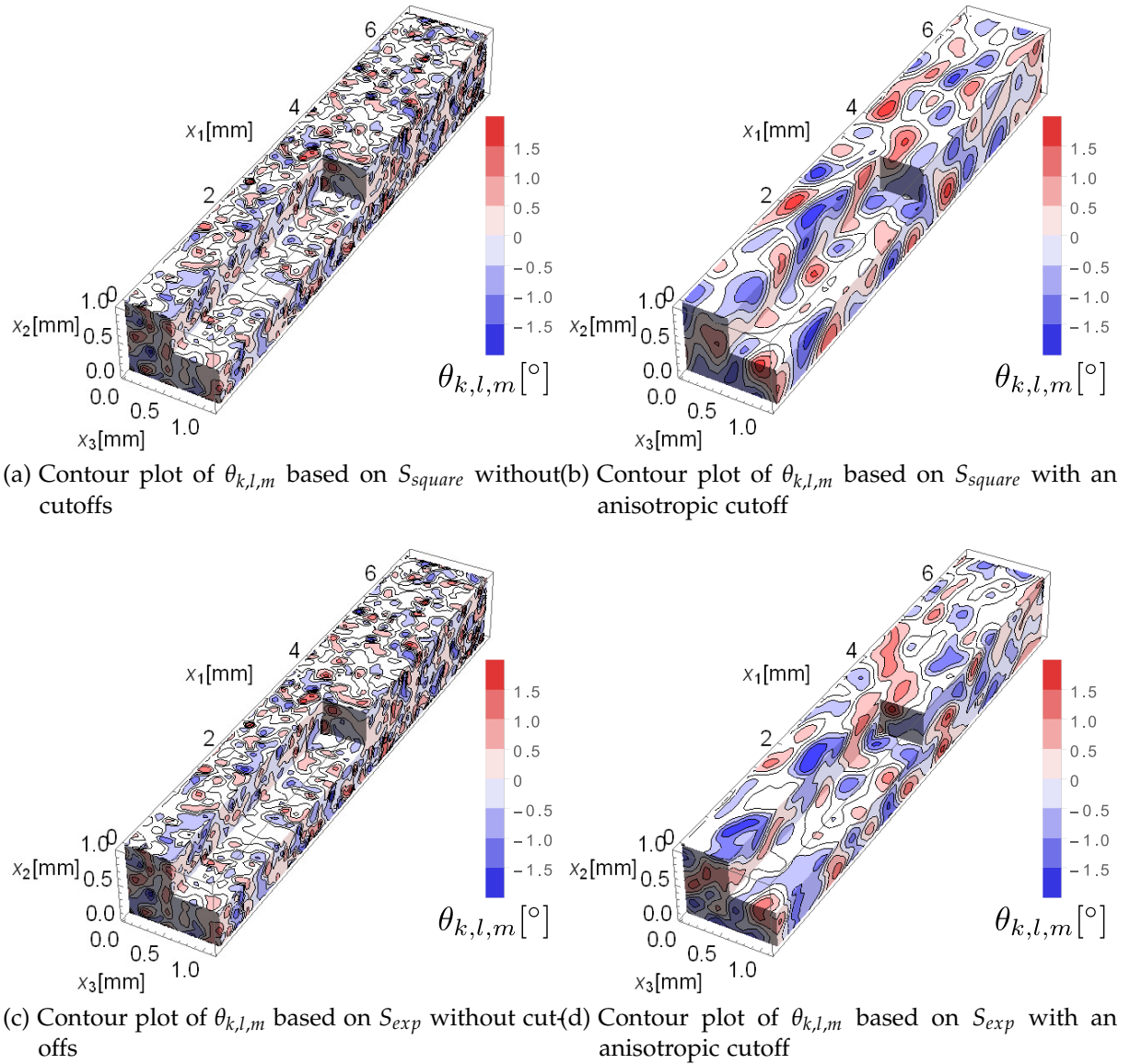


Figure 6.12: Virtually generated 3D contour plots of the in-plane misalignment angle $\theta_{k,l,m}$ using empirical forms of the spectral density as an input. The spectral representation method was used for the generation of virtual topologies of misalignment angles. For comparison with a virtually generated topology based on the experimentally characterized spectral densities, see Fig. 4.6b.

Additionally, the anisotropic behavior in $\theta_{k,l,m}$ of the resulting pattern in the virtually generated topologies can now be modeled. Moreover, it shows that the cutoff frequencies are not necessarily equal in all directions as assumed by the previous authors in literature.

EFFECT OF CUTOFF FREQUENCIES ON THE COMPRESSION STRENGTH PREDICTION: In order to investigate the effect of the cutoff frequencies ω_{c1} , ω_{c2} , and ω_{c3} on the resulting numerical prediction of the compression strength, 250 realization of each model series were simulated. The resulting probabilities of survival of each model are plotted in Fig. 6.14. Additionally, the probability of survival of the model based on *avg* spectral density, derived from the measurements of the fiber misalignment, is also plotted in Fig. 6.14. At a sufficiently low load, all the realizations survive. As the applied far field load σ_{11} increases, the proportion of the realizations failing increases. At a sufficiently high value of σ_{11} , all realizations fail giving a $P(\sigma_{11}^c)$ of 0. The mean and standard deviation values of all the models are provided in Table 6.7.

The first impression of the Fig. 6.14 already shows that even though the mean square spectral densities Ξ^θ and Ξ^ϕ of the models with and without cutoffs are equal, the resulting strength predictions vary widely. The models without any cutoff frequencies have a sizeable proportions of larger frequencies sampled from the functional forms of the spectral densities, which result in a sizeable proportion of small wavelengths in each direction. It results in a large number of weak regions typified by the numerous and sudden changes in the contours of the misalignment angles, which consequently result in a decrease of approximately 16-18% in the mean compression strength compared to the reference *avg* model based on CT scanned driven spectral densities S . The models with the appropriate cutoff frequencies on the other hand show survival probabilities of compression strength very close to the survival probability of the reference *avg* model. This results highlights that in addition to the mean square spectral density of the misalignment, the frequency range of the misalignment also needs to be preserved in virtually generated models. It is to be noted that the ideal scenario is to model virtual topologies of the fiber misalignment using experimentally characterized spectral densities, which is the case here with the reference *avg* model. However, the results of the Fig. 6.14 show that in case of absence of discrete matrices of the experimentally characterized spectral densities, one can use functional forms of spectral densities with the constraints discussed earlier for an approximation of the distribution of the compression strength.

Looking at the range of the results using the corresponding standard deviations of each model's strength distributions, some further observations can be made. All the models show standard deviations of predicted compression strength close to the reference *avg* model, except the model based on S_{square} with cutoffs. Seemingly, when there are no cutoffs, the results of the model series based on S_{square} and S_{exp} are almost identical. When appropriate cutoffs are applied, the mean strengths of both model series are still very close but the standard deviations vary significantly. The standard

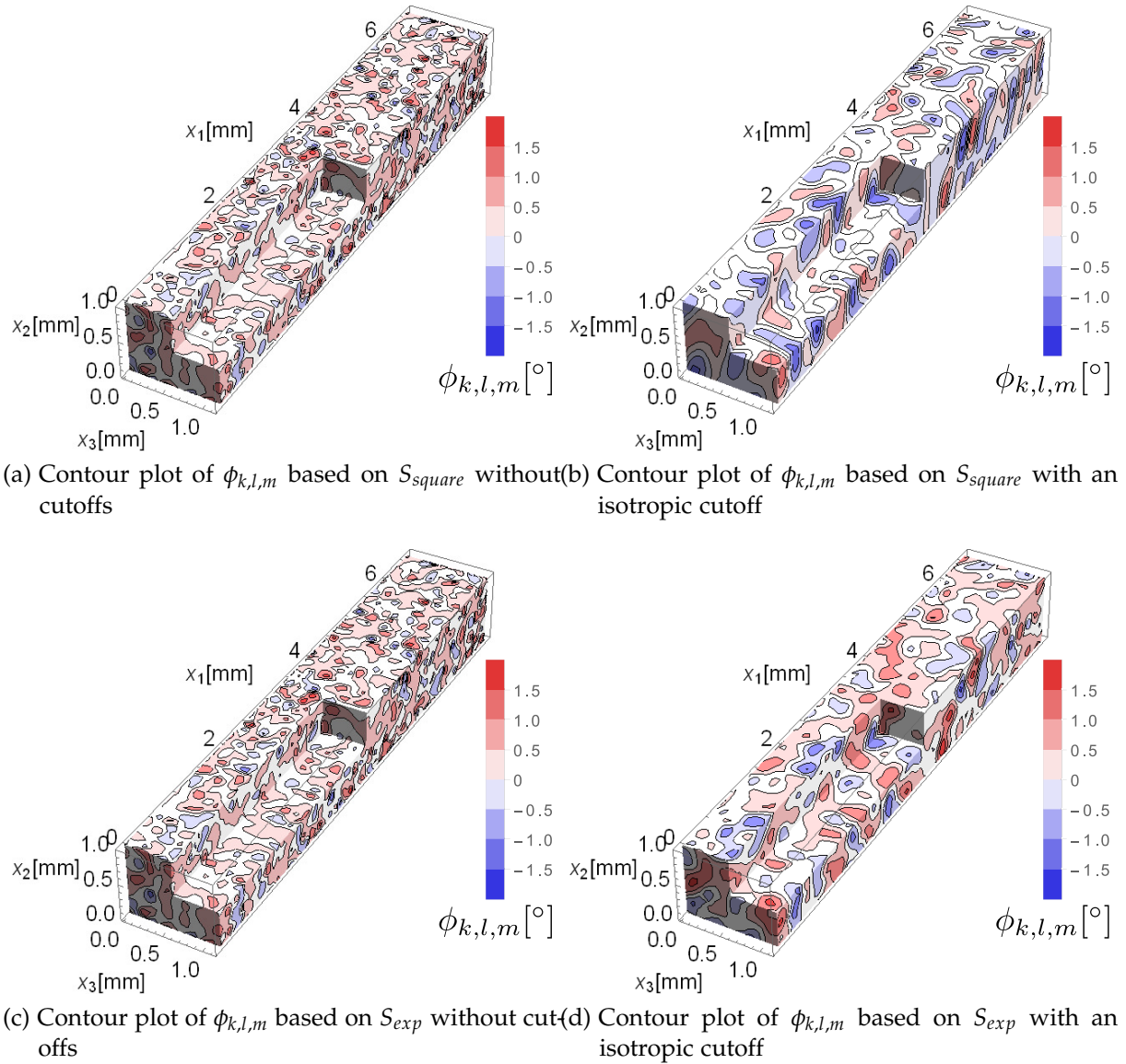


Figure 6.13: Virtually generated 3D contour plots of the in-plane misalignment angle $\phi_{k,l,m}$ using empirical forms of the spectral density as an input. The spectral representation method was used for the generation of virtual topologies of the misalignment angles. For comparison with a virtually generated topology based on the experimentally characterized spectral densities, see Fig. 4.6d.

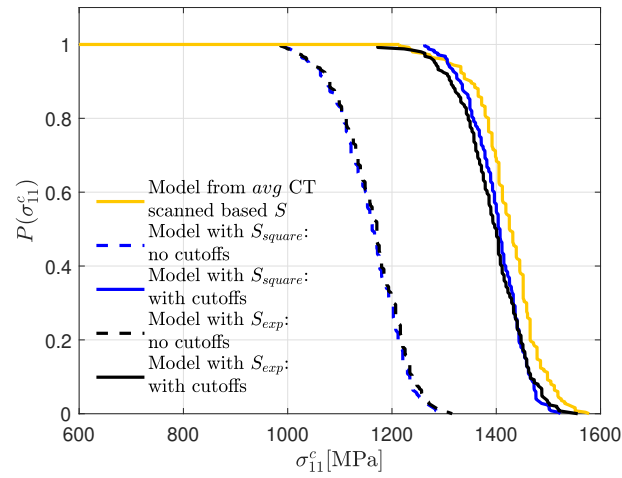


Figure 6.14: Empirical probability of survival $P(\sigma_{11}^c)$ over the compression strength σ_{11}^c for models with cutoff frequencies and models without cutoff frequencies. The survival probability using the reference *avg* model is also plotted for comparison.

Model	Mean [MPa]	s [MPa]
Model from <i>avg</i> CT scanned based <i>S</i>	1424.54	61.96
Model with empirical S_{square} : no cutoffs	1158.76	62.27
Model with empirical S_{square} : with cutoffs	1402.43	51.53
Model with empirical S_{exp} : no cutoffs	1164.54	62.30
Model with empirical S_{exp} : with cutoffs	1394.39	62.86

Table 6.7: Mean and standard deviations of different models using functional forms of spectral densities with and without cutoff frequencies

deviation of the model series based on S_{exp} is almost identical to that of the reference *avg* model. But the standard deviation of the model series based on S_{square} is lower, showing a lower spread of the compression strength prediction. The reason behind this peculiar behavior can be understood in the discretized spectral densities. The experimentally measured spectral densities show larger values at lower frequencies as seen in Fig. 4.3 and in Fig. 4.4. The model based on S_{exp} also discretize the spectral density in a similar fashion, with which the smaller frequencies get larger weightage of the spectral power. On the other hand, the model based on S_{square} discretizes the spectral density with equal weightage for all discretized frequencies. This apparently translates into lower spread of the resulting distribution of the numerically predicted compression strength. It is concluded based on this observation that in addition to the statistical parameters of the distributions, the spectral parameters including the shape of spectral density curve need to be preserved for accurate prediction of the distribution of the compression strength.

EFFECT OF SCALING MEAN SQUARE SPECTRAL DENSITIES ON THE PREDICTION OF THE COMPRESSION STRENGTH: Mean square spectral densities Ξ^θ and Ξ^ϕ quantify the misalignment angle in the frequency domain. Mean square spectral densities Ξ^θ and Ξ^ϕ are directly proportional to the square of the standard deviations s^θ and s^ϕ of the misalignment angles θ and ϕ , see Eq. 4.12. In order to investigate the effect of scaling mean square spectral densities Ξ^θ and Ξ^ϕ on the resulting numerical prediction of the compression strength σ_{11}^c , three scaled models series with each of them using both square and exponential forms of spectral densities were made. The values of Ξ^θ and Ξ^ϕ were scaled by factors of 0.25, 4, and 9, resulting in six new model series. Scaling Ξ^θ and Ξ^ϕ by factors of 0.25, 4, and 9 resulted in s^θ and s^ϕ being scaled by factors of 0.5, 2, and 3, respectively. Using the models resulting from scaled Ξ^θ and Ξ^ϕ , 250 realization of each model series were simulated. The resulting probabilities of survival $P(\sigma_{11}^c)$ of scaled model series are plotted in Fig. 6.15 along with the unscaled models based on the average experimentally determined values of Ξ^θ and Ξ^ϕ . The mean and standard deviation values of the compression strength from all these model series are provided in Table 6.8.

Solid lines in Fig. 6.15 depict results of model series based on S_{square} forms of spectral density whereas dotted lines illustrate results of model series based on S_{exp} for both $\theta_{k,l,m}$ and $\phi_{k,l,m}$. When the values of Ξ^θ and Ξ^ϕ were increased, the resulting distributions of σ_{11}^c were shifted towards lower values and vice versa. This is because increasing values of Ξ^θ and Ξ^ϕ means higher values of misalignment angles $\theta_{k,l,m}$ and $\phi_{k,l,m}$, resulting in lower values of the compression strength σ_{11}^c .

Some further observations can be made when analyzing the range of the results using the corresponding means and standard deviations of distribution of compression strength from each model series given in Table 6.8. Not only does the mean value of each model decreases with an increasing scaling of Ξ^θ and Ξ^ϕ , but the standard deviation values also decrease for both S_{exp} and S_{square} models. The larger the mis-

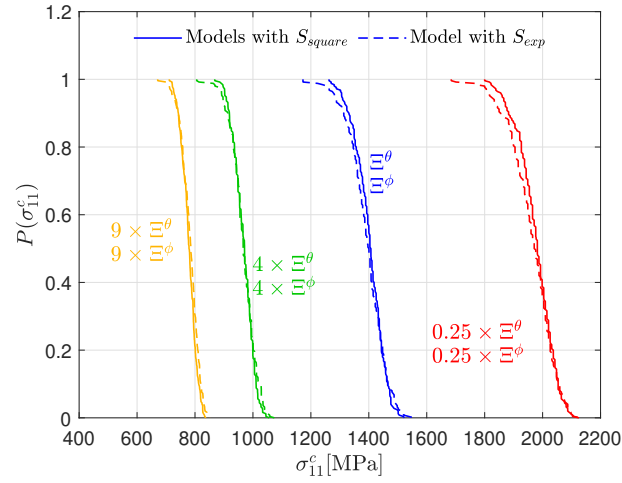


Figure 6.15: Empirical probability of survival $P(\sigma_{11}^c)$ over the compression strength σ_{11}^c for models with cutoff frequencies and different scaled values of the mean square spectral densities Ξ^θ and Ξ^ϕ .

Scaling of mean square spectral density	S_{exp} based models		S_{square} based models	
	Mean [MPa]	s [MPa]	Mean [MPa]	s [MPa]
$0.25 \times \Xi^\theta, 0.25 \times \Xi^\phi$	1964.93	76.65	1977.90	63.64
Ξ^θ, Ξ^ϕ	1394.39	62.86	1402.43	51.53
$4 \times \Xi^\theta, 4 \times \Xi^\phi$	967.21	42.93	967.83	35.84
$9 \times \Xi^\theta, 9 \times \Xi^\phi$	782.85	31.23	778.59	26.67

Table 6.8: Mean and standard deviations of the compression strength σ_{11}^c for models based on functional forms of the spectral densities with cutoff frequencies. Mean squares of the spectral densities were scaled to observe effects of resulting mean and standard deviation of numerically predicted distributions of the compression strength.

alignment is, the more severe certain regions of the misalignment become, resulting in a smaller range of the distributions of σ_{11}^c . It is to be noted that scaling Ξ^θ and Ξ^ϕ only changes the values of the misalignment angles. The topologies of the misalignment in scaled models are same as the realizations of the unscaled models depicted in Fig. 6.12 and Fig. 6.13 albeit with different limits of the values of the misalignment angle. This is because the topology is dependent on the functional forms and cutoff frequencies which are same in scaled and unscaled models of the analysis in this section. Going back to the predicted compression strengths, it is interesting to note that the standard deviation of S_{square} based model becomes comparable with that of the reference *avg* model when Ξ^θ and Ξ^ϕ are scaled by a factor of 0.25. It again highlights that the exponential form of the empirical spectral density is more suitable in light of the measured spectral densities presented earlier in Section 4.1.1.

Using the results of Fig. 6.15, a relation for different percentiles of distribution of compression strength ${}^p\sigma_{11}^c(SF)$ as a function of scaling factor SF of Ξ^θ and Ξ^ϕ was defined. The relation is applicable to all the percentiles of the distribution of the compression strength and is written as:

$${}^p\sigma_{11}^c(SF) = {}^p\sigma_{11}^{c-ref} SF^a \quad (6.39)$$

where a is defined by $3/4^{th}$ of the product of standard deviations of the misalignment of the reference *avg* model, i.e. $a=3/4 \times s^\theta \times s^\phi$, see Table 4.2 for values of s^θ and s^ϕ . The symbol ${}^p\sigma_{11}^{c-ref}$ represents the i^{th} percentile of the distribution of the compression strength of a reference model, which in current case are the unscaled S_{exp} and S_{square} based models. The S_{exp} and S_{square} based models can be scaled using the p values of the corresponding reference S_{exp} and S_{square} models, respectively. The relation given by the Eq. 6.39 is plotted in a double logarithmic plot for both S_{exp} and S_{square} based model series in Fig. 6.16 for 1^{st} , 50^{th} (median), and 99^{th} percentiles of the distribution of σ_{11}^c . Corresponding values of percentiles of the distribution of σ_{11}^c from each case are given in Table 6.9. These values are also plotted as scatter points on top of the curves of Eq. 6.39 in Fig. 6.16. The defined empirical relation fits quite well with the numerical results of the Ξ^θ and Ξ^ϕ scaled models for both S_{exp} and S_{square} based models. It shows that the strength decreases with a power law with an increasing scaling of Ξ^θ and Ξ^ϕ .

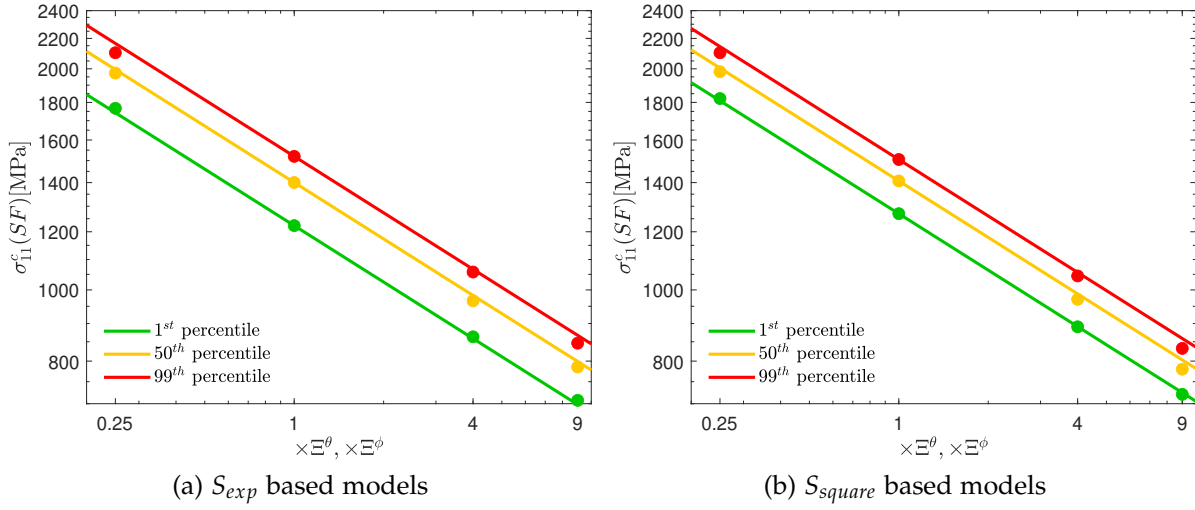


Figure 6.16: 1^{st} , 50^{th} (median), and 99^{th} percentiles of the distribution of the compression strength σ_{11}^c as a function of Ξ based on results of models with cutoff frequencies and different scaled values of the mean square spectral densities Ξ^θ and Ξ^ϕ . The corresponding values from each cases are plotted as scatter points on each curve.

Model parameters	Percentiles of distribution of σ_{11}^c		
	1^{st} [MPa]	50^{th} [MPa]	99^{th} [MPa]
$S_{exp}, 0.25 \times \Xi^\theta, 0.25 \times \Xi^\phi$	1767.12	1973.73	2103.31
$S_{exp}, \Xi^\theta, \Xi^\phi$	1223.35	1400.44	1520.04
$S_{exp}, 4 \times \Xi^\theta, 4 \times \Xi^\phi$	863.29	966.46	1057.73
$S_{exp}, 9 \times \Xi^\theta, 9 \times \Xi^\phi$	707.44	785.52	846.28
$S_{square}, 0.25 \times \Xi^\theta, 0.25 \times \Xi^\phi$	1821.97	1987.84	2103.28
$S_{square}, \Xi^\theta, \Xi^\phi$	1269.96	1407.20	1505.05
$S_{square}, 4 \times \Xi^\theta, 4 \times \Xi^\phi$	890.82	970.99	1044.81
$S_{square}, 9 \times \Xi^\theta, 9 \times \Xi^\phi$	720.86	779.93	.832.57

Table 6.9: 1^{st} , 50^{th} (median), and 99^{th} percentiles of the distribution of the compression strength σ_{11}^c for different models

COMPARISON OF EXPERIMENTAL AND NUMERICAL APPROACHES

Comparison of results from the experimental testing to failure presented in Chapter 5 and results from the numerical modeling given in Chapter 6 under compression dominated loads is discussed in this chapter. A comparison of results under the axial compression load from both approaches will be discussed with the help of a scaling law. Finally, a discussion about differences in shapes of failure envelopes from experimental and numerical approaches will be presented.

7.1 COMPARISON OF EXPERIMENTAL RESULTS UNDER AXIAL COMPRESSION LOAD VERSUS NUMERICAL PREDICTIONS USING WEIBULL SCALING

Homogeneously loaded FRPs show immediate sudden collapse in a transient dynamic manner during MB failure initiation, and the redistribution of load is insubstantial. Several experimental [62, 65, 131] and numerical [35, 109] investigations have shown that strength under axial compression in FRPs decreases with increasing size. Because of extreme difficulties associated with compression testing of FRPs, some inconclusive results have also been reported [130]. Nonetheless, a strength reduction in testing to failure under axial compression load in FRPs is expected due to stochastic considerations [11, 12, 130]. This decrease is attributed to the increasing number of the fiber misalignment induced defects in larger sizes based on the Weibull statistic driven weakest link model [123], similar to the phenomenon observed in brittle materials such as ceramics [11]. To separate the fiber misalignment driven size effect in homogeneously loaded FRP specimens from other size effects, such as hole or notch driven size effects, it is labelled as the statistical size effect.

The reasoning behind the statistical size effect in FRPs is similar to the now well understood size effect in brittle materials with random flaws such as ceramics. The overall strength in brittle materials is controlled by the weakest location, i.e. failure initiated at the weakest location triggers a global catastrophic failure. With an increasing size of the component, the chance of encountering a weakest link increases, giving rise to the statistical size effect. The probability of survival P of a volume V with respect to the applied far field compression load σ_{11} is given by Eq. 7.1 based on a weakest link model. The compression strength is defined by the maximum of the applied far field load, i.e. $\sigma_{11}^c := \max(\sigma_{11})$. There, P_o is the survival probability in a reference specimen with a volume V_o

$$P(\sigma_{11}^c) = \exp\left(\int_V \ln(P_o(\sigma_{11}^c)) \frac{dV}{dV_o}\right) \quad (7.1)$$

A further assumption regarding $P(\sigma_{11}^c)$ is required to obtain a scaling law model [139]. Generally, a power law proposed by Weibull given in Eq. 7.2 is used for this purpose, although the power law assumption by Weibull is not based on any physical arguments which also leads to some criticism [9, 32].

$$P_0(\sigma_{11}^c) = \exp\left(-\left\langle\frac{\sigma_{11}^c - R_t}{R_0}\right\rangle^m\right) \quad (7.2)$$

where R_0 and m are the scale and the shape parameters of the Weibull distribution, and the symbol R_t refers to the threshold parameter. The threshold parameter is optional, below which probability of failure is zero. The parameter R_t is positive for the 3-parameter variant of the Weibull distribution. The 2-parameter variant is obtained by setting the threshold R_t equal to zero. The angled brackets denote Macauley brackets, i.e. $\langle x \rangle = x$ if $x > 0$ else $\langle x \rangle = 0$.

Eq. 7.3 is obtained by combining the weakest link model given in Eq. 7.1 and the Weibull power law model given in Eq. 7.2.

$$P(\sigma_{11}^c) = \exp\left(-\int_V \ln\left(\left\langle\frac{\sigma_{11}^c - R_t}{R_0}\right\rangle^m\right) \frac{dV}{dV_0}\right) \quad (7.3)$$

Given a homogeneously applied far field stress σ_{11} , Eq. 7.3 implies the scaling law given in Eq. 7.4. Writing Eq. 7.3 for each $\sigma_{11}^c = \sigma_i^c$ and $V = V_i$ with $i = [\text{model}, \text{exp}]$, and subsequently equating the probability yields Eq. 7.4.

$$\frac{\sigma_{\text{model}}^c}{\sigma_{\text{exp}}^c} = \left(\frac{V_{\text{model}}}{V_{\text{exp}}}\right)^{-1/m} \quad (7.4)$$

where σ_{model}^c and σ_{exp}^c are strengths from model predictions given in Section 6.2.2 and experimental results given in Section 5.2.3, and m is the Weibull modulus or the shape parameter of the Weibull distribution.

The gauge section dimensions of the numerical models were limited to a volume of $6.657 \times 1.1412 \times 0.951$ mm because of the limited volume of the CT-scans, see Section 6.1.1. Modeling at sizes larger than the scanned volume is not possible as the misalignment measurements and subsequent spectral characterization for any such size is unavailable. One can not assume apriori the form of spectral density curves for larger sizes from available scans of a small volume. Since the volume of the gauge section of the experimental specimens $V_{\text{exp}} = 28.75$ mm³ and the volume of the numerical models $V_{\text{model}} = 7.2247$ mm³ were significantly different from each other, a direct comparison between both results cannot be made. In order to compare numerical results under axial compression against the experimental results, some form of scaling law is required. Therefore, numerical predictions for the axial compression load case were compared against experimental results using the Weibull scaling law given in Eq. 7.4 for the median strengths, i.e. at the cumulative probability of failure of 0.5.

The values of the parameter m for all three series of numerical models are given in Table 6.4. The value of m is 7.11 for the experimental results. Fig. 7.1 shows the

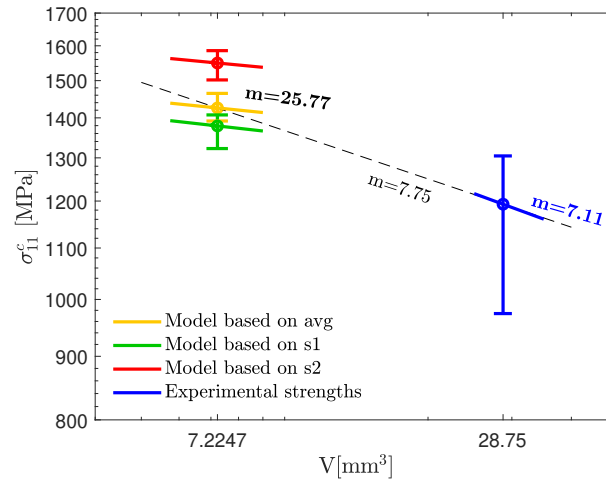


Figure 7.1: Comparison of σ_{11}^c from numerical models against experimental results using the Weibull scaling law. Parameter m is known as the Weibull modulus or the shape parameter. The Weibull scaling law is implied by, but not to be confused with, the Weibull strength distribution itself. The fitted Weibull strength distribution to the experimentally determined σ_{11}^c is presented in Fig. 5.10b and numerically calculated σ_{11}^c is plotted in Fig. 6.7.

aforementioned two parameter form of the scale law for all three model series as well as experiments. The inclination of the scale law is based on the respective m parameter. The scaling law appears as a straight line because of the double logarithmic scale in the figure. To aid the comparison, another variant of the scaling law for 0.5 cumulative probability of failure is included in the plot with a dotted line. For this variant, the line starts at the median strength of the experimental results and the parameter m was adjusted so that it passes through the median strength of the *avg* model. The corresponding value for m is 7.75 which is very close to the value 7.11 of the distribution fitted to the experimental results. This result indicates that given the m value for a volume, e.g. from the experimentally determined σ_{11}^c , one can predict the mean σ_{11}^c for any other volume using the Weibull scaling law.

Results in Fig. 7.1 indicate that there is a significant increase in the predicted median strength with smaller model sizes compared to the experiments, as expected based on the Weibull scaling law. The value $m=7.75$ can predict the numerical median strength of the *avg* model quite accurately, given the median experimental strength. The improvement in the prediction of the median strength value using the *avg* model with the availability of further CT-scans could lead to even closer comparison to the experimental median strength. The m values from the numerical models on the other hand are quite high due to less scatter in corresponding probability distributions. The high m values from numerical models here can be partially attributed to periodic boundary conditions limiting edge driven failure. Similar high values of m parameter were observed by previous investigations in the literature [109]. The variants based on 3-parameter Weibull scaling were very similar over the considered ranges and hence,

are not shown in Fig. 7.1. The complete distributions of the numerically predicted strengths and the experimental strengths are also plotted using error bars in Fig. 7.1.

It is to be noted that the comparison based on the Weibull scaling law is not a direct validation and is a comparison with the underlying assumption of an existence of a scale law. Moreover, the Weibull shape parameter m based extrapolation is still considered an open question and further experiments at different sizes are needed for a complete validation of the scale law. The straight line scale law shown in Fig. 7.1 may not be representing the exact refined shape of the scale law. The Weibull based scale law could even be a curve in double logarithmic plot. Further experiments and numerical simulation at different sizes are required for a verification of the exact shape of the scale law.

7.2 COMPARISON OF FAILURE ENVELOPES OBTAINED FROM EXPERIMENTAL AND NUMERICAL RESULTS

The failure envelopes determined through the experimental approach were found for a gauge section volume of $V_{\text{exp}}=28.75 \text{ mm}^3$, see Chapter 5. On the other hand, the numerically determined failure envelopes given in Chapter 6 are valid for a gauge section volume of $V_{\text{model}}=7.2247 \text{ mm}^3$. Because of the differences in the gauge section volumes and the existence of size effects discussed earlier in Section 7.1, a direct comparison of the failure envelopes is to be carefully analyzed under consideration of the scaling law.

The shear behavior of FRPs is deterministic and does not change with size as is not affected by the fiber misalignment. Compression behavior on the other hand, is uncertain and scales based on size as explained in Section 7.1. Material response under combined compression-shear is complicated, and also scales with the size of the gauge section due to the underlying fiber misalignment. Only a limited number of specimens could be tested in experimental testing to failure due to steep costs of testing and associated difficulties, however, numerical modeling allowed for simulating the response of the material at a lot more combinations of the combined compression-shear. The limited number of experimental data points resulted in a less refined form of the failure envelope in strain spaces which is presented in Fig. 5.12. A much detailed strain space envelope was obtained through numerical modeling which illustrated in Fig. 6.10. Both the numerically obtained and the experimentally determined failure envelopes in strain space are plotted together in Fig. 7.2 for a direct visual illustration. Failure strain from experiments are slightly lower overall due to size effects of larger volume of the experimental gauge section compared to the volume of the numerically modeled gauge section. As a result, the experimentally determined failure envelope shows lower failure strains as expected. Moreover, due to larger number of realizations in numerical modeling compared to the experimentally tested specimens, more extreme percentiles of distribution of failure could be found. An important aspect to notice is the shape of the failure envelopes. When comparing the two failure

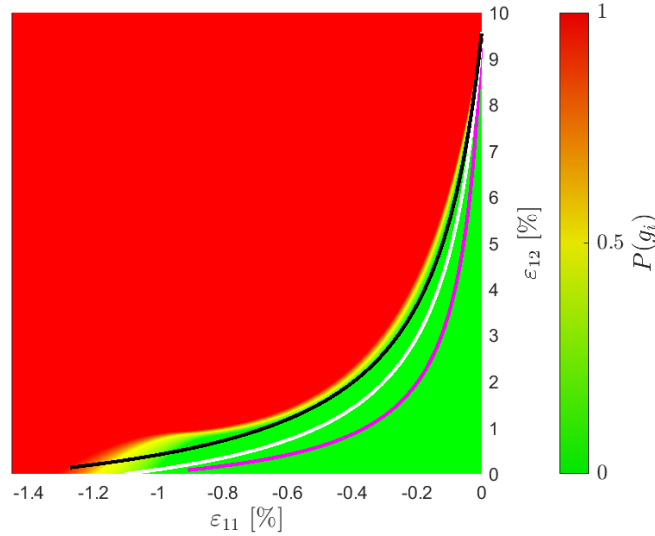


Figure 7.2: Comparison of experimentally and numerically determined failure envelopes in ε_{11} - ε_{12} plane. The experimentally determined failure envelope was presented in Fig. 5.12 and the numerically obtained failure envelope was plotted in Fig. 6.10. The color code depicting the probability of failure $P(g_i)$ is based on numerical results and represents the numerical failure envelope. The solid lines represent experimental failure envelope at 25th (in color magenta), 50th (white), and 75th (black) percentiles of distributions of failure.

envelopes, it is obvious that the intricate shape of the failure envelope could be found more precisely through numerical modeling as more load cases were considered in numerical modeling.

Failure envelope in stress space through experiments could not be directly found as only single load cell was available for force measurements, see detailed discussion in Section 5.2.7. Hence, only an approximation of the median failure envelope giving a linear shape of the envelope could be found through experimental testing to failure. Because of the ability to calculate stresses at failure in numerical modeling, the failure envelope in stress space could be determined in more detail with accuracy. For a comparison of the experimentally approximated and the numerically determined failure envelopes in stress space, they are plotted together in Fig. 7.3. Strengths were only available directly for the axial compression and the pure shear load cases. One can observe the size effect in the median prediction of the failure envelopes at the σ_{11} axis in Fig. 7.3 due to larger volume of experimental gauge section compared to the numerically modeled volume. It is interesting to observe that the shape of stress based failure envelope determined through numerical modeling is similar to corresponding strain based envelope. The complicated shape of the envelope was again obtained in detail through numerical modeling. This was not possible in the approximation of the failure envelope through experimental results in stress space.

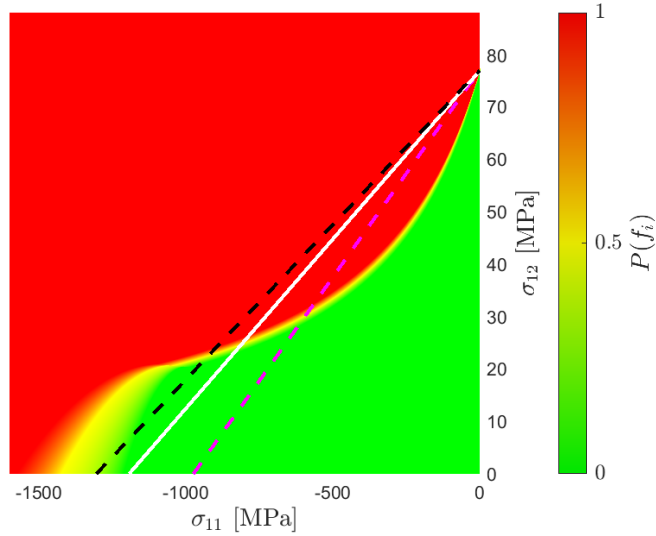


Figure 7.3: Comparison of experimentally and numerically determined failure envelopes in σ_{11} - σ_{12} plane. The experimentally determined failure envelope was presented in Fig. 5.14 and the numerically obtained failure envelope was plotted in Fig. 6.9. The color code depicting the probability of failure $P(f_i)$ is based on numerical results and represents the numerical failure envelope. The solid lines represent an approximation of the experimental failure envelope at 25th (in color magenta), 50th (white), and 75th (black) percentiles of distributions of failure.

Although numerical modeling can provide results in a lot more detail, experimental testing is still required for validation purposes for acceptance of such results. Moreover, results of the experimental testing confirmed microbuckling to be dominant mode of failure under combined compress-shear loads as explained in Section 5.2.2.

The shear strength of the FRPs is deterministic as shear failure is dependent on matrix properties. Compression behavior, however, is not only probabilistic but also scales with the size. The comparison of the failure envelope shown before highlights that probabilistic and scale effects are not limited to pure axial compression but also appear in combined compression-shear part of the envelope. Assuming the shape of the failure envelope would remain same over different volumes and only compression part of the combined compression-shear load scales due to size effects as explained earlier, one can generate failure envelopes for other model sizes by simply scaling σ_{11} -axis of the failure envelope. For this purpose, the Weibull scaling law can be used to predict the axial compression strength at other model sizes. It is to be noted that investigations need to be performed to verify whether the shape of the failure envelope stays the same for scaled sizes. Numerical simulations would need to be repeated with availability of misalignment data for larger volumes. Furthermore, validation of the size effects under the axial compression loads through experimental testing to failure in future investigations would confirm the exact scaling law. These advances

would also allow for verification of the scaling for whole failure envelopes at different sizes.

CONCLUSIONS AND OUTLOOK

The conclusions of the investigations performed in this work are summarized in this chapter. The outlook for future work is also outlined, along with a schematic representation of possible directions of future works.

8.1 CONCLUSIONS

For best utilization of FRP based structures, the prediction of failure uncertainties is a fundamental requirement. Microbuckling (MB) is the dominant failure mode under axial compression and combined compression-shear loads for unidirectional FRPs. The underlying uncertainties in MB failure lead to conservative design practices. This motivated the development of experimental and numerical methodologies for quantifying the uncertainties in MB failure. Present study elucidates use of these approaches for a stochastic investigation of MB failure in unidirectional fiber reinforced composites under compression and combined compression-shear loads. Different aspects of the problem were investigated in this regard. Following conclusion can be drawn based on these investigations:

1. The fiber misalignment was realized as a defining factor for the failure prediction under compression and combined compression-shear loads. The first open question presented in the state of the art Section 2.6 discussed the need of measuring these misalignment. By performing CT scans and analyzing the results, it is shown that the misalignment is indeed dependent on all three spatial directions and volumetric measurements are necessary for a representative measurement of imperfections.
2. The importance of the matrix non-linearity in shear is imperative for prediction of MB failure based on a review of the state of the art. The second open question argues about need of characterizing nonlinearity of material's shear behavior along with other test for characterization of mechanical properties. To fulfil these requirements, standard tests were performed. The resulting material constants and the stress-strain curves from standard tests are presented in Section 3.1.
3. The third open question indicates the need of characterizing the spatial distribution of the fiber misalignment in addition to the usual statistical properties. In this regard, the spectral representation method was employed for characterizing the fiber misalignment in the frequency domain in form of spectral densities of the in-plane and the out-of-plane angles in Section 4.1.1. By highlighting the

deficiency of characterizing spectral densities in 2D frequency domain in Section 4.1.2, it was concluded that the commonly used 2D forms of the spectral density cannot preserve the complete 3D nature of the fiber misalignment.

4. The next item in the open questions talks about the representation of the fiber misalignment in numerical models and identified the spectral representation method as an excellent choice. Using the extended form of the spectral representation method, 3D topologies for the in-plane and the out-of-plane misalignment angles were generated in Section 4.2.1. By comparison of the 3D topologies and 2D topologies, it was confirmed that the true nature of the fiber misalignment can only be captured through 3D modeling.
5. The central open question deals with the development of novel probabilistic failure envelopes under compression and combined compression-shear load cases at different percentiles of failure. Using the results of testing to failure performed on a novel fixture which can apply combined compression-shear loads simultaneously, a probabilistic failure envelope in strain space ε_{11} - ε_{12} was constructed and a mathematical definition of failure envelopes at 25th, 50th, and 75th percentiles is presented, see Section 5.2.5 and 5.2.7.

A comparison of the applied stresses in the loading direction $\sigma_{1'1'}$ is shown in Section 5.2.3 highlighting the fact that the pure axial compression load case shows highest variation in strength. This result emphasizes the dependency of the compressive behavior on the fiber misalignment. By fitting $\sigma_{1'1'}$ with normal and 2/3 parameter Weibull distributions, it is concluded that 3 parameter Weibull distribution shows the best fit among them. As capturing the development of shear band localization leading to microbuckling failure in combined compression-shear load cases is an interesting aspect, it was done through the DIC measurements. Moreover, evidence of MB as the failure mode in combined compression-shear load case was further shown in Section 5.2.2 by fractographic analysis.

Results obtained for the axial compression load case were assessed against an analytical prediction model by Budiansky [21] in Section 5.2.6. The magnitude of the misalignment angles ψ were calculated and compared against the actual measurements of the in-plane misalignment angle $\theta_{k,l,m}$ and the out-of-plane misalignment angle $\phi_{k,l,m}$ through a calculated distribution of the effective global misalignment angle $\psi_{k,l,m}$. The definition of the effective global misalignment angle $\psi_{k,l,m}$ has been improved in comparison to the earlier efforts by including the effects of out-of-plane misalignments. It is concluded in the present case that the 90th percentile of the $\psi_{k,l,m}$ gives a better approximation of the median strength prediction whereas earlier investigations [127] suggested the 99th percentile as appropriate for NCF materials. It appears that the percentile level defining the effective misalignment angle is not transferable without further adjustments. It is also shown that the elastic-perfect plastic material behavior assumption for the

axial compression strength prediction using analytical solutions is not suitable for a material with nonlinear shear behavior.

Finally, using the identified effective misalignment angle and the analytical equation system, median strengths were calculated indirectly for combined load cases. These were then used for defining a failure envelope in stress space σ_{11} - σ_{12} , which shows a linear interaction of stress components as expected, see Section 5.2.7.

6. The second part of the central open question addresses the probabilistic failure investigation under combined compression-shear loads using numerical modeling. An inconsistency of the material axis rotation in Abaqus for homogenized representation was rectified by introduction of additional shear rotation to the preferred material direction in the material model, see Section 6.1.2.2. Effect of the misalignment dimensionality on the compression strength prediction was investigated using simpler sinusoidal misalignment topologies in the homogenized approach. It was shown in Section 6.2.1 that the maximum misalignment angle alone is not the deciding factor but rather the whole topology of the misalignment modeled in appropriate dimension plays a major role in prediction of compression strength.

Using the homogenized representation, probabilistic simulations were carried out under the axial compression loads for different model series. The results based on average spectral densities shown in Section 6.2.2 lie in-between those dependent on individual measurements of scanned specimens, as expected. Therefore, the *avg* model series was considered for further investigations. By analyzing the results of a realization from different load cases given in Section 6.2.3, it was established that MB failure occurred not only under the pure axial compression load, but also under combined compression-shear loads. The differences between the linear axial response and the nonlinear shear response under combined loads were discussed.

Failure envelopes in stress and strain spaces were developed using results obtained via probabilistic analysis of different load cases of combined compression-shear, see Section 6.2.4 and 6.2.5. The failure envelopes were divided into two regions, i.e. the compression dominated MB1 and the shear dominated MB2. Functional forms of failure envelopes were defined and the parameters for 1st, 50th (median), and 99th percentiles were identified. For comparison, established failure criteria were plotted on top of the numerical results. Failure criteria from literature either overestimated the failure, since they do not account for the effects of the fiber misalignment on combined load cases, or they can not model the change in shape of the failure envelopes.

Finally, the assumption of functional forms of spectral densities for generation of virtual topologies of the fiber misalignment was investigated. The results of this investigation given in Section 6.2.6 concludes that functional forms of spectral

density can be assumed as an approximation. It was shown that proper cutoff frequencies need to be used for accurate prediction of compression strength. By analyzing the effect of scaling mean square spectral densities on the prediction of the compression strength, an empirical relation for scaled mean square spectral densities is provided. It was concluded that the exponential form of spectral density compared to the square form of spectral density gave better prediction for whole distribution of the compression strength for the material investigated in the current work.

It is expected that the presented experimental and numerical methodologies and corresponding results of the novel probabilistic definitions of failure envelopes can help in the further exploration of uncertainty quantification in FRPs. Eventually, it may enable more reliable design practices. Additionally, the proposed methodologies offer an easy path to the development of the probabilistic failure envelopes for new fiber reinforced materials.

7. The final open question stated in Section 2.6 discusses the need of a scaling law for comparing experimental and numerical predictions of the compression strength. Hence for validation, the numerical strength prediction of the pure compression load case was compared to the experimental results in Section 7.1. The dissimilar specimen sizes of the measurements and subsequent numerical models on one hand and the experiments on the other required the consideration of a scaling law. For this purpose a Weibull scale law was calibrated using the shape parameter m of experimental results under the pure axial compression load. Accounting for size effects, results of the numerical model are in good agreement with the experimental reference. By comparing the failure envelopes determined experimentally against those obtained numerically, it was concluded that the probabilistic and scale effects also exist under combined compression-shear loads. Given that only the compression behavior scales with change in volumetric size and assuming that the shape of failure envelopes remains same, it is suggested that one can scale the failure envelope using the Weibull scaling law.

8.2 OUTLOOK

The main aim of the numerical and the experimental approaches presented in this work is to understand and quantify uncertainties in failure of FRPs under axial compression and combined compression-shear loads due to the underlying fiber misalignment. The goal is a push for reliable design practices of light-weight structures when using FRP materials with lower factors of safety. In context of further realization of this goal, some prospective works for future are suggested.

A schematic of possible areas of exploration is shown in Fig. 8.1. An interesting open question is that of statistical size effects in strength distribution under compres-

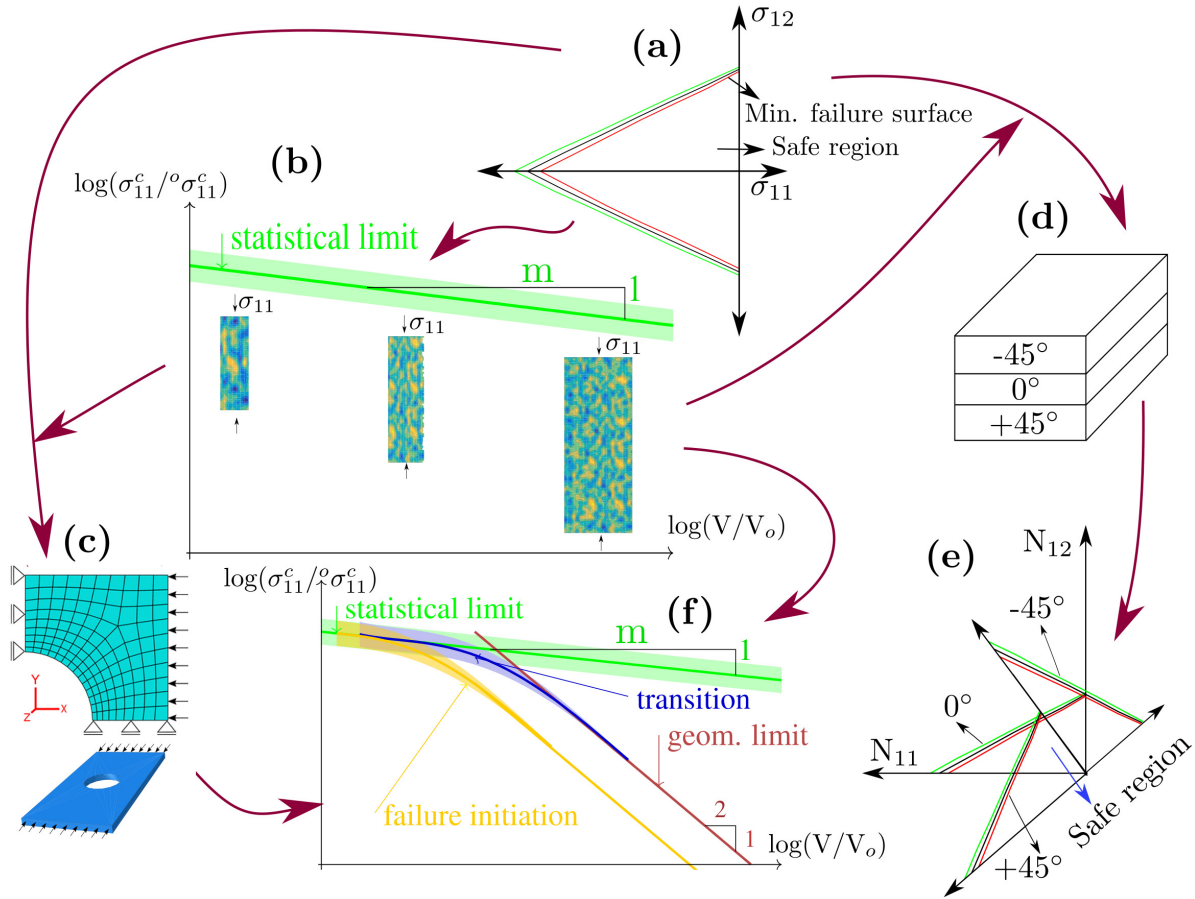


Figure 8.1: Schematic of follow-up works. [Fig. (a) \rightarrow (b)] Numerical determination of a statistical scaling law. [Fig. (a) and (b) \rightarrow (d) \rightarrow (e)] Development of a Stochastic First Ply Failure (FPF) criterion for homogeneously stressed laminate plates. [Fig. (a) \rightarrow (b) \rightarrow (c) \rightarrow (f)] Numerical determination of a scaling law in the geometrical and the transition regimes.

sion loads. By performing numerical simulations at different sizes, informed by the measurements of the fiber misalignment at corresponding sizes, statistical scale law can be defined. The numerical methodology presented here can be used for such a purpose. A corresponding validation of the results by performing experiments under axial compression for unnotched specimens needs to be performed. The combination of such an analysis can result in not only statistical scale law, not only for median strength prediction but also for different percentiles for the distribution of compression strength.

Another topic of interest is the extension of scale laws to multidirectional FRPs where the misalignment in 0° layer might control the failure of the whole laminate. A possible path for such an analysis is shown in Fig. 8.1. By a combined use of the scaled failure envelopes of different layers of the laminate for a particular size and the use of composite laminate theory, a simple methodology for defining a safe region in

the N_{11} - N_{12} plane can be defined. N_{11} and N_{12} are the loads in the global coordinate frame.

In notched specimens, microbuckling typically originates at a location of stress concentration near the structural detail. After initiation, stress can redistribute and hence, a gradual growth of the microbuckle is observed at increasing far field load, similar to stable crack growth in notched metal structures under tension. Eventually, the microbuckle grows to a critical length beyond which load redistribution can no longer offset the local softening, and propagation turns into an unstable dynamic process. In an abstract sense, this behavior is similar to the growth of tensile cracks, with the modification that the microbuckle corresponds to a negative crack opening. In fracture mechanics the critical crack length, i.e. the crack length at which propagation turns unstable, is linked to the critical energy release rate which is a material property. Thus, the critical crack length, or rather the critical microbuckling length, also defines an intrinsic length and introduces an associated scale effect. This is the second type of scale effect under consideration in this text, and it is termed as the geometrical size effect. In addition to the statistical size effects, FRPs also exhibit so-called geometrical size effects. The initiation and final failure of such geometrical size effects can be analyzed using linear elastic fracture mechanics and numerical modeling.

In typical engineering composites sub-components, both statistical and geometrical scaling laws are present at the same time and compete. Actual strength of a component containing such sub-components is thus generally lower of either the statistical or geometrical limit case models. Hence, the applicability of these scaling laws is relevant in certain particular size ranges. Towards the lower limits of length scales of the sub-component, statistical size effect is dominant, see Fig. 8.1. In such cases, failure is catastrophic, showing a snap-back response and the structure is unable to bear extra load through stress redistributions. On the other extreme of larger structural details, the geometrical scaling laws take precedent. In such cases, as discussed earlier in geometrical scaling law section, the increase in releasable energy overpowers the statistical effect. Hence, the ultimate load is controlled by the geometrical scaling law. This can be seen in testing of not only composites with notches or holes, but also other materials such as concrete. Mere proportional up-scaling of some specimen with a notch or cut-out can change the failure regime from scattered statistical dominated to deterministic geometric dominated, cf. insets in Fig. 8.1. However, the transition is not sudden and in between the two limit cases, a stochastic transition regime for a particular geometric detail overtaking the corresponding statistical size effect exists. A probabilistic scaling law for specific laminated sub-components, not only in statistical and geometrical regimes, but also in transition regime, would allow for more efficient and less over-conservative designs. Through nonlinear numerical progressive damage analysis on suitable models, the distribution for both initiation and ultimate loads obtained via stochastic methods forms the basis to formulate an empirical scaling law for the transition regime. These results can serve as a reference for possible further developments and generalizations.

APPENDIX

A.1 ALGORITHM FOR GENERATION OF TOPOLOGIES OF THE 3D FIBER MISALIGNMENT FROM SPECTRAL DENSITIES

Herein, the extension of the artificial generation of 1D and 2D correlated random processes to 3D is presented. The method is based on Fourier transformation principles. It was initially developed for the time dependent signal processing theory. Cebon [27] and Newland [84] employed it for the artificial generation of correlated random isotropic road surfaces. It was later used for microbuckling analysis of unidirectional FRPs in 1D [100] and in 2D [76] considering correlated random topologies of the fiber misalignment.

Consider a 3D topology function $f({}^1x_k, {}^2x_l, {}^3x_m)$ dependent on spatial variables 1x_k , 2x_l , and 3x_m sampled discretely over the intervals $[0, L_1]$, $[0, L_2]$, and $[0, L_3]$, respectively. The topology is periodic over the intervals ${}^1x_k=[0, L_1]$, ${}^2x_l=[0, L_2]$, and ${}^3x_m=[0, L_3]$. It is represented in discrete form as $f_{k,l,m}=f({}^1x_k, {}^2x_l, {}^3x_m)$, where ${}^1x_k=k\Delta_1$, ${}^2x_l=l\Delta_2$, and ${}^3x_m=m\Delta_3$, with $k=0, 1, \dots, N_1 - 1$, $l=0, 1, \dots, N_2 - 1$, and $m=0, 1, \dots, N_3 - 1$, and with $\Delta_1=L_1/N_1$, $\Delta_2=L_2/N_2$, and $\Delta_3=L_3/N_3$. Consequently, the discrete Fourier transform (DFT) $F_{k,l,m}$ of $f_{k,l,m}$ is given by:

$$F_{k,l,m} = \frac{1}{N_1 N_2 N_3} \sum_{r=0}^{N_1-1} \sum_{s=0}^{N_2-1} \sum_{t=0}^{N_3-1} f_{r,s,t} \exp \left(-2\pi i \left(\frac{kr}{N_1} + \frac{ls}{N_2} + \frac{mt}{N_3} \right) \right) \quad \begin{cases} k = 0, 1, \dots, N_1 - 1 \\ l = 0, 1, \dots, N_2 - 1 \\ m = 0, 1, \dots, N_3 - 1 \end{cases} \quad (\text{A.1})$$

ω_{c_1} , ω_{c_2} , and ω_{c_3} are the components of the maximum spatial frequencies (wave numbers) present in the topology $f_{k,l,m}=f({}^1x_k, {}^2x_l, {}^3x_m)$ corresponding to the minimum wavelengths $\lambda_{1_{min}}$, $\lambda_{2_{min}}$ and $\lambda_{3_{min}}$, where $\omega_{c_1}=2\pi/\lambda_{1_{min}}$, $\omega_{c_2}=2\pi/\lambda_{2_{min}}$, and $\omega_{c_3}=2\pi/\lambda_{3_{min}}$. The number of sampling points in each direction must fulfill the criteria $N_1 > \omega_{c_1}L_1/\pi$, $N_2 > \omega_{c_2}L_2/\pi$, and $N_3 > \omega_{c_3}L_3/\pi$ to avoid aliasing which is a well known accuracy eroding artifact in Fourier transformation of the periodic sam-

pled topologies. Some important properties of $F_{k,l,m}$ worth mentioning considering the ensuing algorithm steps are:

$$\begin{aligned}
F_{-k,-l,-m} &= F_{k,l,m}^* & F_{N_1+k,N_2+l,N_3+m} &= F_{k,l,m} & F_{N_1-k,N_2-l,N_3-m} &= F_{-k,-l,-m} \\
F_{N_1-k,l,m} &= F_{-k,l,m} & F_{N_1-k,N_2-l,m} &= F_{-k,-l,m} & F_{N_1-k,l,N_3-m} &= F_{-k,l,-m} \\
F_{k,N_2-l,m} &= F_{k,-l,m} & F_{k,N_2-l,N_3-m} &= F_{k,-l,-m} & F_{k,l,N_3-m} &= F_{k,l,-m}
\end{aligned} \tag{A.2}$$

The spectral density $S_{k,l,m}$ of the topology function $f_{k,l,m}$ is defined as the Fourier transform of its autocorrelation function. The spectral density is sampled discretely over the intervals ${}^1x_k=[0, L_1]$, ${}^2x_l=[0, L_2]$, and ${}^3x_m=[0, L_3]$ as $S_{k,l,m}=S(\omega_k, \omega_l, \omega_m)$, where $\omega_k=2\pi k/L_1$, $\omega_l=2\pi l/L_2$, $\omega_m=2\pi m/L_3$ and $k=0, 1, \dots, N_1 - 1$, $l=0, 1, \dots, N_2 - 1$, $m=0, 1, \dots, N_3 - 1$. The discrete spectral density is related to $F_{k,l,m}$ by:

$$S_{k,l,m} \approx \frac{L_1 L_2 L_3}{(2\pi)^3} F_{k,l,m}^* F_{k,l,m} = \frac{L_1 L_2 L_3}{(2\pi)^3} |F_{k,l,m}|^2 \tag{A.3}$$

It follows from (A.2) and (A.3) that:

$$\begin{aligned}
S_{-k,-l,-m} &= S_{k,l,m}^* & S_{N_1+k,N_2+l,N_3+m} &= S_{k,l,m} & S_{N_1-k,N_2-l,N_3-m} &= S_{-k,-l,-m} \\
S_{N_1-k,l,m} &= S_{-k,l,m} & S_{N_1-k,N_2-l,m} &= S_{-k,-l,m} & S_{N_1-k,l,N_3-m} &= S_{-k,l,-m} \\
S_{k,N_2-l,m} &= S_{k,-l,m} & S_{k,N_2-l,N_3-m} &= S_{k,-l,-m} & S_{k,l,N_3-m} &= S_{k,l,-m}
\end{aligned} \tag{A.4}$$

The condition (A.4) implies that the spectral density is symmetric hence, it is uniquely defined only in the region $k=[0, N_1/2]$, $l=[0, N_2/2]$ and $m=[0, N_3/2]$.

Following the procedure outlined in [27, 84], the correlated random realizations of the discrete topology $f_{k,l,m}=f({}^1x_k, {}^2x_l, {}^3x_m)$ are generated for a given spectral density function $S_{k,l,m}=S(\omega_k, \omega_l, \omega_m)$ through following steps:

1. Identify cut-off frequencies ω_{1c} , ω_{2c} , and ω_{3c} considering physical constraints above which $S_{k,l,m}$ is zero (or approximately zero). Choose even integers N_1 , N_2 and N_3 for desired refinement and satisfying the aliasing avoiding conditions $N_1 > \omega_{c_1} L_1 / \pi$, $N_2 > \omega_{c_2} L_2 / \pi$, and $N_3 > \omega_{c_3} L_3 / \pi$.

2. Sample the spectral density, meanwhile enforcing the constraint (A.4) to obtain:

$$\begin{aligned}
S_{k,0,0} &= S\left(\frac{2\pi k}{N_1\Delta_1}, 0, 0\right), & k &= 0, 1, 2, \dots, N_1/2 \\
S_{N_1-k,0,0} &= S_{k,0,0}, & k &= N_1/2 + 1, \dots, N_1 - 1 \\
S_{0,l,0} &= S\left(0, \frac{2\pi l}{N_2\Delta_2}, 0\right), & l &= 0, 1, 2, \dots, N_2/2 \\
S_{0,N_2-l,0} &= S_{0,l,0}, & l &= N_2/2 + 1, \dots, N_2 - 1 \\
S_{0,0,m} &= S\left(0, 0, \frac{2\pi m}{N_3\Delta_3}\right), & m &= 0, 1, 2, \dots, N_3/2 \\
S_{0,0,N_3-m} &= S_{0,0,m}, & m &= N_3/2 + 1, \dots, N_3 - 1 \\
S_{k,l,m} &= S\left(\frac{2\pi k}{N_1\Delta_1}, \frac{2\pi l}{N_2\Delta_2}, \frac{2\pi m}{N_3\Delta_3}\right), & k &= 0, 1, 2, \dots, N_1/2, l = 0, 1, 2, \dots, N_2/2, \\
& & & m = 0, 1, 2, \dots, N_3/2 \\
S_{N_1-k,N_2-l,N_3-m} &= S_{k,l,m}, & k &= N_1/2 + 1, \dots, N_1 - 1, \\
& & & l = N_2/2 + 1, \dots, N_2 - 1, \\
& & & m = N_3/2 + 1, \dots, N_3 - 1 \\
S_{N_1-k,l,m} &= S\left(\frac{-2\pi k}{N_1\Delta_1}, \frac{2\pi l}{N_2\Delta_2}, \frac{2\pi m}{N_3\Delta_3}\right), & k &= 0, 1, 2, \dots, N_1/2, l = 0, 1, 2, \dots, N_2/2, \\
& & & m = 0, 1, 2, \dots, N_3/2 \\
S_{k,N_2-l,m} &= S\left(\frac{2\pi k}{N_1\Delta_1}, \frac{-2\pi l}{N_2\Delta_2}, \frac{2\pi m}{N_3\Delta_3}\right), & k &= 0, 1, 2, \dots, N_1/2, l = 0, 1, 2, \dots, N_2/2, \\
& & & m = 0, 1, 2, \dots, N_3/2 \\
S_{N_1-k,N_2-l,m} &= S\left(\frac{-2\pi k}{N_1\Delta_1}, \frac{-2\pi l}{N_2\Delta_2}, \frac{2\pi m}{N_3\Delta_3}\right), & k &= 0, 1, 2, \dots, N_1/2, l = 0, 1, 2, \dots, N_2/2, \\
& & & m = 0, 1, 2, \dots, N_3/2 \\
S_{k,l,N_3-m} &= S\left(\frac{-2\pi k}{N_1\Delta_1}, \frac{2\pi l}{N_2\Delta_2}, \frac{-2\pi m}{N_3\Delta_3}\right), & k &= 0, 1, 2, \dots, N_1/2, l = 0, 1, 2, \dots, N_2/2, \\
& & & m = 0, 1, 2, \dots, N_3/2 \\
S_{N_1-k,l,N_3-m} &= S\left(\frac{-2\pi k}{N_1\Delta_1}, \frac{2\pi l}{N_2\Delta_2}, \frac{-2\pi m}{N_3\Delta_3}\right), & k &= 0, 1, 2, \dots, N_1/2, l = 0, 1, 2, \dots, N_2/2, \\
& & & m = 0, 1, 2, \dots, N_3/2 \\
S_{k,N_2-l,N_3-m} &= S\left(\frac{2\pi k}{N_1\Delta_1}, \frac{-2\pi l}{N_2\Delta_2}, \frac{-2\pi m}{N_3\Delta_3}\right), & k &= 0, 1, 2, \dots, N_1/2, l = 0, 1, 2, \dots, N_2/2, \\
& & & m = 0, 1, 2, \dots, N_3/2
\end{aligned}
\tag{A.5}$$

3. Calculate the magnitude of $F_{k,l,m}$ given by relation (A.3) as:

$$|F_{k,l,m}| = \sqrt{\frac{(2\pi)^3}{L_1 L_2 L_3} S_{k,l,m}} \quad (\text{A.6})$$

(A.2) needs to be fulfilled hence, the phase angle of $F_{k,l,m}$ must be periodic in intervals $k=[0, N_1]$, $l=[0, N_2]$, $m=[0, N_3]$ and antisymmetric with respect to $k=N_1/2$, $l=N_2/2$, $m=N_3/2$. The phase angle $\beta_{k,l,m}$ is otherwise chosen randomly from a uniform distribution in range $[0, 2\pi]$. The $F_{k,l,m}$ is thus given by:

$$F_{k,l,m} = \sqrt{\frac{(2\pi)^3}{L_1 L_2 L_3} S_{k,l,m}} \exp(i\beta_{k,l,m}) \quad (\text{A.7})$$

4. To fulfill the aforementioned criterion for the phase angle, following steps are defined for sampling phase angle:

$$\begin{aligned} \beta_{0,0,0} &= \beta_{N_1/2,0,0} = \beta_{N_1/2,N_2/2,0} = \beta_{N_1/2,0,N_3/2} = 0 \\ \beta_{0,N_2/2,N_3/2} &= \beta_{0,0,N_3/2} = \beta_{0,N_2/2,0} = \beta_{N_1/2,N_2/2,N_3/2} = 0 \\ \beta_{k,0,0} &\text{ is random,} & k &= 0, 1, 2, \dots, N_1/2 \\ \beta_{N_1-k,0,0} &= -\beta_{k,0,0}, & k &= N_1/2 + 1, \dots, N_1 - 1 \\ \beta_{0,l,0} &\text{ is random,} & l &= 0, 1, 2, \dots, N_2/2 \\ \beta_{0,N_2-l,0} &= -\beta_{0,l,0}, & l &= N_2/2 + 1, \dots, N_2 - 1 \\ \beta_{0,0,m} &\text{ is random,} & m &= 0, 1, 2, \dots, N_3/2 \\ \beta_{0,0,N_3-m} &= -\beta_{0,0,m}, & m &= N_3/2 + 1, \dots, N_3 - 1 \\ \beta_{k,l,m} &\text{ is random,} & k &= 1, 2, \dots, N_1/2, l = 1, 2, \dots, N_2 - 1, \\ & & m &= 1, 2, \dots, N_3 - 1 \\ \beta_{N_1-k,N_2-l,N_3-m} &= -\beta_{k,l,m}, & k &= 1, 2, \dots, N_1/2, l = 1, 2, \dots, N_2 - 1, \\ & & m &= 1, 2, \dots, N_3 - 1 \end{aligned} \quad (\text{A.8})$$

5. By taking the inverse DFT of Eq. A.7, the correlated random discrete topology is obtained as:

$$f_{k,l,m} = \sum_{r=0}^{N_1-1} \sum_{s=0}^{N_2-1} \sum_{t=0}^{N_3-1} F_{r,s,t} \exp\left(-2\pi i \left(\frac{kr}{N_1} + \frac{ls}{N_2} + \frac{mt}{N_3}\right)\right) \begin{cases} k = 0, 1, \dots, N_1 - 1 \\ l = 0, 1, \dots, N_2 - 1 \\ m = 0, 1, \dots, N_3 - 1 \end{cases} \quad (\text{A.9})$$

Using Fast Fourier Transform (FFT) algorithms, the discrete Fourier transform (A.9) can be efficiently calculated. The resultant real valued realization of generated topologies are random correlated, with approximately zero mean depending on the numerical round-off errors. They are also periodic over the intervals $k=(0, N_1)$, $l=(0, N_2)$ and $m=(0, N_3)$ i.e. $f_{0,l,m}=f_{N_1,l,m}$ ($l=1, 2, \dots, N_2 - 1$, $m=1, 2, \dots, N_3 - 1$) etc.

It is to be noted that the steps 1. and 2. in the above procedure can be skipped if the discrete spectral density $S_{k,l,m}$ is available directly from the measurements of the topology $f_{k,l,m}$ such as a fiber misalignment topology.

BIBLIOGRAPHY

- [1] ABAQUS/Standard User's Manual, Version 6.16. Simulia, 2016.
- [2] ASTM D3410 / D3410M-16e1, Standard Test Method for Compressive Properties of Polymer Matrix Composite Materials with Unsupported Gage Section by Shear Loading. ASTM International, West Conshohocken, PA, 2016. 2016.
- [3] ASTM D6641 / D6641M-16e2, Standard Test Method for Compressive Properties of Polymer Matrix Composite Materials Using a Combined Loading Compression (CLC) Test Fixture. ASTM International, West Conshohocken, PA, 2016. 2016.
- [4] ASTM D695, Standard Test Method for Compressive Properties of Rigid Plastics. ASTM International, West Conshohocken, PA, 2016. 2015.
- [5] D. F. Adams and E. M. Odom. "Influence of specimen tabs on the compressive strength of a unidirectional composite material." In: *Journal of composite materials* 25.6 (1991), pp. 774–786.
- [6] D. F. Adams and J. S. Welsh. "The Wyoming combined loading compression (CLC) test method." In: *Journal of Composites, Technology and Research* 19.3 (1997), pp. 123–133.
- [7] O. Allix, N. Feld, E. Baranger, J.-M. Guimard, and C. Ha-Minh. "The compressive behaviour of composites including fiber kinking: modelling across the scales." In: *Meccanica* 49.11 (2014), pp. 2571–2586. DOI: [10.1007/s11012-013-9872-y](https://doi.org/10.1007/s11012-013-9872-y). URL: <https://doi.org/10.1007/s11012-013-9872-y>.
- [8] A. Argon. *Fracture of Composites, Treatise of Material Science and Technology (Vol. 1, pp. 79-114)*. 1972.
- [9] B. Basu, D. Tiwari, D. Kundu, and R. Prasad. "Is Weibull distribution the most appropriate statistical strength distribution for brittle materials?" In: *Ceramics International* 35.1 (2009), pp. 237–246.
- [10] S. Basu, A. M. Waas, and D. R. Ambur. "Compressive failure of fiber composites under multi-axial loading." In: *Journal of the Mechanics and Physics of Solids* 54.3 (2006), pp. 611–634. DOI: <https://doi.org/10.1016/j.jmps.2005.09.004>. URL: <http://www.sciencedirect.com/science/article/pii/S0022509605001948>.
- [11] Z. P. Bažant. "Size effect on structural strength: a review." In: *Archive of Applied Mechanics* 69.9 (1999), pp. 703–725. DOI: [10.1007/s004190050252](https://doi.org/10.1007/s004190050252). URL: <https://doi.org/10.1007/s004190050252>.

- [12] Z. P. Bažant, J.-J. H. Kim, I. M. Daniel, E. Becq-Giraudon, and G. Zi. "Size effect on compression strength of fiber composites failing by kink band propagation." In: *International journal of Fracture* 95.1 (1999), pp. 103–141. DOI: [10.1061/\(ASCE\)0733-9399\(1991\)117:11\(2609\)](https://doi.org/10.1061/(ASCE)0733-9399(1991)117:11(2609)). eprint: <http://ascelibrary.org/doi/pdf/10.1061/%28ASCE%290733-9399%281991%29117%3A11%282609%29>. URL: <http://ascelibrary.org/doi/abs/10.1061/%28ASCE%290733-9399%281991%29117%3A11%282609%29>.
- [13] B. A. Bednarczyk, J. Aboudi, and S. M. Arnold. "The effect of general statistical fiber misalignment on predicted damage initiation in composites." In: *Composites Part B: Engineering* 66 (2014), pp. 97–108. DOI: <https://doi.org/10.1016/j.compositesb.2014.04.014>. URL: <http://www.sciencedirect.com/science/article/pii/S135983681400170X>.
- [14] *Determination of Strain Rate Dependent Compressive Strengths of Carbon Fiber Composites*. 2005.
- [15] Q. Bing and C. Sun. "Modeling and testing strain rate-dependent compressive strength of carbon/epoxy composites." In: *Composites science and technology* 65.15-16 (2005), pp. 2481–2491.
- [16] M. Bishara, R. Rolfes, and O. Allix. "Revealing complex aspects of compressive failure of polymer composites – Part I: Fiber kinking at microscale." In: *Composite Structures* 169.Suppment C (2017). In Honor of Prof. Leissa, pp. 105–115. DOI: <https://doi.org/10.1016/j.compstruct.2016.10.092>. URL: <http://www.sciencedirect.com/science/article/pii/S026382231632222X>.
- [17] M. Bishara, M. Vogler, and R. Rolfes. "Revealing complex aspects of compressive failure of polymer composites – Part II: Failure interactions in multidirectional laminates and validation." In: *Composite Structures* 169.Suppment C (2017). In Honor of Prof. Leissa, pp. 116–128. DOI: <https://doi.org/10.1016/j.compstruct.2016.10.091>. URL: <http://www.sciencedirect.com/science/article/pii/S0263822316322322>.
- [18] Boeing Document D888-10026. *Test Methods for Advanced Composites, Revision A, Section C.2*. The Boeing Company, Seattle, Washington, 1996.
- [19] Boeing Specification Support Standard BSS 7260. *Advanced Composite Compression Tests*. The Boeing Company, Seattle, Washington, 1982.
- [20] Boeing. *787 dreamliner by design: Advanced composites use*. <https://www.boeing.com/commercial/787/by-design/#/advanced-composite-use>. Accessed: 2021-09-03. 2021.
- [21] B. Budiansky and N. Fleck. "Compressive failure of fibre composites." In: *Journal of the Mechanics and Physics of Solids* 41.1 (1993), pp. 183–211. DOI: [http://dx.doi.org/10.1016/0022-5096\(93\)90068-Q](http://dx.doi.org/10.1016/0022-5096(93)90068-Q). URL: <http://www.sciencedirect.com/science/article/pii/002250969390068Q>.

- [22] B Budiansky, N. Fleck, and J. Amazigo. "On kink-band propagation in fiber composites." In: *Journal of the Mechanics and Physics of Solids* 46.9 (1998), pp. 1637–1653. DOI: [https://doi.org/10.1016/S0022-5096\(97\)00042-2](https://doi.org/10.1016/S0022-5096(97)00042-2). URL: <http://www.sciencedirect.com/science/article/pii/S0022509697000422>.
- [23] B. Budiansky. "Micromechanics." In: *Computers & Structures* 16.1 (1983), pp. 3–12. DOI: [https://doi.org/10.1016/0045-7949\(83\)90141-4](https://doi.org/10.1016/0045-7949(83)90141-4). URL: <http://www.sciencedirect.com/science/article/pii/0045794983901414>.
- [24] B. Budiansky and N. A. Fleck. "Compressive kinking of fiber composites: a topical review." In: *Appl. Mech. Rev* 47.6 (1994), S246–S270.
- [25] E. Camarena, R. J. Clarke, and B. L. Ennis. "Development of a compressive failure model for carbon fiber composites and associated uncertainties." In: *Composites Science and Technology* 211 (2021), p. 108855.
- [26] G. Catalanotti and T. Sebaey. "An algorithm for the generation of three-dimensional statistically Representative Volume Elements of unidirectional fibre-reinforced plastics: Focusing on the fibres waviness." In: *Composite Structures* 227 (2019), p. 111272. DOI: <https://doi.org/10.1016/j.compstruct.2019.111272>. URL: <https://www.sciencedirect.com/science/article/pii/S0263822319321968>.
- [27] Cebon D, Newland DE. "Artificial generation of road surface topography by the inverse FFT method." In: *Vehicle System Dynamics* 12.1-3 (1983), pp. 160–165.
- [28] A. R. Clarke, G. Archenhold, N. C. Davidson, W. S. Slaughter, and N. A. Fleck. "Determining the power spectral density of the waviness of unidirectional glass fibres in polymer composites." In: *Applied Composite Materials* 2.4 (1995), pp. 233–243. DOI: [10.1007/BF00567194](https://doi.org/10.1007/BF00567194). URL: <https://doi.org/10.1007/BF00567194>.
- [29] A. Clarke, G Archenhold, and N. Davidson. "A novel technique for determining the 3D spatial distribution of glass fibres in polymer composites." In: *Composites science and technology* 55.1 (1995), pp. 75–91.
- [30] C. J. Creighton and T. Clyne. "The compressive strength of highly-aligned carbon-fibre/epoxy composites produced by pultrusion." In: *Composites science and technology* 60.4 (2000), pp. 525–533.
- [31] C. J. Creighton, M. Sutcliffe, and T. Clyne. "A multiple field image analysis procedure for characterisation of fibre alignment in composites." In: *Composites Part A: Applied Science and Manufacturing* 32.2 (2001), pp. 221–229.
- [32] R. Danzer, P. Supancic, J Pascual, and T. Lube. "Fracture statistics of ceramics—Weibull statistics and deviations from Weibull statistics." In: *Engineering Fracture Mechanics* 74.18 (2007), pp. 2919–2932.
- [33] B Daum, N Feld, O Allix, and R Rolfes. "A review of computational modeling approaches to compressive failure in laminates." In: *Composites Science and Technology* (May 2019). DOI: [10.1016/j.compscitech.2019.05.020](https://doi.org/10.1016/j.compscitech.2019.05.020).

- [34] B Daum and R Rolfes. "A micropolar approach to microbuckling problems in unidirectionally reinforced polymer composites." In: *Mechanics of Materials* (2021), p. 104112.
- [35] B. Daum, G. Gottlieb, N. Safdar, M. Brod, J.-H. Ohlendorf, and R. Rolfes. "A numerical investigation of the statistical size effect in non-crimp fabric laminates under homogeneous compressive loads." In: *Journal of Composite Materials* (2021), p. 00219983211057346.
- [36] P. Davidson and A. M. Waas. "Mechanics of kinking in fiber-reinforced composites under compressive loading." In: *Mathematics and Mechanics of Solids* 21.6 (2016), pp. 667–684. DOI: [10.1177/1081286514535422](https://doi.org/10.1177/1081286514535422). eprint: <https://doi.org/10.1177/1081286514535422>. URL: <https://doi.org/10.1177/1081286514535422>.
- [37] P. Davidson and A. M. Waas. "Probabilistic defect analysis of fiber reinforced composites using kriging and support vector machine based surrogates." In: *Composite Structures* 195 (2018), pp. 186–198. DOI: <https://doi.org/10.1016/j.compstruct.2018.03.007>. URL: <https://www.sciencedirect.com/science/article/pii/S026382231733948X>.
- [38] A Dean, J Reinoso, S Sahraee, and R Rolfes. "An invariant-based anisotropic material model for short fiber-reinforced thermoplastics: coupled thermo-plastic formulation." In: *Composites Part A: Applied Science and Manufacturing* 90 (2016), pp. 186–199.
- [39] A. Dean, N. Safdar, and R. Rolfes. "A Co-Rotational Based Anisotropic Elasto-Plastic Model for Geometrically Non-Linear Analysis of Fibre Reinforced Polymer Composites: Formulation and Finite Element Implementation." In: *Materials* 12.11 (2019), p. 1816.
- [40] Department of Aviation. *Tabbing Guide for Composite Test Specimens*. Tech. rep. U.S. Department of Transportation, Federal Aviation Administration, 2002.
- [41] E. Edge. "Stress-Based Grant-Sanders Method for Predicting Failure of Composite Laminates." In: *Composites Science and Technology* 58.7 (1998), pp. 1033–1041.
- [42] F. Edgren, L. E. Asp, and R. Joffe. "Failure of NCF composites subjected to combined compression and shear loading." In: *Composites Science and Technology* 66.15 (2006), pp. 2865–2877.
- [43] Elfouhaily T, Chapron B, Katsaros K, Vandemark D. "A unified directional spectrum for long and short wind-driven waves." In: *Journal of Geophysical Research: Oceans* 102.C7 (1997), pp. 15781–15796.

- [44] N. Feld, O. Allix, E. Baranger, and J.-M. Guimard. "Micro-mechanical prediction of UD laminates behavior under combined compression up to failure: influence of matrix degradation." In: *Journal of Composite Materials* 45.22 (2011), pp. 2317–2333. DOI: [10.1177/0021998311401084](https://doi.org/10.1177/0021998311401084). eprint: <https://doi.org/10.1177/0021998311401084>. URL: <https://doi.org/10.1177/0021998311401084>.
- [45] N. Feld, O. Allix, E. Baranger, and J.-M. Guimard. "A micromechanics-based mesomodel for unidirectional laminates in compression up to failure." In: *Journal of Composite Materials* 46.23 (2012), pp. 2893–2909. DOI: [10.1177/0021998311434170](https://doi.org/10.1177/0021998311434170). eprint: <https://doi.org/10.1177/0021998311434170>. URL: <https://doi.org/10.1177/0021998311434170>.
- [46] N. Fleck. "Compressive failure of fiber composites." In: *Advances in applied mechanics*. Ed. by J. Hutchinson and T. Wu. New York, NY: Academic Press, 1948-, 1997, pp. 43–117.
- [47] N. Fleck, L. Deng, and B. Budiansky. "Prediction of kink width in compressed fiber composites." In: *Journal of Applied Mechanics* 62.2 (1995), pp. 329–337.
- [48] N. Fleck and J. Shu. "Microbuckle initiation in fibre composites: a finite element study." In: *Journal of the Mechanics and Physics of Solids* 43.12 (1995), pp. 1887–1918.
- [49] GOM Correlate. *GOM—Precise Industrial 3D Metrology*. Braunschweig, Germany. URL: <https://www.gom.com/>.
- [50] K. W. Gan, T. Laux, S. T. Taher, J. M. Dulieu-Barton, and O. T. Thomsen. "A novel fixture for determining the tension/compression-shear failure envelope of multidirectional composite laminates." In: *Composite Structures* 184 (2018), pp. 662–673.
- [51] R. Glüge and S. Bucci. "Does convexity of yield surfaces in plasticity have a physical significance?" In: *Mathematics and Mechanics of Solids* 23.9 (2018), pp. 1364–1373.
- [52] E. Greenhalgh. *Failure analysis and fractography of polymer composites*. Elsevier, 2009.
- [53] J. Guimard, O. Allix, N. Pechnik, and P. Thevenet. "Statistical Energy and Failure Analysis of CFRP Compression Behavior Using a Uniaxial Microbuckling Model." In: *Journal of Composite Materials* 41.23 (2007), pp. 2807–2828. DOI: [10.1177/0021998307079980](https://doi.org/10.1177/0021998307079980). eprint: <https://doi.org/10.1177/0021998307079980>. URL: <https://doi.org/10.1177/0021998307079980>.
- [54] R. Gutkin, S. Pinho, P. Robinson, and P. Curtis. "Micro-mechanical modelling of shear-driven fibre compressive failure and of fibre kinking for failure envelope generation in CFRP laminates." In: *Composites Science and Technology* 70.8 (2010), pp. 1214–1222. DOI: <https://doi.org/10.1016/j.compscitech.2010.03.009>. URL: <http://www.sciencedirect.com/science/article/pii/S0266353810001107>.

- [55] R. Gutkin, S. Pinho, P. Robinson, and P. Curtis. "On the transition from shear-driven fibre compressive failure to fibre kinking in notched CFRP laminates under longitudinal compression." In: *Composites Science and Technology* 70.8 (2010), pp. 1223–1231. DOI: <https://doi.org/10.1016/j.compscitech.2010.03.010>. URL: <http://www.sciencedirect.com/science/article/pii/S0266353810001119>.
- [56] R. Gutkin, S. T. Pinho, P. Robinson, and P. Curtis. "Physical mechanisms associated with initiation and propagation of kink-bands." In: *Proceedings of the 13th European conference on composite materials (ECCM13), Stockholm, Sweden*. 2008.
- [57] T. HAYASHI. "On the shear instability of structures caused by compressive load." In: *Aircraft Design and Technology Meeting*. 1970, p. 770.
- [58] H. Hahn and J. Williams. "Compression Failure Mechanisms in Unidirectional Composites." In: *STP893-EB Composite Materials: Testing and Design (Seventh Conference)* (1986). DOI: <https://doi.org/10.1520/STP35345S>.
- [59] S.-Y. Hsu, T. Vogler, and S. Kyriakides. "Compressive Strength Predictions for Fiber Composites." In: *Journal of Applied Mechanics* 65.1 (1998), pp. 7–16.
- [60] S.-Y. Hsu, T. Vogler, and S. Kyriakides. "On the axial propagation of kink bands in fiber composites : Part ii analysis." In: *International Journal of Solids and Structures* 36.4 (1999), pp. 575–595. DOI: [https://doi.org/10.1016/S0020-7683\(98\)00030-4](https://doi.org/10.1016/S0020-7683(98)00030-4). URL: <http://www.sciencedirect.com/science/article/pii/S0020768398000304>.
- [61] Jacobs TDB, Junge T, Pastewka L. "Quantitative characterization of surface topography using spectral analysis." In: *Surface Topography: Metrology and Properties* 5.1 (2017), p. 013001. DOI: [10.1088/2051-672x/aa51f8](https://doi.org/10.1088/2051-672x/aa51f8).
- [62] P. Jelf and N. Fleck. "Compression failure mechanisms in unidirectional composites." In: *Journal of Composite Materials* 26.18 (1992), pp. 2706–2726.
- [63] H. M. Jensen and J. Christoffersen. "Kink band formation in fiber reinforced materials." In: *Journal of the Mechanics and Physics of Solids* 45.7 (1997), pp. 1121–1136. DOI: [https://doi.org/10.1016/S0022-5096\(96\)00126-3](https://doi.org/10.1016/S0022-5096(96)00126-3). URL: <http://www.sciencedirect.com/science/article/pii/S0022509696001263>.
- [64] A. M. Johnson and S. D. Ellen. "A theory of concentric, kink, and sinusoidal folding and of monoclinical flexuring of compressible, elastic multilayers: I. Introduction." In: *Tectonophysics* 21.4 (1974), pp. 301–339. DOI: [https://doi.org/10.1016/0040-1951\(74\)90001-8](https://doi.org/10.1016/0040-1951(74)90001-8). URL: <https://www.sciencedirect.com/science/article/pii/0040195174900018>.
- [65] D. P. Johnson, J. Morton, S. Kellas, and K. Jackson. "Scaling effects in sublaminar-level scaled composite laminates." In: *AIAA journal* 36.3 (1998), pp. 441–447.
- [66] A. Kaddour and M. Hinton. "Input data for test cases used in benchmarking triaxial failure theories of composites." In: *Journal of Composite Materials* 46.19–20 (2012), pp. 2295–2312.

- [67] Kay S, Hedley J, Lavender S, Nimmo-Smith A. "Light transfer at the ocean surface modeled using high resolution sea surface realizations." In: *Opt. Express* 19.7 (2011), pp. 6493–6504. DOI: [10.1364/OE.19.006493](https://doi.org/10.1364/OE.19.006493).
- [68] K. K. Kratmann, M. Sutcliffe, L. Lilleheden, R. Pyrz, and O. T. Thomsen. "A novel image analysis procedure for measuring fibre misalignment in unidirectional fibre composites." In: *Composites Science and Technology* 69.2 (2009), pp. 228–238.
- [69] S. Kyriakides, R. Arseculeratne, E. Perry, and K. Liechti. "On the compressive failure of fiber reinforced composites." In: *International Journal of Solids and Structures* 32.6 (1995). Time Dependent Problems in Mechanics, pp. 689 –738. DOI: [https://doi.org/10.1016/0020-7683\(94\)00157-R](https://doi.org/10.1016/0020-7683(94)00157-R). URL: <http://www.sciencedirect.com/science/article/pii/002076839400157R>.
- [70] S Kyriakides, E. Perry, and K. Liechti. "Instability and failure of fiber composites in compression." In: *Appl Mech Rev* 47.6 part 2 (1994), S262.
- [71] S. Kyriakides and A. E. Ruff. "Aspects of the Failure and Postfailure of Fiber Composites in Compression." In: *Journal of Composite Materials* 31.20 (1997), pp. 2000–2037. DOI: [10.1177/002199839703102001](https://doi.org/10.1177/002199839703102001). eprint: <https://doi.org/10.1177/002199839703102001>. URL: <https://doi.org/10.1177/002199839703102001>.
- [72] S. Lee and A. M. Waas. "Compressive response and failure of fiber reinforced unidirectional composites." In: *International Journal of Fracture* 100.3 (1999), pp. 275–306. DOI: [10.1023/A:1018779307931](https://doi.org/10.1023/A:1018779307931). URL: <https://doi.org/10.1023/A:1018779307931>.
- [73] S. Lemanski and M. Sutcliffe. "Compressive failure of finite size unidirectional composite laminates with a region of fibre waviness." In: *Composites Part A: Applied Science and Manufacturing* 43.3 (2012), pp. 435 –444. DOI: <https://doi.org/10.1016/j.compositesa.2011.11.007>. URL: <http://www.sciencedirect.com/science/article/pii/S1359835X11003782>.
- [74] S. Lemanski, M. Sutcliffe, and A. Scott. "Characterisation of waviness defects in industrial composite samples." In: *Proc. ICCM18, Korea* (2011).
- [75] Leopold C, Harder S, Philipkowski T, Liebig WV, Fiedler B. "Comparison of analytical approaches predicting the compressive strength of fibre reinforced polymers." In: *Materials* 10.12 (2018). DOI: [10.3390/ma11122517](https://doi.org/10.3390/ma11122517).
- [76] D. Liu, N. Fleck, and M. Sutcliffe. "Compressive strength of fibre composites with random fibre waviness." In: *Journal of the Mechanics and Physics of Solids* 52.7 (2004), pp. 1481 –1505. DOI: <https://doi.org/10.1016/j.jmps.2004.01.005>. URL: <http://www.sciencedirect.com/science/article/pii/S0022509604000110>.
- [77] K.-S. Liu and S. W. Tsai. "A progressive quadratic failure criterion for a laminate." In: *Failure Criteria in Fibre-Reinforced-Polymer Composites*. Elsevier, 2004, pp. 334–352.

- [78] W Michaeli, M Mannigel, and F Preller. "On the effect of shear stresses on the fibre failure behaviour in CFRP." In: *Composites science and technology* 69.9 (2009), pp. 1354–1357.
- [79] J. Monteiro, R. Campilho, E. Marques, and L. Da Silva. "Experimental estimation of the mechanical and fracture properties of a new epoxy adhesive." In: *Applied Adhesion Science* 3.1 (2015), pp. 1–17.
- [80] A. B. D. Morais. "Modelling Lamina Longitudinal Compression Strength of Carbon Fibre Composite Laminates." In: *Journal of Composite Materials* 30.10 (1996), pp. 1115–1131. DOI: [10.1177/002199839603001003](https://doi.org/10.1177/002199839603001003). eprint: <https://doi.org/10.1177/002199839603001003>. URL: <https://doi.org/10.1177/002199839603001003>.
- [81] A. B. D. Morais. "Prediction of the Layer Longitudinal Compression Strength." In: *Journal of Composite Materials* 34.21 (2000), pp. 1808–1820. DOI: [10.1106/9XG6-F8T7-079T-YAHC](https://doi.org/10.1106/9XG6-F8T7-079T-YAHC). eprint: <https://doi.org/10.1106/9XG6-F8T7-079T-YAHC>. URL: <https://doi.org/10.1106/9XG6-F8T7-079T-YAHC>.
- [82] A. B. D. Morais and A. T. Marques. "A Micromechanical Model for the Prediction of the Lamina Longitudinal Compression Strength of Composite Laminates." In: *Journal of Composite Materials* 31.14 (1997), pp. 1397–1412. DOI: [10.1177/002199839703101403](https://doi.org/10.1177/002199839703101403). eprint: <https://doi.org/10.1177/002199839703101403>. URL: <https://doi.org/10.1177/002199839703101403>.
- [83] D. NF and G. IJ. *Determination of most needed, potentially possible improvements in materials for ballistic and space vehicles*. Tech. Rep. TISR60SD389. General Electric Co., 1960.
- [84] Newland DE. *An introduction to random vibrations and spectral analysis*. Dover Publications, Inc, Mineola, New York, 1984.
- [85] N. Q. Nguyen, M. Mehdikhani, I. Straumit, L. Gorbatikh, L. Lessard, and S. V. Lomov. "Micro-CT measurement of fibre misalignment: Application to carbon/epoxy laminates manufactured in autoclave and by vacuum assisted resin transfer moulding." In: *Composites Part A: Applied Science and Manufacturing* 104 (2018), pp. 14–23.
- [86] K. Oguni, C. Y. Tan, and G. Ravichandran. "Failure Mode Transition in Unidirectional E-Glass/Vinylester Composites under Multiaxial Compression." In: *Journal of Composite Materials* 34.24 (2000), pp. 2081–2097. DOI: [10.1177/002199800772661912](https://doi.org/10.1177/002199800772661912).
- [87] B. Paluch. "Analysis of Geometric Imperfections Affecting the Fibers in Unidirectional Composites." In: *Journal of Composite Materials* 30.4 (1996), pp. 454–485. DOI: [10.1177/002199839603000403](https://doi.org/10.1177/002199839603000403). eprint: <https://doi.org/10.1177/002199839603000403>. URL: <https://doi.org/10.1177/002199839603000403>.

- [88] M. R. Piggott. "A theoretical framework for the compressive properties of aligned fibre composites." In: *Journal of Materials Science* 16.10 (1981), pp. 2837–2845. DOI: [10.1007/BF02402848](https://doi.org/10.1007/BF02402848). URL: <https://doi.org/10.1007/BF02402848>.
- [89] S. Pimenta, R. Gutkin, S. Pinho, and P. Robinson. "A micromechanical model for kink-band formation: Part I — Experimental study and numerical modelling." In: *Composites Science and Technology* 69.7 (2009), pp. 948–955. DOI: <https://doi.org/10.1016/j.compscitech.2009.02.010>. URL: <http://www.sciencedirect.com/science/article/pii/S026635380900061X>.
- [90] P. Prabhakar and A. M. Waas. "Interaction between kinking and splitting in the compressive failure of unidirectional fiber reinforced laminated composites." In: *Composite Structures* 98.Supplement C (2013), pp. 85–92. DOI: <https://doi.org/10.1016/j.compstruct.2012.11.005>.
- [91] T. M. Ricks, T. E. Lacy Jr, E. J. Pineda, B. A. Bednarczyk, and S. M. Arnold. "Computationally efficient High-Fidelity Generalized Method of Cells micromechanics via order-reduction techniques." In: *Composite Structures* 156 (2016), pp. 2–9.
- [92] B. W. Rosen. "Fiber composite materials." In: *American Society for Metals, Metals Park, Ohio* (1965), p. 37.
- [93] N. Safdar, B. Daum, and R. Rolfes. "A numerical prediction of failure probability under combined compression-shear loading for unidirectional fiber reinforced composites." In: *Mechanics of Materials* (2022), p. 104352. DOI: <https://doi.org/10.1016/j.mechmat.2022.104352>. URL: <https://www.sciencedirect.com/science/article/pii/S0167663622001284>.
- [94] N. Safdar, B. Daum, R. Rolfes, and O. Allix. "The representation of fiber misalignment distributions in numerical modeling of compressive failure of fiber reinforced polymers." In: *Virtual Design and Validation*. Ed. by P. Wriggers, O. Allix, and C. Weißenfels. Springer International Publishing, 2020, pp. 147–166. URL: https://link.springer.com/chapter/10.1007/978-3-030-38156-1_{_}8.
- [95] N Safdar, B Daum, S Scheffler, and R Rolfes. "Experimental determination of a probabilistic failure envelope for carbon fiber reinforced polymers under combined compression-shear loads." In: *International Journal of Solids and Structures* (2022), p. 111585.
- [96] H Schuerch. "Prediction of compressive strength in uniaxial boron fiber-metal matrix composite materials." In: *AIAA journal* 4.1 (1966), pp. 102–106.
- [97] C. R. Schultheisz and A. M. Waas. "Compressive failure of composites, part I: Testing and micromechanical theories." In: *Progress in Aerospace Sciences* 32.1 (1996), pp. 1–42. DOI: [https://doi.org/10.1016/0376-0421\(94\)00002-3](https://doi.org/10.1016/0376-0421(94)00002-3). URL: <http://www.sciencedirect.com/science/article/pii/0376042194000023>.

- [98] T. Sebaey, G. Catalanotti, and N. O'Dowd. "A microscale integrated approach to measure and model fibre misalignment in fibre-reinforced composites." In: *Composites Science and Technology* 183 (2019), p. 107793. DOI: <https://doi.org/10.1016/j.compscitech.2019.107793>. URL: <https://www.sciencedirect.com/science/article/pii/S0266353819316537>.
- [99] W. S. Slaughter, N. A. Fleck, and B. Budiansky. "Compressive Failure of Fiber Composites: The Roles of Multiaxial Loading and Creep." In: *J. Eng. Mater. Technol* 115 (1993), pp. 308–313.
- [100] W. Slaughter and N. Fleck. "Microbuckling of fiber composites with random initial fiber waviness." In: *Journal of the Mechanics and Physics of Solids* 42.11 (1994), pp. 1743–1766. DOI: [https://doi.org/10.1016/0022-5096\(94\)90070-1](https://doi.org/10.1016/0022-5096(94)90070-1). URL: <http://www.sciencedirect.com/science/article/pii/0022509694900701>.
- [101] P. Soden, M. Hinton, and A. Kaddour. "Biaxial test results for strength and deformation of a range of E-glass and carbon fibre reinforced composite laminates: failure exercise benchmark data." In: *Failure Criteria in Fibre-Reinforced-Polymer Composites*. Elsevier, 2004, pp. 52–96.
- [102] C Soutis. "Fibre reinforced composites in aircraft construction." In: *Progress in Aerospace Sciences* 41.2 (2005), pp. 143–151. DOI: <https://doi.org/10.1016/j.paerosci.2005.02.004>.
- [103] P. S. Steif. "A model for kinking in fiber composites - I. Fiber breakage via micro-buckling." In: *International Journal of Solids and Structures* 26.5 (1990), pp. 549–561. DOI: [https://doi.org/10.1016/0020-7683\(90\)90028-T](https://doi.org/10.1016/0020-7683(90)90028-T). URL: <http://www.sciencedirect.com/science/article/pii/002076839090028T>.
- [104] P. S. Steif. "A model for kinking in fiber composites—II. Kink band formation." In: *International Journal of Solids and Structures* 26.5 (1990), pp. 563–569. DOI: [https://doi.org/10.1016/0020-7683\(90\)90029-U](https://doi.org/10.1016/0020-7683(90)90029-U). URL: <https://www.sciencedirect.com/science/article/pii/002076839090029U>.
- [105] Q. Sun, H. Guo, G. Zhou, Z. Meng, Z. Chen, H. Kang, S. Keten, and X. Su. "Experimental and computational analysis of failure mechanisms in unidirectional carbon fiber reinforced polymer laminates under longitudinal compression loading." In: *Composite Structures* 203 (2018), pp. 335–348. DOI: <https://doi.org/10.1016/j.compstruct.2018.06.028>.
- [106] Q. Sun, G. Zhou, H. Guo, Z. Meng, Z. Chen, H. Liu, H. Kang, and X. Su. "Failure mechanisms of cross-ply carbon fiber reinforced polymer laminates under longitudinal compression with experimental and computational analyses." In: *Composites Part B: Engineering* 167 (2019), pp. 147–160. DOI: <https://doi.org/10.1016/j.compositesb.2018.12.041>. URL: <https://www.sciencedirect.com/science/article/pii/S1359836818330294>.

- [107] Q. Sun, G. Zhou, Z. Meng, H. Guo, Z. Chen, H. Liu, H. Kang, S. Keten, and X. Su. "Failure criteria of unidirectional carbon fiber reinforced polymer composites informed by a computational micromechanics model." In: *Composites Science and Technology* 172 (2019), pp. 81–95. DOI: <https://doi.org/10.1016/j.compscitech.2019.01.012>. URL: <https://www.sciencedirect.com/science/article/pii/S0266353818323704>.
- [108] W. Sun, A. P. Vassilopoulos, and T. Keller. "Finite element analysis of initial imperfection effects on kinking failure of unidirectional glass fiber-reinforced polymer composites." In: *Composite Structures* 203 (2018), pp. 50–59. DOI: <https://doi.org/10.1016/j.compstruct.2018.07.010>. URL: <http://www.sciencedirect.com/science/article/pii/S0263822318309425>.
- [109] M. Sutcliffe. "Modelling the effect of size on compressive strength of fibre composites with random waviness." In: *Composites Science and Technology* 88.Supplement C (2013), pp. 142–150. DOI: <https://doi.org/10.1016/j.compscitech.2013.09.002>. URL: <http://www.sciencedirect.com/science/article/pii/S0266353813003552>.
- [110] M. Sutcliffe, S. Lemanski, and A. Scott. "Measurement of fibre waviness in industrial composite components." In: *Composites Science and Technology* 72.16 (2012), pp. 2016–2023. DOI: <https://doi.org/10.1016/j.compscitech.2012.09.001>. URL: <http://www.sciencedirect.com/science/article/pii/S0266353812003235>.
- [111] O. T. Thomsen and K. K. Kratmann. "Experimental characterisation of parameters controlling the compressive failure of pultruded unidirectional carbon fibre composites." In: *Applied Mechanics and Materials*. Vol. 24. Trans Tech Publ. 2010, pp. 15–22.
- [112] J.-L. Tsai and C. Sun. "Strain rate effect on in-plane shear strength of unidirectional polymeric composites." In: *Composites Science and Technology* 65.13 (2005), pp. 1941–1947.
- [113] J. Tsai and C. Sun. "Dynamic compressive strengths of polymeric composites." In: *International journal of solids and structures* 41.11-12 (2004), pp. 3211–3224.
- [114] L. Varandas, G. Catalanotti, A. Melro, R. Tavares, and B. Falzon. "Micromechanical modelling of the longitudinal compressive and tensile failure of unidirectional composites: The effect of fibre misalignment introduced via a stochastic process." In: *International Journal of Solids and Structures* 203 (2020), pp. 157–176. DOI: <https://doi.org/10.1016/j.ijsolstr.2020.07.022>. URL: <https://www.sciencedirect.com/science/article/pii/S0020768320302997>.
- [115] M. Vogler, R. Rolfes, and P. Camanho. "Modeling the inelastic deformation and fracture of polymer composites - Part I: Plasticity model." In: *Mechanics of Materials* 59 (2013), pp. 50–64. DOI: <https://doi.org/10.1016/j.mechmat>.

- 2012.12.002. URL: <http://www.sciencedirect.com/science/article/pii/S016766361200213X>.
- [116] T. Vogler, S.-Y. Hsu, and S Kyriakides. "Composite failure under combined compression and shear." In: *International Journal of Solids and Structures* 37.12 (2000), pp. 1765–1791.
- [117] T. Vogler, S.-Y. Hsu, and S Kyriakides. "On the initiation and growth of kink bands in fiber composites. Part II: analysis." In: *International Journal of Solids and Structures* 38.15 (2001), pp. 2653–2682.
- [118] T. Vogler and S Kyriakides. "On the initiation and growth of kink bands in fiber composites: Part I. experiments." In: *International Journal of Solids and Structures* 38.15 (2001), pp. 2639–2651.
- [119] C. Völlmecke and R. A. E. Zidek. "Geometric modelling of kink banding in multidirectional composites." In: *Journal of Engineering Mathematics* 95.1 (2015), pp. 173–191. DOI: [10.1007/s10665-014-9749-7](https://doi.org/10.1007/s10665-014-9749-7). URL: <https://doi.org/10.1007/s10665-014-9749-7>.
- [120] M. A. Wadee, C. Völlmecke, J. F. Haley, and S. Yiatros. "Geometric modelling of kink banding in laminated structures." In: *Philosophical Transactions of the Royal Society of London A: Mathematical, Physical and Engineering Sciences* 370.1965 (2012), pp. 1827–1849. DOI: [10.1098/rsta.2011.0380](https://doi.org/10.1098/rsta.2011.0380). eprint: <http://rsta.royalsocietypublishing.org/content/370/1965/1827.full.pdf>. URL: <http://rsta.royalsocietypublishing.org/content/370/1965/1827>.
- [121] M. A. Wadee and C. Völlmecke. "Semi-analytical modelling of buckling driven delamination in uniaxially compressed damaged plates." In: *IMA Journal of Applied Mathematics* 76.1 (2011), pp. 120–145. DOI: [10.1093/imamat/hxq062](https://doi.org/10.1093/imamat/hxq062). eprint: [/oup/backfile/content_public/journal/imamat/76/1/10.1093/imamat/hxq062/2/hxq062.pdf](http://oup/backfile/content_public/journal/imamat/76/1/10.1093/imamat/hxq062/2/hxq062.pdf). URL: <http://dx.doi.org/10.1093/imamat/hxq062>.
- [122] P. M. Wegner, D. F. Adams, et al. *Verification of the combined load compression (CLC) test method*. Tech. rep. University of Wyoming, 2000.
- [123] W. Weibull. "A statistical distribution function of wide applicability." In: *Journal of applied mechanics* (1951).
- [124] J. Welsh and D. Adams. "Current status of compression test methods for composite materials." In: *SAMPE journal* 33.1 (1997), pp. 35–43.
- [125] M. Whiteside, S. Pinho, and P. Robinson. "Stochastic failure modelling of unidirectional composite ply failure." In: *Reliability Engineering & System Safety* 108 (2012), pp. 1–9. DOI: <https://doi.org/10.1016/j.res.2012.05.006>. URL: <http://www.sciencedirect.com/science/article/pii/S0951832012000890>.
- [126] D Wilhelmsson and L. Asp. "A high resolution method for characterisation of fibre misalignment angles in composites." In: *Composites Science and Technology* 165 (2018), pp. 214–221.

- [127] D. Wilhelmsson, R. Gutkin, F. Edgren, and L. Asp. "An experimental study of fibre waviness and its effects on compressive properties of unidirectional NCF composites." In: *Composites Part A: Applied Science and Manufacturing* 107 (2018), pp. 665–674. DOI: <https://doi.org/10.1016/j.compositesa.2018.02.013>. URL: <http://www.sciencedirect.com/science/article/pii/S1359835X1830054X>.
- [128] M. Wilkins, R. Streit, and J. Reaugh. *Cumulative-strain-damage model of ductile fracture: simulation and prediction of engineering fracture tests*. Tech. rep. Lawrence Livermore National Lab., CA (USA); Science Applications, Inc., San . . . , 1980.
- [129] J. L. Wind, S. Steffensen, and H. M. Jensen. "Comparison of a composite model and an individually fiber and matrix discretized model for kink band formation." In: *International Journal of Non-Linear Mechanics* 67 (2014), pp. 319–325. DOI: <https://doi.org/10.1016/j.ijnonlinmec.2014.10.005>. URL: <http://www.sciencedirect.com/science/article/pii/S0020746214001991>.
- [130] M. Wisnom. "Size effects in the testing of fibre-composite materials." In: *Composites Science and Technology* 59.13 (1999), pp. 1937–1957.
- [131] M. Wisnom, J. Atkinson, and M. Jones. "Reduction in compressive strain to failure with increasing specimen size in pin-ended buckling tests." In: *Composites science and technology* 57.9-10 (1997), pp. 1303–1308.
- [132] M. R. Wisnom. "The effect of specimen size on the bending strength of unidirectional carbon fibre-epoxy." In: *Composite Structures* 18.1 (1991), pp. 47–63. DOI: [https://doi.org/10.1016/0263-8223\(91\)90013-0](https://doi.org/10.1016/0263-8223(91)90013-0). URL: <http://www.sciencedirect.com/science/article/pii/0263822391900130>.
- [133] M. R. Wisnom. "Nonlinear analysis of misaligned unidirectional carbon fibre-epoxy compression specimens." In: *Composites Engineering* 3.6 (1993), pp. 547–556.
- [134] Wolfram Research Inc. *Mathematica, Version 11.1.1*. URL: <https://www.wolfram.com/mathematica>.
- [135] C. Yerramalli and A. Waas. "A failure criterion for fiber reinforced polymer composites under combined compression–torsion loading." In: *International Journal of Solids and Structures* 40.5 (2003), pp. 1139–1164.
- [136] C. S. Yerramalli and A. M. Waas. "The effect of fiber diameter on the compressive strength of composites-A 3D finite element based study." In: *Computer Modeling in Engineering and Sciences* 6 (2004), pp. 1–16.
- [137] S. Yurgartis. "Measurement of small angle fiber misalignments in continuous fiber composites." In: *Composites Science and Technology* 30.4 (1987), pp. 279–293. DOI: [https://doi.org/10.1016/0266-3538\(87\)90016-9](https://doi.org/10.1016/0266-3538(87)90016-9). URL: <http://www.sciencedirect.com/science/article/pii/0266353887900169>.

- [138] R. A. Zidek and C. Völlmecke. “On the influence of material non-linearities in geometric modeling of kink band instabilities in unidirectional fiber composites.” In: *International Journal of Non-Linear Mechanics* 62.Supplement C (2014), pp. 23–32. DOI: <https://doi.org/10.1016/j.ijnonlinmec.2014.02.004>. URL: <http://www.sciencedirect.com/science/article/pii/S0020746214000262>.
- [139] F. W. Zok. “On weakest link theory and Weibull statistics.” In: *Journal of the American Ceramic Society* 100.4 (2017), pp. 1265–1268.

CURRICULUM VITAE

PERSONAL DATA

Name Nabeel Safdar
Date of Birth 26.02.1991
Place of Birth Mandi Bahauddin, Pakistan
Citizen of Germany

ACADEMIC EDUCATION AND CAREER

- 2016– 2022 Research Associate at Institute of Structural Analysis,
Gottfried Wilhelm Leibniz Universität Hannover
Hanover, Germany
- 2016 Student Research Assistant for five months at Chair of Applied
Laser Technologies, Ruhr University Bochum
Bochum, Germany
- 2014 Student Research Assistant for six months at Interdisciplinary
Centre for Advanced Materials Simulation, Ruhr University
Bochum
Bochum, Germany
- 2013– 2016 Masters studies at Ruhr University Bochum
Bochum, Germany
Final degree: Master of Science (M.Sc.) in Computational Engi-
neering
- 2008– 2012 Bachelor studies at University of Engineering and Technology
Lahore
Lahore, Pakistan
Final degree: Bachelor of Science (B.Sc.) in Industrial and Manu-
facturing Engineering
- 2004 – 2008 Secondary and Higher secondary school
Mandi Bahauddin, Pakistan
Final degree: (University entrance qualification)

PUBLICATIONS

PUBLICATIONS

- (1) **N. Safdar**, B. Daum, and R. Rolfes. A numerical prediction of failure probability under combined compression-shear loading for unidirectional fiber reinforced composites. *Mechanics of Materials*, 2022.
DOI: <https://doi.org/10.1016/j.mechmat.2022.104352>
- (2) **N. Safdar**, B. Daum, S. Scheffler, and R. Rolfes. Experimental determination of a probabilistic failure envelope for carbon fiber reinforced polymers under combined compression-shear loads. *International Journal of Solids and Structures*, 2022.
DOI: <https://doi.org/10.1016/j.ijsolstr.2022.111585>
- (3) B. Daum, G. Gottlieb, **N. Safdar**, M. Brod, J.H. Ohlendorf, and R. Rolfes. A numerical investigation of the statistical size effect in non-crimp fabric laminates under homogeneous compressive loads. *Journal of Composite Materials*, 2021.
DOI: <https://doi.org/10.1177/00219983211057346>
- (4) A. Dean, **N. Safdar**, and R. Rolfes. A Co-Rotational Based Anisotropic Elasto-Plastic Model for Geometrically Non-Linear Analysis of Fibre Reinforced Polymer Composites: Formulation and Finite Element Implementation. *Materials*, 2019.
DOI: <https://doi.org/10.3390/ma12111816>
- (5) **N. Safdar**, B. Daum, R. Rolfes, and O. Allix. The Representation of Fiber Misalignment Distributions in Numerical Modeling of Compressive Failure of Fiber Reinforced Polymers. *Springer book "Lecture Notes in Application and Computational Mechanics"*, 2019.
DOI: https://doi.org/10.1007/978-3-030-38156-1_8
- (6) **N. Safdar**, B. Daum, and R. Rolfes. Compressive Failure Surface Modelling for the Unidirectional Fibre Reinforced Composites under Plainstress. *Conference paper in 6th European Conference on Computational Mechanics, Glasgow*, 2018.

CONFERENCE PRESENTATIONS

- (1) **N. Safdar**, N. Safdar, B. Daum, S.Scheffler, and R. Rolfes. Probabilistic Failure Prediction under Combined in-plane Compression-Shear Loading for Unidirectional Fiber Reinforced Composites. *8th ECCOMAS Thematic Conference on The Mechanical Response of Composites*, (Online event: Composites 2021), 2021.
- (2) **N. Safdar**, R. Rolfes, B. Daum, and S.Scheffler. Experimental Characterization of Fibre Waviness and Probabilistic Compressive Failure Surface of Continuous Unidirectional Fibre Reinforced Composites. *7th ECCOMAS Thematic Conference on the Mechanical Response of Composites: COMPOSITES 2019*, Girona, Spain, 2019.
- (3) **N. Safdar**, R. Rolfes, O. Allix, and B. Daum. A Stochastic Approach for Compressive Failure Analysis of Composites. *IRTG1627 colloquium at Leibniz University Hannover*, Hannover, Germany, 2019.
- (4) **N. Safdar**, B. Daum, and R. Rolfes. Stochastic Compressive Failure Surface Modelling for the Unidirectional Fibre Reinforced Composites under Plainstress. *6th European Conference on Computational Mechanics*, Glasgow, Scotland, 2018.

EIDESSTATTLICHEVERSICHERUNG

Ich erkläre hiermit, dass ich

- 1.) die Regeln der geltenden Promotionsordnung kenne und eingehalten habe und mit einer Prüfung nach den Bestimmungen der Promotionsordnung einverstanden bin,
- 2.) die Dissertation selbst verfasst habe, keine Textabschnitte von Dritten oder eigener Prüfungsarbeiten ohne Kennzeichnung übernommen habe und alle von mir benutzten Hilfsmittel und Quellen in meiner Arbeit angegeben habe,
- 3.) Dritten weder unmittelbar noch mittelbar geldwerte Leistungen für Vermittlungstätigkeiten oder für die inhaltliche Ausarbeitung der Dissertation erbracht habe,
- 4.) die Dissertation noch nicht als Prüfungsarbeit für eine staatliche oder andere wissenschaft-liche Prüfung eingereicht habe,
- 5.) nicht die gleiche oder eine in wesentlichen Teilen ähnliche Arbeit und auch nicht eine andere Arbeit bei einer anderen Hochschule als Dissertation eingereicht habe,
- 6.) damit einverstanden bin, dass die Dissertation auch zum Zwecke der Überprüfung der Einhaltung allgemein geltender wissenschaftlicher Standards genutzt wird, insbesondere auch unter Verwendung elektronischer Datenverarbeitungsprogramme.

Hannover, den 17.05.2022

Nabeel Safdar

Mitteilungen des Instituts für Statik und Dynamik der Leibniz Universität Hannover

1	R. Rolfes/ C. Hühne	Eröffnungskolloquium (Tagungsband)	2005
2	H. Rothert/ M. Kaliske/ L. Nasdala	Entwicklung von Materialmodellen zur Alterung von Elastomerwerkstoffen unter besonderer Berücksichtigung des Sauerstoffeinflusses (DFG-Abschlußbericht)	2005
3	L. Nasdala	Simulation von Materialinelastizitäten bei Nano-, Mikro- und Makrostrukturen – Stabilitätsprobleme, Schädigungs- und Alterungsprozesse bei Kohlenstoffnanoröhren und Elastomerwerkstoffen (Habilitationsschrift)	2005
4	C. Hühne	Robuster Entwurf beulgefährdeter, unverteilter Kreiszyinderschalen aus Faserverbundwerkstoff (Dissertationsschrift)	2006
5	L. Nasdala/ K.-U. Schröder	Finite Element Applications in Structural Analysis (Skript zur Hörsaalübung)	2006
6		Klausuraufgabensammlung, 4. Auflage	2007
7	R. Rolfes/ W.-J. Gerasch/ D. Rotert	Vorlesung Tragwerksdynamik	2007
8	K.-H. Elmer/ K. Betke/ Th. Neumann	Standardverfahren zur Ermittlung und Bewertung der Belastung der Meeresumwelt durch die Schallimmission von Offshore-Windenergieanlagen (Abschlussbericht zum BMU-Forschungsvorhaben)	2007
9	K.-U. Schröder	Zur nichtlinearen Berechnung von Stahlbeton- und Verbundbauteilen (Dissertationsschrift)	2007
10	G. Ernst	Multiscale Analysis of Textile Composites – Stiffness and Strength (Dissertationsschrift)	2008

11	G. Haake	Systemidentifikation mit Autoregressiven Modellen und Validierung numerischer Strukturmodelle bei Offshore-Windenergieanlagen (Dissertationsschrift)	2010
12	T. Griebmann	Dynamisches Tragverhalten von Stahlbetonbiegebalken im Experiment und in der Simulation (Dissertationsschrift)	2011
13	S. Zerbst	Global Approach for Early Damage Detection on Rotor Blades of Wind Energy Converters (Dissertationsschrift)	2011
14	N. Wieczorek	Semiaktive Schwingungsdämpfung leichter Fußgängerbrückenkonstruktionen (Dissertationsschrift)	2011
15	B. Kriegesmann	Probabilistic Design of Thin-Walled Fiber Composite Structures (Dissertationsschrift)	2012
16	J. Reetz	Schadensdiagnose an Tragstrukturen von Windenergieanlagen mit der Multiparameter-Eigenwertproblem-Methode (Dissertationsschrift)	2012
17	R. Rolfes/ D. Rotert	Vorlesung Baustatik	2012
18	R. Rolfes/ D. Rotert	Vorlesung Stabtragwerke	2012
19	H. Krüger	Ein physikalisch basiertes Ermüdungsschädigungsmodell zur Degradationsberechnung von Faser-Kunststoff-Verbunden (Dissertationsschrift)	2012
20	S. Czichon	Multi scale Failure Analysis of Fibre Reinforced Polymers with production induced Porosity Defects (Dissertationsschrift)	2013
21	T. Pahn	Inverse Load Calculation for Offshore Wind Turbines (Dissertationsschrift)	2013
22	M. Fricke/ B. Neddermann/ A. Lübben/ J. Gabriel	Realistische Hydroschallszenarien auf der Basis von Prognosemodellen und Monitoring für den Bau von Offshore-Windparks in der deutschen Nordsee („HyproWind“) (Abschlussbericht zum BMU-Forschungsvorhaben)	2014
23	M. Vogler	Anisotropic Material Models for Fiber Reinforced Polymers (Dissertationsschrift)	2014

24	M. Fricke	Ein physikalisch basiertes Gesamtmodell für hydroakustische Immissionsprognosen bei Offshore-Pfahlrammungen (Dissertationsschrift)	2015
25	M. Häckell	A holistic evaluation concept for long-term structural health monitoring (Dissertationsschrift)	2015
26	J. Rustemeier	Optimierung von Blasenschleiern zur Minderung von Unterwasser-Rammschall (Dissertationsschrift)	2016
27	S. Hühne	A two-way loose coupling procedure for buckling and damage analysis of composite structures (Dissertationsschrift)	2016
28	A. Meurer	Filtering Geometric Imperfection Patterns for Analysis and Design of Composite Shell Structures (Dissertationsschrift)	2017
29	A. Dean	Material Modeling of Short Fiber Reinforced Polymeric Composites: Theory, Numerical Aspects, and Applications (Dissertationsschrift)	2017
30	M. Bishara	Compressive Failure of Polymer Composites Including Fiber Kinking and Interaction of Failure Mechanisms (Dissertationsschrift)	2017
31	K. Schröder	Advanced Model Updating Strategies for Structural Dynamic Systems (Dissertationsschrift)	2018
32	S. Tsiapoki	Transmissibility-Based Monitoring and Combination of Damage Detection Decisions within a Holistic Structural Health Monitoring Framework (Dissertationsschrift)	2018
33	S. R. Nabavi	Failure analysis of polycrystalline silicon-based photovoltaic modules considering the effects of residual stresses and mechanical loading (Dissertationsschrift)	2018
34	S. Scheffler	Ein neuer Modellierungsansatz zur systematischen numerischen Untersuchung des Versagensverhaltens von Verbindungen in FVK (Dissertationsschrift)	2018
35	J. Häfele	A numerically efficient and holistic approach to design optimization of offshore wind turbine jacket substructures (Dissertationsschrift)	2019
36	C. Hübler	Efficient probabilistic analysis of offshore wind turbines based on time-domain simulations (Dissertationsschrift)	2019

37	M. Akterskaia	Global-local progressive failure analysis of composite panels including skin-stringer debonding and intralaminar damage (Dissertationsschrift)	2019
38	C. Gebhardt	Robust computational procedures for the nonlinear dynamic analysis of beam and shell structures (Habilitationsschrift)	2020
39	A. Haldar	Multistable morphing structures using variable stiffness laminates (Dissertationsschrift)	2020
40	R. Unger	Multi-scale constitutive modelling of nanoparticle/epoxy nanocomposites: Molecular simulation-based methods and experimental validation (Dissertationsschrift)	2020
41	J. Fankhänel	A Multi-Scale Framework for Nanocomposites including Interphase and Agglomeration Effects (Dissertationsschrift)	2020
42	N. Penner	Monitoring ambient angeregter baodynamischer Systeme durch mehrschichtige Perzeptren (Dissertationsschrift)	2021
43	C. Gerendt	A finite element-based continuum damage model for mechanical joints in fiber metal laminates under static and fatigue loading: Theory and experimental validation (Dissertationsschrift)	2022
44	M. Brod	Damage prediction of unidirectional fiber composites under cyclic loading with different amplitudes (Dissertationsschrift)	2022
45	R. Berger	Multi-Objective Structural Optimization of Repairs of Blisk Blades (Dissertationsschrift)	2022
46	G. Balokas	Metamodel-based uncertainty quantification for the mechanical behavior of braided composites (Dissertationsschrift)	2022
47	S. Wernitz	Damage Localization in Data-Driven Vibration-Based Structural Health Monitoring Using Linear Quadratic Estimation Theory (Dissertationsschrift)	2022
48	B. Daum	On the computational analysis of microbuckling via mesoscale approaches (Habilitationsschrift)	2022

49	N. Safdar	A Stochastic Failure Investigation of Composites under Combined Compression-Shear Loads (Dissertationsschrift)	2022
----	-----------	---	------